Spatially tunable spin interactions with Rydberg atoms in optical tweezers

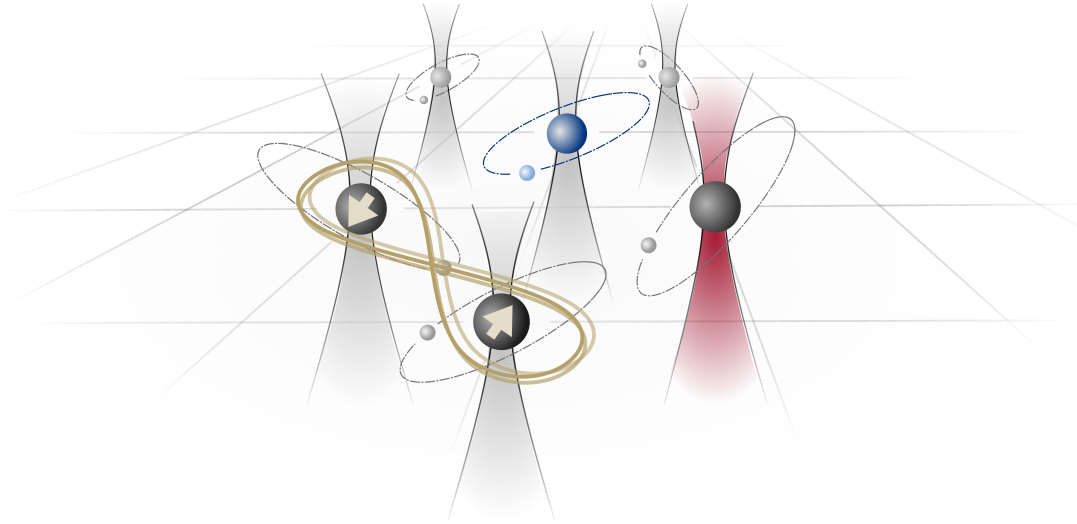

Lea-Marina Steinert

Tübingen
2023

Spatially tunable spin interactions with Rydberg atoms in optical tweezers

Dissertation
der Mathematisch-Naturwissenschaftlichen Fakultät
der Eberhard Karls Universität Tübingen
zur Erlangung des Grades eines
Doktors der Naturwissenschaften
(Dr. rer. nat.)

vorgelegt von
Lea-Marina Steinert
aus Ulm

Tübingen
2023

Gedruckt mit Genehmigung der Mathematisch-Naturwissenschaftlichen Fakultät der Eberhard Karls Universität Tübingen.

Tag der mündlichen Qualifikation:	19.Dezember 2023
Dekan:	Prof. Dr. Thilo Stehle
1.Berichterstatter:	Prof. Dr. Christian Groß
2.Berichterstatter:	Prof. Dr. Igor Lesanovsky
3.Berichterstatterin:	Assoc. Prof. Monika Schleier-Smith

Zusammenfassung

Quantensimulatoren erweisen sich insbesondere dann als wertvolles Instrument, wenn konventionelle Computer und gängige Rechenmethoden bei der Modellierung von komplexen, stark korrelierten Vielteilchensystemen an ihre Kapazitätsgrenzen geraten. Ihre Stärke liegt in ihrer ressourcenschonenden, analogen Umsetzung des zu untersuchenden Hamilton-Operators. Von den zahlreich etablierten Plattformen zur Entwicklung funktionaler Quantensimulatoren, erweisen sich jene als besonders vielversprechend, welche einzelne Atome in flexiblen Anordnungen von optischen Pinzetten halten und positionieren. Die Wechselwirkung zwischen den Atomen kann kontrolliert eingestellt werden durch die Anregung der Atome zu hochenergetischen sogenannten Rydberg-Zuständen.

In unserer experimentellen Plattform präparieren wir einzelne Kaliumatome in optischen Pinzetten und regen diese zu Rydberg-Zuständen an. Die Kopplung an diese Zustände erfolgt entweder durch direkte, resonante Anregung oder durch das sogenannte 'Rydberg-Dressing', bei welchem einem Grundzustandsatom ein einstellbarer Anteil von Rydberg-Atom-Eigenschaften verliehen wird. Um Rydberg-Dressing in unserem experimentellen Aufbau realisieren zu können, kühlen wir zunächst die Atome mittels Raman-Seitenbandkühlung nahe ihres Bewegungsgrundzustands. Dieser Schritt ist essenziell, da ansonsten thermische Effekte jeden weiteren experimentellen Schritt dominieren würden.

Für die Anregung der Grundzustandsatome zu Rydberg-Zuständen nutzen wir einen Einzelphotonenübergang, für das ein Lasersystem konstruiert wurde, welches bis zu $1\,\mathrm{W}$ ultraviolettes Licht bei $286\,\mathrm{nm}$ erzeugt. Diese Umsetzung ermöglicht zunächst eine mikroskopische Untersuchung von kaskadenartigen Verlustphänomenen, die wir während der Implementierung des Rydberg-Dressings beobachteten. Diese Verluste führen wir auf Kontaminationen durch Atome in verschiedenen Rydbergzuständen zurück, die infolge von Schwarzkörperstrahlung induzierten Übergänge auftreten. Solche Kontaminationen können Dipol-Dipol-Wechselwirkungen auslösen, was zu Resonanzen von Rydberg-Paarzuständen führen kann. Dies fördert eine beschleunigte Anregung und verkürzt die Lebensdauer des Rydberg-dressed Zustands, was unsere experimentellen Daten untermauert.

Basierend auf diesen Erkenntnissen und Herausforderungen, richtet sich danach unser Haupt-augenmerk auf die Umsetzung von Ising- und XYZ-Spin Modellen. Das zugrundeliegende effektive Spin-1/2-System wird dabei innerhalb der Hyperfeinstruktur-Grundzustände kodiert. Dies ermöglicht es uns, die Wechselwirkungen durch die nicht-resonante Kopplung an Rydberg-Zustände gezielt einzustellen und durch eine geschickte Wahl von Laserparametern die unterschiedlichen Spin-Achsen zu kontrollieren.

Zusammenfassend zeigt die vorliegende Arbeit die erfolgreiche Realisierung von Rydberg-Dressing-Experimenten mit einzelnen Kaliumatomen in optischen Pinzetten. Wir analysierten die grundlegenden Mechanismen im Rydberg-Dressing-Regime und demonstrierten, wie Spin-Wechselwirkungen gezielt eingestellt werden können. Unsere Ergebnisse unterstreichen das erhebliche Potenzial des Rydberg-Dressing-Verfahrens um eine flexible Realisierung von Hamilton-Operatoren in analogen Quantensimulatoren zu ermöglichen.

Abstract

Quantum simulation is a valuable tool for investigating complex quantum systems. It bridges theory and experiment, especially when standard computational methods fail to handle the complexities of strongly correlated many-body scenarios. The effectiveness of quantum simulators arises from their hardware-efficient analog representation of the Hamiltonian under study. Among the emerging platforms, simulators employing Rydberg atoms in optical tweezer arrays are particularly promising.

Within this thesis, we detail an experimental platform using single potassium atoms confined within optical tweezer arrays. Interactions between these atoms are induced via excitation to Rydberg states, characterized by high principal quantum numbers. The coupling to Rydberg states can be achieved through direct, resonant excitation or off-resonant Rydberg dressing, where the ground state atom is admixed with a fraction of the Rydberg atom character. In our approach, we trap and cool individual atoms near their motional ground state using Raman sideband cooling. This technique represents an important enhancement in the experiment, thus, making Rydberg dressing feasible, which would otherwise be constrained by thermal broadening.

We directly excite the ground state atoms to Rydberg states using a single-photon transition, performed by a laser system that generates up to $1\,\mathrm{W}$ of ultra-violet light at $286\,\mathrm{nm}$. This setup facilitates a microscopic study of black-body radiation-induced contaminations of Rydberg states, observed as an avalanche loss process within the atom array. The underlying mechanism for these losses is the dipole-dipole interaction shifts originated by the impurities. These shifts render a previously detuned laser resonant with a Rydberg pair state, consequently reducing the experimentally observed dressed state lifetime. Our findings confirm that the interactions catalyze these accelerated excitations.

Furthermore, we can tailor interactions for both Ising-type and XYZ-type spin models via off-resonant coupling to Rydberg states when encoding the effective spin-1/2 system within the electronic ground states. This configuration enables us to design spin-spin couplings across the different spin directions determined by the chosen laser parameters.

To conclude, our work successfully demonstrates Rydberg dressing experiments within optical tweezer arrays of single potassium atoms. We have studied the underlying processes in the Rydberg dressing regime and validated our ability to tune spin interactions within the array through Rydberg dressing. Overall, our findings underscore the potential of Rydberg dressing in paving the way for advanced Hamiltonian design in analog quantum simulators.

Contents

List of Figures

Chapter 1

Introduction

At the core of science is the quest to deepen our understanding of the natural world, improve accuracy in predictions, and solve complex problems. Gaining a deep understanding of interacting quantum many-body systems is a fundamental yet challenging task in modern physics. These complex systems underpin various phenomena across multiple disciplines. Examples include exotic forms of quantum magnetism [1–4], high-temperature superconductivity [5–7], nuclear magnetic resonance spectra [8], protein folding mechanisms [9], and even cancer cell modelling [10]. The complexity and high degree of correlation in these systems pose computational challenges that exceed the capabilities of traditional simulation techniques and analytical methods [11, 12].

This puzzle led Richard Feynman to ask a groundbreaking question in 1982: "Can these [quantum systems] be simulated using a new kind of computing device - a quantum computer?" [13] and therefore obtain a "probabilistic simulator of a probabilistic nature" [13] as an alternative way to handle these complex systems. Two primary strategies have been developed for quantum simulation. The first approach, known as "analog quantum simulation," involves a second, physical quantum system that is specifically engineered to mimic the behavior and characteristics of the system under study [11, 12]. The second approach employs a generalized quantum computer, operating with quantum gates, to simulate the system in question [14, 15]. The latter approach builds upon conventional computing architectures while leveraging the unique properties of quantum mechanics.

However, analog quantum simulators possess a unique advantage over their digital counterparts: they naturally evolve under their own Hamiltonian while providing a hardware-efficient representation of the system under study. Various platforms have been developed to investigate a range of quantum phenomena, each offering a high level of control over individual quantum particles [11, 12, 16–18]. Among these, simulators that utilize arrays of neutral atoms have proven particularly effective for exploring complex many-body systems. These arrays are typically generated via optical lattices or optical tweezers. Optical lattices emerge from the interference of multiple laser beams, which create a periodic light pattern that replicates, for example, the crystal structure of a solid [17, 19]. On the other hand, optical tweezers use various technologies like holography with spatial light modulators [20–25], acousto-optic deflectors [26–28], or microlens arrays [29]. These technologies are combined with a microscope objective, forming tightly focused beams of light capable of trapping individual atoms [30].

In these systems, interactions can be precisely engineered using Rydberg states, which are highly excited states characterized by a large principal quantum number and exaggerated atomic properties [18, 25, 31]. Notably, the spatial scaling of these interactions is on the order of a few micrometers, which closely aligns with the typical atom-trapping distances achievable in such atomic arrays [32–50]. In contrast to solids, where electron to phonon coupling leads to energy dissipation, these atomic arrays act as almost fully isolated quantum systems and exhibit coherent dynamics over long periods [25]. Numerous research groups have achieved not only large system sizes but also extended coherence times utilizing the properties of Rydberg atoms [39, 42]. These accomplishments make the platforms highly effective for simulating quantum magnets through, for example, direct excitation to Rydberg states, whether in equilibrium states [49, 51, 52] or under dynamic conditions [53].

Another intriguing approach to studying these systems involves off-resonant coupling of electronic ground states to Rydberg states, thereby introducing only a fraction of the Rydberg character to the ground-state atoms. This technique not only offers additional control parameters, which facilitates the manipulation of interactions to explore various quantum many-body systems, such as Ising quantum magnets or gates [54–56], but also allows for arbitrary single particle terms to be implemented in the ground state [57, 58].

The ultimate goal of these quantum simulators is to develop a platform capable of universally programmable analog qubit couplings. Nevertheless, while these simulators and their associated replication methods do reduce control overhead, they come with limitations. Specifically, they are often constrained to problems that are intrinsically tied to the characteristics of the device-dependent platform, making it a significant challenge to achieve this ultimate objective of universal programmability.

This work reports on the progress in this direction by implementing Rydberg dressing in optical tweezer arrays using single ^{39}K atoms. The choice of potassium offers distinct advantages, particularly its small fine structure and ground-state energy splittings [59–61]. These attributes help to reduce vector shifts in the traps. Furthermore, we successfully generate both Ising-type by single-color and freely tunable short-range XYZ-type spin interactions by two-color Rydberg dressing. Importantly, this work marks the first realization of these XYZ-type spin interactions in tweezer arrays through two-color Rydberg dressing [4, 62]. While we demonstrate the spatial dependence and tunability of the system, it currently operates in an incoherent regime due to existing technical limitations. The major limitations are the Rydberg excitation laser phase noise and trap depth inhomogeneities within the tweezer array, which will be discussed in detail throughout this thesis. Despite the many advantages of Rydberg states, they are prone to rapid decoherence caused by environmental and technical factors, that compromises the simulation's accuracy over extended periods [63].

Accordingly, this work outlines these limitations and discusses various solutions to address the issues inherent in Rydberg dressing. Our results highlight the significant progress and remarkable opportunities that Rydberg dressing offers for Hamiltonian design in analog quantum simulators.

Outline

This thesis is structured as follows:

In Chapter 2, we highlight the advantageous characteristics of Rydberg atoms that make them particularly suitable for quantum simulation.

In Chapter 3, we present the process of loading, cooling, and preparing single atoms within optical tweezer arrays. In addition, we describe the challenge of trap depth homogeneity, detail our approach to Raman sideband cooling in optical tweezer arrays, and its benefits to our experiment. Additionally, we investigate how Raman transitions are implemented for precise and coherent control over the ground state.

In Chapter 4, we describe the derivation of Rydberg interactions and introduce our single-photon Rydberg excitation laser setup. The excitation laser phase noise, a key limitation in the presented Rydberg measurements, is discussed. This chapter also provides insights into the first Rydberg dressing measurements, especially concering the lifetime of Rydberg dressed states. It also demonstrates measurements of the dynamics of Ising-type spin interactions via single-color Rydberg dressing.

In Chapter 5, we introduce our two-color Rydberg dressing scheme, laying the foundation for realizing tunable spin interactions. While our measurements demonstrate the spatially-dependent interactions, we also discuss the present technical challenges that hinder us from measuring coherent interactions.

Publications

The following articles have been published in the context of this thesis:

Spatially tunable spin interactions in neutral atom arrays
Lea-Marina Steinert, Philip Osterholz, Robin Eberhard, Lorenzo Festa, Nikolaus Lorenz, Zaijun Chen, Arno Trautmann, Christian Groß
Phys. Rev. Lett. 130, 243001 (2023)

Blackbody-radiation-induced facilitated excitation of Rydberg atoms in optical tweezers
Lorenzo Festa, Nikolaus Lorenz, Lea-Marina Steinert, Zaijun Chen, Philip Osterholz, Robin Eberhard, Christian Groß
Phys. Rev. A. 105, 13109 (2022)

Raman Sideband Cooling in Optical Tweezer Arrays for Rydberg Dressing
Nikolaus Lorenz, Lorenzo Festa, Lea-Marina Steinert, Christian Groß
SciPost Phys. 10, 052 (2021)

Chapter 2

Properties of Rydberg atoms

The beginning of Rydberg physics can be traced back to the late 19th century when Balmer and Rydberg formulated a series explaining the spectral lines of atomic hydrogen [64]. This pioneering work revealed the existence of highly excited atomic states, now known as Rydberg atoms, characterized by one electron orbiting far from the nucleus, leading to their distinct and exaggerated properties [65]. For years, these atoms were more subject of theoretical fascination. However, at the beginning of the 20th century, the advancements in experimental techniques marked a turning point. Since then, efforts in the field have grown rapidly, starting with new approaches and many new platforms of quantum technology [32, 46, 66]. In this chapter, our goal is to understand the scaling of Rydberg properties and to demonstrate their suitability for implementation into these experimental frameworks.

2.1 The anatomy of Rydberg atoms: structure and energy levels

We first turn our attention to the key characteristics of Rydberg atoms, namely their binding energy and wavefunction. The mentioned historical description led to the derivation of the energy level spacing of hydrogen, given by $E_n = -R_\infty/n^2$, where R_∞ is the Rydberg constant [64, 65, 67]. However, when increasing the number of electrons in an atom, this formula no longer accurately predicts the energy levels. This discrepancy necessitates the introduction of quantum defect theory, which accounts for deviations in atomic energy levels caused by electron-electron interactions [68]. In our experiment, we work with the alkali metal ^{39}K. Characterized by one valence electron in the outermost $4S$ shell (with S denoting the electronic angular momentum state $\ell = 0$), we can effectively model this electron as orbiting around a single positively excited core, much like the hydrogen atom. With correction factors from quantum defects arising from the core electrons, we obtain the binding energies as

$$E_{n\ell j} = -\frac{R^*}{(n-\delta_{n\ell j})^2} = \frac{R^*}{(n^*)^2} \propto (n^*)^{-2}. \tag{2.1}$$

For ^{39}K, the mass-corrected Rydberg constant is $R^* = m_K/(m_K + m_e) \cdot R_\infty$, where m_e represents the mass of the electron and m_K the mass of ^{39}K. In this scenario, n^* is the

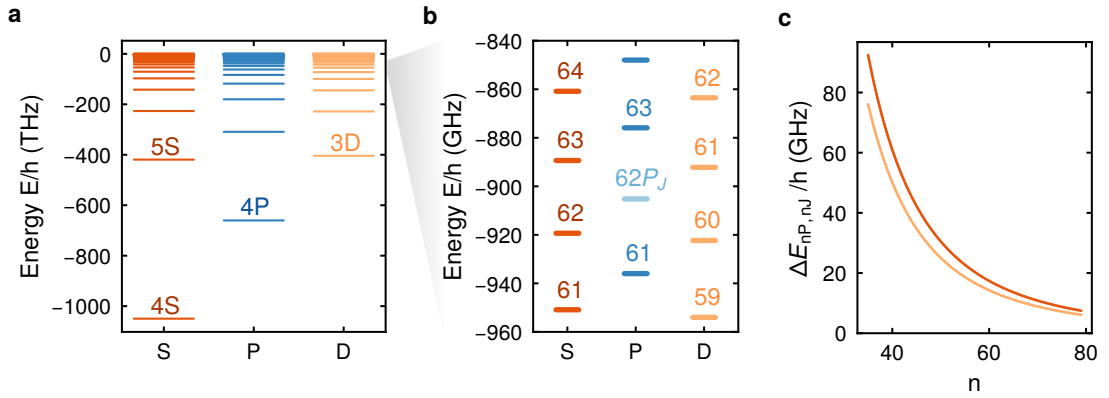

Figure 2.1 Energy level structure of ^{39}K. a. Depicted are the binding energies for the various $nS_{1/2}$ ($\ell = 0$, red), nP_J ($\ell = 1$, blue), and nD_J ($\ell = 2$, yellow) orbital angular momentum states, characterized by the quantum number ℓ. The energy levels were computed using ARC [68], which builds upon the NIST [69] database and the data of quantum defects from reference [70]. **b.** Zoom into a focusing on the Rydberg manifold surrounding the $62P_j$ state. This particular state was selected as it represents the Rydberg state with which the experiments in this thesis are performed. **c.** Calculated energy splittings $\Delta E_{nP,nj}$ between $nP_{3/2}$ and $(n+1)S_{1/2}$ states (dark orange), and between $nP_{3/2}$ and $(n-1)D_{3/2}$ states (light orange) are displayed. This highlights the diminishing energy splitting with an increasing principal quantum number n, signifying their experimental practicability with standard microwave sources.

effective principal quantum number, including the quantum defects $\delta_{n\ell j}$. Here, the principal quantum number n, the orbital angular momentum ℓ and the electron's total angular momentum j factor into this formula. The varying energy levels for potassium are depicted in Fig. 2.1. Notably, when increasing ℓ, the influence of the quantum defect reduces. This becomes particularly pronounced in circular states with $\ell = n-1$ and $m_\ell = \pm\ell$, where the valence electron orbits with nearly zero radial extents, resembling almost a classical orbit around the nucleus [71].

The next significant characteristic of Rydberg states is the size of their wavefunction. To understand this, we consider the separability of atomic wavefunctions into their radial $R_{n\ell}(r)$ and spherical components $Y_{\ell jm}(\theta,\phi)$:

$$\Psi_{n\ell jm} = R_{n\ell}(r) \cdot Y_{\ell jm}(\theta,\phi). \tag{2.2}$$

The separability facilitates a numerical solution of the Schrödinger equation using the radial component:

$$\left[-\frac{1}{2\mu}\left(\frac{d^2}{dr^2} + \frac{2}{r}\frac{d}{dr}\right) + \frac{\ell(\ell+1)}{2\mu r^2} + V(r)\right] R_{n\ell}(r) = E_{n\ell j} R_{n\ell}(r). \tag{2.3}$$

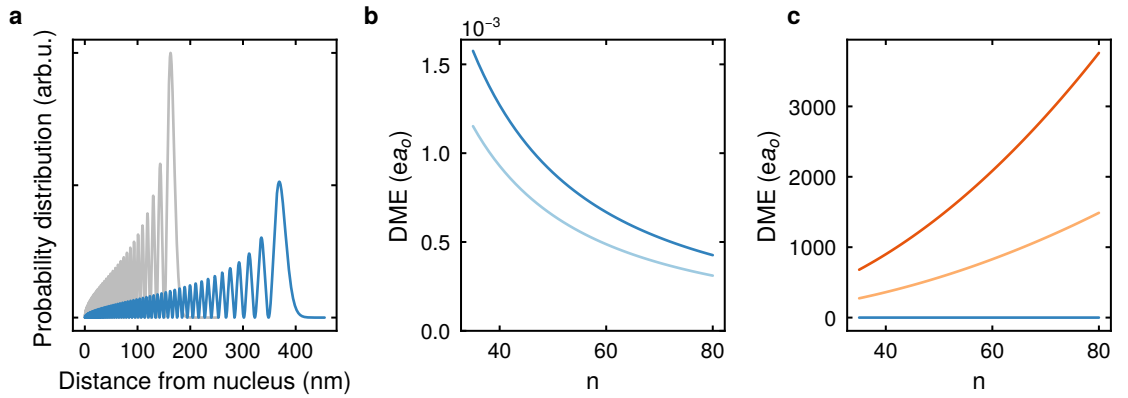

Figure 2.2 Scaling of Rydberg wavefunction and Rydberg state dipole matrix elements. a. Exemplary shown are the calculated wavefunctions for two Rydberg states, the $62P_{3/2}$ (blue) and $42P_{3/2}$ (grey) for the probability distribution $|rR(r)|^2$, illustrating the exaggerated size of Rydberg atoms. **b.** Computed dipole matrix elements (DME) between the electronic ground state $|4S_{1/2}, m_J = -1/2\rangle$ and the Rydberg $|nP_{1/2}, m_J = +1/2\rangle$ state (light blue) and the $|nP_{3/2}, m_J = -3/2\rangle$ (dark blue) state. These matrix elements underscore the characteristic transition probabilities between ground and Rydberg states, based on the spatial overlap of the ground state and the wavefunction of the Rydberg state. **c.** Dipole matrix elements (DME) are computed between various Rydberg states: between $|nP_{3/2}, m_J = -3/2\rangle$ and $|(n+1)S_{1/2}, m_J = -1/2\rangle$ (dark orange), and also between $|nP_{3/2}, m_J = -3/2\rangle$ and $|(n-1)D_{3/2}, m_J = -1/2\rangle$ (light orange). These values present a strong contrast, differing by approximately six orders of magnitude when compared to the DME depicted in b. For reference, the dark blue line from b is included to emphasize this difference. The origin of these substantial DMEs can be attributed to the large size of the Rydberg atoms, given by the considerable distance between the Rydberg electron and the nucleus.

Here, the reduced mass is given by $\mu = m_K m_e/(m_K + m_e)$, and the potential $V(r)$ contains the Coulomb potential at large distances, adjustments for the influence of the valence electron at short distances and a (relativistic) spin-orbit interaction term[68].

In the absence of a magnetic field, all projection number m_j substates for the total angular momentum j are degenerate. However, many experiments are performed in the presence of non-zero fields, causing a splitting in the energy of the m_j states. The dependence of the wavefunction on j is originated in the quantum defects and a result of the spin-orbit coupling, which is included as a correction term in $V(r)$ [68]. Analyzing the Rydberg wavefunction and computing the root-mean-square distance of electrons in Rydberg states, one obtains the wavefunction scaling $\propto (n^*)^2$. Fig. 2.2 shows the probability distribution $|rR(r)|^2$ of the atomic wavefunction for two distinct Rydberg states, $62P_{3/2}$ and $42P_{3/2}$. This emphasizes the wavefunction's size significant scaling with n. This size can be compared to the one of the ground state of $\approx 2\,$Å. As n increases, it is possible to reach a point where the wavefunction's size surpasses the tweezer spacing, usually in the range of a few micrometers. For instance, at $n = 200$, the wavefunction spans roughly $4\,\mu$m.

2.2 Rydberg atoms' practical aspects: transitions and couplings

Building on our understanding of the energy and wavefunction structure of Rydberg atoms, we now focus on the dipole matrix elements. These lay the foundation to understand the couplings and interactions of Rydberg states elaborated in Section 4.1. The matrix element of the dipole operator $\hat{\mathbf{d}} = e\hat{\mathbf{r}}$ between two (for example Rydberg) states $|r_A\rangle = |n_a, \ell_a, j_a, m_a\rangle$ and $|r_B\rangle = |n_b, \ell_b, j_b, m_b\rangle$ can be represented as:

$$\mathbf{d}_{ab} = \langle r_a | e\hat{\mathbf{r}} | r_b \rangle. \tag{2.4}$$

Furthermore, we express $\hat{\mathbf{r}}$ in terms of the spherical basis $\hat{\mathbf{r}} = \{\hat{r}_{-1}, \hat{r}_0, \hat{r}_{+1}\}$. Here, $\hat{r}_0 = \hat{z}$ and $\hat{r}_{\pm 1} = \mp 1/\sqrt{2}(\hat{x} \pm i\hat{y})$ [72]. This allows us to introduce the parameter $q \in -1, 0, +1$, which are arising from applying the selection rules. For instance, $\hat{r}_0$ can only couple states with $\Delta m = 0$ states and so on. This parameter allows an easier formalism in the subsequent formulae. Relying on the separation in Eq. (2.2) and following references [68, 72, 73], the dipole matrix element can be presented as:

$$\begin{aligned} \mathbf{d}_{ab} &= \langle n_a, \ell_a, j_a, m_a | e\hat{\mathbf{r}} | n_b, \ell_b, j_b, m_b \rangle \\ &= (-1)^{j_a + j_b + \ell_b + s - m_a + 1} \begin{Bmatrix} 1 & \ell_b & \ell_a \\ s & j_a & j_b \end{Bmatrix} \langle n_a \ell_a j_a || r || n_b \ell_b j_b \rangle \sum_q \mathbf{e}^q \begin{pmatrix} 1 & j_a & j_b \\ q & m_a & -m_b \end{pmatrix} \end{aligned} \tag{2.5}$$

where the spherical unity vector is denoted as $\mathbf{e}^q$. We have also introduced the spin of the electron $s = 1/2$. The round and curly brackets represent the Wigner-3j and Wigner-6j symbols, respectively. These symbols significantly simplify the calculation and formalism. Specifically, the 3-j symbol evaluates the coupling between two distinct total angular momenta $j_{a,b}$ with respective projections $m_{a,b}$, while the 6-j symbol combines three angular momenta. Notably, these symbols can be transformed using the Clebsch-Gordan coefficients [72]. The term $\langle n_a \ell_a j_a || r || n_b \ell_b j_b \rangle$ is directly proportional to the integral of the radial wavefunctions of the two given states.

In Fig. 2.2, we present calculations for the dipole matrix element between the ground state $|4S_{1/2}, m_j = -1/2\rangle$ and the Rydberg states $|nP_{3/2}, m_j = -3/2\rangle$ and $|nP_{1/2}, m_j = 1/2\rangle$. Additionally, we depict the dipole matrix elements for transitions between various Rydberg states. Remarkably, there is a difference of six orders of magnitude between these cases. For instance, when coupling from the ground state to the $|62P_{3/2}\rangle$ state, we obtain a dipole matrix element of $d_{ab} = 6.3 \cdot 10^{-4}\,\mathrm{ea_o} \propto (n^*)^{-3/2}$ [74], where e denotes the electron charge and a_0 represents the Bohr radius. The scaling is based on spatial overlap between the ground state and the Rydberg state wavefunction. In contrast, the coupling between this Rydberg state and the $|61D_{3/2,m_j=-1/2}\rangle$ Rydberg state yields $d_{ab} = 886\,\mathrm{ea_o} \propto (n^*)^2$ [74], which is due to the exaggerated size of the Rydberg atoms and thus the large distance from the respective nucleus. Comparing this value to ^{87}Rb, another alkali metal quite

commonly used in experiments, the ground state coupling is almost a factor of three smaller. This difference directly affects the Rydberg state lifetime, a topic we will address in the subsequent section.

The modest dipole matrix elements between the ground and Rydberg states directly impact the Rabi frequencies. To derive these, we introduce the coupling between the nuclear spin **I** and the total electronic angular momentum **J**. For ^{39}K, the nuclear spin is $I = 3/2$, and for the ground state, we obtain $J = 1/2$. The total angular momentum F is then $\mathbf{F} = \mathbf{I} + \mathbf{J}$. The ground state hyperfine splitting between the two hyperfine states $F = 1$ and $F = 2$ of the $4S_{1/2}$ ground state is $462\,\mathrm{MHz}$. When determining the Rabi couplings, it is important to note that the projection of the nuclear spin is not considered, as it remains unchanged throughout the transition. By driving transitions with a field strength denoted by $\boldsymbol{E} = \epsilon E_0 \cos \omega t$, the Rabi coupling can be expressed as [74]:

$$\hbar\Omega = eE_0 \langle n_a, \ell_a, j_a, m_a | \epsilon \cdot \hat{\mathbf{d}} | n_g, \ell_g, j_g, F_g, m_{F,g} \rangle. \tag{2.6}$$

Another essential characteristic of Rydberg atoms is their polarizability. This can be estimated using the second-order perturbation theory of the atom's Hamiltonian $H = H_0 + \mathbf{E}_{dc}$ [65]. In this context, we investigate the Hamiltonian of the Rydberg atom when subjected to an external electric field $\mathbf{E}_{dc}$. By treating this field as a perturbation, we directly derive the DC Stark shift $\Delta_{dc} \approx \alpha E_{dc}^2$, where the polarizability α is given by:

$$\alpha = \sum_i \frac{|\langle n_a \ell_a j_a m_a | \hat{z} | r_i \rangle|^2}{\Delta E_{r_i}} \propto (n^*)^7 \,. \tag{2.7}$$

In this expression, $\sum_i |r_i\rangle$ sums over all nearby Rydberg states. The energy spacing between these states is defined by $\Delta E_{r_i} = E_{n\ell j} - E_{r_i}$. Utilizing the scaling of the dipole matrix element between neighboring Rydberg states as $(n^*)^2$ and the scaling of the energy separation between nearby states $\Delta E_{r_i} \propto (n^*)^{-3}$, we deduce that the polarizability scales with the seventh power of the reduced principal quantum number [65].

Consequently, Rydberg atoms exhibit a pronounced response to external electric fields, meaning they can be controlled and manipulated using such fields. Additionally, this amplified polarizability is the origin of the strong long-range interactions, which we will delve into in Section 4.1. All these features render Rydberg atoms as attractive candidates for quantum technologies [25, 31, 32, 46].

2.3 The extended lifetime of Rydberg atoms

Rydberg atoms exhibit an extended lifetime, which proves valuable for quantum simulation and information processing. This extended lifetime is rooted in the small matrix elements to low lying states and expands the experimental duration available during a single measurement to microseconds or milliseconds, depending on various parameters. We will now take a closer look at these scalings and parameters.

The lifetime of a Rydberg state is primarily constrained by two factors. Firstly, the radiative spontaneous decay back to the low-lying (ground) states, represented as $1/\tau_{\text{spon}}$. Secondly, the transition to neighboring Rydberg states, stimulated by the thermal black-body microwave background, defined as $1/\tau_{bb}$. We will further discuss the impact of both factors on the Rydberg state lifetime:

$$1/\tau = 1/\tau_{\text{spon}} + 1/\tau_{bb}\,. \tag{2.8}$$

The connection between these terms is shown in Fig. 2.3. Spontaneous decays can be quantified using the Einstein A coefficient and summing over all possible decay channels to the lower-lying states [65]:

$$\tau_{\text{spon}} = \sum_j A_{ji} = \sum_j \frac{16\pi^3 e^2 \nu_{ji}^3}{3\epsilon_0 h c^3} \frac{\ell}{2\ell+1} |R_{ij}|^2\,. \tag{2.9}$$

In this equation, ν_{ji} denotes the transition frequency between the initial Rydberg state i and a decay state j, while R_{ij} represents the radial matrix element between these two Rydberg states. Notably, following Fermi's golden rule, the ground states have the most significant influence here, primarily due to their high transition frequency in the numerator. The scaling is subsequently proportional to the radial matrix element, leading to a relation $\tau_{\text{state}} \propto (n^*)^3$. The decays due to black-body radiation are governed by Planck's law:

$$1/\tau_{bb} = \sum_j \frac{A_{ji}(\nu_{ji})}{\exp(h\nu_{ji}/k_B T) - 1}\,. \tag{2.10}$$

From the exponential decay term, it is evident that the probability of the microwave background radiation facilitating a transition diminishes as the transition frequency increases. In other words, decays to lower-lying states become almost negligible when considering black-body transitions, resulting in a peaked black-body transition rate profile: The rate first rises steeply, peaks, and then decreases more slowly at higher principal quantum numbers [68]. Here, the temperature modifies both the peak's amplitude and the gradual decrease, indicating that transitions involving higher principal quantum numbers (and thus longer transition wavelengths) become more apparent at higher temperatures. The effect of black-body radiation on the decay scales as $\tau_{bb} \propto (n^*)^2$.

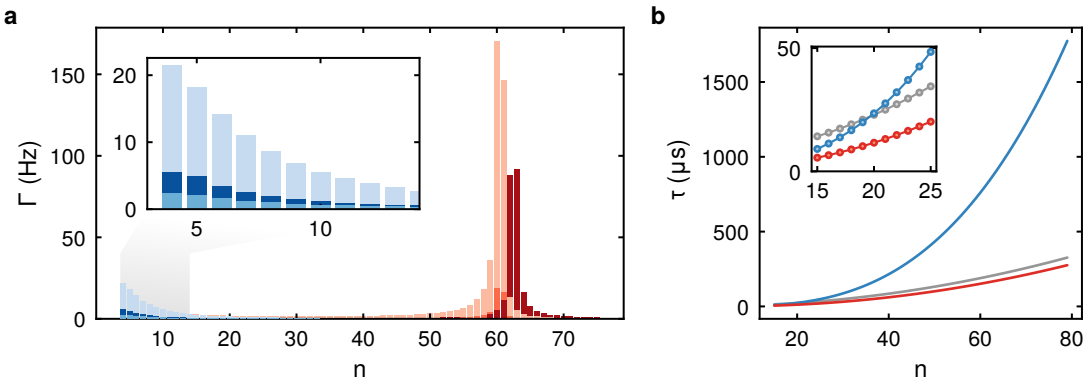

Figure 2.3 Rydberg state lifetime. a. Histogram of decay channels for the $62P_{3/2}$ Rydberg state. Without black-body decay included, only spontaneous decay into low-lying states occurs (depicted in blue). The transitions are, in order from dark blue to light blue, to the $nS_{1/2}$, $nD_{3/2}$, and $nD_{5/2}$ states. The inset provides a closer look at transitions from $n = 4$ to $n = 15$. At a temperature of $300\,\mathrm{K}$, black-body radiation induces transitions to nearby Rydberg states, which are indicated in shades of red - dark red to light red represent transitions to the $nS_{1/2}$, $nD_{3/2}$, and $nD_{5/2}$ states, respectively. **b.** Calculated lifetimes include: the Rydberg state lifetime without black-body influence, represented as τ_{spon} (in blue); the state-dependent black-body transition lifetime at $300\,\mathrm{K}$, represented as τ_{bb} (in grey); and the black-body reduced lifetime, represented as $\tau_{\mathrm{ryd,bb}}$ (in red). The inset zooms into the states with principal quantum numbers ranging from $n = 15$ to $n = 25$, showing that at $n = 19$ the black-body transition equates the Rydberg state lifetime and is for larger principal quantum numbers dominating the black-body reduced lifetime $\tau_{\mathrm{ryd,bb}}$.

Comparing the scaling of both spontaneous and black-body decays, we can identify a specific principal quantum number at which these two rates become equal. This point of convergence is depicted in the inset of Fig. 2.3. For high principal quantum numbers at room temperature $(300\,\mathrm{K})$, black-body decay becomes predominant and sets the scaling tone. Referring to Fig. 2.3, one can observe that for a principal quantum number of $n = 62$, a state lifetime of $841\ \mu\mathrm{s}$ would be anticipated in the absence of black-body transitions. Yet, at room temperature, this lifetime gets reduced by a factor of five, yielding an actual lifetime of $160\ \mu\mathrm{s}$.

Without the black-body losses, the radiative lifetimes for ^{39}K would be about 60% longer than those for ^{87}Rb. However, since black-body losses dominate, both alkali metals face similar operational conditions, resulting in roughly equivalent black-body-limited lifetimes, despite the differences in the ratios between black-body and ground state decays.

In this chapter, we studied the properties of Rydberg atoms, characterized by their energy structure and wavefunction, which make them highly sensitive to external fields. We derived typical scalings for couplings to and within Rydberg states and highlighted their extended lifetimes. In the following chapter, we will introduce the experimental platform designed to leverage the distinctive properties of Rydberg atoms.

Chapter 3

Preparation of single ^{39}K atoms in optical tweezer arrays

Over the last few decades, Rydberg atoms trapped in optical tweezers have attracted significant attention mainly due to their long-range interactions, prolonged coherence, and the scalability of tweezer arrays, which opened up new paths for quantum simulation, quantum computing and the study of quantum many-body systems. In our experiment, we work with single ^{39}K atoms confined within adjustable tweezer arrays and probe interactions via (detuned) excitations to Rydberg states.

This chapter will introduce the most relevant features of this thesis' experimental setup and procedures. Most of the measurements in this thesis follow the exemplary sequence shown in Fig. 3.1.

The sections are structured as follows. First, the setup and technique for trapping single ^{39}K atoms in optical tweezers are described in Section 3.1, followed by a description of the fluorescence imaging technique in Section 3.2. However, after taking most of the data discussed in this thesis, there were numerous refinements and modifications to the techniques for loading, cooling, and imaging single atoms. For documentary reasons, we also present the updated status of the experiment in Section 3.3.

The atom's remaining finite temperature leads to a thermal broadening of the Rydberg transition, which imposes a severe limitation for Rydberg experiments. To overcome this issue, we cool the atoms close to their motional ground state via Raman sideband cooling (RSC), as described in Section 3.4. Next, we implemented a coherent ground state control technique to perform interferometry measurements, as shown in Section 3.5.

All sections will only focus on details relevant to this thesis' measurements. The complete technical details of the vacuum system and the experiment's laser setups have been described in the Ph.D. theses of Nikolaus Lorenz and Lorenzo Festa [60, 75].

3.1 Loading atoms in optical tweezers

The first step of every experimental sequence is loading optical tweezer arrays with single atoms, which we focus on in this chapter. In the measurements presented in the upcoming

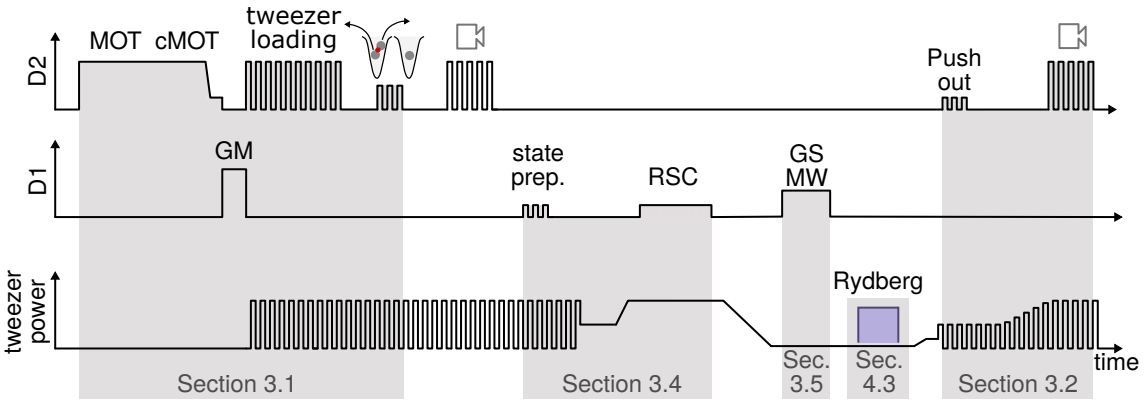

Figure 3.1 Exemplary experimental sequence. Atoms are loaded in a magneto optical trap (MOT), and further compressed using the compressed MOT (cMOT) and grey molasses cooling(GM). The tweezers are loaded using a chopped molasses technique [76], and followed by a parity projection pulse, resulting in singly occupied traps. Then, a first fluorescence picture is taken. Afterward, we continue with a state preparation pulse, preparing all the atoms in the $|F = 2, m_F = \pm 2\rangle$ state. Further, we continue with cooling the atoms to the motional ground state via Raman sideband cooling (RSC). In the case of interferometry measurements, we apply a ground state control pulse (GS MW) and continue with a pulse of Rydberg excitation laser. In the case of spin-selective imaging, we remove atoms in the $|F = 2\, m_F = \pm 2\rangle$ state from the tweezer array via a push out pulse on the closed D2 cycling transition before taking a second fluorescence image. Comparing both fluorescence images gives insights into the physics and dynamics applied between them.

chapters, we load the tweezers with atoms by alternating between trapping light and near-resonant D2-light, following the method detailed in reference [76]. Please refer to Appendix A for the ^{39}K D1 and D2 level scheme. A key aspect of this method is ensuring the pulsing frequency of the trapping and near-resonant light is significantly higher than the trapping frequency of the tweezers. However, after a more in-depth study of the loading process, we were able to simplify the loading procedure. Now, the tweezers can be filled during the compressed magneto optical trap (cMOT) stage, discussed later in Section 3.3.

Each measurement starts with loading atoms into the magneto-optical trap (MOT) from a Zeeman slower, as illustrated in Fig. 3.1. Typically, our tweezer-based measurements require a MOT loading duration of at least $250\,\mathrm{ms}$. Following this, we adjust the detunings and powers of the MOT lasers, targeting a spatially compressed MOT (cMOT). Through a time-of-flight measurement, we extract the average temperatures to be $T_{\mathrm{MOT}} = 230\,\mu\mathrm{K}$ for the MOT and $T_{\mathrm{cMOT}} = 150\,\mu\mathrm{K}$ for the cMOT. Unfortunately, ^{39}K possesses a narrow hyperfine splitting in the excited $4P_{3/2}$ state. This characteristic complicates sub-Doppler cooling as it permits only minimal detunings from the cycling transition, demanding precise tuning of experimental parameters. To mitigate this, we introduce a supplementary grey molasses (GM), which not only reduces the atoms' temperature to $T_{GM} = 17\,\mu\mathrm{K}$ with an added $20\,\mathrm{ms}$ of cooling time but also crucially provides a settling period for the magnetic fields before the red-detuned (D2) molasses cooling stage [77]. Consequently, we can continue with a red

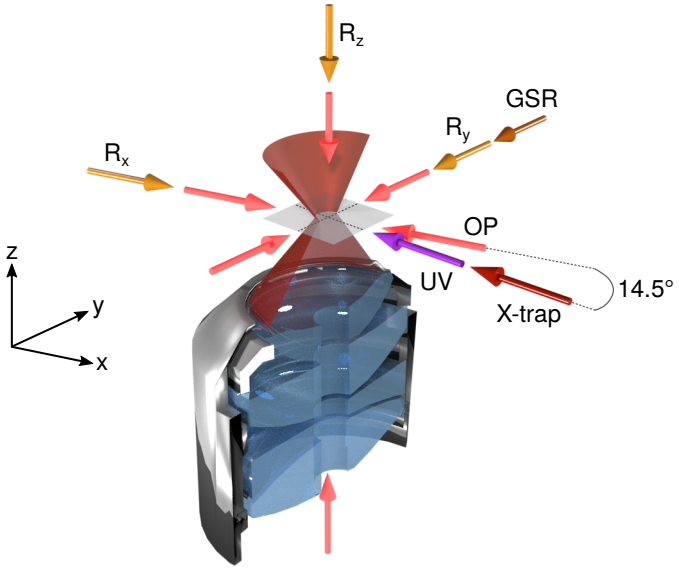

Figure 3.2 Experimental setup of laser beams around the in-vacuum built objective. For the MOT and GM we use two beams for each axis (red). One beam in x-direction is also used for optical pumping. We use three beams for Raman sideband cooling (R_x, R_y, R_z), two overlapped beams from the same direction to drive ground-state Raman transitions (GSR), one Rydberg excitation beam (UV) and a dipole trap along the x-axis of the experiment (X-trap).

molasses cooling stage without adiabatic tuning from residual or settling fields, improving the overall robustness of the experiment.

We then generate the optical tweezers, by emploing a $50\,\mathrm{W}$, $1064\,\mathrm{nm}$ fiber laser[1]. This beam is then intensity stabilized using an AOM[2] and afterward directed onto a liquid crystal spatial light modulator[3] (SLM), imprinting a specific phase pattern onto the trapping light. Then, the beam is reflected from the SLM and aligned to the in-vacuum objective[4], which focuses this beam within our primary vacuum chamber (see Fig. 3.2 for an overview of the used laser beams). More details about the generation of the tweezer patterns can be found in the Ph.D. Thesis of Lorenzo Festa [75]. Using an SLM offers the flexibility to prepare almost arbitrary array designs.

However, we face challenges by working with ^{39}K: Its $4P$ states experience a significant repulsive light shift at the trapping light wavelength of $1064\,\mathrm{nm}$, attributed to the nearby $3D_{3/2}$ and $3D_{5/2}$ transitions at $1170\,\mathrm{nm}$ and $1178\,\mathrm{nm}$ [60]. This renders the in-trap D1 cooling process (in trap GM cooling [78, 79]) highly sensitive to the trapping potentials. The cooling efficiency for each trap can be compromised by the spatial variation of the

[1] Azur Light Systems ALS-IR-45-SF
[2] Gooch & Housego AOM 3080-197
[3] Hamamatsu LCOS-SLM X10468-03WR
[4] Special Optics 54-40-33 @ 770,1064nm

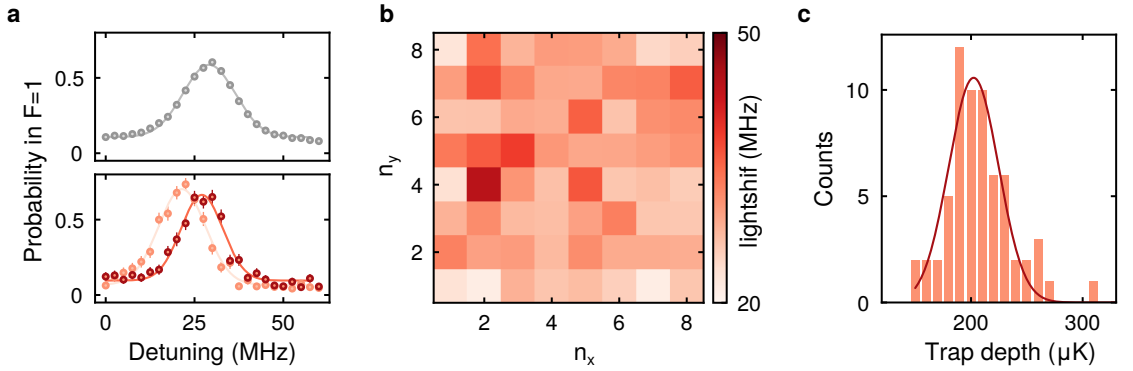

Figure 3.3 Trap depth inhomogeneities. a. To characterize trap depths, we measured a spectroscopy of the D1-lines: Atoms are prepared in the $|4S_{1/2}\,F=2,\,m_F=2\rangle$ state and the D1 laser is tuned through the $|4P_{1/2}\,F'=2\rangle$ resonance. On resonance, atoms scatter and might end up in the $|4S_{1/2}\,F=1\rangle$ ground state. Subsequently, a heat-out pulse targets the D2 line's closed cycling transition, removing remaining atoms in $|4S_{1/2}\,F=2,\,m_F=2\rangle$. The detuning, relative to free space resonance, reflects the light shift. The upper plot averages over all 64 tweezers, while the lower plot highlights two selected tweezers. Solid lines represent Gaussian fits to evaluate and compare the fit's center as an estimate for the trap depth. **b.** The Gaussian fit's center gives the light shift for each tweezer in the 8×8 array. **c.** The light shift lets us deduce the trap depth. For the shown measurement, the tweezer power was reduced to 20% of the initial loading power, corresponding to a trap depth of $U/k_B = 202\pm 2\,\mu\mathrm{K}$. The Gaussian distribution width is $\sigma = 18.6\pm 1.7\,\mu\mathrm{K}$, indicating an inhomogeneity of 11% in trap depth.

detuning which can be on the order of several MHz. Moreover, our system exhibits trap depth inhomogeneities of around 10%, as visualized in Fig. 3.3. Such inhomogeneities can drive the cooling beam to be trap-dependent on resonance, leading to photon scattering. The outcome is undesirable: increased atom heating and potential atom loss.

To address the challenges associated with light shifts and anti-trapping, we adopt a strategy proposed by Hutzler et al. [76] by alternating the use of trapping and near-resonant cooling light pulses. This chopping method ensures that atoms do not undergo any light shifts or anti-trapping effects during the cooling phase. Essentially, it renders the cooling process as if it were happening in a free-space configuration. The key to this technique lies in its switching frequency. It must be considerably faster than the trap frequency, ensuring that atoms only undergo an averaged trapping potential, thereby avoiding the risks of parametric heating. To achieve this, we set the chopping frequency at $1.4\,\mathrm{MHz}$, one order of magnitude faster than the axial trap frequency. This frequency was carefully selected; it represents the optimum speed at which the rise time of the switching trap AOM enables nearly rectangular-shaped pulses. In addition, the pulsing is four times slower than the atomic natural linewidth of $\Gamma/2\pi = 5.96\,\mathrm{MHz}$, which enables multiple scattering events within a single cooling pulse. This ensures that atoms revert to their ground state before the subsequent pulse of trapping light is introduced.

While this technique offers certain advantages, it also has drawbacks, encouraging us to develop a new loading scheme detailed in Section 3.3. The primary challenge with tweezer loading using this method arises from the need for more trapping power to ensure a consistent average trapping potential during chopping. Consequently, our experiment demands a peak power of 2.25 times higher than required in continuous operation for a trap depth of $U/k_B \approx 1\,\mathrm{mK}$, given the averaged power over a single duty cycle [80]. As a result, the maximum possible number of our tweezers is constrained by the accessible laser power and this specific amplification factor.

Furthermore, when evaluating the trap lifetime during fast pulsing with the one for continuous wave (cw) operation, we found that the $1/e$ lifetime is $90\,\mathrm{s}$ for cw operation, whereas, in pulsed mode, it is $40\,\mathrm{s}$ [75]. These durations exceed our typical experimental cycle of maximally $3\,\mathrm{s}$ by one to two orders of magnitude, varying based on the length of additional sequence components. In practice, we perform a continuous $40\,\mathrm{ms}$ pulsed atom loading. To ensure only a single atom occupies each trap, we perform a light-assisted collision pulse lasting $10\,\mathrm{ms}$ [80]. This process leaves each trap with a previously odd atom number occupied by just one atom and all traps with an even atom number empty. After allowing a $30\,\mathrm{ms}$ interval to wait for background atoms to escape, we take the first fluorescence image, capturing the array's filling.

3.2 Pulsed fluorescence imaging to prevent light shifts

This chapter describes our technique to detect single atoms within our tweezer array. For most of the measurements discussed in this thesis, we use a technique where the imaging and trapping light are pulsed similar to the initial loading process. However, following our system upgrade, we implemented a technique that does not require this chopping method. Instead, we adopt the approach detailed in [79], which involves using both resonant D2 scattering and off-resonant D1 cooling light during imaging. Nonetheless, as the results in Section 3.3 indicate, our experiment encounters challenges with this technique. The primary obstacle stems from the significant anti-trapping of the excited state, worsened by trap depth inhomogeneities.

When designing the experiment, we wanted to avoid such challenges, and that is why we adopted the same chopping method used for the light-assisted collisions, as described in Section 3.1. This involves alternating between trapping and cooling light pulses, which we applied for an imaging duration of $10\,\mathrm{ms}$. For the analysis, we set a region of interest (ROI) for each tweezer, summing the counts within each specified region. This process yields a typical count histogram, depicted in Fig. 3.4. Utilizing this data, we can set a classification threshold, distinguishing tweezers that either contained or lacked a single atom. It is worth noting that imaging with GM light is ineffective because the grey molasses technique is based on a dark state that suppresses scattering, thus reducing the photon count we can collect.

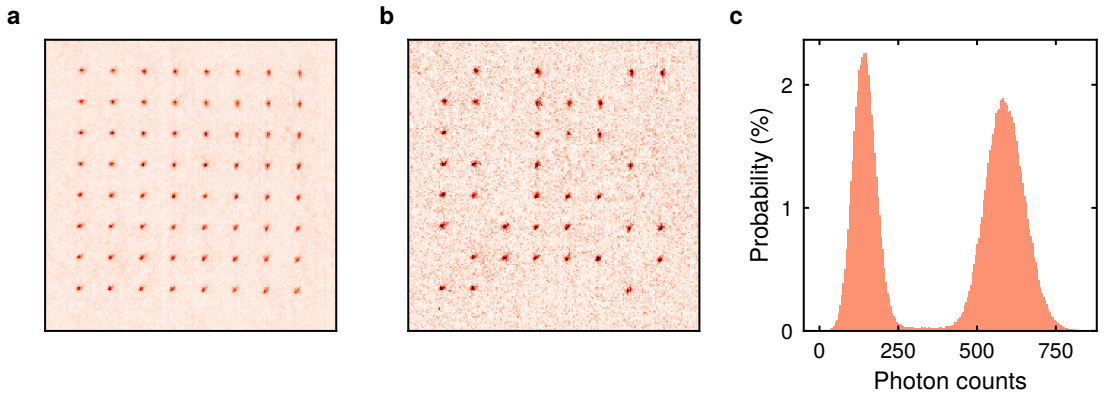

Figure 3.4 Fluorescence images using the chopped imaging method. a. Displayed is an averaged fluorescence image of the 8×8 tweezer array. **b.** A selected single shot from the array illustrates the statistical filling. **c.** A typical histogram of the photon counts derived from 4960 shots using the chopped imaging method.

Unfortunately, we experienced an atom loss rate of 2.7% [75] after each fluorescence picture. This loss arised from the lifetime of the trapped atoms when having interleaved molasses light during the trap pulsing switched on, which was around $332\,\mathrm{ms}$ for a $1\,\mathrm{mK}$ trap depth [75].

There are several possible solutions to circumvent this: The simplest among these is increasing the average trap depth. For example, doubling the trap depth to $2\,\mathrm{mK}$ extended the lifetime to $895\,\mathrm{ms}$ [75]. The trap depth can also be increased by refining the pulse shape to be more rectangular. Nonetheless, we face constraints caused by the limited power output of our laser source. These challenges led to the development of the in-trap imaging technique, which we will discuss in the next section.

3.3 Experimental modifications for loading, cooling and imaging single atoms

After further optimization on the trapping and cooling sequences of the MOT and cMOT, we achieve temperatures of $T_{\mathrm{cMOT}} = 74\,\mu\mathrm{K}$. Additionally, we upgraded our D1 and D2 laser systems to provide more power during these phases. The configuration of this enhancement can be seen in Fig. 3.5 and the laser lock settings are described in Appendix A.

The primary motivation behind this setup change is increasing the available laser power using consecutive tapered amplifiers (TA). Our system now includes two separate pathways, one for the D2 laser and another for the D1 laser setup. Each pathway has a TA that boosts the seed light to approximately $1\,\mathrm{W}$. In addition, we have also incorporated an acousto-optic Modulator (AOM) in a double-pass arrangement for each path. An electronic switch between

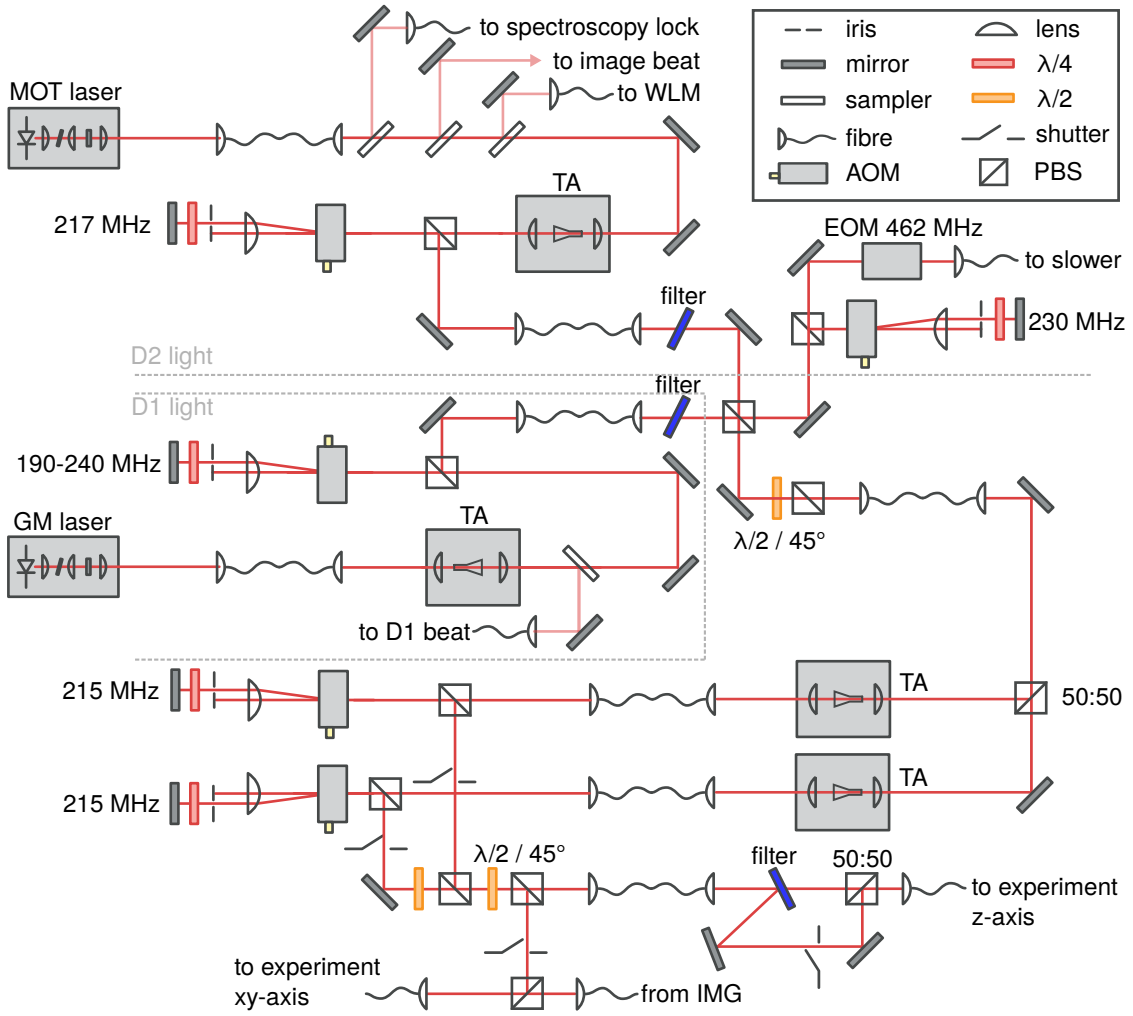

Figure 3.5 Simplified new optics setup for D1 and D2 laser. The MOT laser is locked to an MTS spectroscopy and serves as a reference for the IMG laser beat-lock. The MOT light is amplified using a tapered amplifier (TA) and aligned through an AOM in a double-pass configuration to be able to tune frequency and amplitude. The GM laser is amplified by a TA and beat-locked to a D1 Master laser, which is locked to a spectroscopy. The GM light passes a broadband AOM for amplitude and frequency control. An electronic switch enables the AOM either exclusively in the GM or MOT path. Both paths are spectrally filtered using an interference filter as described in the main text. Before overlapping, the D2 light is split into the Zeeman slower AOM setup and the overlap fiber. After this fiber, the beam passes a non-polarising beam splitter (50:50) and is amplified each by a TA and frequency shifted by a consecutive AOM in a double-pass configuration. The two beam paths, which we refer to as Cooler and Repumper paths due to their frequency shift, are again overlapped and split into two paths to the experiment. In the z-axis, there is an additional interference filter included and shutter to filter out D2 light if needed.

their AOM drivers ensures that exactly one is activated at any given time. These beam paths are fiber-coupled, overlapped on a separate breadboard, and coupled into the same fiber. Following the outcoupling from this, the light is split into two paths, each having another TA, producing around $1\,\mathrm{W}$, and an AOM. We have assigned these two paths as the Cooler and Repumper paths, where the AOMs are calibrated to span the ground state splitting of potassium, which is $462\,\mathrm{MHz}$. This setup effectively increases the available power for each path by a factor of four compared to the previous laser setup used in the sections before, which is described in detail in reference [60].

Furthermore, with this setup, we improve the atom cooling procedure. To compress the MOT, we ramp the magnetic field from $110\,\mathrm{G/cm}$ to $30\,\mathrm{G/cm}$ within a duration of $10\,\mathrm{ms}$. These measures enables us to cool the atoms down to $74\,\mu\mathrm{K}$, representing an impressive reduction by almost half, a result we obtain using a time of flight measurement. A notable advantage of this approach is the ability to load our tweezers as early as in the cMOT phase. For effective atom loading, the trap depth we require is on average $U/k_B = 1\,\mathrm{mK}$.

After loading the tweezers, we apply a pulse to allow for light-assisted collisions to ensure that only a single atom remains trapped. To achieve this, we introduce a pulse of $40\,\mathrm{MHz}$ blue detuned D1 light for $15\,\mathrm{ms}$. Subsequently, we continue to cool the atoms within the trap for $20\,\mathrm{ms}$, employing the technique described in reference [79]. This method employs an in-trap lambda-enhanced GM cooling. The cooling performance is primarily constrained by our tweezer inhomogeneities, which were $\approx 4.5\%$ at the time.

Two essential factors for the effectiveness of this cooling method are the lambda condition and the detuning from resonance. A potential enhancement for the loading probability would involve adopting the approach from reference [79] using the D1 cooling method for enhanced trap filling: At its core, the idea is to increase the detuning to a point where the energy absorbed by an atom pair during a collision is sufficient to eject only one of the atoms. With more homogeneous traps in the future, implementing this technique could be both promising and beneficial for a large filling.

For the imaging technique, we adopt the methods outlined in the same reference [79]. However, as we will proceed, a critical factor for the success of this method is achieving homogeneous tweezer trap depths to ensure uniform cooling across all tweezers. In the imaging setup utilized for the measurements presented in Fig. 3.6, we apply three-dimensional GM cooling for an imaging duration of $100\,\mathrm{ms}$ in the traps with an average trap depth of $U/k_B = 0.5\,\mathrm{mK}$. GM Cooler and Repumper beam are in lambda condition and are detuned by $16\,\mathrm{MHz}$. This detuning was selected as a compromise between minimizing background scattering during fluorescence imaging using low optical powers and ensuring efficient cooling for the average array. Contrarily, we apply the D2 imaging light in the two-dimensional axis of the atom plane (xy-plane). This minimizes stray light scattering at $767\,\mathrm{nm}$ in the axis of the camera, as the imaging system cannot filter this scatter. Additionally, we replaced our CMOS[5] camera with an EMCCD[6] camera. This change was motivated by

[5] Andor Zyla 4.2 PLUS.
[6] Andor iXon.

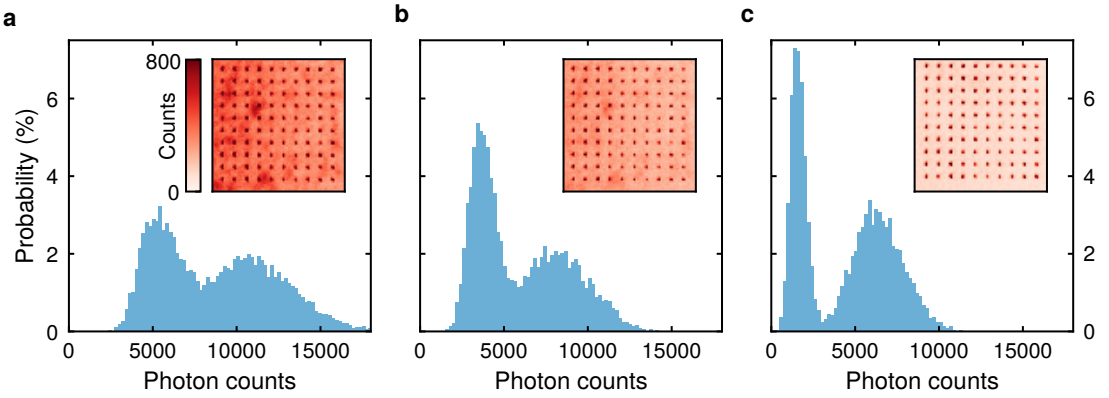

Figure 3.6 Influence of ASE from D1 TAs on imaging background. For all depicted measurements, we implemented four bandpass filters into the imaging tube, blocking both the trapping and D1 cooling light, as detailed in the main text. **a.** Acquisition of 100 shots, then averaging the counts for each tweezer ROI without any interference filters after the seed TAs. **b.** Introduction of an interference filter after each D1 and D2 seed TA significantly reduced the observed background scatter. **c.** In addition to the interference filter, we included an obstacle that blocks the central part of the imaging beam, significantly reducing scatter originating from the hole of the objective.

the superior quantum efficiency of the EMCCD, necessitating fewer scattered photons and, ideally, allowing for shorter imaging durations. Moreover, the electron multiplying (EM) process effectively boosts pixel signals, increasing the signal beyond the camera's readout noise.

Furthermore, we modified our imaging system by replacing the focusing achromat[7], achieving an image magnification of 30.14. This results in a resolution of $0.53\,\mu\mathrm{m/px}$. To minimize background scatter, potentially originating from trapping or imaging light, we added four bandpass filters: The first filter[8] the light hits blocks the $1064\,\mathrm{nm}$ trapping light. This is then followed by three filters[9] that block the $770\,\mathrm{nm}$ cooling light, but allow the $767\,\mathrm{nm}$ imaging light to transmit.

Despite these filters, we still observe significant background scattering, as depicted in Fig. 3.6. We trace the source of this background to the amplified spontaneous emission (ASE) noise from the D1 TA. The bandwidth of this noise spans several nm, causing visible background on the camera. We adopt the following approach to improving this: First, we place narrow interference filters after the MOT and GM TAs, ensuring that the subsequent TAs do not further amplify the ASE from these. However, as in our setup, we need to switch between the two TA seeds, we can not place a narrowband filter after the cooler and repumper TAs. Consequently, we add an additional switching setup in the z-axis path of our

[7] Exchanged the focusing achromat with $f = 250\,\mathrm{mm}$ from Thorlabs AC508-250-B to an achromat with $f = 1000\,\mathrm{mm}$ from Thorlabs AC508-1000-B.
[8] Semrock FF01-766/13-25 at $0°$ tilt.
[9] Semrock FF01-747/33-25 at $0°$ tilt.

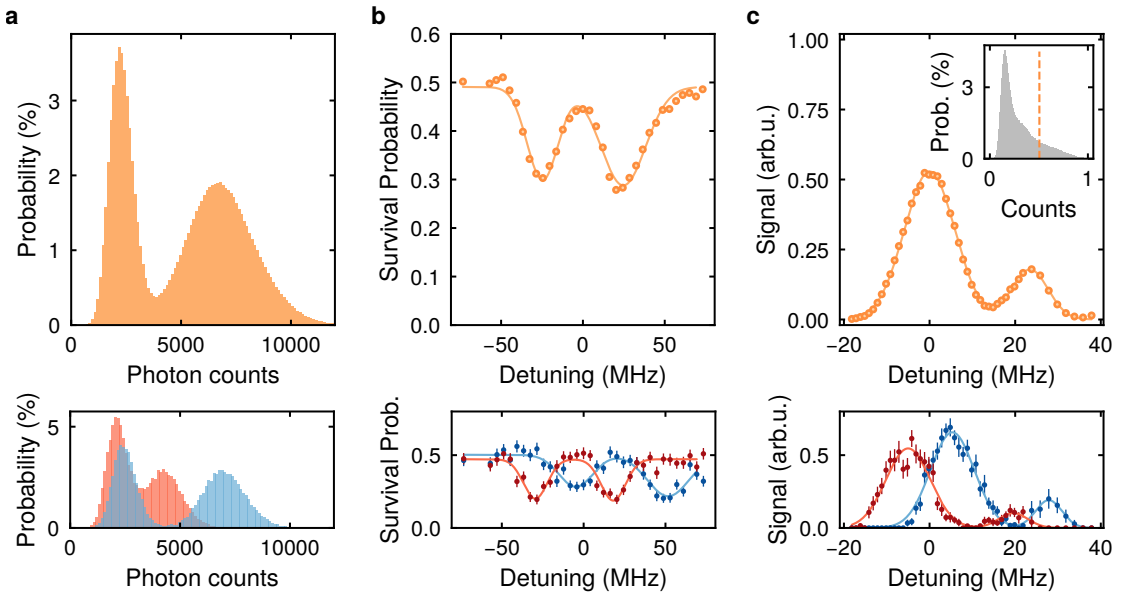

Figure 3.7 Imaging performance and calibration measurements. The upper plot averages over 100 tweezers (orange), while the lower plots represent results from two selected individual tweezers (red and blue). **a.** Typical histogram of the photon counts from several experimental realizations within each tweezer's defined region of interest. **b.** D1-spectroscopy signal showing the $4P_{1/2}F' = 2$ (right) and $4P_{1/2}F' = 1$ (left) levels. **c.** D2-spectroscopy signal of the $4P_{3/2}F' = 3$ (left) and $4P_{3/2}F' = 2$ resonances. During the measurement, we scanned the detuning of the imaging laser and took fluorescence images for these scanned values. This adjustment produced a smeared-out photon count histogram, as depicted in the inset. A high classification threshold (indicated by the orange dashed line) was set to identify the resonance through scattered photons.

laser setup, including an interference filter[10] that reflects D2 light. This light is then blocked by an additional beam shutter, as illustrated in Fig. 3.5. Second, one significant source of scattering is the aperture of our in-vacuum objective. We found that by blocking the central part of the imaging beam, with a diameter of around $1\,\mathrm{cm}$ (given the imaging beam's width of roughly two inches), we further reduced noise. However, this also results in a minor loss of imaging photons. The cumulative effect of these measures is depicted in Fig. 3.6.

We capture a fluorescence image with an imaging duration of $100\,\mathrm{ms}$ after completing the following calibration measurements: We first perform a D1 spectroscopy, resolving the hyperfine states of the $4P_{1/2}$ excited state, and select a blue detuning of $16\,\mathrm{MHz}$ of the $4P_{1/2}\,F' = 2$ state for in-trap cooling. Next, we perform a D2 spectroscopy that resolves the $4P_{3/2}\,F' = 3$ and $4P_{3/2}\,F' = 2$ levels. As previously illustrated in Fig. 3.7, we again encounter challenges due to trap depth inhomogeneities, shown in the exemplary set of two selected tweezers. When taking a fluorescence image of traps with a depth of $U/k_B = 0.5\,\mathrm{mK}$, the photon counts histogram reveals a noticeable pedestal between the bimodal distribution.

[10] LASEROPTIK.

This pedestal can be attributed to the aforementioned inhomogeneities. In Fig. 3.7, this effect is again showcased by two selected tweezers, where one does not scatter sufficiently, making the two distributions indistinguishable. This results in a persistent offset between the averaged histogram's 'zero' and 'one' atom distributions.

In summary, although notable improvements were made in diminishing background scattering, it is apparant that further refinements are required. Here, it is evident that improving the trap depth uniformity is the cardinal step toward optimizing our imaging capabilities. During the writing of this thesis, we achieved an average trap inhomogeneity of $\approx 1.5\,\%$, an improvement by an order of magnitude. Further details on this advancement and its resulting improvement for the imaging will be discussed in the PhD thesis of Philip Osterholz.

3.4 Cooling single atoms in optical tweezers to their motional ground-states

Preparing low-entropy systems of neutral atom arrays is one piece of the jigsaw for quantum many-body experiments. These low temperatures increase the experiment's robustness regarding coherence time for quantum state manipulation such as mesoscopic superposition states. Even after in-trap optical molasses cooling to (several) tens of microkelvin, the atoms' remaining temperature presents a severe limitation for the abovementioned measurements [38, 81, 82]. Here, Raman sideband cooling (RSC) offers a powerful tool to prepare the atoms in confined optical traps in their vibrational ground state [83–86].
This section will introduce our experimental implementation of RSC relying on transitions between different hyperfine ground states. First, we prepare the atoms in a defined m_F Zeeman sub-state, as described in Section 3.4.1. Then, in Section 3.4.2, we describe how we cool the atoms to their vibrational ground state and discuss our technique's limitations and possible solutions.
Detailed information about the laser setups can be found in the thesis of Nikolaus Lorenz [60]. The section for RSC is based on the material from our publication [80].

3.4.1 Optical pumping for spin state preparation

After the first fluorescence image, described in Section 3.2, we usually post-select on the presence of one atom and continue with optically pumping and preparing the atoms in the $|4S_{1/2}\, F = 2,\, m_F = 2\rangle$ state, similar to reference [87]. Usually, we prepare the atoms in one of these stretched states for two reasons. First, they have a complete projection of the total angular momentum quantum number $m_j = \pm 1/2$. And second, they offer a maximal Rabi coupling to the Rydberg states later.

For the preparation, we use the D1 light (GM laser) of one of the six MOT axes beams around the science chamber and block the beams in the other directions with mechanical

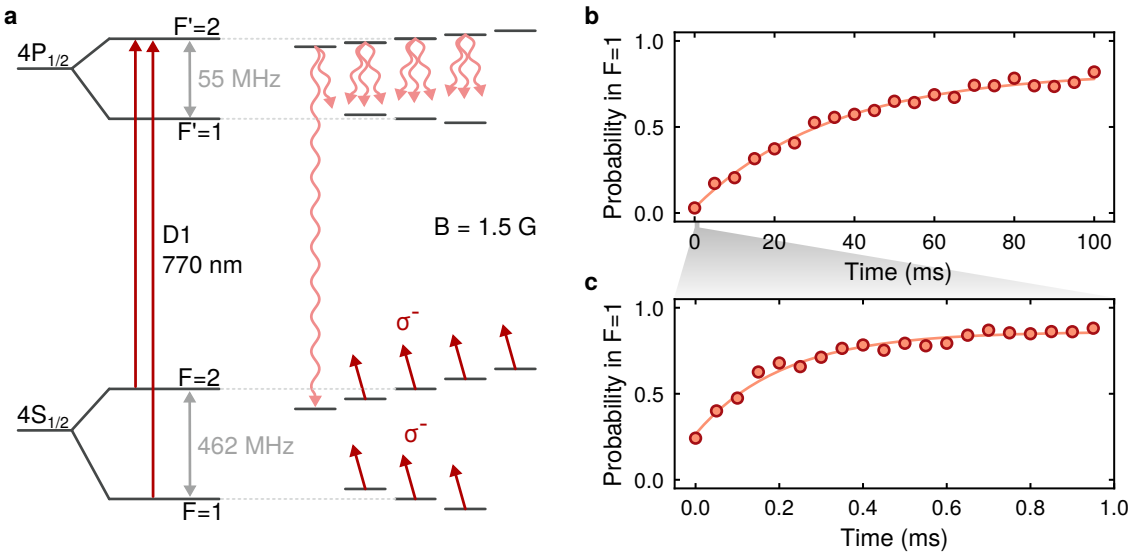

Figure 3.8 Level diagram and measurements of the state preparation efficiency. a. Level scheme for the state preparation in the $|F = 2, m_F = -2\rangle$ state with driving σ^- transitions at a magnetic field of $1.5\,\mathrm{G}$. After several scattering and decay processes, the atoms end up in the $|F = 2, m_F = -2\rangle$ state, which appears dark to the pumping light. **b.** Measurement of the optical depumping time for a maximally polarized beam. **c.** Measurement of the optical pumping time for a magnetic field perpendicular to the pumping beam. This also adds σ^+ and π transitions.

shutters. The lasers' beat lock is tuned to the $|4P_{1/2}\, F' = 2\rangle$ resonance. Furthermore, we implement a Glan Taylor polariser in combination with a quarter waveplate to guarantee a high degree of the desired circular polarization. We then apply a magnetic field of $1.5\,\mathrm{G}$ parallel to the pumping beam (in our case, one of the MOT x-axis beams), which is tilted by $14.5\,^\circ$ w.r.t. to the x-axis (see Fig. 3.2). By changing the orientation of the magnetic field, we can tune the driving transitions on the atoms from σ^- to σ^+ and vice versa.

For optical pumping, we apply a pulse of $200\,\mu\mathrm{s}$ with D2 Repumer and Cooler beams. Afterward, we switch off the optical Cooler beam $200\,\mu\mathrm{s}$ before the Repumper beam. Both beams are set to a power of $0.3\,\mathrm{I_{sat}}$, where $I_{\mathrm{sat}} = 1.75\,\mathrm{mW/cm^2}$ is the saturation intensity for the D2 line. Note that for the state preparation, we also alternate between trapping and resonant light like done in reference [76]. This way, we can circumvent the issue of undesired trap inhomogeneities (as discussed in Section 3.1) and prepare all atoms in free space in the accurate m_F state.

For the measurement and optimization of the state preparation efficiency, we employ a similar technique as used in reference [85]. We start with preparing all atoms in the $|F = 2, m_F = -2\rangle$ state, then switch on the optical pumping light without repumping light and scan the pulse duration. As shown in Fig. 3.8, we apply this measurement for two different pump polarizations, which are tuned by rotating the magnetic field orientation. In the case of σ^- polarization, the prepared atoms remain in the $m_F = -2$ state, which

appears dark when illuminated with D1 light. After the D1 pulse, the remaining atoms in the $|F = 2, m_F = -2\rangle$ state are heated by using a resonant D2 beam driving a closed transition from $F = 2$ to $F' = 3$ and ejected from the trap. Atoms in other m_F states can decay into the $F = 1$ sub-states and, therefore, stay trapped. Finally, we capture the remaining atoms in the $F = 1$ state with a second fluorescence image. We extract $1/e$ decay of $\tau_{\mathrm{DP}} = 35.93 \pm 2.54\,\mathrm{ms}$ from an exponential fit to this optical depumping measurement.

Afterward, we repeat the measurement with a tilted magnetic field such that the pump light can also drive π and σ^+ transitions. Now, the atoms in $F = 2$ are not dark anymore and can be depumped to $F = 1$. In this case, we measure a $1/e$ optical pumping time of $\tau_{\mathrm{OP}} = 0.20 \pm 0.02\,\mathrm{ms}$. From this, we can extract the state preparation efficiency as the ratio between the optical pumping and depumping time to be $P(F = 2, m_F = -2) = 1 - \tau_{\mathrm{OP}}/\tau_{\mathrm{DP}} = 99.44 \pm 0.08\,\%$.

The obtained efficiency is sufficient to proceed. However, the fidelity is primarily limited by the polarization adjustment of the beam, which has been so far fine-tuned by hand. Suppose this is getting limiting in the future, one could optimize the polarization by adding multiple waveplates or by implementing motorized rotational mounts, enabling an automized and, therefore, more precise adjustment.
The state preparation is implemented for all further measurements and presents a good starting point for RSC.

3.4.2 Resolved Raman sideband cooling in tweezer arrays

In our experiment, we implemented RSC to cool the atoms in tight optical traps to their motional ground state. Initially, RSC has been used to cool ions in dipole traps [83] and since then implemented in various other experiments for neutral atoms trapped in optical lattices [81, 84] and tweezers [85, 86, 88–90]. In the following, we explain and discuss our experimental implementation of RSC using an array of 8×8 tweezers [60, 80].

Our scheme uses off-resonant D1 light to drive transitions between vibrational manifolds of the trap linked with two hyperfine ground states, $|F = 2, m_F = 2\rangle$, and $|F = 1, m_F = 1\rangle$. The cooling procedure consists of two steps, as illustrated in Fig. 3.9. First, the atoms undergo a spin flip via a stimulated Raman process from the $|F = 2, m_F = 2\rangle$ to the $|F = 1, m_F = 1\rangle$ state, where the vibrational state is reduced by one motional quantum from n to $n - 1$. In the second step, optical pumping beams transfer the atom back into the initial spin state via a spontaneous Raman process, where the photon carries away the entropy. The probability of the atom remaining in the same vibrational state during this spin-flip is crucial for a successful cooling process. The coupling between the atom's internal and motional states is described by $(2\bar{n}+1)\eta_{LD}^2$. Here, the temperature of the atoms is expressed by the mean vibrational quantum number $\bar{n}$ and the Lamb-Dicke parameter $\eta_{LD} = k \cdot a_{HO}$, where k is the wave number of the pumping light, and $a_{HO} = \sqrt{\hbar/2m\omega}$ the oscillator length with m the mass of the atom and ω the oscillator frequency [85]. For a

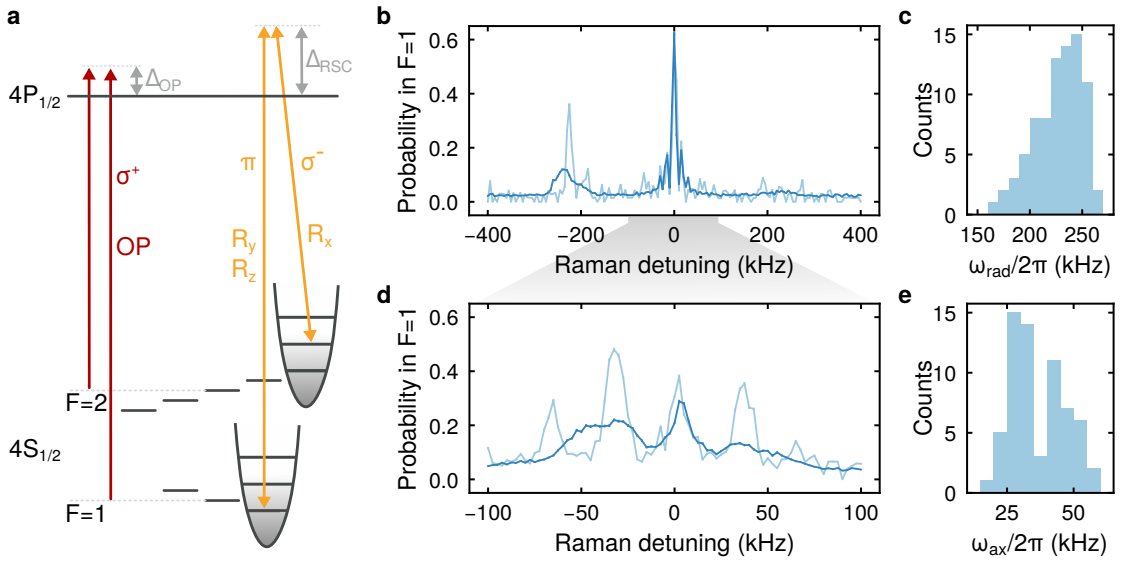

Figure 3.9 Level diagram and spectroscopy measurements of vibrational modes. a. We implemented three beams for RSC corresponding to the three coordinate axis R_x,R_y, and R_z. The combination of R_x and R_y cools the radial axis, and the combination of the R_x and R_z the axial axis. **b.** Radial Raman spectroscopy measurements for an average of 64 tweezers (dark blue) and a selected single tweezer (light blue) after RSC w.r.t. to the carrier, where the vibrational quantum state remains the same. The shown peak for negative detunings corresponds to the first red sideband. The double feature of the sideband is due to an elliptical trapping potential. Figure adapted from [60, 80]. **c.** Evaluated radial trapping frequencies in an array of 8×8 tweezers. In the case of elliptical tweezers, this leads to two radial trapping frequencies. For efficient Raman cooling, a chirp over $120\,\mathrm{kHz}$ is required to cover the frequency spread. Figure adapted from [60, 80]. **d.** Axial Raman spectroscopy measurements around the carrier. In the case of a single tweezer, one can resolve the first and second red sideband. **e.** Evaluated axial trapping frequencies of the tweezer array.

successful Raman cooling, we require low initial temperatures of the atoms (small mean vibrational number) and high trapping frequencies.

Assuming tight optical traps like in our setup, the radial trapping frequency $\omega_{\mathrm{rad}}^2 = {}^{4V_0}/_{mw_0^2}$ and axial trapping frequency $\omega_{ax}^2 = {}^{2V_0}/_{mz_r^2}$ scale with the trap depth V_0, the mass of the atom m, the waist of the trapping beam w_0, and its Rayleigh range $z_r = {}^{\pi w^2}/_{\lambda}$, where λ is to the trapping wavelength. By comparing the trapping frequencies, we recognize that $\omega_{ax} < \omega_{\mathrm{rad}}$ and, therefore, the axial trapping frequency is more critical for an efficient Raman cooling process.

For this reason, we increase our overall trap depth by a factor of 2.25 compared to the power at which we load the tweezers, corresponding to a mean trap depth of $2\,\mathrm{mK}$, which is also the peak power during chopping. We maintain the magnetic field defining our quantization axis from the state preparation in Section 3.4.1, which is pointing along our MOT x-axis with an amplitude of $1.5\,\mathrm{G}$ and an angle of $14.5\,^\circ$ to the x-axis of the main chamber. The

magnetic field is sufficiently strong, allowing us to neglect vector light shifts caused by a highly focused trapping beam [86]. Here, the use of a trapping wavelength of $1064\,\mathrm{nm}$ for potassium is especially beneficial, resulting in negligible vector shifts of the ground states [60].

We implemented in total three Raman beams for each coordinate axis R_x, R_y, R_z (see Fig. 3.2) with a beam waist of $250\,\mu\mathrm{m}$. Each path contains an AOM, where R_x uses the -1. order and the other beams the $+1$. order to bridge the ground state splitting of $461.7\,\mathrm{MHz}$ as shown in Fig. 3.9. This allows us to freely tune the frequency in order to precisely drive Raman transitions between vibrational states. With beam intensities of $1.6\,\mathrm{W/cm^2}$ for R_x and $0.9\,\mathrm{W/cm^2}$ for R_y and R_z and a laser detuning of $\Delta_{\mathrm{RSC}} = 2\pi \times 40\,\mathrm{GHz}$ we measure Rabi frequencies of $\Omega_{Raman} = 2\pi \times 43\,\mathrm{kHz}$ for transitions from $|F = 2,\, m_F = 2\rangle$to $|F = 1,\, m_F = 1\rangle$. For a first rough alignment of the beams onto the tweezer array, we tune the laser onto the D1 resonance and align the beam as a measure of pumping probability to $F = 1$ or $F = 2$, respectively. The fine adjustment is further done by improving the abovementioned Rabi coupling. The laser frequency is stabilized to the modes of an ultra-low expansion cavity (ULE) and, therefore, adjustable in steps of the free spectral range $FSR = 1.5\,\mathrm{GHz}$.

The optical pumping beams during RSC are the same ones as those used for the state preparation. However, we stabilized the laser to be blue detuned by $\Delta_{OP}/2\pi = 80\,\mathrm{MHz} \pm 30\,\mathrm{MHz}$ from the in-trap D1 resonance to avoid heating from the anti-trapped excited states [91]. The uncertainty is given by the standard deviation of the trap inhomogeneity of the array.

The full cooling process takes $150\,\mathrm{ms}$ and consists in total of 30 cycles [80]. Each cycle cools the radial axis for $2\,\mathrm{ms}$, applying frequency chirps over $120\,\mathrm{kHz}$ with a duration of $200\,\mu\mathrm{s}$ to cover trap depth inhomogeneities. In addition, we cool the axial trapping axis with three pulses, each of $200\,\mu\mathrm{s}$ duration and driving transitions from the fourth to the first motional blue sideband [90]. In the latter case, the cooling begins outside the Lamb-Dicke regime and requires step-by-step cooling from high vibrational quantum numbers to lower ones. The optical repumpers are turned on during the whole cooling process. The lower threshold of the cooling process is mainly limited by the trap inhomogeneities, which fixes the chirp duration and frequency width. After a successful cooling process, the atoms end up in the $|F = 2,\, m_F = 2\rangle$, $n = 0$ state, which is dark to the optical pumping and Raman beams.

We evaluate the cooling efficiency by measuring the sideband spectroscopy. Here, we use the combination of Raman beams R_x and R_y for the radial spectroscopy and the pair R_x and R_z for the axial spectroscopy. During the measurement, we keep the same trap power as throughout the cooling. However, the Raman pulse duration is set such that we drive a $\sim \pi/2$ pulse on the carrier transition for the radial, and a π pulse for the axial spectroscopy. Afterward, we ramp the overall trap power down to $20\,\%$ of the initial trap loading power, start chopping again, and heat out the atoms remaining in the $|F = 2,\, m_F = 2\rangle$ state with resonant D2 light on the $4P_{3/2}$, $|F' = 3,\, m_{F'} = 3\rangle$ cycling transition. With a second fluorescence picture, we only capture atoms transferred to the $F = 1$ state via the sideband

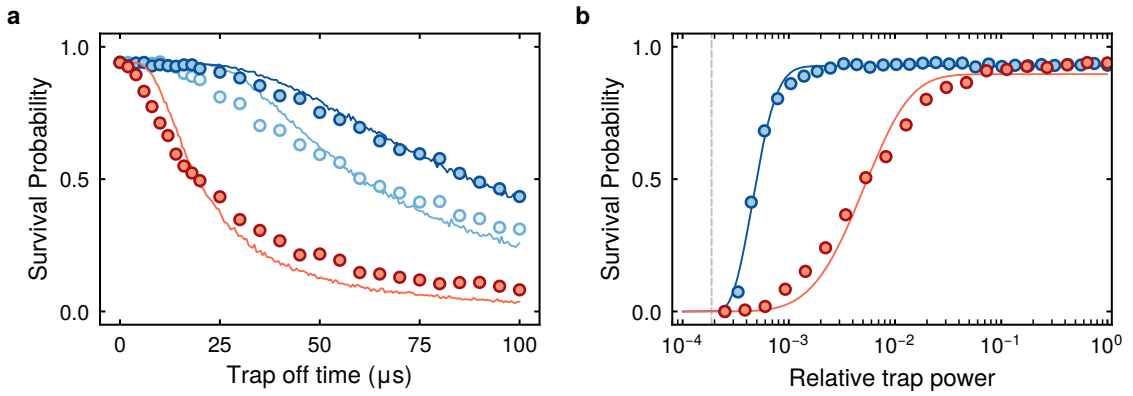

Figure 3.10 Temperature of the atoms before and after Raman sideband cooling. Figures based on data and simulation from [60, 80] **a.** Measurement of the survival probability versus trap switch-off durations for two different atom temperatures. Before switching off the trap, we ramp down the trap power to $20\,\%$. For non-cooled atoms (red), we lose the atoms basically within the first few μs. For a Raman sideband cooled system (both blue), we can switch off the trap for $20\,\mu$s without atom loss. When ramping the trap power to $0.5\,\%$ before releasing the atoms (dark blue), we additionally adiabatically "cool" the atoms and increase the available switch-off duration. The solid lines are Monte Carlo simulations. **b.** Measurement of the survival probability versus trap depth for non-cooled (red) and Raman sideband cooled (blue) atoms. Solid lines are theory fits using a Boltzmann distribution. The vertical, dashed line corresponds to the trap depth, where gravity pulls open the trap.

pulse. Fig. 3.9 shows the spectroscopy measurements for a cooled system. We can extract the mean vibrational quantum number $\bar{n}$ via the asymmetry of the amplitude of the red and blue sideband $I_{\text{blue}}/I_{\text{red}} = \bar{n}/(\bar{n}+1)$.

After cooling, we obtain a mean vibrational number $\langle \bar{n}_{\text{rad}} \rangle = 0.225 \pm 0.217$ for the radial axis and $\langle \bar{n}_{ax} \rangle = 1.04 \pm 1.05$ for the axial axis. The brackets indicate the mean value over all 64 tweezers, leading the standard deviation to be this large. With these values, we obtain an average groundstate fraction of $37\% \pm 18\%$. However, checking the performance of the best single tweezer, we obtain a mean vibrational number of $\bar{n}_{\text{rad}} = 0.13$ in the radial and $\bar{n}_{ax} = 0.23$ in the axial axis, corresponding to a ground state fraction of $69\,\%$. Therefore, the cooling performance in our experiment is strongly limited by the trap inhomogeneity and the relatively small axial trapping frequency.

To optimize the cooling parameters, we use a ballistic expansion technique, where we switch off the trapping potential for a variable amount of time. The atoms' temperature strongly limits the trap's switch-off duration. The effect of RSC and, therefore, the atoms' temperature on the switch-off period is shown in Fig. 3.10. The trap power is lowered to $20\,\%$ before switching off a non-cooled and a Raman sideband cooled system. Furthermore, for the latter case, we also measure the recapture probability if the trap depth was ramped to $0.5\,\%$ before releasing the atoms. With a Monte Carlo simulation done in references [60, 80], we extract the atoms' temperature to be $9.3\,\mu$K, $1.4\,\mu$K, and $200\,$nK for the non-cooled, the

Raman sideband cooled, and the Raman sideband and further adiabatically cooled system [92], respectively. We choose a switch-off time where the atom recapture is significantly reduced to optimize the cooling parameters mentioned above. Thus, we are very sensitive to the parameters linked to the atoms' temperature.

Another important advantage of RSC is that it allows us to reduce the trap depth further while keeping the atoms trapped. This is an essential measure for Rydberg dressing (see Section 4.2), as the absolute trap inhomogeneities are reduced with decreased trap depth. In addition, this allows us to further adiabatically cool the atoms within the traps [92]. For the measurements in Fig. 3.10, we measure the atoms' probability of staying trapped versus the trap depth. Therefore, we ramp the trap depth down within $50\,\mathrm{ms}$ and keep this trapping power for $50\,\mathrm{ms}$ until we ramp back to $1\,\mathrm{mK}$ for imaging. We do this procedure for two different initial temperatures. For a non-cooled system, we can lower the trap depth to $10\,\%$ before losing the atoms, corresponding to a trap depth of roughly $100\,\mu\mathrm{K}$. However, in the case of a Raman sideband cooled system, we can ramp the trap depth to $0.5\,\%$, corresponding to a trap depth of $3.7\,\mu\mathrm{K}$. The latter is limited by gravity, as indicated by the vertical, dashed line in Fig. 3.10b. Below $0.02\,\%$ trap power, the atoms are no longer trapped in the axial direction.

From a D1-lightshift measurement of the tweezers we extract a trap depth of $0.906\,\mathrm{mK}$ for $100\,\%$ tweezer power [80]. For RSC, we increase the tweezer power by a factor of 2.25 and measure an average radial trapping frequency of $240\,\mathrm{kHz}$ and an axial trapping frequency of $38\,\mathrm{kHz}$. With these trapping frequencies we calculate a tweezer beam waist of $w_{\mathrm{tweezer}} = 0.89\,\mu\mathrm{m}$ (neglecting any ellipticity of the beam) and a Rayleigh range of $z_{\mathrm{r,tweezer}} = 3.96\,\mathrm{mm}$. The Rayleigh range, however, is slightly different when comparing it to the theoretically calculated one $\pi w^2/\lambda = 2.3\,\mathrm{mm}$, which could come from aberrations and the real diffraction profile [93].

In summary, implementing RSC offers three major advantages for our experiment: First, it enables longer trap switch-off durations, which we need for, e.g., measuring Rydberg Rabi oscillations. Here, we want to avoid the anti-trapping of the excited state. Second, after cooling, we can further lower the trap depth, cool the atoms adiabatically [92], and reduce the absolute differences in trap inhomogeneities as they scale linearly with the trap depth. Third, the cooling also reduces the Doppler shift, which depends on the atom's finite temperature and the k-vector of the excitation beam [63]. The latter could be, for example, decreased by using counterpropagating beams for the two-photon Rydberg excitation or three-photon excitations with specific geometries to partially or even completely cancel the recoil effect [94]. In the case of a single-photon excitation, the atom's temperature is the only knob to reduce the Doppler shift, which is responsible for the damping of the Rabi oscillations and due to a broadening of the excitation linewidth.

However, there is definitely room for improvement. One possible solution to increase the efficiency of RSC could be a better confinement of the atoms in the axial direction by additionally implementing an optical lattice [95] or a horizontal light sheet as shown in Fig. 3.11. This figure shows the calculation of an elliptically shaped light sheet at a

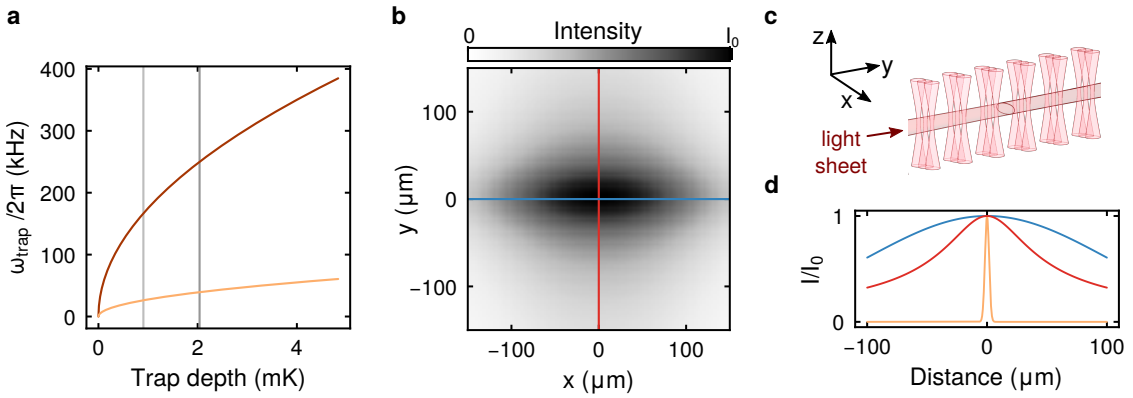

Figure 3.11 Trap frequencies for single tweezers and a horizontal light sheet. a. Radial (red) and axial (orange) trap frequencies for single tweezers at varying trap depths. The grey right vertical line indicates the trap depth used for RSC. The left vertical grey line indicates the trap depth used for loading and imaging the tweezer. **b.** A two-dimensional slice through a light sheet in the plane of the tweezers. The color map represents the intensity relative to $I_0 = 9 \times 10^3\,\mathrm{W/mm^2}$. The corresponding laser power and beam waists yield weak and strong radial trapping frequencies $\{\omega_{\mathrm{rad,strong}}, \omega_{\mathrm{rad,weak}}\}/2\pi = \{48.42\,\mathrm{kHz}, 0.82\,\mathrm{kHz}\}$ and axial trapping frequencies $\{\omega_{\mathrm{ax,strong}}, \omega_{\mathrm{ax,weak}}\}/2\pi = \{3.41\,\mathrm{kHz}, 0.98\,\mathrm{Hz}\}$. Note that $\omega_{\mathrm{rad,strong}}$ is overlapped with the axial axis of the tweezers. **c.** A sketch illustrating the light sheet propagating along the y-axis, with the tweezer array situated within the x-y plane. **d.** Normalized intensity, depicted for cuts through the experimental x-axis (blue), y-axis (red), and z-axis (yellow).

wavelength of $1064\,\mathrm{nm}$, power of $10\,\mathrm{W}$, a horizontal waist (in the x-direction) of $200\,\mu\mathrm{m}$ and a vertical (in z-direction) waist of $3.4\,\mu\mathrm{m}$. The light sheet would be aligned along the experimental y-axis. Since we are interested in the trapping frequency, which is overlapped with the propagation direction of the tweezers, we are calculating the vertical trapping frequency ω_z in the tweezer (x-y) plane. Here, we are limited by the Rayleigh range of $z_r = 34\,\mu\mathrm{m}$ along the y-axis and the horizontal waist along the x-axis. Nevertheless, the additional light sheet would boost the confinement of the tweezers and allow for better sideband cooling on this axis. In addition, it would also allow further lowering of the tweezer trapping potential and increase the tweezer switch-off time. Another very advantageous aspect is to load the tweezers out of the light sheet, preventing Talbot planes from filling with atoms.

3.5 Ground-state spin control using Raman transitions

One mandatory requirement to study spin Hamiltonians using Rydberg atoms is the precise preparation and initialization of quantum spin states. Depending on the choice of effective spins, they are prepared via optical pumping and coherent transfer pulses between electronic ground and/or excited states. In our case, after the Raman-assisted optical pumping

during the state preparation and the RSC sequence (see previous section), the atoms are initialized in the $|F = 2,\, m_F = \pm 2\rangle$ hyperfine ground state. For the measurements in this thesis, we usually encode our spins in two hyperfine ground states $|F = 2,\, m_F = +2\rangle$, and $|F = 1,\, m_F = +1\rangle$ or in the $|F = 2,\, m_F = -2\rangle$, and $|F = 1,\, m_F = -1\rangle$ states. Furthermore, we require to drive coherent Raman pulses between them in order to perform Ramsey interferometry measurements as done in Section 4.6. In the following, we will introduce and characterize the corresponding ground-state Raman laser setup.

3.5.1 Ground state Raman laser setup and characterization

We implemented two co-propagating Raman beams along the experimental y-axis to facilitate coherent transitions between atomic spin states. This configuration effectively mitigates any effect of the atom's Doppler shift onto the coherent state transfer. The polarizations of the beams are set both linear and orthogonal to each other. Given that our quantization axis is parallel to the x-axis, this setup drives $\Delta m_F = \pm 1$ transitions. Notably, the choice of linear polarizations avoids any vector light shifts [91].

In more detail, the ground state Raman (GSR) laser is beat-locked to the RSC laser, which is stabilized to a ULE at a detuning $\Delta_{\text{RSC}} = 2\pi \times 40\,\text{GHz}$ from the D1-resonance. The laser setup includes two AOMs in double-pass configuration to bridge the ground state hyperfine splitting of $461.7\,\text{MHz}$. Then, both paths are overlapped with perpendicular polarizations and coupled into the same fiber, making the alignment procedure onto the atoms easier. After the fiber out-coupler, the Raman beams are shaped to be elliptical to maintain a homogeneous coupling for large tweezer arrays. Using an anamorphic prism pair, we obtain a $1/e^2$ waist of $250\,\mu\text{m}$ for the short axis in z-direction and $500\,\mu\text{m}$ for the long axis along the x-direction.

First, we want to measure the ground-state Raman spectroscopy. We apply a ground state Raman pulse of $7\,\mu\text{s}$. Afterward, we ramp the tweezer depth to $20\,\%$ of the initial loading depth. Since we cannot distinguish between the two spin states during fluorescence imaging, we remove the atoms in the $|F = 2,\, m_F = -2\rangle$ state. By applying a resonant D2 pulse, driving the closed $|F = 2,\, m_F = -2\rangle$ to $|F' = 3,\, m_{F'} = 3\rangle$ cycling transition, we heat the atoms such that they escape from the trapping potential. As shown in Fig. 3.12, we measure the probability of finding the atoms in the $F = 1$ state. We can fit the spectroscopy with a $sinc(f)$ envelope with a width of $132.32 \pm 1.87\,\text{kHz}$, which we expect for the applied rectangular-shaped Raman pulse. For the Rabi measurement, we fit an average Rabi frequency of $79.64 \pm 0.15\,\text{kHz}$. The dephasing exceeds the scanned Raman pulse duration and is within the order of several hundreds of microseconds. Due to the Gaussian shape of the Raman beam, we see a Gaussian envelope of the Rabi couplings when evaluating the coupling per tweezer row, which is parallel to the Raman beams. We fit a Gaussian beam with a $1/e^2$ waist of $425.6 \pm 12.1\,\mu\text{m}$. Small offsets in the spectroscopy and Rabi measurements can be explained by an inefficient state preparation to $|F = 2,\, m_F = 2\rangle$ and heat-out pulse of the same state.

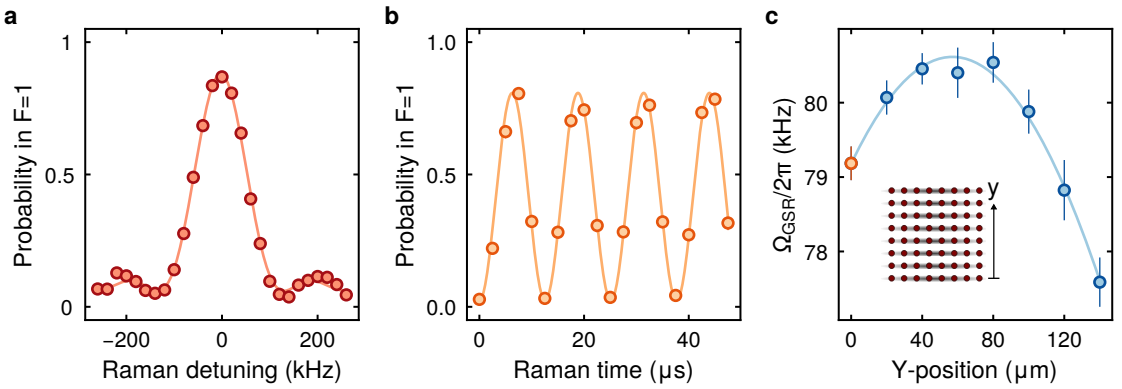

Figure 3.12 Ground state Raman spectroscopy and Rabi oscillation measurements. a. Scan of Raman detuning with a pulse duration of $7\,\mu$s. We average over 64 tweezers and fit a sinc function with a width of $132.32 \pm 1.87\,$kHz, as expected from a rectangular pulse. **b.** Raman Rabi oscillations between the $|F = 2,\, m_F = -2\rangle$ and $|F = 1,\, m_F = -1\rangle$ ground states, averaged over 64 tweezers. The fit shows ocillations with a frequency of $79.64 \pm 0.15\,$kHz. **c.** Raman Rabi oscillation evaluated per tweezer row along the experimental y-axis. The array spacing is $20\,\mu$m. The fit for the Gaussian beam corresponds to a beam with a $1/e^2$ waist of $425.6 \pm 12.1\,\mu$m. The inset shows a schematic of the tweezer array illustrating the plotted y-distance.

3.5.2 Calibrating magnetic offset fields using ground state Raman spectroscopy

We use the narrow Raman transition line to precisely calibrate the magnetic compensation field at the position of the atoms. Given that our experimental setup contains two magnetic offset coils in the x, y, and z directions, it is important to relate the amplitude of the magnetic fields to one another, especially when performing field rotations. The choice of linear polarization for the ground state Raman beams proves beneficial in this context. Without it, vector light shifts could compromise our measurements. Previously, we measured the required magnetic compensation fields using the D2 optical molasses, whose cooling efficiency is very sensitive to stray magnetic fields.

For the calibration measurement, we apply an offset field of $5\,$G aligned along the x-axis and ramp the tweezer power to $0.5\,\%$ to minimize the influence of inhomogeneous trap depths on the width of the averaged spectroscopy signal. We apply a Hahn-shaped Raman pulse between $500 - 700\,\mu$s to drive transition between the $|F = 2,\, m_F = -2\rangle$ to the $|F = 1,\, m_F = -1\rangle$ ground state. Afterward, we heat out the remaining atoms in the $|F = 2,\, m_F = -2\rangle$ state. Changes in the Raman resonance center frequency can directly be translated into magnetic field shifts due to a magnetic field sensitivity of the transition of $3 \times 0.7\,$MHz/G. For α_{xy} (α_{xz}) of $90\,^\circ$ and $270\,^\circ$, we align the field parallel with the y-axis (z-axis). As shown by the grey data points in Fig. 3.13, we measure changes in the Raman resonance frequency due to two effects: The asymmetry of the dips corresponds to a wrong "zero field" setting along the axis. When inverting the magnetic field direction, we would expect the same Raman resonance frequency for a correct zero field. The difference in the

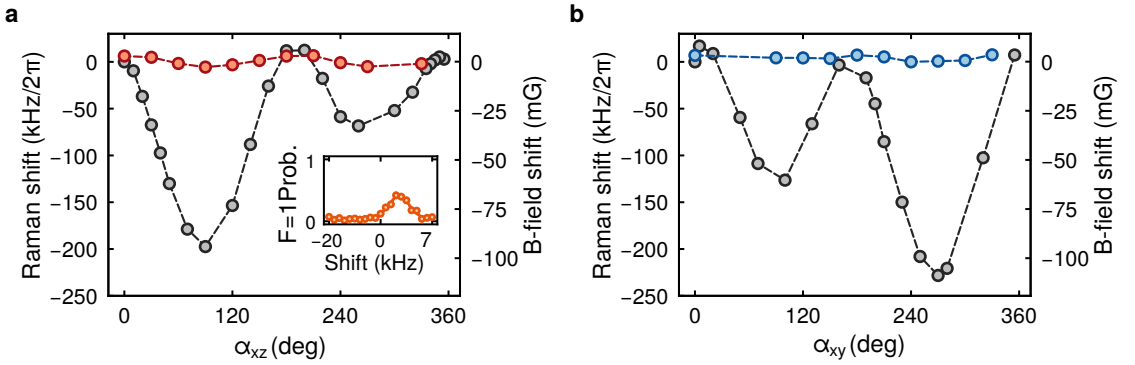

Figure 3.13 Calibrating the magnetic compensation fields. Rotating a magnetic field in the x-z plane (**a**) and in the x-y plane (**b**). The data points correspond to the Raman center frequency of the fitted spectroscopy signals. The inset in **a** shows an exemplary spectroscopy measurement with a Gaussian fit. The measurement was done before (grey data points) and after (red data points) correcting the magnetic compensation fields. The y-axis label on the right of each plot is the calculated magnetic field shift having a magnetic field sensitivity of $3 \cdot 0.7\,\mathrm{MHz/G}$.

y-direction (z-direction) is $\approx 100\,\mathrm{kHz}$ ($\approx 130\,\mathrm{kHz}$), which is consistent with a change in the magnetic field of about $\approx 50\,\mathrm{mG}$ ($\approx 65\,\mathrm{mG}$). The peak-to-peak magnetic field change between x and y axis (z axis) is $\approx 95\,\mathrm{mG}$ ($\approx 110\,\mathrm{mG}$). After correcting the magnetic zero field and referencing the amplitudes of the magnetic compensation field direction between each other, we repeat the measurement (red and blue data points in Fig. 3.13). We measure a maximal difference of $8\,\mathrm{kHz}$ ($3.6\,\mathrm{mG}$), when rotating the field bei $90\,^\circ$ in the x-y-plane and $12\,\mathrm{kHz}$ ($5.8\,\mathrm{mG}$) as the maximal difference in the x-z-plane. The applied calibration is sufficient to continue with the Rydberg measurements in the next section. However, the accuracy of the magnetic field can be improved further with a second optimization iteration using longer Raman pulse durations, not being Fourier limited, and evaluating the resonance frequency per tweezer and not averaged. The atoms' temperature will then limit the highest achievable accuracy.

3.5.3 Implementing a Ramsey interferometric sequence

Now, we want to characterize the dephasing of the ground state control. We start with preparing all atoms in the $|F = 2,\, m_F = -2\rangle$ state, ramp the tweezer power to $0.05\,\%$ and apply a Ramsey interferometry sequence with two $\pi/2$ pulses, separated by the scanned evolution time. We set the laser to be detuned by $\Delta/2\pi = 30\,\mathrm{kHz}$ from the Raman resonance and measure the characteristic sinusoidal oscillations with a frequency equal to the set detuning in Fig. 3.14. We fit a Gaussian decay T_2^* of $81 \pm 5.3\,\mu\mathrm{s}$. One of the major reasons for the fast dephasing are fluctuations in the magnetic field during the measurement arising from the $50\,\mathrm{Hz}$ power grid. These fluctuations lead to a normal distribution of oscillation frequencies.

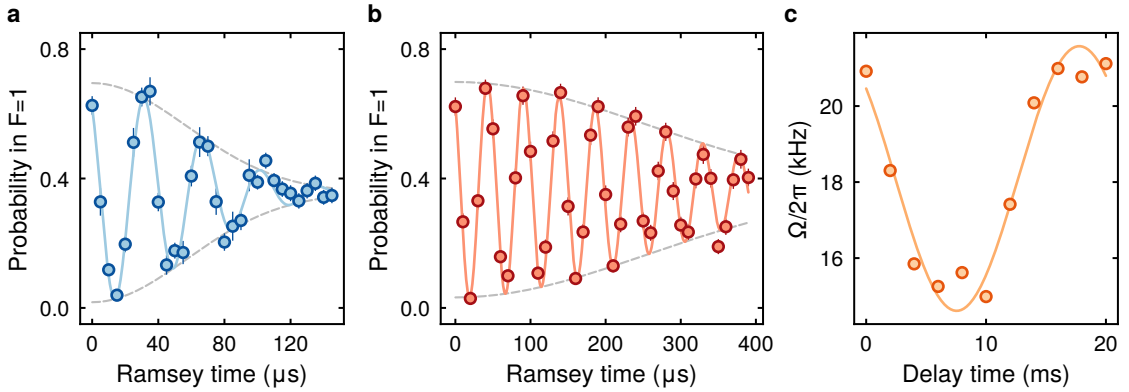

Figure 3.14 Ramsey fringes with and without power line trigger. a. Measurement of Ramsey fringes without a line trigger. We apply a $\pi/2$ pulse of $3.2\,\mu s$ and fit a $\sin$ (solid line) with a frequency of $2\pi \times 28.26 \pm 0.32\,\mathrm{kHz}$. The dashed line is the fitted Gaussian decay of $81 \pm 5.3\,\mu s$. **b.** Ramsey fringes measureme nt when using an in-sequence line trigger. The applied $\pi/2$ pulse duration is $3.7\,\mu s$. The fit (solid line) gives an oscillation frequency of $20.92 \pm 0.054\,\mathrm{kHz}$ with a Gaussian decay (dashed line) of $358.5 \pm 20.7\,\mu s$. **c.** Data points are the fitted oscillation frequencies of Ramsey fringes when applying the Ramsey measurements at different timings w.r.t. to the line trigger. We fit $\sin$ with a frequency of $48.9 \pm 3.1\,\mathrm{Hz}$.

To correct for fluctuations in the power grid, we implemented a so-called "line trigger". It pauses the cycle at a specific time during the sequence and holds the experimental parameters until the next zero crossing of the $50\,\mathrm{Hz}$ line occurs such that the residual magnetic offset fields are in-phase afterward. We repeat the same Ramsey interferometry sequence as before at a detuning of $2\pi \times 20\,\mathrm{kHz}$ and measure a T_2^* time of $358.5 \pm 20.7\,\mu s$. Furthermore, we repeat the same measurement with various delays of the Ramsey pulse sequence w.r.t. the zero crossing of the power grid and fit the resulting oscillation. Fig. 3.14 shows the measured oscillation frequency, where we applied a sinusoidal fit, and obtained a frequency of $48.9 \pm 3.1\,\mathrm{Hz}$.

The dephasing can be improved further by implementing a spin-echo pulse (π pulse) centered between the $\pi/2$ pulses. Additionally, one could eliminate any magnetic field fluctuations when encoding the spin in the magnetically insensitive Zeeman sublevels $m_F = 0$ and driving the so-called clock transition $\Delta m_F = 0$ [37, 38, 54].

In summary, we have characterized the coherent ground state atom control between the $|F = 2\, m_F = -2\rangle$ and $|F = 1\, m_F = -1\rangle$ states and calibrated the magnetic compensation fields using Raman spectroscopy. Additionally, we have shown how the so-called line trigger improves the dephasing measuring characteristic Ramsey fringes by a factor of ≈ 4.

In this chapter, we explored the characteristics of our experimental setup and elaborated on the methods used to load and image tweezers. Building on this foundation, we described our state preparation technique and detailed the implementation of Raman sideband cooling. With our atoms prepared, the next logical step is to introduce interactions. We achieve this through the use of Rydberg atoms, which will be the central focus of the next chapter.

Chapter 4

From theory to practice – Probing Rydberg interactions and dressing

Having introduced the concept of Rydberg atoms and their advantageous properties in Chapter 2, we now focus on their interactions. The structure of this chapter is as follows: We begin by exploring the interaction dynamics between two Rydberg atoms in Section 4.1. This leads us to discuss their potential applications in the context of quantum technology. A resulting characteristic of prime significance is the Rydberg blockade effect. This phenomenon, studied extensively in multiple settings, holds the promise of pioneering results, particularly regarding qubit implementation for quantum computation [32, 37, 38, 43, 45, 46, 48, 96–99]. A noteworthy alternative approach of using Rydberg interactions in the context of quantum simulation is the so-called Rydberg dressing. Here, we transfer Rydberg characteristics to ground-state atoms by admixing them with Rydberg states. In Section 4.2, the properties and advantages of Rydberg dressing are presented.

Transitioning from theory to practice, we describe the single-photon Rydberg excitation laser setup used in the subsequent experimental sections. Section 4.3 provides a brief overview of the laser configuration, its general alignment technique, initial calibration procedures, and discourse on challenges regarding optical components encountered when operating at the Rydberg excitation wavelength of $286\,\mathrm{nm}$.

Next, we turn our attention to the practical side, presenting measurements of Rydberg-dressed atoms, especially characterizing the dressed lifetime. A significant constraint here emerges from resonant scattering light during Rydberg dressing due to the phase noise of the Rydberg excitation laser. This issue is discussed in Section 4.4, where we also provide a potential solution by introducing measurements using a spectral filter, an optical cavity. The building process of this setup and the subsequent measurements were collaboratively done with Ludwig Müller, with further insights available in Ludwig Müller's Master thesis [100].

In preparation for our subsequent Rydberg experiments, we measure the light shift induced by the Rydberg dressing laser across different detunings from the Rydberg resonance, as detailed in Section 4.5. This procedure serves as a pre-calibration for all further measurements regarding the Rydberg Rabi couplings.

In Section 4.6, we present our findings from implementing Ising-type spin interactions. We use a Ramsey-interferometric measurement technique to resolve these spin interaction

dynamics. Our analysis identifies the excitation laser phase noise and black-body-induced losses as the predominant sources of decoherence.

Finally, in Section 4.7, our attention turns to black-body induced losses, particularly in the context of Rydberg dressing using optical tweezer arrays. This section offers a qualitative analysis of these effects, concluding with a discussion on potential strategies to address the challenges presented by contaminant atoms introduced during the process.

4.1 Dynamics of interacting Rydberg atoms

The interest in Rydberg interactions has grown since the early 2000s, thanks to the advances in experimental techniques for cooling and trapping atoms. The development of optical tweezers and optical lattices, featuring lattice spacing on the order of the interaction range of Rydberg atoms, has further amplified this curiosity. With their long-range characteristics and the ability to manipulate quantum systems over mesoscopic scales, Rydberg interactions have become a promising subject to study [27, 32, 46, 99, 101–103]. The following section will derive the interaction scaling and explore its importance.

The interactions among Rydberg atoms arise from the large transition dipole matrix elements between adjacent Rydberg atoms, combined with the substantial polarizability of these atoms as detailed in Section 2.2. As a result, even minor perturbations, such as those caused by the presence of a second Rydberg atom at characteristic distances of a few micrometers, can induce a non-vanishing dipole moment [46, 65]. Throughout the derivation and discussion of the interactions in this thesis, we assume that the atoms are sufficiently far apart such that the wavefunctions of the Rydberg electrons do not overlap.

A conventional approach for deducing these interactions employs the electrostatic interaction potential between the valence electron and the apparent nuclei. Considering two atoms, designated as **A** and **B**, the Coulomb interaction $\hat{V}_c$ can be defined as [104, 105]

$$\hat{V}_c = \frac{e^2}{4\pi\epsilon_0}\left(\frac{1}{|\mathbf{R}|} - \frac{1}{|\mathbf{R}-\hat{\mathbf{a}}|} - \frac{1}{|\mathbf{R}+\hat{\mathbf{b}}|} + \frac{1}{|\mathbf{R}-\hat{\mathbf{a}}+\hat{\mathbf{b}}|}\right). \tag{4.1}$$

Here, $\mathbf{R}$ corresponds to the distance between the two nuclei, while $\hat{\mathbf{a}}$ and $\hat{\mathbf{b}}$ represent position operators describing the distance from the Rydberg electrons to their respective nuclei. The different terms express the repulsive potential between the two nuclei and Rydberg electrons, as well as the attractive potential seen by the Rydberg electrons from the nucleus of the other atom. When performing a Taylor expansion up to the third order, under the assumption that $|\mathbf{a}|, |\mathbf{b}| \ll |\mathbf{R}|$, we obtain the leading electrostatic interaction term in the form of the distance-dependent dipole-dipole operator [46, 104]

$$\hat{V}_{dd} = \frac{1}{4\pi\epsilon_0 R^3}(\hat{\mathbf{d}}_a \cdot \hat{\mathbf{d}}_b - 3(\hat{\mathbf{d}}_a \cdot \hat{\mathbf{n}})(\hat{\mathbf{d}}_b \cdot \hat{\mathbf{n}})) \tag{4.2}$$

where we used $\hat{\mathbf{n}} = \mathbf{R}/|\mathbf{R}|$ as a unit vector for the interatomic axis along the direction of $\mathbf{R}$. In addition, we replaced the positional operators $\hat{\mathbf{a}}, \hat{\mathbf{b}}$ with the electric dipole operators $\hat{\mathbf{d}}_a = e\hat{\mathbf{a}}$ for the individual atoms [46].

The previously derived interaction operator acts simultaneously on two atoms. Hence, it is convenient to define the two-atom basis for the atoms A and B, written as $|r_a\rangle \otimes |r_b\rangle = |r_a r_b\rangle$. Here, each $|r_a\rangle = |n_a \ell_a, j_a, m_a\rangle$ represents the quantum numbers of the atomic states described by the wavefunction

$$\psi_{n\ell jm}(r, \theta, \phi) = R_{n\ell}(r) \cdot Y_{\ell jm}(\theta, \phi)\,. \tag{4.3}$$

The wavefunction is described by the product of the radial part $R_{n\ell}(r)$ and the spherical harmonics $Y_{\ell jm}(\theta, \phi)$, describing the angular component of the wavefunction. With this description, we want to evaluate the dipole matrix element $\langle r_a r_b|\hat{V}_{dd}(\mathbf{R})|r_c r_d\rangle$, describing how the Rydberg atoms interact in the given two-atom basis.

$$\langle r_a r_b|\hat{V}_{dd}(\mathbf{R})|r_c r_d\rangle = \frac{1}{4\pi\epsilon_0 R^3} f_{a,b,c,d}(r) \left(\mathbf{C}_a^c \mathbf{C}_b^d - 3(\mathbf{C}_a^c \cdot \hat{\mathbf{n}})(\mathbf{C}_b^d \cdot \hat{\mathbf{n}})\right)\,. \tag{4.4}$$

In this expression, we used

$$f_{a,b,c,d}(R) = \int r^3 dr R_{n_a \ell_a}(R) R_{n_b \ell_b}(R) R_{n_c \ell_c}(R) R_{n_d \ell_d}(R) \tag{4.5}$$

which encounts for the product of the various radial components and the Clebsch-Gordan coefficients

$$\mathbf{C}_a^c = \int \sin\theta d\theta d\phi\, \hat{\mathbf{e}}_r Y^*_{\ell_a j_a m_a}(\theta, \phi) Y_{\ell_c j_c m_c}(\theta, \phi)\,. \tag{4.6}$$

The individual coefficients contain the angular contribution to the matrix elements and can be evaluated in terms of Wigner $3j$-symbols, which is done for each component in [104]. Nevertheless, due to the characteristics of these symbols, the angular dependence carries some crucial informations recognized as the dipole selection rules [104, 106], which are also exemplary shown by descrite coupling channels in Fig. 4.1:

- **The ℓ-selection rule**: The orbital angular momentum must change by ± 1, such that $\ell_c = \ell_a \pm 1$ and $\ell_d = \ell_b \pm 1$. This rule allows us to define discrete coupling channels contributing to the interaction. Throughout this thesis, we primarily work

a

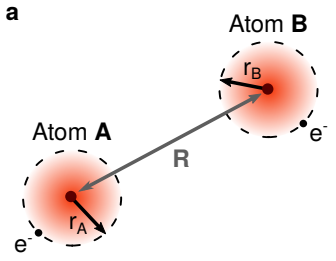

b

$\lvert\ell_a j_a, m_a\rangle + \lvert\ell_b j_b, m_b\rangle \rightarrow$	$\lvert\ell_c j_c, m_c\rangle + \lvert\ell_d j_d, m_d\rangle$
$\lvert P_{1/2}, \frac{1}{2}\rangle + \lvert P_{1/2}, \frac{1}{2}\rangle \rightarrow$	$\lvert S_{1/2}, \frac{1}{2}\rangle + \lvert S_{1/2}, \frac{1}{2}\rangle$
$\lvert P_{1/2}, \frac{1}{2}\rangle + \lvert P_{1/2}, \frac{1}{2}\rangle \rightarrow$	$\lvert D_{3/2}, \{-\frac{1}{2}, \frac{3}{2}\}\rangle + \lvert D_{3/2}, \{\frac{3}{2}, -\frac{1}{2}\}\rangle$
$\lvert P_{1/2}, \frac{1}{2}\rangle + \lvert P_{1/2}, \frac{1}{2}\rangle \rightarrow$	$\lvert S_{1/2}, \{-\frac{1}{2}, \frac{1}{2}\}\rangle + \lvert D_{3/2}, \{\frac{3}{2}, \frac{1}{2}\}\rangle$
$\lvert P_{1/2}, \frac{1}{2}\rangle + \lvert P_{1/2}, \frac{1}{2}\rangle \rightarrow$	$\lvert D_{3/2}, \{\frac{3}{2}, \frac{1}{2}\}\rangle + \lvert S_{1/2}, \{-\frac{1}{2}, \frac{1}{2}\}\rangle$

Figure 4.1 Interacting Rydberg atoms and coupling channels. a. Sketch for two interacting atoms **A** and **B**, with corresponding Rydberg orbits (shading), separated at distance **R**. **b.** Example for the dipole-dipole interaction coupling atom pairs in $P_{1/2}, m_j = 1/2$ states to different state channels. Note that the change in the m quantum number allows for spatial restrictions due to the polarization of the virtually emitted photons [106] thus defining the spatial interaction shape.

with Rydberg P-states, where $\ell = 1$. These states provide coupling channels to Rydberg S and D states.

- **The m_j-selection rule**: This constraint restricts the allowed transitions to those where the magnetic quantum number m_j changes by $\{0, \pm 1\}$. This rule influences the spatial interaction profile between two Rydberg atoms. Since the total angular momentum is conserved during these transitions, the sum of the m-quantum numbers must also remain the same, meaning that $m_a + m_b = m_c + m_d$ needs to be fulfilled.
- **The j-selection rule**: This rule emerges from the previous rules and only allows for transitions of $0, \pm 1$, further narrowing the number of channels to which a Rydberg atom can couple under the influence of the interaction.

In addition, the product of the radial components, as described in Eq. (4.5), significantly affects the number of states contributing to the interaction. Specifically, it explains why the influence is more effective when Δn is small. If this is not the case, the overlap between the different states vanishes and effectively nullifies their contribution to the interaction.
This aspect and the selection rules above play an essential role in calculating atomic transitions and consequently also in describing the Rydberg atom interactions, carefully considering the quantum numbers involved in these processes [46, 65].

We now want to analyse the dipole-dipole interaction in Eq. (4.4) more in depth. Specifically we are interested in different intial pair-state configurations, depending on whether the pair of atoms do show same or opposite parity of states. We can thus differ between two major types of interactions [46, 107, 108], which we will discuss in the following two sections.

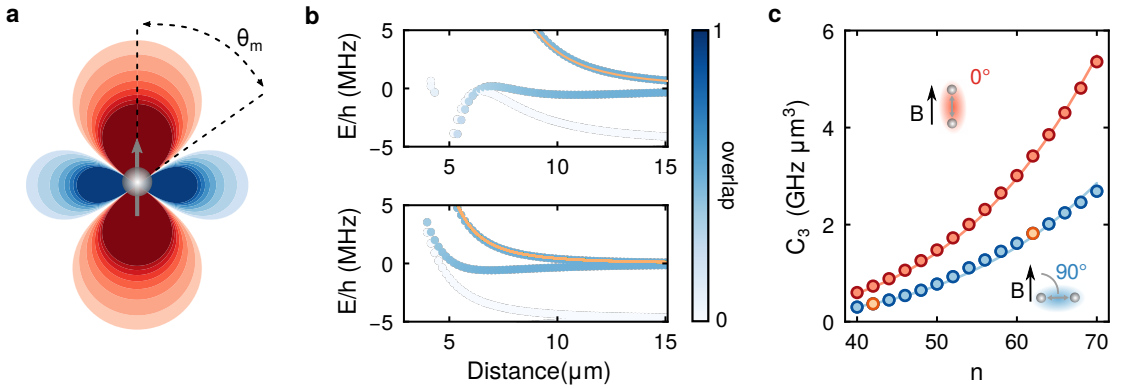

Figure 4.2 Schematic and interaction calculations for the resonant interaction type. a. Spatial interaction profile of the dipole-dipole interaction. The dashed line at $54.7°$ indicated the magic angle, at which die interactions vanish. **b.** Calculations of Rydberg pair potentials for the $|\Psi_{ab}\rangle = |42P_{1/2}, m_j = 1/2\rangle \otimes |42S_{1/2}, m_j = 1/2\rangle$ state (lower) and $\Psi_{ab} = |62P_{1/2}, m_j = 1/2\rangle \otimes |62S_{1/2}, m_j = 1/2\rangle$ state (upper), where the overlap indicates the quadratic overlap $|\langle\Psi_{ab}|\Psi_\alpha\rangle|^2$, where $|\Psi_\alpha\rangle$ corresponds to the Rydberg manifold. The orange line is a fit of the upper branch using a $f(r) = C_3/r^3 + C_6/r^6$ fit function. For the calculation, the atoms are oriented perpendicular to the magnetic field with $|\mathbf{B}| = 5G$. The calculations of the Rydberg pair potentials have been done with the aid of PAIRINTERACTION [105]. **c.** Extracted values for the C_3 coefficients from the fits as shown in b., but for principal quantum numbers from 40 to 70 in steps of 2. The blue (red) data points correspond to a setting, where the atoms are oriented perpendicular (parallel) to the magnetic field. The two orange points are the obtained C_3 coefficients from b. The solid line is a $\propto n^4$ fit. Errorbars of the individual fits are smaller than the data points.

4.1.1 Resonant dipole-dipole transitions

The resonant interaction emerges when two atoms occupy different Rydberg states with opposite parity, thereby obtaining a non-zero dipole matrix element $|\langle r_a|\hat{\mathbf{d}}|r_b\rangle| = d_{ab} \neq 0$. In the rotating frame, we define the energy reference point as $E_a = 0$ and thus $E_b = \Delta$. The interaction that arises between the two different Rydberg states is based on the dipole matrix element, which in turn is incited by the coupling between the different Rydberg states, as previously discussed.

Defining the interaction Hamiltonian in the pairstate basis of these two Rydberg states reads as

$$\hat{H}_{dd} = \begin{matrix} \\ |r_a r_b\rangle \\ |r_b r_a\rangle \end{matrix} \begin{matrix} \langle r_a r_b| & \langle r_b r_a| \end{matrix} \begin{pmatrix} \hbar\Delta & V_{dd} \\ V_{dd}^* & \hbar\Delta \end{pmatrix}. \tag{4.7}$$

This matrix illustrates the oscillation between the two states $|r_a r_b\rangle$ and $|r_b r_a\rangle$, occuring at an oscillation frequency of $2/hV_{dd}$ [109]. The off-diagonal coupling terms are the well-known dipolar interaction [46]

$$V_{dd}(R,\theta) = \frac{1}{4\pi\epsilon_0 R^3} d_{ab}^2 \left(1 - 3\cos^2\theta\right) . \tag{4.8}$$

The interaction is maximal, when the two atoms are oriented perpendicular to the quantization axis and it is zero for the so-called magic angle of $\theta_m = 54.7^\circ$ [33], as depicted in Fig. 4.2.

The experimental realization of these exchange oscillations requires the initiation of two atoms in different Rydberg states. This has been achieved by preparing the atoms in one Rydberg state and additionally integrating a microwave source, which usually drives transitions in the GHz regime and couples to nearby Rydberg states [52, 109]. Furthermore, local excitations within a tweezer array have been accomplished using off-resonant beams on selected traps to induce a light shift and thus shifting them either selectively in resonance or off-resonance to the microwave transition [110, 111]. This technique emphasizes the beneficial combination of optical microtraps and Rydberg interactions.

4.1.2 Off-resonant dipole-dipole interactions

The off-resonant interaction, also known as the van der Waals interaction, emerges between two atoms occupying the same Rydberg state (having the same parity). Due to the absence of direct coupling between the atoms ($|\langle r_a|\hat{\mathbf{d}}|r_a\rangle| = d_{aa} = 0$), the first-order dipole-dipole interaction vanishes, such that C_3 coefficients are zero. As a consequence, second-order processes, after applying a second-order perturbative treatment of the dipole-dipole interaction, represent then the leading terms of this interaction. In other words, the interaction can be understood as virtual processes where atoms couple to virtual states while preserving energy conservation (see selection rules). These states, detuned from the intial Rydberg pair state by the so-called Förster defects $\Delta_{aa,cd} = E_c + E_d - 2E_a$, can only be virtually populated in a second-order process:

$$V_{\text{vdW},aa} = \sum_{cd} \frac{|\langle r_c r_d|V_{dd}(R)|r_a r_a\rangle|^2}{\Delta_{aa,cd}} = C_6(\theta)/R^6 . \tag{4.9}$$

The sum of all these coupling channels results in an effective interaction between the atoms. This interaction is quantified by the characteristic $C_6(\theta)$ coefficient, leading to the interaction scaling as $V_{\text{vdW}} \propto n^{11}$ [32, 112–119].

This type of interaction is widely known due to its role in the blockade mechanism. Here, an excited atom suppresses the excitation of surrounding atoms to the same Rydberg state, leading to a characteristic blockade radius R_b defined as

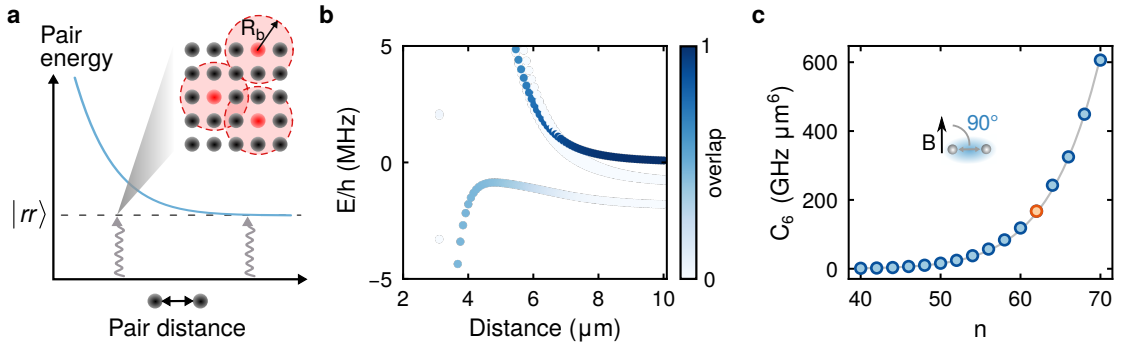

Figure 4.3 Schematic and interaction coefficient calculations for the off-resonant interaction type. a. The schematic illustrates the concept of the blockade radius. Due to the van der Waals interaction (blue line), the laser is unable to simultaneously couple both atoms to the Rydberg state, depending on the distance between the atoms, the excitation laser frequency, and the state linewidth. **b.** Calculations of Rydberg pair potentials for the $|\Psi_{ab}\rangle = |62P_{1/2}, m_j = 1/2\rangle \otimes |62P_{1/2}, m_j = 1/2\rangle$ state, with the overlap representing the quadratic overlap $|\langle\Psi_{ab}|\Psi_\alpha\rangle|^2$. For these calculations, atoms are aligned perpendicular to the magnetic field with $|\mathbf{B}| = 1G$. The Rydberg pair potentials were calculated using PAIRINTERACTION [105]. **c.** We derive the C_6 coefficients from each pair potential using a fit of the form $f(r) = C_3/r^3 + C_6/r^6$ for principal quantum numbers ranging from 40 to 70 in steps of 2. The solid line represents a $\propto n^{11}$ fit. Error bars for the individual fits are smaller than the data points.

$$R_b = \sqrt[6]{\frac{|C_6|}{\Omega}}\,. \tag{4.10}$$

In this equation, Ω refers to the laser coupling, which power broadens the line. The radius basically defines a distance between a pair of atoms, where the strength of the laser driving is equal to the absolute value of the Rydberg-Rydberg interaction. This mechanism plays a key role in the design of interactions and the engineering of quantum gates [32, 37, 38, 43, 45, 46, 48, 96–99, 120]. From an experimental standpoint, this interaction is relatively straightforward to realize, as both ground-state atoms can be coupled to the same Rydberg state.

A unique case emerges when the Rydberg states are prepared or tuned to approach Förster resonances, whereby the Förster defect is almost vanishing. In this situation, the interaction scaling changes drastically, transitioning to a $1/R^3$ scaling [68]. Förster resonances naturally arise when the C_6 coefficient undergoes a sign shift. A possible workaround to obtain Förster resonances involves implementing electric fields to artificially shift the Rydberg levels, creating conditions that allow for Förster resonances to occur [121]. This case illustrates how the characteristics of the interaction can be exploited through the specific characteristics of the Rydberg atoms involved.

4.1.3 Quantum technology applications of Rydberg interactions

Over the past few decades, Rydberg atoms have proven to be a versatile platform for many applications in quantum technology. These applications take advantage of the unique properties of Rydberg atoms, including controllable interactions, the blockade mechanism, long state lifetimes, large polarizabilities, and other features [31, 46, 65, 66, 122]. This opens up a range of applications for:

- **Quantum computing and quantum information processing**: The Rydberg blockade mechanism is fundamental to the engineering of gates in Rydberg-based quantum computers [32, 37, 38, 43, 45, 46, 48, 96–99]. Despite significant advancements, achieving high-fidelity two-qubit entangling gates with neutral atoms remains challenging, particularly regarding feasible quantum error correction. Nonetheless, Rydberg atoms are strong candidates for implementing quantum error correction protocols [123–125]. Additionally, the unique properties of Rydberg atoms open new pathways for encoding, manipulating, and transferring quantum information. Their potential for coherent state transfer, combined with long coherence times relative to interaction timescales, make them promising for quantum memory applications – a key component for long-distance quantum communication and quantum repeaters [46, 126–128].
- **Quantum simulation within the Rydberg manifold**: Rydberg interactions have proven to be a powerful tool to simulate complex quantum many-body systems in a highly controllable experimental setting. The long-range nature of these tunable interactions enables realizing complex models such as the XY-Hamiltonian and the transverse-field Ising Hamiltonian [66]. In the XY model, interactions between the different components (spins) depend on their respective orientation and are thus based on resonant exchange interactions. Besides the fact that it can be used to study quantum magnetism, it is also exploited to analyze transport properties in various settings, such as the spread of spin excitations in a chain [109, 129]. On the other hand, the transverse-field Ising Hamiltonian is used to describe magnetic materials and quantum phase transitions, leading to an improved understanding of these systems [21, 49, 66, 99, 130]. Recently, the engineering of XXZ Hamiltonians in arrays of Rydberg atoms has been realized [52], where the resonant dipole-dipole interaction has been used. This opens perspectives to study frustration for different array geometries or domain-wall dynamics for large systems.
- **Quantum metrology**: The strong interactions between Rydberg atoms offer the possibility to prepare and generate large entangled states, an advantageous feature in quantum metrology. The correlations within these states enable enhanced precision measurements, which is particularly beneficial in the context of spin squeezing [58, 131, 132]. Moreover, the non-linear response of Rydberg atoms to external electric and magnetic fields makes them very favorable candidates for constructing highly sensitive quantum sensors [68, 122]. By working with circular Rydberg states, which have a high orbital angular momentum quantum number, the radiative lifetime,

sensitivity, and polarizability can be further enhanced, optimizing their suitability for high-precision measurements [133].

- **Nonlinear quantum optics**: The nonlinear scaling of interactions within Rydberg ensembles, originating from the blockade effect, finds a significant advantage within the context of nonlinear quantum optics. The impact of the nonlinearity can be amplified to the extent that one is sensitive at a few or even single photon level [134]. This leads to innovative applications, including single-photon transistors, where a single photon controls the transmission of subsequent photons, or single-photon switches, where the direction of light is controlled on a single photon level [122, 135].
- **Rydberg dressing**: Instead of operating entirely within the Rydberg manifold, it is possible to transfer a part of the Rydberg-Rydberg interactions to the ground state, thus preparing ground state atoms with an experimentally controllable fraction of Rydberg characteristics [4, 54, 56, 57, 136–142]. The derivation and relevance of this technique, called Rydberg dressing, will be discussed in more detail in the next section.

While the listed applications offer a broad snapshot of the growing field of Rydberg physics, they represent just the tip of the iceberg. The variety and prospects of the platform have grown remarkably in recent years. Beyond what is listed, other areas of active research include the exploration of Rydberg molecules [143–146], which present a unique combination of atomic and molecular physics. Multi-valence electron atomic species, such as alkaline earth or alkaline earth like atoms, have also gained attention, especially in the context of quantum computing, due to their richer electronic structure and the possibility to enhance or facilitate specific Rydberg properties [36, 89, 147, 148]. To tackle the intrinsic challenge of decoherence and black-body limited Rydberg state lifetimes, several groups have turned to circular Rydberg atoms, recognized for their extended lifetimes especially in cavities or even in cryogenic environments [71, 149, 150]. In addition, the integration of cryogenic environments offers another avenue to mitigate decoherence, providing a 'quieter' environment for Rydberg experiments [149]. Researchers are pushing boundaries even further by integrating Rydberg atoms into ultrafast physics, where one can, with sophisticated laser pulses, dive into the fast dynamics of dipole-dipole interactions [151]. Furthermore, various groups are researching Rydberg excitons, an interesting field of research combining Rydberg excitations and solid-state materials [152]. However, there is also research on creating hybrid quantum systems combing trapped, ultracold atoms with on-chip microwave resonators [153, 154]. Other research groups also combine Rydberg physics with ion physics to so-called Rydberg ions [155], or trap Rydberg atoms inside optical cavities [56, 58].

In summary, the applications of Rydberg atoms cover a broad landscape from quantum computing to precision sensing, reflecting the miscellaneous nature of this field.

4.2 Atoms with a Rydberg dress

In this section, we have a closer look at another fascinating aspect of Rydberg physics: Rydberg dressing. This phenomenon broadens our perspective of Rydberg atoms by demonstrating how (a collection of) ground-state atoms can undergo an interaction induced two-atom energy shift when admixed with Rydberg states, effectively 'dressing' them with Rydberg properties.

4.2.1 Rydberg dressed interaction

We will begin by deriving this energy shift for a two-atom system. Initially, both atoms are prepared in the ground state $|g\rangle$ and are off-resonantly coupled to the Rydberg state $|r\rangle$ via the Rabi coupling Ω and the laser detuning Δ. Thus, we can compose a new, dressed state $|\tilde{g}\rangle$ that is mainly in the ground state but additionally offers a tunable fraction of Rydberg characteristics: $|\tilde{g}\rangle \approx |g\rangle + \beta|r\rangle$ [156]. Here, the Rydberg admixture $\beta = \Omega/2\Delta$, purely dependent on the laser parameters, offers an additional level of control in adjusting the Rydberg probability (which scales with β^2) and, thus, the contribution from Rydberg interactions. Assuming, for example, a Rabi coupling of $\Omega = 2\pi \times 1\,\mathrm{MHz}$ and laser detuning of $\Delta = 2\pi \times 2\,\mathrm{MHz}$, we have an admixture of $\beta^2 = 6.25\,\%$. This representation sticks to a fully coherent picture, implying the absence of other decoherence and loss mechanisms.

We begin with two atoms, prepared in the ground state and well-separated, such that we can consider them as individual atoms. When switching on the detuned coupling beam, both atoms experience an energy shift δ_{AC}. This so-called light shift can be calculated using perturbation theory and is understood as a correction term to the atom's Hamiltonian $H_\Delta = \hbar\Delta|r\rangle\langle r|$, treating the laser driving as a pertubation $H_\Omega = \hbar\Omega/2(|g\rangle\langle r| + |r\rangle\langle g|)$, where $\Omega = \langle g|\hat{\mathbf{d}} \cdot \mathbf{E}|r\rangle$ with the laser driving field $\mathbf{E}$ (see also Section 2.2 for detailed derivation of the dipole matrix element and Rabi frequency). The first-order correction is zero because the time-averaged fast oscillating driving field equals zero. The same scenario applies to all odd orders of the perturbative treatment and can be understood from symmetry arguments: Odd orders contain a product of an odd number of field operators, where the negative and positive contributions cancel out when averaging over time. Consequently, only the even orders will contribute to the single-atom energy shift [30]:

$$\delta_{AC} = \frac{\hbar\Omega^2}{4\Delta} + \frac{\hbar\Omega^4}{16\Delta^3} + \mathcal{O}\left(\left(\frac{\Omega}{2\Delta}\right)^6\right). \tag{4.11}$$

As we decrease the distance between the two atoms, interactions between the Rydberg components become apparent. In an intuitive picture, we would expect these interactions to scale with the product of the Rydberg probabilities of the two individual atoms, thus scaling with β^4. However, this cannot hold true for all distances. As we continue to reduce the atom-atom distance, the Rydberg fraction will gradually decrease due to the scaling

behaviour of the interaction potential until it effectively vanishes due to the increased effective pair-detuning. Thus, we will expect a saturation behavior for the interaction contribution to the state $|\tilde{g}\tilde{g}\rangle$.

We now want to calcuate this interaction induced potential, and start with defining our two-atom Hamiltonian. In addition, we transfer to a rotating frame, which simplifies the atom-light interaction treatment. The two-atom Hamiltonian in the $|gg\rangle$, $|+\rangle = (|rg\rangle + |gr\rangle)/\sqrt{2}$, $|rr\rangle$ basis can then be expressed as:

$$\hat{H} = \begin{array}{c} \\ |gg\rangle \\ |+\rangle \\ |rr\rangle \end{array} \begin{array}{c} \begin{array}{ccc} \langle gg| & \langle +| & \langle rr| \end{array} \\ \begin{pmatrix} 0 & \hbar\Omega/\sqrt{2} & 0 \\ \hbar\Omega/\sqrt{2} & -\hbar\Delta & \hbar\Omega/\sqrt{2} \\ 0 & \hbar\Omega/\sqrt{2} & -\Delta^{(2)} \end{pmatrix} \end{array}. \tag{4.12}$$

In this Hamiltonian, we neglected the anti-symmetric state $|-\rangle = (|rg\rangle - |gr\rangle)/\sqrt{2}$ since it is not coupled by any laser due to the interference between the two excitation paths. Additionally, we introduced the two-photon detuning $\Delta^{(2)} = 2\hbar\Delta - V_{\text{vdW}}(R,\theta)$, where we restored the van der Waals interaction potential $V_{\text{vdW}}(R,\theta)$. From this definition, the impact of the sign of the laser detuning relative to the interaction potential becomes evident: When both signs are identical, the laser can become resonant with the atomic transition. To obtain an exact solution for the $|\tilde{g}\tilde{g}\rangle$ state under these circumstances, it is necessary to diagonalize the full Hamiltonian of the system. Diagonalizing the matrix in Eq. (4.12), we obtain three distance-dependent eigenenergies $E_{rr}, E_+, E_{\tilde{g}\tilde{g}}$, referring to the asymptotic states $|rr\rangle$, $|+\rangle$ and $|\tilde{g}\tilde{g}\rangle$. The distance-dependent eigenenergies for a Rabi coupling of $\Omega/2\pi = 1\,\text{MHz}$ and a detuning of $\Delta = \pm 2\pi \times 5\,\text{MHz}$ are illustrated in Fig. 4.4, where the previously mentioned saturation behavior of $E_{\tilde{g}\tilde{g}}$ is clearly visible. This demonstrates that our earlier intuitive approach provided valuable insights into the interaction shape.

Nevertheless, the Hamiltonian can become quite complex for larger many-body systems, making it impossible to find an exact analytical expression. One possible solution to this issue is to employ an approximate method, such as perturbation theory. Thus, we now apply a perturbative approach to estimate the energy correction associated with the Rydberg-Rydberg interaction, following the procedure from reference [157]. Note that this derivation is applicable when $\Omega/\Delta \ll 1$, thereby ensuring we do not cross any atomic resonance.

Similar to the treatment for Eq. (4.11), we consider the laser coupling term $\hat{H}_\Delta$ as a perturbation to the single atom Hamiltonian $\hat{H}_\Delta$. As we have observed earlier, the k-th order of the perturbation series contains a product of k field operators, thereby describing the influence of k virtual processes (photons). In the two-atom picture, this requirement means we need a total of four virtual photons to effectively couple the Rydberg-Rydberg interactions to the pair of ground-state atoms. Thus, we will calculate the energy correction terms $u^{gg}_{(k)}$ up to the $4th$ order [157, 158]:

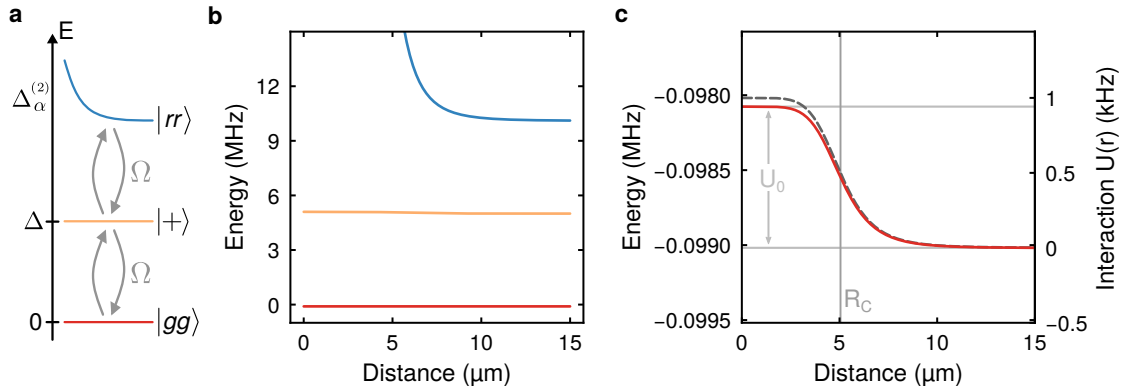

Figure 4.4 Rydberg-dressing potentials for a two-atom system. a. Illustration of the perturbative treatment. A pair of ground state atoms $|gg\rangle$ is coupled via the Rabi coupling Ω to the state $|+\rangle$, with a detuning of Δ. The singly excited state is subsequently coupled to the Rydberg pair state $|rr\rangle$ with a detuning $\Delta_\alpha^{(2)}$. The latter includes the Rydberg-Rydberg interaction V_{vdW}, which gives rise to the soft-core interaction type potential illustrated in c. **b.** The figure displays the three eigenenergies $E_{rr}, E_+, E_{\tilde{g}\tilde{g}}$ (in blue, yellow, and red) for a detuning $\Delta/2\pi = -5\,\text{MHz}$ and Rabi coupling $\Omega/2\pi = 1\,\text{MHz}$, assuming an interaction coefficient of $C_6 = 166\,\text{GHz}/\mu\text{m}^6$ extracted from Fig. 4.3 for the $62P_{1/2}$ state. **c.** A detailed view of the $E_{\tilde{g}\tilde{g}}$ eigenenergy. The dashed line corresponds to the perturbative result from Eq. (4.14). The two horizontal lines represent the soft-core height U_0, and the vertical line indicates the soft-core radius $R_C = 5.05\,\mu\text{m}$.

$$
\begin{aligned}
u_{(1)}^{gg} &= \langle gg|\hat{H}_\Omega|gg\rangle = 0 \\
u_{(2)}^{gg} &= \frac{|\langle gg|\hat{H}_\Omega|+\rangle|^2}{\langle +|\hat{H}_\Delta|+\rangle} = \hbar\frac{\Omega^2}{2\Delta} \\
u_{(3)}^{gg} &= \frac{\langle gg|\hat{H}_\Omega|+\rangle\langle +|\hat{H}_\Omega|rr\rangle\langle rr|\hat{H}_\Omega|gg\rangle}{\langle +|\hat{H}_\Delta|+\rangle\langle rr|\hat{H}_\Delta|rr\rangle} - u_{(1)}^{gg}\frac{|\langle gg|\hat{H}_\Omega|rr\rangle|^2}{(\langle rr|\hat{H}_\Delta|rr\rangle)^2} = 0 \\
u_{(4)}^{gg} &= \frac{|\langle gg|\hat{H}_\Omega|+\rangle\langle +|\hat{H}_\Omega|rr\rangle|^2}{(\langle +|\hat{H}_\Delta|+\rangle)^2\langle rr|\hat{H}_\Delta|rr\rangle} - u_{(2)}^{gg}\frac{|\langle gg|\hat{H}_\Omega|+\rangle|^2}{(\langle +|\hat{H}_\Delta|+\rangle)^2} = \hbar^2\frac{\Omega^4}{4\Delta^2\cdot\Delta^{(2)}} - \hbar\frac{\Omega^4}{4\Delta^3}\,.
\end{aligned}
\tag{4.13}
$$

From these calculations, we identify that the first and third-order terms are zero. This is intuitively clear, as we always require an equal amount of virtual photons to couple to the ground state. Moreover, we notice similarities when comparing the second and the fourth-order terms with the light shift calculated in Eq. (4.11). For example, the second-order term corresponds exactly to twice the second-order light shift. This factor two is attributed to the two-atom system under consideration. However, as expected, there are no Rydberg-Rydberg interactions in the second order, which is why proceeding to the fourth order is necessary. Furthermore, as we are only interested in the interaction-induced shift of the dressed ground

state potential U_{gg}, we normalize the energy corrections by subtracting the light shift for two atoms, as calculated in Eq. (4.11), from the sum of all energy correction terms:

$$U_{gg} = u^{gg}_{(1)} + u^{gg}_{(2)} + u^{gg}_{(3)} + u^{gg}_{(4)} - 2\delta_{AC} = \frac{\hbar^2\Omega^4}{4\Delta^2\Delta^{(2)}} - \frac{\hbar\Omega^4}{8\Delta^3} = \frac{U_0}{(R/R_c)^6 - 1}. \tag{4.14}$$

Here, we used Eq. (4.9) to extract the soft-core potential

$$U_0 = \frac{\hbar\Omega^4}{8\Delta^3} \tag{4.15}$$

and the soft-core radius

$$R_C = \sqrt[6]{\frac{C_6}{2\hbar\Delta}}. \tag{4.16}$$

Interestingly, as previously mentioned, the extracted soft-core potential scales with $U_0 = 2\hbar\Delta\beta^4$ and, thus, purely depends on laser parameters. The soft-core radius, on the other hand, scales according to the ratio between the interaction coefficient C_6 and the laser detuning and is maximal when both are identical. We also note some similarities with the blockade radius in Eq. (4.10) as both describe the ratio between the van der Waals coefficient and the effective power broadening $\Omega_{\text{eff}} = \sqrt{\Omega^2 + (2\Delta)^2}$, which corresponds to $\Omega_{\text{eff}} = \Omega$ for resonant physics and $\Omega_{\text{eff}} = 2\Delta$ for the dressing regime, where $\Omega^2 \leqq \Delta^2$ [136].

4.2.2 Lifetime of Rydberg dressed atoms

Another key aspect of Rydberg dressing is the extended lifetime of Rydberg states, which scales with the square of the principal quantum number n^2. This principle is discussed in Chapter 2. When operating in the Rydberg dressing regime, we encounter an additional significant timescale. Since a fraction of the Rydberg characteristics β is transferred to the ground state, the resulting dressed atom also exhibits a shortened lifetime. This dressed lifetime is influenced both by the Rydberg admixture and by the black-body limited lifetime of the Rydberg states:

$$\tau_{dr} = \frac{\tau_{bb}}{\beta^2}\,. \tag{4.17}$$

Consider a laser coupling of $\Omega = 2\pi \cdot 1\,\text{MHz}$ and a laser detuning of $\Delta = 2\pi \times 2\,\text{MHz}$. A commonly used Rydberg state throughout this thesis is the $62P$ state, which has a black-body limited lifetime of $\tau_{bb} = 160\,\mu\text{s}$. With the calculated admixture, we therefore obtain a dressed lifetime of $\tau_{dr} = 2.56\,\text{ms}$.

However, in experimental conditions, we also need to consider the laser's linewidth Γ_{Las}. In the calculations above, we assumed an infinitely small laser linewidth. Yet, a finite laser

width becomes critical when it is of the same order or larger than the state linewidth. Thus, we have to combine both linewidths to obtain an effective, experimental linewidth:

$$\Gamma_{\text{eff}} = \Gamma_{bb} + \Gamma_{\text{Las}} \tag{4.18}$$

Besides the linewidth of the laser, the most limiting characteristic of the laser's spectral line is its phase noise, not expressed by this formula [159–161]. Even for lasers with sub-Hertz linewidth, a significant fraction of the overall power can be found in the broad phase-noise pedestal surrounding the carrier, typically extending up to a few megahertz [161]. This can become easily limiting for Rydberg dressing experiments: The additional noise pedestal can cause incoherent, resonant excitations to the Rydberg state, thereby reducing the experimentally observed lifetime of the dressed state [56, 57]. For instance, by locking the laser to a reference cavity [161], the feedback loop can tightly stabilize the laser to the cavity resonance such that $\Gamma_{\text{Las}} \ll \Gamma_{bb}$ can be rather easily reached. However, due to the finite range of the feedback bandwidth, the intrinsic noise of the laser can only be partially compensated.

To carry out Rydberg dressing measurements within a detuning range of a few megahertz, it's crucial to minimize the laser's noise as much as possible. The characterization of the laser and possible solutions to reduce its phase noise are discussed in Section 4.4.

4.2.3 Advantages and limitations of Rydberg dressing

Rydberg dressing has emerged as an active field of study [4, 54, 56, 57, 136–142, 156, 162–165] and provides various advantages compared to resonant Rydberg physics:

- **Controlled interaction strength and range**: Rydberg dressing introduces extra control parameters, namely the laser parameters, which enable tuning the interaction strength and spatial behavior, as well as the ability to turn the interactions on or off as needed. This is in contrast with resonant interactions, where the interactions are always present.
- **Long range interactions in optical traps**: Dressed interactions inherit the long-range scaling of Rydberg interactions, making them especially suitable for the implementation in optical lattices and tweezers [23]. Moreover, the trapping potential can remain on during dressing experiments. In contrast, resonant excitation generally repell atoms from ponderomotive light potentials, which forces the experiments to switch off the trapping potential during the excitation pulse and interaction evolution [60, 78]. This imposes an upper limit on the possible evolution time. Alternatively experiments also investigate trapping Rydberg atoms.
- **Exotic interaction shape**: One proposed method to engineer interactions with an exotic distance dependence is by implementing Rydberg dressing in the presence of Förster resonances [139]. Operating close to these resonances can significantly

enhance the effectiveness of Rydberg dressing, resulting in interaction couplings that exceed the related decoherence rates. If one does not operate near the Förster resonances, the effectiveness of these interactions is given by the ratio of interaction strength to the effective decay of the system. This ratio tends to be lower for Rydberg dressing than for the resonant case.

- **Advanced Quantum Simulation**: Rydberg dressing enables to engineer and simulate complex quantum systems, such as spin systems [55, 57, 137], quantum phase transitions [139], and novel phases of matter, such as crystalline states. It also has applications in quantum logic operations, providing the potential to construct quantum gates [54, 141, 164]. The perspectives and advantages will be elaborated more in detail within the next chapters.

In summary, Rydberg dressing provides a versatile platform for exploring and manipulating quantum systems, with wide-ranging applications in quantum information, quantum simulation, and beyond. Despite these advantages, significant challenges remain, such as undesired losses to and interactions with other Rydberg states [57, 75, 166], and the laser noise [56, 62, 75].

4.3 Single-photon Rydberg excitation setup

Now, we turn our focus to the Rydberg excitation laser setup. There are various possible configurations, with the two-photon Rydberg excitation schemes being the most commonly used ones. For alkali atoms like potassium, these schemes involve a combination of two lasers operating at very different frequencies. Over the past few years, the so-called “inverted” scheme has become the standard. This scheme couples the electronic ground state $4S$ to a $(n+1)P$ state first and then couples to any Rybderg $n'S$ or $n''D$ state. Previously, it was quite common to use a combination of a D2-laser (also used for MOT transitions) and an additional laser to couple to the Rydberg states via an intermediate state. However, this configuration has a much smaller dipole matrix element than the inverted excitation scheme. This shortcoming cannot be compensated due to the limited available laser power.

Alternatively, the single-photon excitation from the $4S$ state to any Rydberg $n'P$ state could offer a significant advantage by not requiring any intermediate state to couple to the Rydberg manifold. However, the single-photon excitation setup is more complex and often requires one to several frequency-doubling stages, limiting the maximum achievable output power and setting an upper limit of the attainable Rabi coupling.

Rydberg dressing experiments, as discussed in the previous chapter, are highly sensitive to laser noise. Consequently, the intermediate-state scattering from the two-photon excitation scheme further reduces coherence in the system, which is why we use a single-photon Rydberg excitation laser setup for the Rydberg dressing experiments presented in this thesis. In Section 4.3.1, we briefly introduce the home-built laser setup, which is described in

detail in the thesis of Nikolaus Lorenz [60]. Then, we present a step-by-step guide of the alignment procedure for the fast and optimal alignment of the tightly focused excitation beam onto the tweezer array in Section 4.3.2.

Additionally, we discuss the performance of the laser setup and evaluate potential sources of imperfections. Unfortunately, the used excitation wavelength caused damage to certain optics coatings, which prompts us to share our understandings, experiences, and improvements in Section 4.3.3.

4.3.1 Single photon excitation laser setup

As of now, there are no commercial laser sources available that operate at the required wavelength of $286\,\mathrm{nm}$ while also offering a high optical power of at least $1\,\mathrm{W}$. Additionally, these lasers must meet the specific requirements for driving transitions to Rydberg states, having narrow linewidths. To address this gap, we have developed a custom laser system. This system starts with an infrared seed laser, which is amplified and undergoes two frequency-doubling stages to generate the desired ultraviolet wavelength.

First, we focus on the seed laser, which is the first component in our setup. It is a home-built external cavity diode laser (ECDL) with an output wavelength of $1143\,\mathrm{nm}$. The design of our home-built lasers and a detailed description of the optical and electric setup around this laser can be found in the thesis of Nikolaus Lorenz [60]. This laser is stabilized to an ultra-low expansion cavity (ULE) with a Finesse of $F \approx 10000$. For tuning the laser to any desired frequency, we implemented a fiber EOM[1], enabling to modulate the light at a range from 50-700 MHz. Consequently, we stabilize the laser to one of the modulation sidebands instead of locking it to the carrier. We use a Pound Drever Hall locking scheme [167], which includes additional locking sidebands at $21.3\,\mathrm{MHz}$.

Then, the output of the laser is amplified to a power of $8\,\mathrm{W}$ using a Raman fiber amplifier[2]. We guide the beam through two consecutive frequency doubling stages as illustrated in Fig. 4.5. The first second-harmonic generation cavity has a coupling efficiency of $80\,\%$ into the Gaussian mode, resulting in an output power of $\approx 3.3\,\mathrm{W}$ of green light at a wavelength of $572\,\mathrm{nm}$. The beam is subsequently directed through an AOM for intensity stabilization. The feedback signal for this AOM can be either measured with a PD in the green beam path after the AOM or with a PD in the UV beam path after the second cavity, operating in sample-and-hold mode.

We utilize two different locking methods for these cavities. For the first (green) one, we use the Pound Drever Hall locking method [167]. For this lock, we implemented a free-space EOM into the beam path before the RFA, which modulates the light at about $51\,\mathrm{MHz}$. For the second cavity, we want to avoid introducing modulated sidebands, which could

[1] EOspace 10Gb/s Lithium Niobate Phase Modulator at 1140-1160nm - PM-0S5-10-PFA-PFA-1140/1160.
[2] MPB Communications Inc. Single frequency NIR Raman Fiber Amplifier

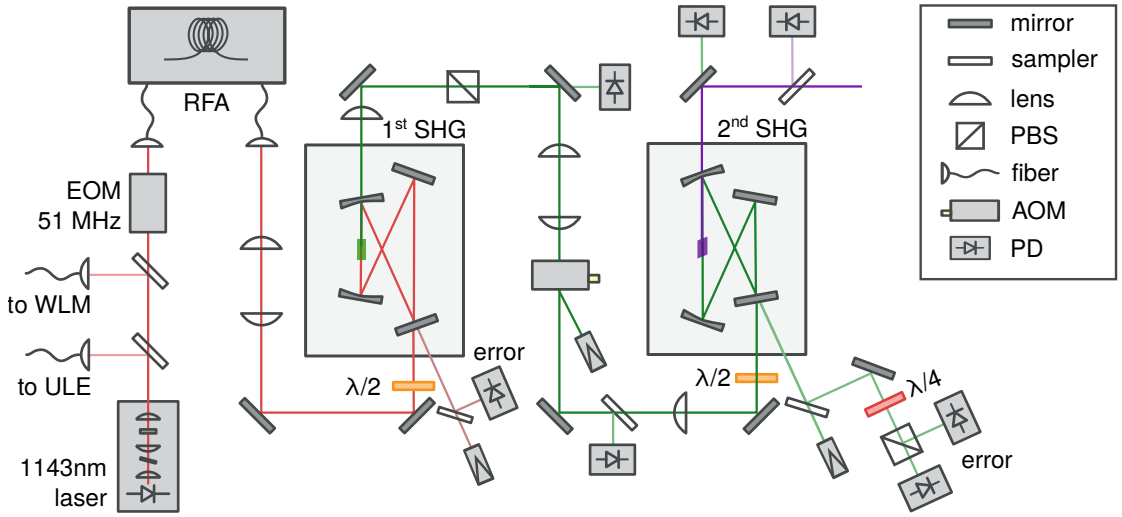

Figure 4.5 Single photon Rydberg excitation laser setup. The seed laser is a home-built ECDL, which is stabilized using a Pound-Drever-Hall (PDH) lock to an ultra-low-expansion (ULE) cavity. This seed light is then amplified by a Raman Fiber Amplifier (RFA) and is subsequently frequency-doubled twice using non-linear doubling cavities. The first cavity is stabilized by employing a PDH lock, whereas the second uses a Hänsch-Couillaud locking technique. Between the two cavities, the intensity of the green light is stabilized using an AOM.

interfere with the atoms. Instead, we use a polarization-dependent lock, namely the Hänsch-Couillaud lock [168]. This requires a polarization-dependent element such as a Brewster cut crystal, which results in polarization-dependent reflection and transmission of the cavity. For locking both cavities, we use a digital FPGA-based PID controller[3]. While the first cavity is permanently locked, the second one is kept in scanning mode, with a triangular function applied to the slow piezo of the second cavity. In case a laser pulse is needed in the sequence, we lock the cavity a few tens of milliseconds beforehand to allow for thermalization, keeping it scanning otherwise. This approach prevents the degradation of the intra-cavity optics and non-linear crystal of the second cavity. The second cavity delivers a maximum output power of $1\,\mathrm{W}$ at a wavelength of $286\,\mathrm{nm}$.

The diverging beam following the second cavity is then collimated using a lens with a focal length of $500\,\mathrm{mm}$. As we will discuss in the next section, we observe intensity-dependent damage to our optics within the UV path, which is the reason we aim to increase the beam size as much as possible for free space alignment onto the atoms.

After collimation, we adjust the beam diameter to match the aperture of the subsequent AOMs using a sequential lens telescope. Using a polarized beam splitter, we divide the beam into two paths, each featuring an AOM; one in the -1st order, the other in the +1st order. Then, we combine these two beams using a non-polarized beam splitter (50:50). To

[3] Red Pitaya STEMLab 125-14, firmware and interface from Fabian Schmid: https://github.com/schmidf/rp-lockbox.

enable independent precision adjustments of the two beams later, we implemented a piezo actuator mirror mount into one of the paths, as illustrated in Fig. 4.6. After combining the two beams, we adjust the beam size again using a second telescope.

Throughout this thesis, we employed various telescope configurations to adjust the beam focus onto the atoms. For the measurements in this chapter, we used a beam waist of $20\,\mu\mathrm{m}$. For the measurements in the subsequent chapter, we maintained the 1:4 ellipticity of the UV output beam, resulting in an elliptical beam with a height of roughly $10\,\mu\mathrm{m}$ and an in-tweezer-plane beam waist of $40\,\mu\mathrm{m}$. The reason for this variation in beam waist is to enable the homogeneous coupling of a larger spread atom array.

To ensure the beam has circular polarization at the position of the atoms, we implemented a Brewster thin film polarizer[4] in combination with corresponding waveplates before and after it. Furthermore, we implement intensity stabilization for the two beam paths. For measurements requiring brief excitation pulses, we employ a sample-and-hold technique for both beams sequentially. This stabilization method also requires a beam shutter[5], which remains shut during pre-stabilization. After several milliseconds of stabilization, the PI parameters are set to hold, the AOM is turned off, and the shutters are opened to permit an excitation pulse onto the atoms. As both beams require the same polarization on the atoms, they cannot be intensity stabilized simultaneously.

To stabilize the position of the excitation beam onto the atom array, we image the beam at the position of the atoms using a spatial detector[6]. This detector simplifies the alignment process during the thermalization time of the entire laser system, which can take from several hours up to a full day. Once thermalized, the system does not exhibit any significant long-term drifts. Moreover, this detector allows for a triggered beam stabilization between each measurement iteration.

4.3.2 Alignment technique and characterization

Aligning the tightly focused Rydberg excitation beam onto the tweezer array can be quite challenging. When aligning the UV beam from scratch, we use the following techniques for efficient and reliable alignment:

For a preliminary rough alignment, we overlap the UV beam with the pre-aligned dipole trap at 1064nm in the same direction before and after the main chamber. However, after a setup change that involved the removal of the dipole trap, we employed a different initial alignment method: After several years of Rydberg measurements, we noted that the viewports showed less fluorescent spots where the UV beam was before transmitted. These spots, likely resulting from the UV beam, served as position markers, allowing us to guide the beam through the chamber and align it before and after the viewport. This method is

[4] Altechna Brewster Tzpe Thin Film Polarizer.
[5] Uniblitz VCM-D1.
[6] TEM µAligna 140 with the PSD 2D 4 DUV.

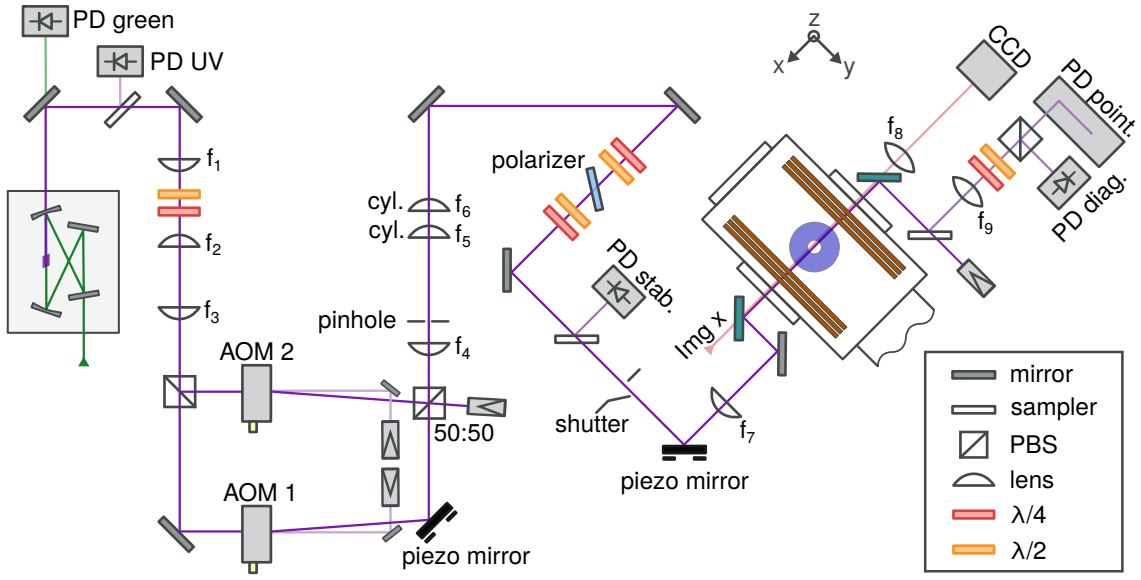

Figure 4.6 UV optics setup. The output from the final frequency-doubling cavity is collimated using lens f_1, and the beam diameter is decreased using a subsequent telescope comprised of lenses f_2 and f_3. A polarizing beam splitter then splits the beam into two paths. Each path contains an AOM: one operates in the -1^{st} order and the other in the $+1^{st}$ order, so both together cover the electronic ground state splitting. These paths are subsequently combined using a 50:50 beam splitter. The beam's astigmatism is corrected with a second telescope of lenses (f_4, f_5, f_6), with the last two being cylindrical lenses. A precision pinhole is located at the focus of this telescope and is projected in a 4f-configuration (f_5, f_6, and f_7) onto the atoms. The polarization of the beam on the atoms is set to circular using a Brewster thin-film polarizer and appropriate waveplates. The intensity of both beams is stabilized in sequence using a photodiode placed after the polarization optics, and this stabilization employs a sample-and-hold technique. The beam is then overlapped with the imaging x-axis beam and the dipole trap in x-direction through a dichroic mirror, which is the last optical component before, and the first one after, the main vacuum chamber. After the main chamber, the beam is aligned onto two photodiodes. The first one serves as a diagnostic tool to ensure the beam shutter operates with the correct timing, while the second one acts as a spatial detector and beam aligner. This aligner provides automatic feedback to the last piezo mirror to correct any beam drifts.

typically sufficient to align the beam onto the atom cloud (e.g., grey molasses). If the beam is still significantly off, we employ another pre-alignment step: We remove all filters and dichroics that sample out the D1 and D2 and trapping light before the CCD camera (see Fig. 4.6) and align the UV beam at very low power onto the camera. This is feasible as we have a non-coated lens in front of the camera. After reinstalling the filter and dichroic, we check for a signal of the Rydberg beam on the GM. The beam can be seen as a 'hole' within the atom cloud when on resonance and for a long enough pulse, as shown in Fig. 4.7. As soon as we see a signal on the atom cloud, we can conveniently guide the beam onto the position of the tweezers.

Before proceeding with the fine adjustment, we adjust the polarization of the excitation beam by spectroscopy. For this purpose, we overlap the excitation beam with the dipole trap in the x-axis. This method is preferred over using tweezers primarily because there are more atoms in each dipole trap, leading to a stronger signal and facilitating real-time optimization using absorption imaging. We load the dipole trap from the grey molasses and prepare all atoms in one of the stretched states of the hyperfine ground state $|4S_{1/2}\, F = 2,\, m_F = -2\rangle$, similar as done in tweezers as discussed in Section 3.4. We apply a magnetic field of $10\,\mathrm{G}$ along the x-axis and use a Rydberg spectroscopy measurement, where we measure, depending on the excitation beam's polarization, the transition lines to the $|62P_{3/2},\, m_j = \{-3/2, -1/2, 1/2\}\rangle$ Rydberg substates, corresponding to the σ^-, π, and σ^+ transitions. We adjust the polarization by tuning the waveplates while keeping the laser frequency fixed to one of the Rydberg resonances requiring a σ-transition. We fine-tune the waveplates to minimize the excitation of the atoms to the Rydberg state. This process implies that we are purely driving the other polarized sigma transition. An example for the spectroscopic measurements before and after polarization adjustment is shown in Fig. 4.7. Alternatively, instead of the dipole trap we used, one could employ the light sheet mentioned in Section 3.4.2 to achieve a similar adjustment.

Then, we continue with the fine adjustment of the beam onto the array. Essentially, we have to ensure that the beam is centered on the atoms, the focus is adjusted at the atom's position, and the beam is not tilted to obtain a homogeneous illumination over several columns and rows within the tweezer array. We start with centering the beam onto the array by adjusting the vertical and horizontal alignment of the beam via the piezo mirror mount before the chamber. For the adjustment of the focus and beam position, we measure Rabi oscillations and maximize the coupling with the fine adjustment onto the tweezer array. We follow the single atom loading and cooling procedure as described in Section 3.1 for this measurement. We prepare the atoms in the same hyperfine ground state $|4S_{1/2}\, F = 2,\, m_F = -2\rangle$, ramp down the overall trapping power, and switch off the tweezer trap for up to $20\,\mu\mathrm{s}$. During this time, we apply a Rydberg excitation pulse with varing durations. We measure the Rydberg excitation probability indirectly via atom loss, as shown in Fig. 4.7. The beam is aligned parallel to the tweezer columns, and knowing the spacing between them, we can calculate the beam size at the position of the array. Then, we can adjust the focusing lens, which is mounted on a micrometer stage, and measure the beam size for each position by extracting the Rabi frequency for each tweezer column, thereby finding the position of the focus.

To verify that the UV beam is aligned parallel to the plane of the atom array, we evaluate the Rabi coupling of five individual tweezers in a column along the direction of beam propagation. The averaged Rabi coupling over one column is depicted in Fig. 4.7. With each tweezer separated by a distance of $39\,\mu\mathrm{m}$, the total span across the column measures $156\,\mu\mathrm{m}$. We calculate the standard deviation of the Rabi coupling of the individual tweezers to be $18\,\mathrm{kHz}$. This deviation corresponds to a 2% variation in the Rabi coupling of $\Omega/2\pi = 808 \pm 2\,\mathrm{kHz}$, aligning well with the Rayleigh range for the smaller axis, represented as $z_r = 1.1\,\mathrm{mm}$, given a beam waist of the smaller (vertical) axis of $10\,\mu\mathrm{m}$.

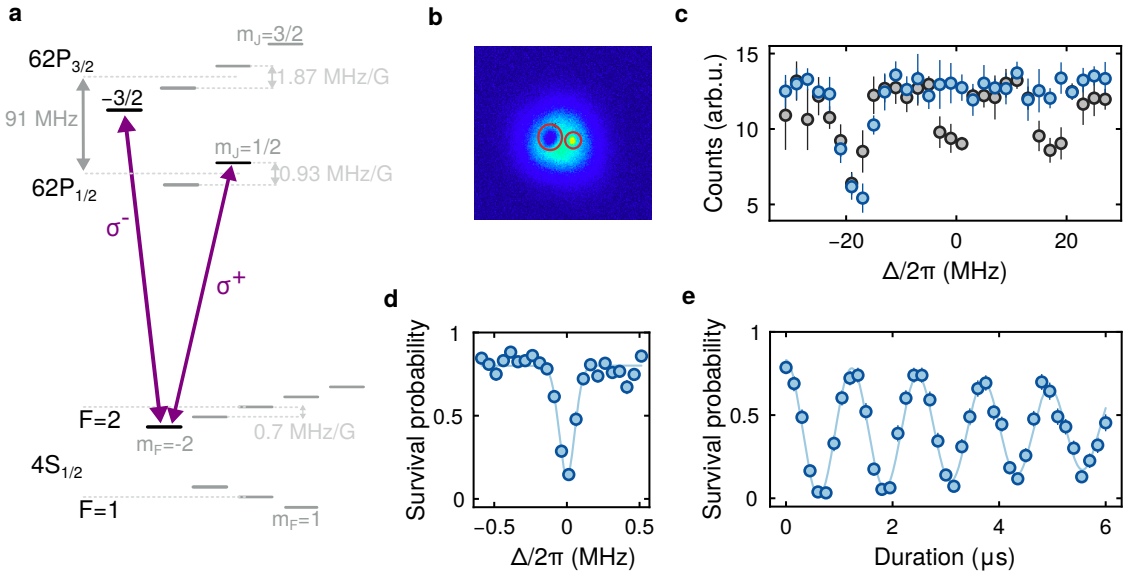

Figure 4.7 Single photon Rydberg excitation level scheme and calibration measurements. **a.** Generally, in the experiment, the atoms are prepared in one of the stretched states $F = 2$, $m_F = \pm 2$, and are coupled to the Rydberg states. The circular polarization of the beam, in combination with the direction of the quantization axis, allows for different excitation paths. **b.** The first alignment step involves aligning the UV beam onto the grey molasses. For the alignment, we apply a resonant pulse and capture an absorption image afterwards. The excitation to the Rydberg state generates a hole in the atom cloud. Conversely, the dipole trap in the x-direction appears as a denser spot within the atom cloud (indicated by the right red circle). Subsequently, the UV beam is moved onto the dipole trap, which was previously aligned to the position of the tweezers. **c.** For precise polarization alignment, we conduct spectroscopy scans within the dipole trap. The atoms are prepared in the $F = 2$, $m_F = -2$ state and are coupled to the $62P_{3/2}$ state. Upon applying a magnetic field perpendicular to the incident beam with a strength of $5\,\mathrm{G}$, we observe three transitions (grey data points) to the $m_j = \{-3/2, -1/2, 1/2\}$ substates (from left to right). These correspond to the σ^-, π, σ^+ transitions. After adjusting the polarization of the incoming beam and aligning the magnetic field with the beam's direction, only a single transition (blue data points) is observed. The x-axis is offset with respect to the π-transition. **d.** The spectroscopy signal of the $62P_{3/2}$, $m_j = -3/2$ state in tweezers is depicted. The Gaussian fit indicates a FWHM of $126 \pm 10\,\mathrm{kHz}$ and a center position uncertainty of $\pm 4\,\mathrm{kHz}$. **e.** Rabi oscillation measurements in tweezers, when coupling to the $62P_{3/2}$, $m_j = -3/2$ state, are shown. The fit is an exponentially damped sinusoidal function and yields an oscillation frequency of $\Omega/2\pi = 808 \pm 2\,\mathrm{kHz}$ and a damping time of $\tau = 9.9 \pm 2\,\mu\mathrm{s}$.

Additionally, we observed damping in the Rabi oscillation, which can be attributed to the following major factors, further elaborated in reference [63]:

- **Doppler broadening:** After RSC, the remaining ground state momentum uncertainty of the atoms introduces a Doppler broadening. We define the Doppler shift as $\Delta_D =$

$k \cdot v$, where the wave vector k is determined by $k = 2\pi/\lambda$ and λ denotes the UV laser wavelength. Meanwhile, the velocity v is given by $v = \sqrt{k_B T/m}$, considering the atomic temperature T and atomic mass m. The finite temperature of the atoms leads to irregular detuning offsets in consecutive experimental runs, defining an effective Rabi coupling as $\Omega_{\text{eff}} = \sqrt{\Omega^2 + \Delta_D^2}$. After RSC and reducing the trap depth to 20% of the original loading power, we calculate a Doppler shift of $\Delta_D = 2\pi \times 50\,\text{kHz}$. Notably, the influence of the Doppler shift diminishes with increasing Rabi frequencies. For instance, at a Rabi coupling of $\Omega/2\pi = 800\,\text{kHz}$, this effect becomes negligible.

- **Intensity fluctuations:** The shot-to-shot intensity fluctuations in the excitation pulse area induce changes in the Rabi frequency, leading to variations in the evolution time for each shot. The intensity noise restricts the number of coherent oscillations, which is inversely proportional to the standard deviation of the pulse area, as shown in [39].
- **Phase Noise:** The carrier's phase noise is another contributor to the oscillation damping. The noise introduces variations in the evolution of each measurement shot. Improving the excitation laser's phase noise can significantly increase the achievable coherent oscillations, as experimentally demonstrated in [63, 169, 170].

Having completed these steps on setting up and fine-tuning the UV beam and with an understanding of the remaining limitations that may become relevant later, we now have a closer look into optics for ultraviolet wavelengths and begin with initial dressing measurements in the upcoming sections.

4.3.3 Experience and challenges with ultraviolet optics

We require high-reflectivity, high-quality optics to align the single-photon Rydberg excitation beam in free space onto the atoms. However, optical coatings in the UV-B range $(280 - 315\,\text{nm})$ demand a careful selection of optics. For this purpose, we use mirrors with customized, narrow-band coatings that result in no measurable power loss. Conversely, when we employ complex coatings, such as those provided with custom dichroic mirrors, we measure a power loss exceeding 3%. For commercially available broadband UV-enhanced aluminum-coated mirrors[7], we have observed an average power loss of 10%. Plus, we have one specific mirror in our optics setup that adjusts the beam from the AOM plane to the chamber plane, resulting in an incident angle of $22.5\,^\circ$. To minimize loss for this mirror as much as possible, we used a commercial mirror[8].

In addition to the variations in reflections across distinct optics, we observed different long-term behaviors. As depicted in Fig. 4.8, some coatings suffered irreversible damage at the position where the UV beam hit the surface. Notably, anti-reflection coatings, which are employed for lenses, beam splitters, dichroic mirrors (like the outcoupling mirror of the UV

[7] Thorlabs PF10-03-F01.
[8] OptoSigma TFM-25. 4C05-266.

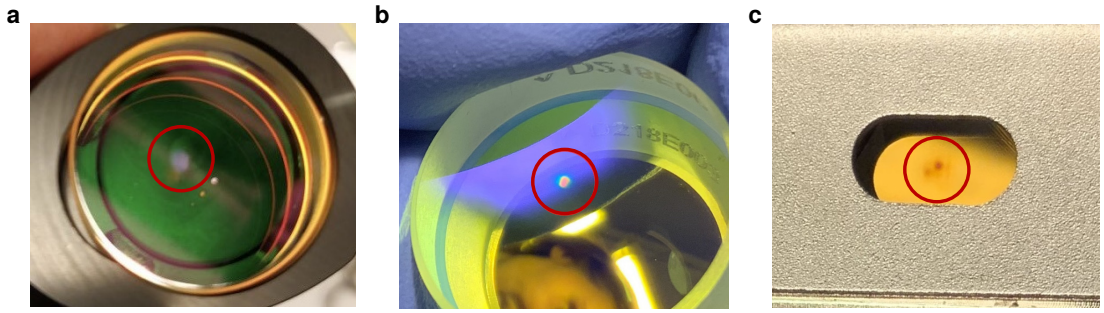

Figure 4.8 Examples of contaminations on optic and coating damages. **a.** Contamination (indicated within the red circle) on a mirror diminished the reflectivity of the optics. Fortunately, the contamination was removable and did not lead to any additional damage to the coating. **b.** Damage to the coating of the outcoupling mirror from the UV doubling cavity. **c.** Damage to the coating on the surface of the crystal within an acousto-optical modulator.

doubling cavity), and polarization optics, were particularly affected. This damage reduced the transmission and necessitated frequent replacements. Regarding polarization optics, we found that those provided by ALTECHNA exhibited the best endurance over time.

We attribute the damage to the UV optics to two major factors:

Laser-induced contamination (LIC) of the surfaces by hydrocarbons

These organic compounds can be found outgassing from organic materials and surfaces. They can interact with the laser via different processes, which can ionize or polymerize them at the short wavelength we use. Eventually, these molecules may be deposited on the optical surface under laser illumination. LIC is an interdisciplinary topic that requires a combined understanding of material science and optical engineering. It is extensively studied in space science, where hydrocarbon contamination can damage laser-based measurement instruments [171–175]. This issue is even more severe in space, as repairing or replacing components can be difficult, if not impossible. Although we can clean and exchange the optics in our laser setup whenever necessary to a certain extend, it is still highly desirable to slow down the contamination process as much as possible.

The contamination depends on several factors, such as the intensity of the radiation. We, therefore, implemented telescopes to enlarge the beam size at an early stage and reduce the intensity on the optics. In addition, we found that constantly flushing the optics with pure nitrogen also slowed down the contamination process. However, we are unable to completely prevent the process from occurring, meaning that we need to clean the optics from time to time.

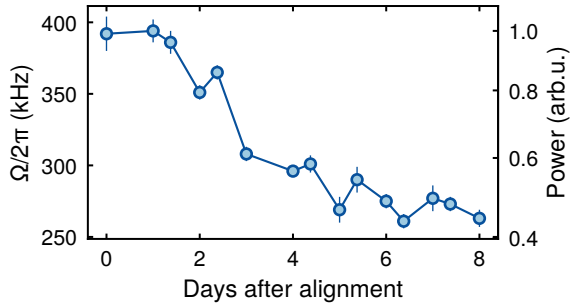

Figure 4.9 Long-term drift of the UV SHG output power after setup initialization. Measurement of the maximal Rabi coupling over eight days following the optimization and maximization of the output power from the UV doubling cavity. The beam alignment for the excitation beam was confirmed for each Rabi oscillation measurement. Over the course of one week, we observed a 50% drop in the total output power as shown by the normalized power on the right y-axis.

Photo-degradation of optical coatings

UV radiation can break chemical bonds in the optical coatings on optics. In the case of oxygen-containing coatings, such as metal oxide coatings for the mid-UV range, bonds between the metal and oxygen can be disrupted, leading to the escape of oxygen atoms (a process known as desorption). This conclusion is supported by the findings of reference [176], which measured a change in absorption losses over time and temperature and found correlations with alterations in the oxygen concentration on the surfaces. As a result of this change in chemical composition, the remaining coating exhibits modified optical properties.

Our observations indicate that optics with anti-reflection coatings are the ones mainly degrading under UV illumination as shown for the outcoupling mirror of the UV doubling cavity in Fig. 4.9. Reducing the intensity also slows down the process of oxygen depletion in this case. However, there are several more options for coatings, each with its own set of advantages and disadvantages. For example, one could choose uncoated optics or fluoride coatings for anti-reflection purposes. Still, these come with the disadvantage of power loss for the $286\,\mathrm{nm}$ wavelength [177]. Another possibility is the use of nano-textured optics, which have a high damage threshold as the anti-reflection texture is directly etched into the surface of the fused silica window [178]. We integrated such a window[9] at the output for the second doubling cavity. However, this is not a feasible option for the outcoupling mirror of the second doubling cavity, since we require high reflectivity for the fundamental light at $572\,\mathrm{nm}$. In this instance, we changed the coating type from HfO_2 to Al_2O_2, as the latter one has a higher damage threshold [179]. So far, we have not completed a long-term characterization of these two upgrades. Moreover, several groups have reported that degradation can be reduced by flushing the optics with oxygen or ozone to replace

[9] Newport 10Q20RAR.S.

the desorbed oxygen on the surface [180]. For this reason, we have designed new mounts for the AOMs that allow us to flush the crystal with ozone produced by a commercial ozone generator[10] (more details can be found in the master thesis of Ludwig Müller [100]). Unfortunately, we cannot utilize the ozone generator during measurements since ozone exhibits pronounced absorption in both the UV and green spectra.

4.4 Experimental lifetime of Rydberg dressed atoms

We now aim to carry out Rydberg dressing characterization measurements, focusing first on the Rydberg-dressed lifetime. As described in Eq. (4.17), this lifetime should scale proportionally with $1/\beta^2$. However, as previously discussed in Section 4.2.2, the experimentally observed dressed lifetime is also influenced by the laser's frequency and phase noise. In our experiment, phase noise poses the most significant constraint, leading to a reduced effective lifetime.

For the measurements, we arrange the atoms in a 5×5 tweezer array, with a spacing of $40\,\mu\mathrm{m}$, to prevent interatomic interactions when dressing to the $|62P_{3/2},\, m_j = -3/2\rangle$ state. The Rydberg excitation beam is aligned to one column. After loading single atoms into the tweezer array, we cool the atoms using Raman sideband cooling and then optically pump and prepare them in the hyperfine ground state $|4S_{1/2}\, F = 2,\, m_F = -2\rangle$ (refer to Section 3.4 for a more detailed description). As previously mentioned, we are challenged by trap depth inhomogeneities, which become significant due to their contribution to additional tweezer-dependent detuning offsets. In order to reduce the absolute tweezer-to-tweezer difference, we lower the trap depth to 0.5% of the original loading power. With an average tweezer inhomogeneity of $\approx 10\%$, the trap depth differences result in a few tens of kHz, which is two to three orders of magnitude smaller than the set of detunings used in the measurement presented here. During the Rydberg dressing pulse, we apply a magnetic field of $B = 5\,\mathrm{G}$ along the experimental x-axis. The choice of state and the magnetic field will be justified in the upcoming measurements, which involve smaller tweezer spacings. For these parameters and when being red detuned, no Rydberg pair state resonances are observed down to atom separations of $3\,\mu\mathrm{m}$. During the measurement, we keep the Rabi coupling fixed at $\Omega = 2\pi \times (355 \pm 5)\,\mathrm{kHz}$ and modify the theoretical admixture by tuning the laser detuning from resonance, ranging from $\Delta = 2\pi \times 500\,\mathrm{kHz}$ to $\Delta = 2\pi \times 5\,\mathrm{MHz}$ in steps of $200\,\mathrm{kHz}$. For each detuning parameter, we scan the Rydberg excitation pulse duration and apply a fit with an exponential function, scaling with $\propto \exp(-t/\tau)$. In our analysis, we derive the decay time τ for each detuning and compare it to the theoretically predicted Rydberg dressed lifetime of an ideal (delta-function-like) laser $\tau_{dr} = \tau_{bb}/\beta^2$. We then calculate the ratio between both, expressed as $\alpha(\Delta) = \tau_{dr}/\tau_{eff}$, as illustrated in Fig. 4.10.

[10] Anseros COM-AD-02.

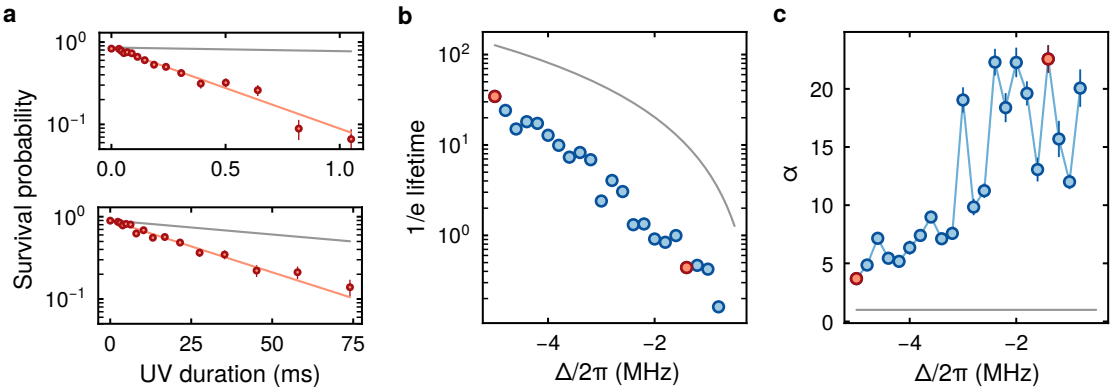

Figure 4.10 Experimental dressed lifetime measurements of the $62P_{3/2}$ state. **a.** Scanning the duration of the Rydberg excitation pulse for $\Delta = 2\pi \times 1.4\,\mathrm{MHz}$ (upper) and $\Delta = 2\pi \times 5\,\mathrm{MHz}$ (lower), with a resonant Rabi coupling of $355 \pm 2\,\mathrm{kHz}$. We measure the survival probability after the excitation pulse (accounting for trap losses) and apply an exponential fit (red solid line). From this, we determine dressed lifetimes of the ground states to be $0.44 \pm 0.02\,\mathrm{ms}$ (upper) and $34.4 \pm 2.01\,\mathrm{ms}$ (lower). The solid grey line represents $\tau_{dr} = \tau_{bb}/\beta^2$ with a blackbody limited lifetime of $\tau_{bb} = 160\,\mu\mathrm{s}$ for the $|62P_{3/2}\rangle$ state. Error bars denote 1 s.e.m. **b.** Repeating the measurement from a. for various laser detunings and extracting the $1/e$ lifetime from each fit. The two red points represent the measurements shown in a. The grey solid line denotes the theoretical dressed lifetime, τ_{dr}. **c.** Plotting the ratio between the theoretical dressed lifetime and the measured lifetime as $\alpha = \tau_{dr}/\tau_{\mathrm{meas}}$. The grey line visualizes a ratio of one for an ideal laser linewidth.

As we increase the detuning, we find that this ratio decreases from $\alpha = 20$ to less than $\alpha = 5$ across a detuning range of $-2\pi \times \{0.8, 5\}\,\mathrm{MHz}$. Such ratios cannot be solely attributed to intensity noise, which results in a shot-to-shot variation of the area of the UV pulse, thereby inducing variations in the Rabi frequency, as mentioned earlier.

Furthermore, we observe a modulation in this ratio α, showing spikes at intervals of $600\,\mathrm{kHz}$. This modulation does not correspond to the bandwidth of the ULE lock of the seed laser, which was tuned to $400\,\mathrm{kHz}$ for these measurements.

We attribute the notable reduction in the measured dressed lifetime to the performance of the laser setup, specifically its noise spectrum. When analyzing a laser's spectral profile, we differentiate between low-frequency and high-frequency noise. Each of these frequency characteristics has unique origins and consequences regarding laser behavior.

To describe the spectral profile of a laser with an ideal gain medium, we begin with a Lorentzian line shape originating from the laser's cavity. Several external factors, such as disturbances within the laser cavity and the electronic noise from the laser driver, lead to a low-frequency Gaussian line shape. The convolution of these two shapes results in a Voigt profile, with the Gaussian profile determining the laser's linewidth [159–161, 181, 182]. One can further refine and control this linewidth by stabilizing the noise sources.

Nevertheless, when considering a realistic gain medium such as laser diodes, we observe an additional so-called phase noise pedestal – a wide, low-intensity noise component surrounding the carrier. This phase noise results from the laser diode's spontaneous emission, inducing random fluctuations in the population inversion and thus random fluctuations within the resonant field of the laser [183], primarily contributing to the wings of the laser's spectrum [181, 182]. Such noise poses the most profound challenge in our Rydberg dressing experiment and emphasizes that a laser with a narrow linewidth does not guarantee spectral purity.

As observed by Matveev et al. [184], the phase noise becomes even more significant when the laser radiation undergoes multiple frequency conversions to higher harmonics. They proposed a description where the power fraction contained in the laser's carrier is denoted as $\eta = \exp(-\phi_{\text{rms}}^2)$, scaling with the root-mean-square phase deviation of the laser. In the absence of any phase noise ($\phi_{\text{rms}} = 0$), all power resides in the carrier, resulting in a monochromatic field. Because the generation of one ultraviolet photon requires a total of four infrared photons, the power fraction in the carrier is further reduced after the conversion, resulting in $\eta' = \eta^{n^2} = \eta^{4^2} = \eta^{16}$ [184].

The phase noise pedestal surrounding the laser's carrier can become a limitation in Rydberg dressing experiments. This effect can be interpreted as incoherent, resonant excitations, which consequently reduce the measured Rydberg state lifetime and coherence for Rydberg dressed interactions [62, 63, 78]. In the following section, we will present potential techniques to mitigate the laser's phase noise as observed by the atoms.

4.4.1 Strategies for phase noise mitigation

In our experiment, the spectral properties, including linewidth and phase noise of the single-photon Rydberg excitation laser setup, are dictated by the seed laser operating at $1143\,\text{nm}$. As highlighted in the previous section, this phase noise amplifies when undergoing the two frequency doubling stages [185], as well as the Raman fiber amplifier may add noise [186]. Therefore, by merely minimizing the seed laser's noise, we can achieve significant improvements of the performance of Rydberg-dressing measurements.

There are various strategies available for reducing the phase noise experienced by the atoms: As a first approach, we can consider replacing the seed laser with a source that possesses intrinsically low phase noise. As demonstrated in reference [185], the phase noise and spectral linewidth of the laser can be reduced by extending the length of the external cavity of the ECDL. However, this adjustment makes the system less stable. An alternative approach involves the use of Titanium-Sapphire lasers or Dye lasers, which are well-known for their exceptionally low phase noise emissions, thanks to their long cavity [63, 169, 170]. However, our specific needs call for either a high-power output laser at $1143\,\text{nm}$ or the second harmonic at $572\,\text{nm}$. These wavelengths surpass the capabilities of any Ti:Sa laser. While Dye lasers are available for these wavelengths, their impracticality necessitates our reliance on the ECDL. In response, we designed a laser with an external cavity of $7\,\text{cm}$,

although this still left us with the phase noise issue discussed in the previous section. Many alternatives exist, such as sum-frequency mixing and Vecsel lasers that are presently under development [187, 188]. These advancements are expected to present new opportunities and possible solutions in the near future.

Secondly, one could use an additional optical cavity. In this setup, the 'noisy' incident laser is coupled into a high finesse cavity, with only the transmitted light from the cavity being further utilized. The storage time of the photons, denoted as τ_{st}, can be long enough to suppress the frequency fluctuations of the light for Fourier frequencies higher than $1/\tau_{st}$ [189]. Consequently, the cavity acts as a spectral low-pass filter, resulting in a suppression with its characteristic Lorentzian line shape. One issue with this approach is that the 'cavity-filtered' transmission of high finesse cavities usually is roughly about a few μW, and as such, does not provide sufficient power for further procedures. As a workaround, this transmission is used to injection lock a second laser diode. The slave laser obeys the frequency noise fluctuations of the master laser and follows the linewidth of the incident master light field, only adding spontaneous emissions. Successful implementations of this scheme, resulting in a significant reduction in phase noise, have been reported by various research groups [169, 190, 191]. However, our setup presents another challenge: the absence of injectable laser diodes suitable for our required wavelength. By 'injectable,' we refer to a diode with a medium AR coating on the front facet, which allows the diode to lase independently and form a cavity. Our proposed solution to this issue is to couple enough power into the cavity such that the transmission power is sufficient for further seeding the RFA, bypassing the need for a second slave diode [100]. The results of this approach will be discussed in the following subsection.

The third strategy is based on an active noise cancellation technique that employs a feedforward mechanism, as demonstrated by Li et al. [192]. In this method, a beat is measured between the laser and the transmission through a high-finesse reference cavity, which allows for the real-time measurement of the laser's frequency deviation, which can be compensated using an electro-optic modulator. They reported a noise suppression of $20\,\mathrm{dB}$ at the peak of their locking bandwidth, marked as a servo bump, of $250\,\mathrm{kHz}$, and a noise suppression bandwidth of $5\,\mathrm{MHz}$. However, noise exceeding this bandwidth remains unaffected. Alternatively, some research groups have reported using a fiber-based delay line interferometer to analyze phase noise. They applied feedback on electro-optical modulators to compensate for this noise, suggesting an alternative approach [193, 194].

In the upcoming section, we will delve into the modifications we implemented to our UV laser system to address the phase noise issue. Specifically, we employed the second strategy containing an additional optical cavity to reduce the effects of phase noise.

4.4.2 Advances in dressed lifetime measurement via cavity filtering

In terms of system upgrades, we implemented two significant changes to our setup, of which only one demonstrated notable improvement in phase noise reduction. The first

significant upgrade was the implementation of an optical filter cavity into our setup. The second modification was the implementation of an ultra-narrow linewidth laser[11] as the seed laser. Both changes were set up in the context of Ludwig Müller's Master thesis [100]. What follows is a brief overview of the central components of this setup. For an in-depth understanding of the individual components or electrical circuitry, please refer to that thesis.

Two key constraints existed when implementing the filter cavity: First, as stated earlier, no injectable laser diodes are available for the wavelengths at 1143nm. In order to circumvent this, we decided to couple sufficient power into the filter cavity with a finesse of $F = 10,000$, thereby avoiding the need for a second diode, that needs to be injected. As a result, we could attain enough power in the transmission to proceed and to seed the Raman fiber amplifier. The incoupling power is typically around $30\,\mathrm{mW}$, with a transmission efficiency of $\approx 65\,\%$ for an incoupling efficiency of $90\,\%$. The filter cavity is locked to the frequency of the laser while adjusting the cavity length as one cavity mirror is mounted on a piezo actuator stack. We utilized an FPGA-based digital lock for this cavity lock, which automatically re-locks the cavity, a useful feature during the cavity's thermalization time.

The second constraint was to ensure that the Raman fiber amplifier (RFA) always remains seeded. This stops to be the case if the cavity lock fails and the transmission power drops to zero. Although the RFA has an internal interlock that switches off the amplification when not sufficiently seeded – a highly undesirable event that can lead to laser degradation – we've developed a setup with an additional laser and a switching acousto-optic modulator (AOM). If the filter cavity lock fails, the setup switches to a second laser. This laser is a home-built ECDL laser, in free-running configuration at the same wavelength, thus ensuring that the RFA remains seeded at all times. The illustration of this setup is presented in Fig. 4.11.

Regarding the second modification, a new IR seed laser, it is important to remember that a laser with a narrow linewidth does not automatically guarantee low phase noise behavior, which is precisely what we observed when we performed a new set of measurements on the Rydberg dressed lifetime following these system upgrades. As these measurements were carried out after multiple upgrades and modifications to the entire experiment, the measurement procedure slightly differs from the one outlined in Section 4.4:

First, the loading and imaging of the atoms in the tweezers have changed, as we have adopted the techniques presented in Section 3.3. Instead of chopping the trap light for these stages, we now switch them to continuous wave operation.
Second, we did not employ Raman sideband cooling for these measurements. Instead, we used in-trap grey molasses cooling exclusively, where we continuously switch on the traps and cool the atoms with D1 light, as discussed in Section 3.3 . This explains why during the Rydberg dressing pulses, we could only reduce the overall trap depth to $\approx 0.5\,\mathrm{MHz}$.
Third, we prepared the atoms in the $F = 2$, $m_F = +2$ state using optical pumping, this time from a different direction (z-axis), different to the approach described in Section 3.4. It's important to highlight that the state preparation performance is not optimal, as indicated

[11] Menlo ORS Ultrastable Laser.

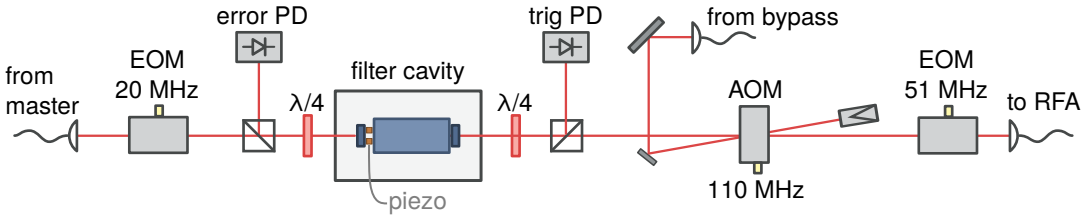

Figure 4.11 System upgrade: filter cavity setup. The master laser at $1143\,\mathrm{nm}$ is aligned through an EOM, which modulates sidebands for the PDH lock of the filter cavity. The filter cavity is stabilized to the laser by applying feedback to the piezo on one of the cavity mirrors. The cavity's transmission is then aligned in 0th-order through an AOM and fiber-coupled for amplification by the RFA. Prior to the fiber coupler, an EOM is implemented to modulate sidebands for the PDH lock of the first (green) doubling cavity. If the filter cavity lock fails, the transmission through the cavity will drop to zero and thus the RFA would not be seeded. To circumvent this issue, we installed a photodiode to monitor the transmission. When the transmission power drops below a specified threshold, the AOM is triggered to switch to the light from a second ('bypass') laser. This secondary beam is aligned with the deflected order of the AOM. When the AOM is activated, this backup laser is deflected to seed the RFA, while the original light from the master laser is directed away from the fiber coupler.

by a constant offset following the heat-out pulse (see Fig. 4.12). This could potentially be attributed to inadequate adjustment of the beam polarization. As previously noted, we modified the setup for optical pumping. In the earlier configuration, we employed Glan-Taylor polarizers to ensure a better extinction ratio, a component yet to be integrated into the new setup.

The $|F = 2,\, m_F = +2\rangle$ state is coupled to the $|62P_{1/2},\, m_j = -1/2\rangle$ state and we observed a Rabi coupling of $367 \pm 9\,\mathrm{kHz}$. We then conducted a dressed lifetime measurement for a detuning set of $\{-8, -4, -2, -1\}\,\mathrm{MHz}$ for two different cases: The first one utilized only the new seed laser, while the second set of measurements also included the optical filter cavity between the RFA and the seed laser. The results are depicted in Fig. 4.12. In the case where we did not use the filter cavity, we observed a deviation of a factor 100 compared to the ideal lifetime. This substantial influence is primarily attributed to the new seed laser exhibiting a higher phase noise pedestal. When the cavity filtering is activated, we see a clear improvement in the deviation, especially for smaller laser detunings. For example, in the case of the smallest detuning, we measured a reduction of 60%. However, we have not yet achieved the values of the previously shown data set using the home-built laser as the seed laser. It's worth recognizing that this home-built design was specifically tuned to feature less phase noise due to a longer external cavity length. Thus, the next approach should involve using this laser and the optical filter cavity to decrease the phase noise further and/or further phase noise reduction methods, such as a feedforward technique, as presented in the previous section.

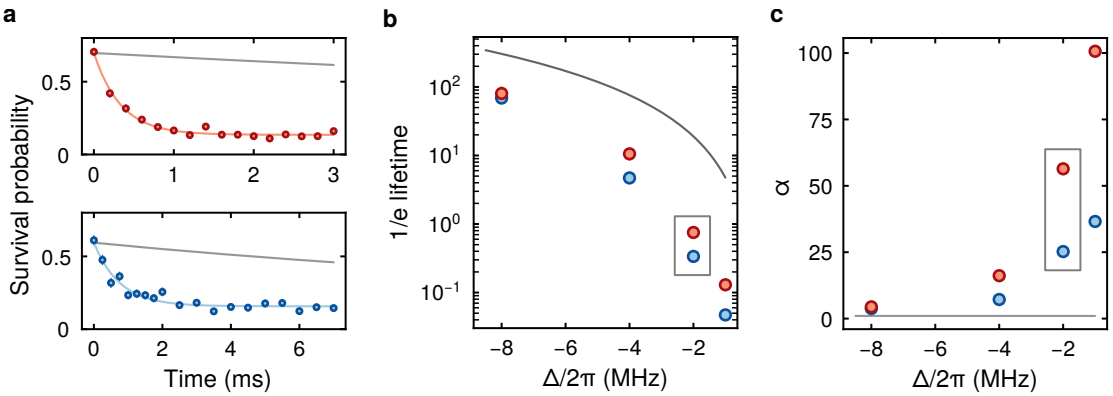

Figure 4.12 Comparison of experimentally dressed lifetime measurements of the $62P_{1/2}$ state for a new seed laser with and without including a filter cavity setup. a. Scanning the survival probability of the atoms by varying the UV dressing pulse duration with a fixed laser detuning of $2\,\mathrm{MHz}$ and a resonant Rabi coupling of $367 \pm 9\,\mathrm{kHz}$. The upper plot corresponds to a setup using a new (commercial) seed laser without cavity filtering. The lower plot displays measurements using the same laser but with cavity filtering included. **b.** Repeating the measurements with (blue) and without (red) cavity filtering as done in a. for various laser detunings and extracting the $1/e$ lifetime from each fit. The box surrounding the two data points at $2\,\mathrm{MHz}$ highlights the values extracted from the fits in a. The grey line indicates the theoretically dressed lifetime, τ_{dr}. **c.** Shown is the ratio between τ_{dr} and the experimentally measured dressed lifetime. The grey line represents a ratio of one. When compared to the results from the home-built laser in Fig. 4.10, the ratio for the new seed laser from MENLO seems to have a noticeably more phase noise leading to an even larger ratio α.

Before proceeding with these system upgrades, we will first conduct a self-heterodyne measurement of different laser setups to characterize the lasers' spectral profiles.

4.4.3 Insights from self-heterodyne measurements

The linewidth of a laser can be measured by heterodyning the laser with a reference source – in which case the laser with the broader linewidth will always be the one measured – or by self-heterodyne interferometry measurements using a long optical delay line, as initially proposed in 1980 by T. Okoshi [195]. In the latter approach, the laser field is split into two paths. One path includes a frequency shifter, in our case, an acousto-optic modulator (AOM), that shifts the signal by a frequency of f_s. The second path passes through a long optical fiber, introducing a delay of τ_d. Subsequently, the two beams are recombined, and their beat note is detected using a photodiode. The purpose of the AOM is to shift the beat note frequency, making the measurement easily accessible to the spectral analysis electronics. More importantly, the delay line introduces a phase difference between the two paths. This phase shift leads to periodic maxima and minima in the interferometer's

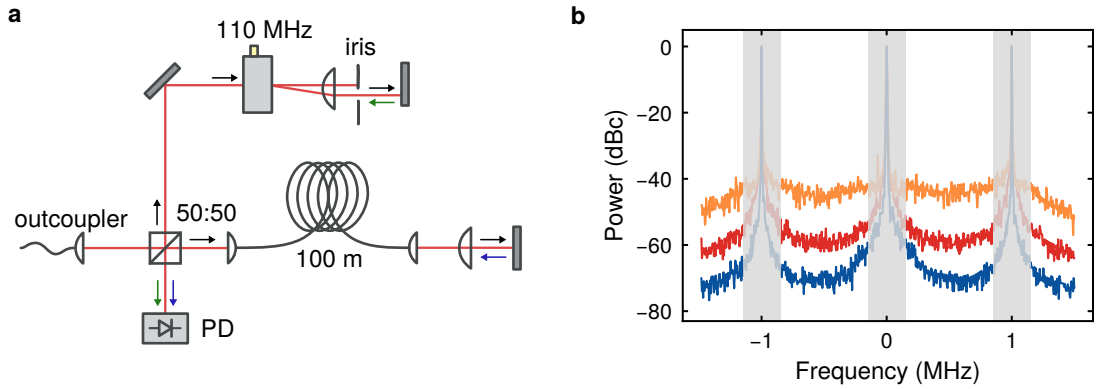

Figure 4.13 Self-heterodyne setup and phase noise measurement of the home-built ECDL IR seed. a. For the self-heterodyne measurements, we split the laser beam into two paths using a 50:50 non-polarizing beam splitter. One path is frequency-shifted via an AOM in a double-pass configuration. The second path is coupled into a $100\,\mathrm{m}$ long fiber and afterward back reflected. The reflected beams from both paths are recombined using the same 50:50 splitter and directed onto a diagnostic photodiode, which detects the beat at the AOM modulation frequency. **b.** The measurement spanned a $3\,\mathrm{MHz}$ frequency range with a resolution bandwidth (RBW) of $100\,\mathrm{Hz}$. The signal was further processed, accounting for the sensitivity of the interferometer using $\sin^2(\pi \cdot f \cdot \tau_d)$. The grey-shaded areas indicate regions where the detection efficiency of the interferometer is reduced (around the sensitivity minimum due to scaling systematics). The displayed traces represent setups in which the commercial IR laser was implemented (orange), the home-built ECDL without (red), and with (dark blue) cavity filtering before the RFA.

sensitivity due to a length-dependent $\pi/2$ phase shift, displaying as a scalloped pattern around the beat note.

The interferometer shown in Fig. 4.13, built by Ludwig Müller, is utilized in the following to characterize the spectral profile of the different IR seed lasers of the single-photon excitation setup. Additionally we have a second interferometer to analyze the spectral profil after the first frequency doubling stage in the green wavelength.

In the IR interferometer, we use an AOM[12] with a center frequency of $f_s = 110\,\mathrm{MHz}$ and a $100\,\mathrm{m}$ long fiber[13], through which the light passes twice. For the green interferometer, we employ an AOM[14] with a center frequency of $f_s = 200\,\mathrm{MHz}$ and a fiber[15] of the same length. Using these fiber lengths, we achieve a delay time of $\tau_d = nl/c = 0.976\,\mu\mathrm{s}$ for the IR interferometer, where the calculated refractive index of the core is $n = 1.4625$ at a wavelength of $1143\,\mathrm{nm}$. For the green interferometer, we obtain a delay time of $\tau_d = 0.973\,\mu\mathrm{s}$, with a calculated refractive index of $n = 1.459$ at a wavelength of $572\,\mathrm{nm}$. As mentioned

[12] Gooch & Housego 3110-191.
[13] Thorlabs 980HP.
[14] Gooch & Housego 3200-125.
[15] Thorlabs S405-XP fiber.

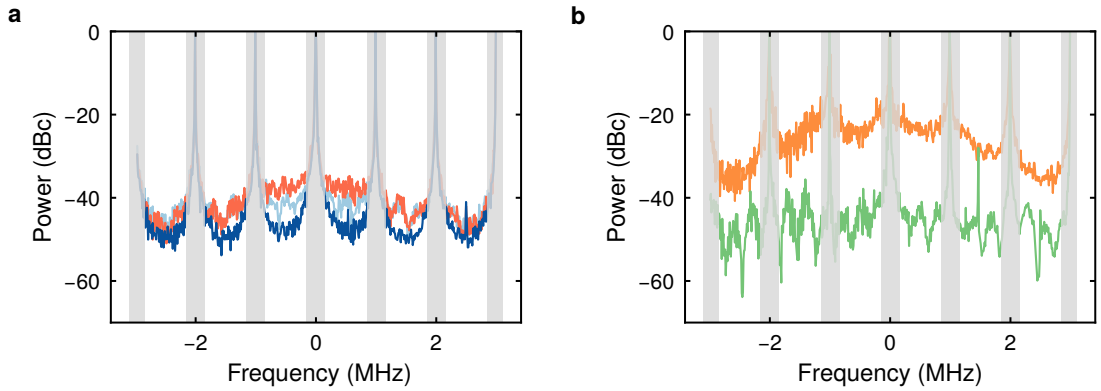

Figure 4.14 Self-heterodyne measurements of different IR seed laser setups before and after the first doubling stage, and before and after the RFA. a. Measurements of the home-built ECDL with cavity filtering, both before (in dark blue) and after (in light blue) the RFA. Additionally, we measured the home-built ECDL without cavity filtering after the RFA (in light red). These measurements spanned a $6\,\mathrm{MHz}$ frequency range and utilized an RBW of $100\,\mathrm{Hz}$. **b.** Noise spectra were captured in the green path using two distinct setups: the home-built ECDL combined with the filter cavity (light green), and the commercial laser without the filter cavity (light orange). These measurements spanned a $6\,\mathrm{MHz}$ frequency range and utilized an RBW of $100\,\mathrm{Hz}$. The displayed trace was adjusted to account for the sensitivity of the green interferometer. Grey-shaded areas denote regions where the detection efficiency of the interferometer drops.

above, the delay time defines the sensitivity of the interferometer with $1/\tau_d$, which is in our case approximately $1\,\mathrm{MHz}$. We use commercially available function generators[16] as the frequency source for the RF signal to the AOMs in both paths. Both arms of the interferometer are then overlapped on the same photodetector, and the beat note is analyzed using an RF spectrum analyzer[17].

Before amplifying the light using an RFA, we have a closer look at the noise spectrum around the carrier. We aim to compare three different scenarios: the noise spectrum of the commercially purchased narrow-linewidth laser, and the home-built laser before and after the implementation of the optical filter cavity. For the measurements displayed in Fig. 4.13, we also consider the interferometer's sensitivity, which is determined by the length of the delay line. Consequently, we apply a deconvolution function of $\sin^2(\pi \cdot f \cdot \tau_d)$ to the measured noise spectrum. We represent the sensitivity breakdown of the measurements with grey bars in the plot. All three measurement traces were carried out with the same resolution bandwidth of $10\,\mathrm{Hz}$ and a $3\,\mathrm{MHz}$-frequency window. When comparing the two seed lasers without any cavity filtering, a significant difference is evident, with the home-built laser demonstrating approximately $15\,\mathrm{dB}$ less noise. Additionally, we observe clear evidence

[16] SRS SG382.
[17] Rhode and Schwarz FSC6.

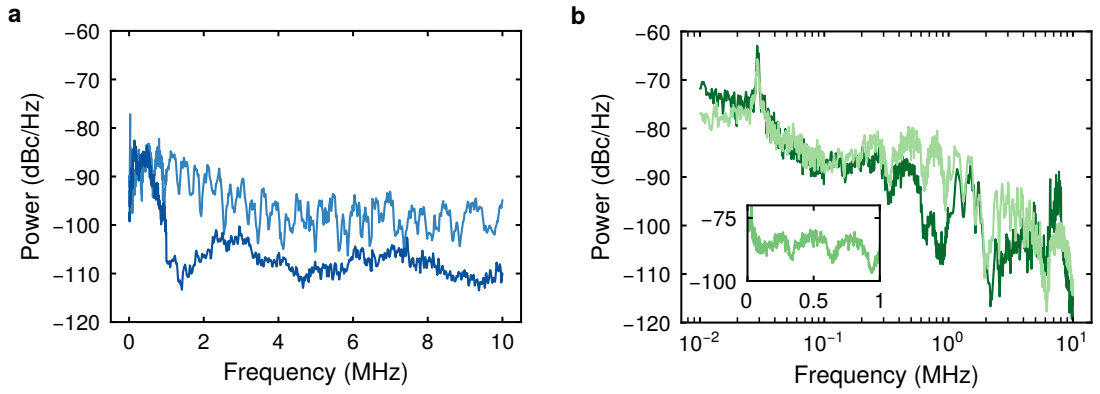

Figure 4.15 RIN in the IR and green path of the UV setup. a. Noise spectrum measured in the IR path for the home-built ECDL with the filter cavity, both before (dark blue) and after (light blue) the RFA. Measurements were performed with a RBW of $10\,\mathrm{Hz}$ and converted into RIN using Eq. (4.19), considering an input impedance of $R_{SA} = 50\,\Omega$. **b.** Utilizing the home-built ECDL with the filter cavity setup as the IR seed, we measured the noise spectrum after the first frequency doubling stage at $572\,\mathrm{nm}$. This was done both with (light green) and without (dark green) intensity stabilization, employing the built-in AOM. The inset provides a closer look at the frequency range up to $1\,\mathrm{MHz}$ of the signal filtered through intensity stabilization.

of the effect of the cavity filtering, which further reduces the noise by about $10\,\mathrm{dB}$ for a detuning of $500\,\mathrm{kHz}$.

In the next set of measurements, we compare the noise spectrum of the home-built laser with the optical filter cavity before and after it passes through the RFA with the one of the Menlo laser after the RFA. Both measurements are displayed in Fig. 4.14. These measurements were performed using a resolution bandwidth (RBW) of $100\,\mathrm{Hz}$ within a frequency span of $6\,\mathrm{MHz}$. We observe that the RFA introduces additional periodic noise at $\approx 250\,\mathrm{kHz}$, adding nearly $10\,\mathrm{dB}$ at a frequency detuning of $0.5\,\mathrm{MHz}$ from the beat note. This modulation pattern has been observed by other research groups as well as by the manufacturer of the RFA [196]. It is attributed to the relative intensity noise (RIN), which can be understood as intensity noise arising from the intensity noise of the pump fiber laser as the beam propagates through the RFA fiber [186, 196].

This is also visible, when evaluating the impact of frequency doubling on the noise spectrum around the carrier after the first doubling stage using the green interferometer (IF) at a wavelength of $572\,\mathrm{nm}$. Regarding the noise spectrum in Fig. 4.14, we now distinguish between two cases: the use of a commercial laser as the seed for the RFA, and the employment of a home-built laser in combination with the filter cavity as the seed for the RFA. A noticeable improvement of approximately $10 - 20\,\mathrm{dB}$ is observed. This underlines the significance of utilizing a spectrally pure seed laser.

Finally, we performed a RIN measurement of the filtered home-built laser, both before and after the RFA, as illustrated in Fig. 4.15. In both scenarios, we installed photodiodes and used the same spectrum analyzer as in the previous measurements to resolve the spectrum from $10\,\mathrm{kHz}$ to $10\,\mathrm{MHz}$ with an RBW of $10\,\mathrm{Hz}$. To convert the measurement of the spectrum analyzer $S_{\mathrm{dBm}/\Delta\nu}$ into relative intensity noise $S_{\mathrm{dBc}/Hz}$, we apply the following conversion [197]:

$$S_{\mathrm{dBc}/Hz} = S_{\mathrm{dBm}/\Delta\nu} - 10\log_{10}\left(\frac{\mathrm{RSB}\cdot U_c^2}{1\,\mathrm{Hz}\cdot 1\,\mathrm{mW}\cdot R_{SA}}\right). \tag{4.19}$$

Here, RBW is the resolution bandwidth, $R_{SA} = 50\,\Omega$ is the input impedance, and U_c is the voltage induced by the carrier of the laser. For the measurement before the RFA, we recorded a voltage of $U_c = 3.28\,\mathrm{V}$ from the carrier, and after the RFA, we measured $U_c = 3.5\,\mathrm{V}$. The data presented in Fig. 4.15 underscore that after optimizing the seed laser's phase noise, the predominant limitation emerges from the RIN induced by the RFA. Addressing this noise necessitates implementing additional compensation strategies involving applying feedback on, for example, AOMs or EOMs.

4.5 Implications of lightshift in Rydberg dressed systems

In the Rydberg-dressing regime, each spin experiences a constant offset, often referred to as the longitudinal field [57]. By studying spin-precession dynamics, we aim to measure this shift using a Ramsey measurement, as detailed in Section 3.5. We systematically analyze the precession frequency across various detunings scaling with $\nu_{AC}\cdot 2\pi = \delta_{AC} = -\Delta/2 + 1/2\cdot\sqrt{\Omega^2+\Delta^2}$, which is equivalent to Eq. (4.11). For the measurement, we place atoms in an 5×5 array with $39\,\mu\mathrm{m}$ spacing and optically pump them to the $|4S_{1/2}\,F=2,\,m_F=-2\rangle$ ground state, following the protocol in Section 3.4. We then apply a $\pi/2$ pulse on the $|F=1,\,m_F=-1\rangle$ transition, wait for $350\,\mu\mathrm{s}$, apply a π-pulse, wait another $350\,\mu\mathrm{s}$ and introduce a second $\pi/2$ pulse, mapping the atoms to the $|F=1,\,m_F=-1\rangle$ state. We then eliminate any remaining atoms in the $|F=2,\,m_F=-2\rangle$ state using a heat-out pulse on the closed cycling transition on the D2 line.

In addition, we apply pulses from the single-photon Rydberg excitation beam during the waiting time between the two pulses for varying durations. This beam couples the $|4S_{1/2}\,F=2,\,m_F=-2\rangle$ state to the Rydberg state $|62P_{3/2},\,m_j=-3/2\rangle$. Suppose this coupling is detuned from the resonance. In that case, the resulting light shift causes a phase difference between the two ground states, triggering a periodic oscillation in the populations of the coupled and uncoupled ground states. By repeating this measurement at different detunings and fitting an exponentially damped sinusoidal curve to the data, we determine the oscillation frequency, as illustrated in Fig. 4.16.

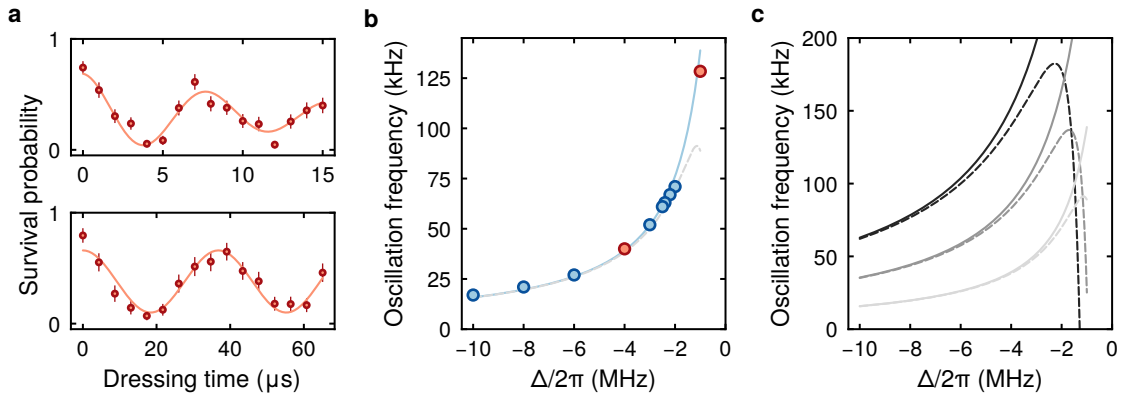

Figure 4.16 Dressed lightshift and oscillation frequency. a. In a Ramsey measurement with an echo pulse, we scanned the UV dressing duration at two distinct detunings: $\Delta/2\pi = 1\,\mathrm{MHz}$ and $\Delta/2\pi = 4\,\mathrm{MHz}$, each accompanied by a Rabi coupling of $\omega/2\pi = 816 \pm 11\,\mathrm{kHz}$. Using exponentially damped sinusoidal fits, we determined the oscillation frequencies $\nu_{AC}/2\pi = 128 \pm 3\,\mathrm{kHz}$ (upper) and $\nu_{AC}/2\pi = 27 \pm 0.4\,\mathrm{kHz}$ (lower). **b.** We perform the same measurement for different laser detunings and extract the oscillation frequencies. By applying the fit from Eq. (4.11) (solid blue line), we obtain a Rabi coupling of $\Omega_{\mathrm{meas}}/2\pi = 795 \pm 6\,\mathrm{kHz}$ aligning within error margins with our Rabi coupling measured on resonance. As the atoms within the tweezer array are spaced at intervals of $39\,\mu\mathrm{m}$, no additional collective field shifts have to be considered. The dashed line represents a hypothetical scenario where the atom spacing is reduced so that $n_{\mathrm{eff}} = 2$. **c.** Simulations displaying the detuning-dependent oscillation frequency, ν_{AC}, for different Rabi couplings: $2\Omega_{\mathrm{meas}}$, $1.5\Omega_{\mathrm{meas}}$, and Ω_{meas} (solid lines, dark to light grey respectively). Additionally, the effects of collective field shifts for $n_{\mathrm{eff}} = 2$ are shown (dashed lines).

As we position our atoms at a distance where Rydberg interactions are vanishing, we neither expect nor observe any collective field shift [57]. If this were not the case, we would need to factor in these interactions by applying a correction value, $\Delta_i^{(\mathrm{coll})} = n_{\mathrm{eff}}\Omega^4/16\Delta$. This value accounts for the van der Waals interactions among n_{eff} atoms and can be interpreted as a first indication of dressed interactions [57], including the soft-core potential from Eq. (4.17). A theoretical scenario with $n_{\mathrm{eff}} = 2$ and varying Rabi couplings is illustrated in Fig. 4.16. As expected, the impact of the interactions strongly depends on the Rabi coupling, leading to noticeable deviations, even at large detunings.While this scenario represents a hypothetical construct, n_{eff} could contain any number of atoms. An example of this can be seen in reference [57]. This optical lattice experiment measured 19 effective particles contributing to the shift.

Notably, the measured oscillation frequency is lower than in the 'interaction-free' case, indicating that the laser detuning and the interaction potential have different signs. This difference results in a larger detuning and, therefore, a reduced oscillation frequency. Given that we are red-detuned from the Rydberg resonance, it follows that the collective field shift is repulsive.

Using these measurements, we can calibrate our Rabi couplings by allowing Ω to act as a fit parameter. Hence, the AC-Stark shift induced on the ground state by the ultraviolet beam will enable us to infer a Rabi coupling of $\Omega_{\text{meas}}/2\pi = 795 \pm 6\,\text{MHz}$. However, this method depends on accurately determining the laser detuning, which in turn requires a precise spectroscopy measurement beforehand. An example of a spectroscopy measurement is displayed in Fig. 4.7, where the center of the applied Gaussian fit reveals an uncertainty of a few kHz.

4.6 Probing dynamics in dressed spin interactions

We now present an experimental approach to realize coherent effective spin-spin interactions. The measurement technique we employ is consistent with the procedure demonstrated in reference [57], utilizing a Ramsey sequence. Similar to the technique discussed in the section before, we employ a second ground state, $|\downarrow\rangle$, which is not coupled to the Rydberg state. Instead, we couple this state via a ground state Raman transition to the distinct ground state $|\uparrow\rangle$, which is off-resonantly coupled to the Rydberg manifold. This dressing procedure, therefore, introduces the 'dressed' ground state interactions to the system, which we have elaborated on in Section 4.2. Moreover, we decrease the separations between the atoms. As a result, we achieve Ising-type interactions described by the subsequent interaction Hamiltonian [57]:

$$\hat{H} = \hbar \sum_{i}^{N} \left(\delta_{AC} + \Delta_i^{(\text{coll})} \right) \hat{S}_i^z + \sum_{i \neq j}^{N} \frac{U_{i,j}}{2} \hat{S}_i^z \hat{S}_j^z \,. \tag{4.20}$$

Here, $\hat{S}_i^z$ represents the spin-1/2 operators. We also included the single-atom light shift, δ_{AC}, and the collective field shift, $\Delta_i^{(\text{coll})}$, which were covered in the previous section. Furthermore, the interaction $U_{i,j}$ characterizes the dressing-induced interactions between two spins situated at positions i and j. Given that both the collective field shift and single-atom light shift result in a measurable frequency shift in the Ramsey protocol – acting effectively as a constant offset – we will primarily concentrate on the dressed interactions.

For the measurement, we prepare the atoms at a fixed distance of $3.4\,\mu\text{m}$ in an array of six groups, each containing three tweezers. Within each group, the atoms are aligned perpendicular to the magnetic field $|\mathbf{B}| = 5\,\text{G}$. The groups are spaced by $30\,\mu\text{m}$ along the magnetic field to prevent any interactions between the groups and only allow interactions within the groups. We prepare the atoms in the $|\uparrow\rangle = |F = 2,\, m_F = -2\rangle$ spin state, which can be coupled to the $|r\rangle = |62P_{3/2},\, m_j = -3/2\rangle$ Rydberg state. The Ramsey protocol is illustrated in Fig. 4.17 and structured as follows: We begin with a $\pi/2$-pulse on the $|\uparrow\rangle - |\downarrow\rangle$ ground state transition, leading to a superposition of both spin states. We then apply two identical Rydberg dressing pulses $\tau_{dr}/2$, separated by a spin-echo (π) pulse on the ground states. After a total Ramsey time of $700\,\mu\text{s}$, we apply a second $\pi/2$-pulse, but

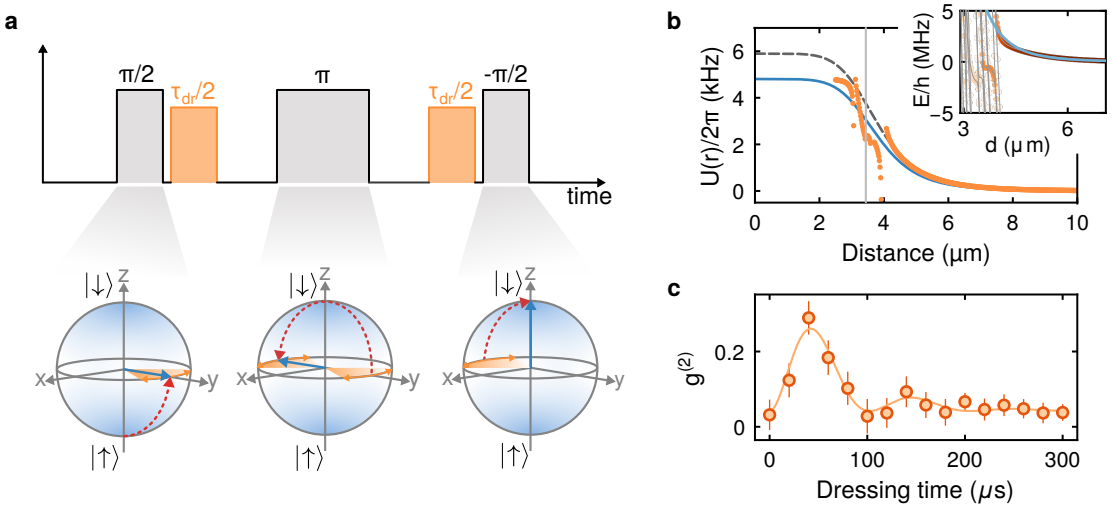

Figure 4.17 Dressed Ising-type interaction. a. Schematic of the Ramsey measurement. The atoms are initially prepared in the stretched state $|\uparrow\rangle = |F = 2, m_F = -2\rangle$. A subsequent $\pi/2$-pulse is applied (indicated by the red dashed error on the Bloch sphere), which is followed by a variable duration of a dressing pulse $\tau_{dr}/2$ (highlighted by the yellow shaded area). This is followed by an echo pulse, another dressing pulse, and a $\pi/2$-pulse with a phase shift of $180°$ to transfer the atoms to the $|\downarrow\rangle = |F = 1, m_F = -1\rangle$ state. **b.** Calculation of the distance dependent interaction strength $U(R)$. The vertical grey line indicates the spacing of atom pairs in the experiment. The blue curve represents the diagonalization of the Hamiltonian in Eq. (4.12), assuming that $C_6 = 14.3\,\mathrm{GHz}\cdot\mu\mathrm{m}^6$. In contrast, the dashed grey line depicts the interaction strength deduced from a perturbative approach, as done in Eq. (4.14). The orange data points reflect the exact diagonalization of the Hamiltonian in Eq. (4.21) but include all the Rydberg pair potentials $|\Psi_\alpha^{(2)}\rangle$, with their weight determined by the overlap $\langle\Psi_\alpha^{(2)}|rr\rangle$, where $|r\rangle = |62P_{3/2}, m_j = -3/2\rangle$. The inset shows a glimpse into the analysis of the Rydberg pair potentials (calculated with PAIRINTERACTION [105]) surrounded by the $|rr\rangle$ Rydberg pair potential, with the solid orange line representing a C_6/R^6 fit, emphasizing its inadequacy for smaller pair distances. **c.** Measurement of the nearest neighbor pair correlation $g^{(2)}$ for different dressing durations. We employ an exponentially damped $\sin^2$ fit function to deduce an interaction strength of $U/2\pi = 4.88 \pm 0.23\,\mathrm{kHz}$.

with a $180°$ phase shift, which transfers the system into the $|\downarrow\rangle = |F = 1, m_F = -1\rangle$ state if no interactions occurred. To distinguish between the two ground states, we perform a heat-out pulse on the $|\uparrow\rangle$ state by driving the closed cycling transition of the D2-line.

For the coupling to the Rydberg state, we measure a Rabi frequency of $\Omega/2\pi = 813 \pm 3\,\mathrm{kHz}$ and set a laser detuning of $\Delta/2\pi = -2.1\,\mathrm{MHz}$. Using these parameters, we estimate a soft-core potential of $U_0 = \Omega^4/8\Delta^3 = 2\pi \times 5.9\,\mathrm{kHz}$. We extract a C_6 coefficient by fitting a $f(r) = C_6/r^6$ function to the Rydberg pair potentials calculated with PAIRINTERACTION[18]

[18]For the calculations, we assumed the following boundary parameters: $\Delta n = 1$, $\Delta\ell = 1$, $\Delta E_{1\,\mathrm{atom}} = 200\,\mathrm{GHz}$ and $\Delta E_{\mathrm{pair}} = 100\,\mathrm{GHz}$.

[105], as depicted in the inset of Fig. 4.17. As clearly visible, the fit is valid only for large spacings. For spacings below $4\,\mu\mathrm{m}$, other Rydberg pair potentials influence the shape, which renders the C_6 curve fit inapplicable. Nevertheless, from this analysis, we extract $C_6 = 12.26 \pm 0.06\,\mathrm{GHz}\cdot\mu\mathrm{m}^6$ when only fitting the eigenenergies up to the smallest distance of $4.5\,\mu\mathrm{m}$. Consequently, we deduce a cut-off radius of $R_C = 3.8\,\mu\mathrm{m}$. We then calculate the interaction strength at the distance of the atom pairs in our experiment in three different scenarios:

The first approach follows the perturbative treatment as outlined in Eq. (4.14). Here, we determine an interaction strength of $U(R = 3.4\,\mu\mathrm{m})/2\pi = 3.76\,\mathrm{kHz}$.
The second method involves a diagonalization of the Hamiltonian in Eq. (4.12) and assumes $\Delta^{(2)}(R) = -2\pi\Delta + C_6/R^6$. This yields an interaction strength of $U(R = 3.4\,\mu\mathrm{m})/2\pi = 3.1\,\mathrm{kHz}$, which differs by hundreds of Hertz but is of the same order of magnitude as the first method.
However, we consider the third method the most accurate. Unlike the other methods, it does not rely on assumptions or rounding of the C_6 coefficient but directly uses the pair potentials calculated with PAIRINTERACTION. This approach diagonalizes the Hamiltonian described below in the basis of $|\uparrow\uparrow\rangle$, the symmetric singly-excited state $|+\rangle$, and the Rydberg manifold $|\Psi_\alpha^{(2)}(r,\theta)\rangle$:

$$\hat{H} = \sum_\alpha \begin{matrix} \\ |\uparrow\uparrow\rangle \\ |+\rangle \\ |\Psi_\alpha^{(2)}(r,\theta)\rangle \end{matrix} \begin{matrix} \begin{matrix} \langle\uparrow\uparrow| & \langle+| & \langle\Psi_\alpha^{(2)}(r,\theta)| \end{matrix} \\ \begin{pmatrix} 0 & \hbar\Omega/\sqrt{2} & 0 \\ \hbar\Omega/\sqrt{2} & -\hbar\Delta & \hbar\Omega/\sqrt{2}\cdot c_\alpha^{mn}(r,\theta) \\ 0 & \hbar\Omega/\sqrt{2}\cdot c_\alpha^{mn}(r,\theta) & -\hbar\Delta + E_\alpha^{(2)}(r,\theta) \end{pmatrix} \end{matrix}. \tag{4.21}$$

Here, α indexes the new pair distance- and angle-dependent eigenstates $|\Psi_\alpha^{(2)}(r,\theta)\rangle$, expressed as a composition of different asymptotic pair states $|r^m r^n\rangle$, where m and n denote different Rydberg states. The eigenstate is represented by $|\Psi_\alpha^{(2)}(r,\theta)\rangle = \sum_{mn} c_\alpha^{mn}(r,\theta)|r^m r^n\rangle$. In the following, we will omit the explicit mention of distance and angle dependence to enhance readability. Additionally, we consider the state-dependent admixture $c_\alpha^{mn} = \langle\Psi_\alpha^{(2)}|r^m r^n\rangle$, which accounts for the different geometric configurations of the atom pair. Since we can only couple to one Rydberg pair state $|rr\rangle$, the expression simplifies by dropping all m and n terms. In this formalism, the matrix element between $|+\rangle$ and $|\Psi_\alpha^{(2)}\rangle$ is weighted by the state overlap c_α.

Furthermore, instead of using any C_6-potential curve, we directly include the eigenenergy of each eigenstate E_α. As it can be seen in Fig. 4.17 at the atom's distance, we encounter Rydberg pair potential crossings, making the potential non-smooth. From the atom distance, we extrapolate an interaction strength of $U(R = 3.4\,\mu\mathrm{m})/2\pi \approx 2.4\,\mathrm{kHz}$.

In the Ramsey measurement, this interaction can be measured as a correlated phase shift given by $\phi_{\text{int}} = \int_0^{\tau_{dr}} U(R)tdt = U(R) \cdot \tau_{dr}$. This will lead to detectable spin correlations after this sequence. Paired with our site-resolved detection method, we can directly deduce the two-body correlation function:

$$g^{(2)}_{i,j} = \langle (n_i - \langle n_i \rangle) \cdot (n_j - \langle n_j \rangle) \rangle \,. \tag{4.22}$$

In this expression, n_i denotes the state population in the $|\downarrow\rangle$ spin state at site i. For the subsequent analysis, we select on the nearest neighbor pairs that were initially loaded within the sets of three available tweezers.

Following the exact solution for the final many-body state detailed in references [57, 198], and restricting the system to those with two (neighboring) atoms, we find that the correlation function scales as:

$$g^{(2)}(R) \propto \sin^2(\phi_{\text{int}}) = \sin^2(U(R) \cdot \tau_{dr}) \,. \tag{4.23}$$

We utilize this scaling to fit an exponentially damped quadratic sinusoidal function to our nearest neighbor correlation amplitudes for various dressing durations τ_{dr}, as illustrated in Fig. 4.17. From the fit parameters, we determine the interaction strength to be $U_{\text{meas}}/2\pi = 4.88 \pm 0.23\,\text{kHz}$ and a rapid damping rate of $1/\gamma = 126 \pm 24\,\mu\text{s}$. Notably, this interaction strength differs from the theoretical prediction. With the third method, this difference is approximately a factor of two. We explain this variation by two significant effects: The first one stems from the lack of accurate calibration of the imaging magnification and, consequently, the tweezer spacing. Studying the interaction shape more closely, we observe that atoms spaced $300\,\text{nm}$ closer at $3.1\,\mu\text{m}$, the coupling strength achieves $4.8\,\text{kHz}$, coinciding within error margins with our measurement. The rapid increase in interaction amplitude can be attributed to the nearby Rydberg pair state resonances. This emphasizes the need for a refined calibration technique for our imaging magnification system to enhance our understanding and subsequent analyses. The second factor arises from the need to reduce our overall trap depth to its minimum before gravity takes over, opening the trap and allowing for larger ground-state wavepacket sizes. This results in radial and axial trapping frequencies of $\omega_{\text{rad}} = 2\pi \times 11\,\text{kHz}$ and $\omega_{ax} = 2\pi \times 1.7\,\text{kHz}$. We only focus on the radial trapping frequency since the axial leads merely to out-of-plane motion, effectively increasing pair distances. Using the radial trapping frequency, we compute the ground state wavepacket size in the radial direction as $\sigma^0_{\text{rad}} = \sqrt{\hbar/(m\omega_{\text{rad}})} = 150\,\text{nm}$. Given that the atomic temperature $k_B T = h \cdot 4.2\,\text{kHz}$ is below the radial trapping frequency, we consider the ground state wavepacket size to account for the fluctuations in the radial pair-distances with $\sigma_{\text{rad}} = \sqrt{2}\sigma^0_{\text{rad}} = 212\,\text{nm}$, where $\sqrt{2}$ factors in the movement of two atoms. This roughly equates to the positional deviation observed when contrasting the measured interaction with the calculated one.

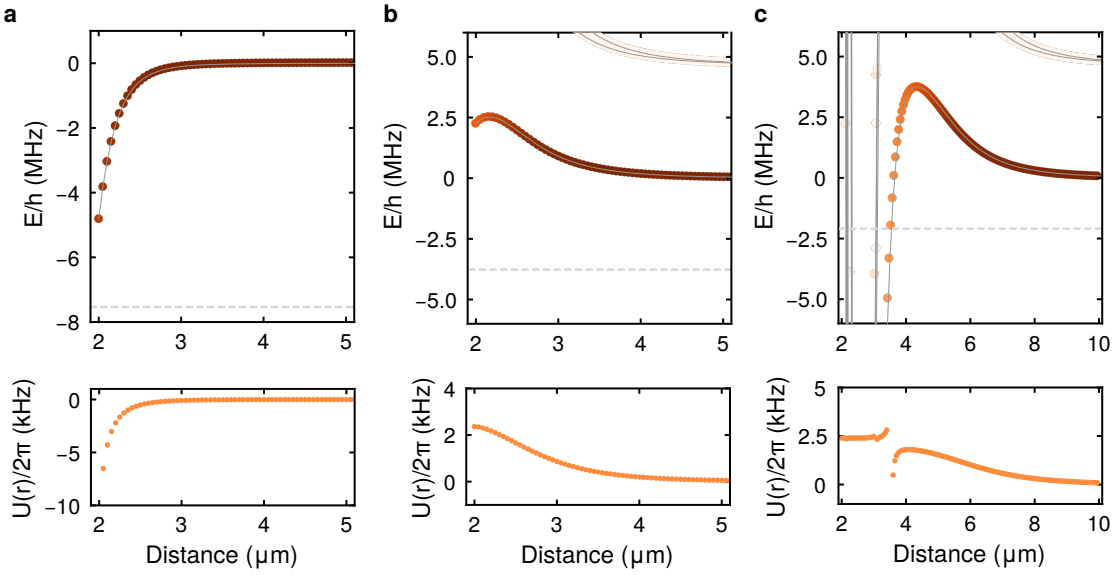

Figure 4.18 Rydberg pair potentials and dressed interactions for selected Rydberg states. Simulations for these pair potentials were performed using the PAIRINTERACTION software [105]. We set the magnetic field to $B = 5\,\mathrm{G}$ with pairs oriented at a $90°$ angle relative to the magnetic field. Across all simulations, we maintained a consistent Rydberg fraction of $\beta^2 = 3.7\%$. **a.** Pair potentials and interactions for the $|42P_{3/2}, m_j = -3/2\rangle$ state. The Rabi coupling for this state is $\Omega/2\pi = 1.46\,\mathrm{MHz}$, with a detuning at $\Delta/2\pi = -3.8\,\mathrm{MHz}$ (horizontal dashed line). **b.** Pair potentials and interactions for the $|42P_{1/2}, m_j = -1/2\rangle$ state. The Rabi coupling here is calculated as $\Omega/2\pi = 813\,\mathrm{kHz}/2 \cdot (42/62)^{-3/2} = 729\,\mathrm{kHz}$, with a set detuning of $\Delta/2\pi = -1.9\,\mathrm{MHz}$ (horizontal dashed line). **c.** The pair potentials and interactions correspond to the $|62P_{1/2}, m_j = -1/2\rangle$ state. We accounted for a smaller Rabi coupling, set at $\Omega/2\pi = 407\,\mathrm{kHz}$, which is half of the Rabi coupling for the $P_{3/2}$ state as seen in Fig. 4.17. The detuning was set at $\Delta/2\pi = -1.05\,\mathrm{MHz}$ (horizontal dashed line).

Additionally, we also identify a fast damping in the oscillation. Although there are various constraints, like potentially non-adiabatic ramping of the dressing pulses, the primary source of this dephasing seems to be the shortened experimental dressed lifetime and the consequent increased Rydberg fraction. Given our prior discussion on laser detuning and Rabi frequency, we had anticipated a theoretically 'ideal' dressed lifetime of $4.4\,\mathrm{ms}$. Nonetheless, due to the phase noise of our laser, which we addressed previously, we estimate a lifetime reduction by a factor of 20. As such, the expected dressed lifetime decreases to $220\,\mu\mathrm{s}$, which is shorter than our measurement's longest duration of $300\,\mu\mathrm{s}$. This means that the correlation strength diminishes in proportion to the number of atoms excited in the system, manifesting as losses from this mechanism. This phenomenon has also been identified as a significant source of decoherence in reference [56]. The effect of the black-body-limited lifetime, resulting from decays into adjacent Rydberg states, imposes additional significant constraints, which we will discuss in the following chapter.

Moreover, when looking closely at the Rydberg pair potential plot in Fig. 4.17, we notice numerous resonances for pair distances under $4\,\mu\mathrm{m}$. Meaning our selection of the Rydberg state was not optimal. Exploring different Rydberg states would be beneficial for future works, as showcased in Fig. 4.18. Here, we contrast two distinct principal quantum numbers ($n = 42$ and $n = 62$), evaluating the dressed interactions for Rydberg $nP_{1/2}$ and $nP_{3/2}$ states. The magnetic field remained consistent at $B = 5\,\mathrm{G}$ for all simulations, and the Rydberg fraction $\beta^2 = 3.7\%$ was held constant. Since the dipole matrix element for the $P_{1/2}$ states is less than that for the $P_{3/2}$ states, the coupling was adjusted to reflect a twofold difference, verified experimentally. The Rabi frequencies were adapted with $n^{-3/2}$, as elucidated in Section 2.2 to include the estimate for varying principal quantum numbers. Two scenarios in Fig. 4.18 are particularly interesting: One option is the $42P_{3/2}$ state, where one could amplify the proportion of Rydberg pair states in the system while operating close to a pair resonance that is approached when reducing the distance to $2\,\mu\mathrm{m}$. Here, one could maintain the fraction of single excitations and enhance the interaction strength with $V = \Omega^4/U_0^2\Delta^{(2)}$, where $\Delta^{(2)} = 2\Delta - U(R)$ denotes the pair detuning [139]. In this context, $\Delta^{(2)}$ could be smaller than Δ, thereby increasing the Rydberg pair fraction and yielding a more favorable balance between interactions and decoherence rates. Another option could be working at the $42P_{1/2}$ state, yielding a clean system without crossing pair resonances until $2\,\mu\mathrm{m}$ and an interaction strength of roughly $U/2\pi = 2\,\mathrm{kHz}$ at this distance.

While we have studied several aspects influencing the interaction dynamics and challenges, the influence of black-body radiation cannot be understated. Black-body-induced losses significantly influence Rydberg dressing and the behavior of Rydberg systems. In the upcoming chapter, we'll investigate the mechanisms behind these losses and explore potential strategies to mitigate their impact on our experiment.

4.7 Resolving the effect of black-body induced losses on Rydberg dressing

In previous chapters, our measurements have underlined the importance of understanding the various channels of decoherence in Rydberg physics, especially as its applications continue to evolve. In this chapter, we turn our attention to one of the 'Achille's heels' of Rydberg dressing: the losses induced by black-body radiation. The content of this chapter is built upon the material and discussions found in our publication [75]. Black-body radiation at room temperature initiates incoherent transitions between adjacent Rydberg states, effectively shortening the lifetime of a Rydberg state. For instance, the $62P$ Rydberg state has a blackbody-constrained lifetime of $\tau_{bb} = 160\,\mu\mathrm{s}$ at $T = 300\,\mathrm{K}$. In contrast, at a temperature of $T = 4\,\mathrm{K}$, its lifetime would be extended fivefold to $\tau_{bb} = 829\,\mu\mathrm{s}$. Black-body radiation facilitates transitions to neighboring states of opposite parity, as illustrated in Fig. 4.19. These transitions give rise to new dipolar interactions, acting beyond the range of the van-der-Waals interactions typical of Rydberg states with identical parity. These

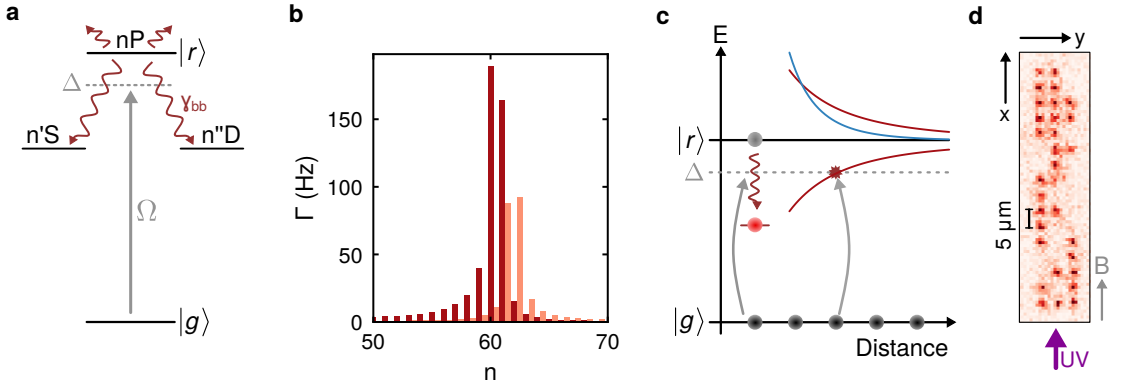

Figure 4.19 Principle of black-body decay induced losses. a. Schematic of the process. In our experiment, we excite the atoms to Rydberg nP states via a single photon excitation. These states can decay to nearby Rydberg $n'S$ or $n''D$ states via black-body decay γ_{bb}. **b.** Histogram of transition rates at $T = 300\,\mathrm{K}$, when exciting the atoms to the Rydberg $|62P_{1/2}, m_j = -1/2\rangle$ state, computed with the ARC software package [68]. Via a black-body photon, atoms can decay into $nS_{1/2}$ states (light red) and $nD_{3/2}$ states (dark red). Here, we only show a snapshot of the main contributing states sorted via the principal quantum number n. **c.** Schematic of the black-body induced contamination losses in the system, which can be read from left to right: We excite the atoms off-resonantly to the Rydberg state $|r\rangle$. This state produces a van-der-Waals-like (C_6) interaction potential (light blue) for all surrounding atoms. In the case of a black-body decay into nearby states, this new contamination leads to a dipole-dipole-like (C_3) interaction shift of the surrounding atoms (red solid line), which might lead to resonant excitations of atoms at a certain distance with the then-in-resonance laser. **d.** Example of a single shot fluorescence picture of the $3x16$-array we use for the experiments shown in this chapter. The average atom spacing is $5\,\mu\mathrm{m}$. The magnetic field and the Rydberg excitation beam are aligned with the long axis of the array.

interaction ranges often align with the tweezer array's spacing or the spacing within an optical lattice [57, 199].

These dipolar interactions induce level shifts in neighboring atoms. When operating in the off-resonant Rydberg dressing regime, these shifts can render a previously detuned laser into a resonance with a Rydberg pair state. This facilitates excitations to the Rydberg manifold. Such excitations manifest as losses in the array, since the excited states most often are anti-trapped, leading them to escape from the trap.

In the subsequent part, we will delve into the analysis of losses induced by Rydberg state contamination in a two-dimensional array of single atoms, particularly within the Rydberg dressing regime. Our primary objective is to offer a detailed quantitative estimation of the interaction range, and further discuss potential avalanche excitations, which have been identified as limiting factors in various other experiments [56, 57, 199]. Central to our implementation is the observation that the interaction range is proportional to the

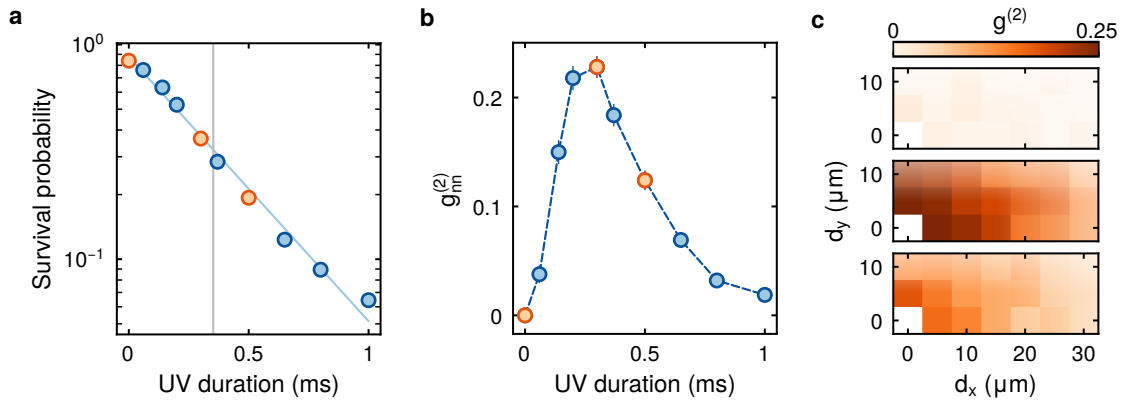

Figure 4.20 Growth of correlation with varying dressing durations. a. Dressed lifetime measurement for the 3×16-atom array, with a Rabi coupling of $\Omega/2\pi = 424 \pm 8\,\mathrm{kHz}$ and a detuning of $\Delta/2\pi = -2\,\mathrm{MHz}$. The blue solid line represents an exponential fit, yielding a $1/e$ lifetime of $\tau_{dr} = 352 \pm 16\,\mu\mathrm{s}$. The horizontal line marks a point where 60% of the atoms are recaptured. The three yellow data points denote the timings corresponding to the correlations plotted in c. **b.** Evaluation of the nearest neighbor correlation amplitude, $g^{(2)}_{nn}$, for the same data points as in a. **c.** Depicted are the correlations within the array at three distinct dressing durations, as indicated in a and b: $0\,\mathrm{ms}$, $0.3\,\mathrm{ms}$, and $0.5\,\mathrm{ms}$, from top to bottom.

interatomic spacing in our tweezer array and the detuning of the laser. In our experiments, this spacing is on the order of a few micrometers.

For our measurements, we employ a 3×16 tweezer array with a spacing of $5\,\mu\mathrm{m}$, as shown in Fig. 4.19. The Rydberg excitation beam, aligned with the long axis of the array, is parallel to a magnetic field of magnitude $|\mathbf{B}| = 10\,\mathrm{G}$.

Our standard experimental procedure is as follows: After loading the tweezers – with an average loading probability of around 50% – we capture an initial fluorescence image. Subsequently, we perform RSC and prepare the atoms in the $|F = 2, m_F = -2\rangle$ ground state. Then, we reduce the trap depth to 0.5% of its initial power for loading, and while ensuring the atoms remain trapped, expose them to a Rydberg dressing pulse of varying duration and laser detuning. This excitation beam drives σ^--transitions to the Rydberg state $|r_i\rangle = |62P_{1/2}, m_j = -1/2\rangle$. We can quantify the losses arising during this sequence by comparing both fluorescence images.

We now aim to identify interaction-induced losses within the array as a function of detuning. Our general approach aligns with the steps illustrated in Fig. 4.20. First, we measure the dressed lifetime of the atom array to calibrate the dressing pulse duration. We then adjust this duration to maintain about 60% of the atoms within the trap. This careful calibration allows for the accumulation of interactions without substantial atom loss. For the analysis, we use the correlation function defined in Eq. (4.22). Fig. 4.20 shows the evolution of two-point correlations over time and their spatial trace for three specific dressing durations.

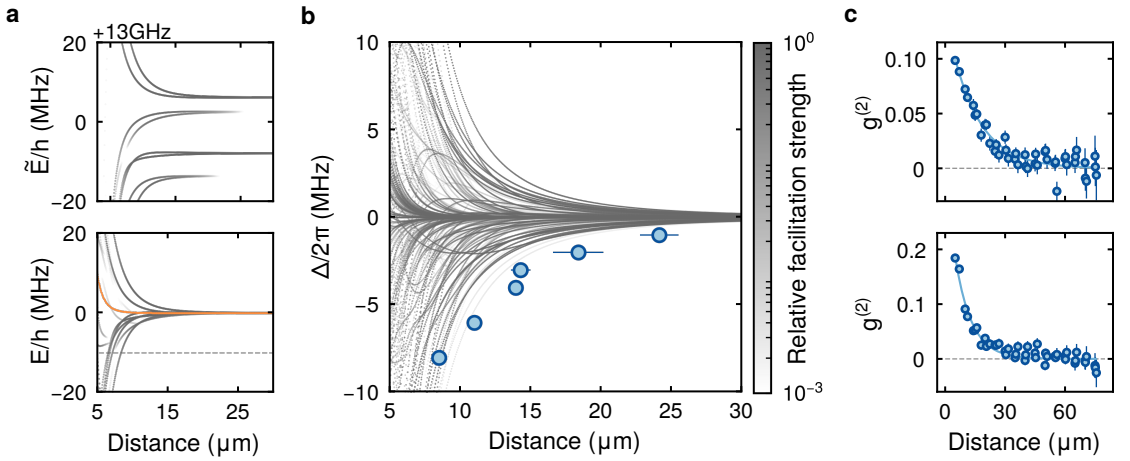

Figure 4.21 Dipolar interaction potentials. Figures are adapted from [78]. **a.** The upper plot visualizes the pair potentials of the laser-coupled Rydberg state $|62P_{1/2}, m_j = -1/2\rangle$ with the magnetic substates of its most strongly coupled states, $|61D_{3/2}\rangle$ and $|61D_{5/2}\rangle$, at a magnetic field amplitude of $|\mathbf{B}| = 10\,\mathrm{G}$. The color coding corresponds to the logarithmic relative facilitation strength shown in the color bar in b. When a black-body process is initiated, the microwave photon provides the energy difference of $13\,\mathrm{GHz}$, effectively causing all pair potentials to collapse asymptotically, as demonstrated in the lower plot. For comparison, the orange line represents a van-der-Waals potential of the $|r_i r_i\rangle$ pair potential, highlighting its significantly shorter range in contrast to the dipolar interaction potentials. These potentials are computed using the PAIRINTERACTION software [105]. **b.** This panel showcases the collapsed dipolar potentials, weighted by the logarithmic relative facilitation strength. This weighting takes into account the normalized transition rate and the state overlap with $|r_i r_j^{bb}\rangle$. The plotted data points signify typical correlation distances deduced from an exponential fit to $g^{(2)}(d, \Delta)$ for a 3x16 array spaced at $5\,\mu\mathrm{m}$. The specifics of this spacing can be found in Fig. 4.20. The error bars indicate fit errors. **c.** Examples of the measured two-body correlations, along with exponential fits used to determine the decay length. For $\Delta/2\pi = -3\,\mathrm{MHz}$ (upper plot), the decay length is $d_c = 14.3 \pm 0.7\,\mu\mathrm{m}$, while for $\Delta/2\pi = -8\,\mathrm{MHz}$ (lower plot), it stands at $d_c = 8.2 \pm 0.4\,\mu\mathrm{m}$.

Furthermore, we derive the two-point correlation amplitude for various distances within the array and fit it with an exponential decay function, $f(d) \propto \exp(d/d_c)$. This empirical approach is effective for an initial estimate of the interaction range, allowing us to determine the decay length, d_c. Subsequently, we repeat this measurement at different laser detunings, ensuring the theoretical admixture $\beta = \Omega/2\Delta$ remains constant without factoring in any incoherent processes.

To calculate the diverse dipolar interaction potentials, we utilize the PAIRINTERACTION software [105]. These potentials are delineated in the GHz domain. Transitions into other Rydberg states are facilitated by blackbody photons, causing the different Rydberg pair potentials to converge to a unified energy level. An illustrative representation of this process is provided in Fig. 4.21 for the most strongly coupled Rydberg states $61D_{3/2}$ and

$61D_{5/2}$. This figure also shows the merged dipolar pair interactions of the dipolar pair potentials. Each of these potentials is weighted based on the relative facilitation strength of the respective pair potential, represented as $|r_i r_j^{bb}\rangle$, where r_j^{bb} denotes the Rydberg state that has undergone black-body decay:

$$\gamma_j^{\text{rel}} = c_{ij} \cdot \frac{\Gamma_{ij}^{bb}}{\Gamma_{\text{max}}^{bb}} \,. \tag{4.24}$$

In this equation, c_{ij} signifies the quadratic overlap of the asymptotic Rydberg pair state $|r_i r_j\rangle$ with the eigenstate $|\Psi_\alpha^{(2)}(d)\rangle$. Here, α spans all computed eigenstates at position d: $c_{ij} = |\langle \Psi_\alpha^{(2)}(d)|r_i r_j^{bb}\rangle|^2$. Transition rates into closeby Rydberg states, represented by Γ_{ij}^{bb}, are depicted in Fig. 4.19.

Upon analyzing the two-point correlation function over various distances, one might expect to resolve individual potential lines. In addition, the interaction range observed in our detuning scans is larger than the theoretical predictions shown in Fig. 4.21.

This deviation can be attributed to the motion of the Rydberg atoms. Several factors influence this motion, including the atom's temperature, the ponderomotive potential of the tweezers, and atomic recoil. The recoil velocity v_r is described by $v_r = hk/m = 36\,\mu\text{m/ms}$ [78]. Here, k represents the wavevector of the excitation wavelength, defined as $k = 2\pi/\lambda = 2\pi/286\,\text{nm}$, and m is the atom's mass. Interestingly, this velocity is comparable with the velocity, v_U, that an atom gets accelerated to by the ponderomotive potential: $v_U = \sqrt{2\hbar U/m} = 40\,\mu\text{m/ms}$, given a trap depth of $U = 3.7\,\mu\text{K}$. Furthermore, the thermal velocity, dictated by the atom's temperature $T = 200\,\text{nK}$, is described as $v_T = \sqrt{k_B T/m} = 6.5\,\mu\text{m/ms}$.

Considering that the decay to low-lying states takes several hundreds of microseconds, atoms excited to the Rydberg state move through the array, covering a wide range of pair distances. This movement hinders us from distinguishing between individual potential resonances. Furthermore, the trapping potentials serve as 'barriers', influencing the atoms' trajectories. For an in-depth exploration of the effects of atomic motion, please refer to our publication [78].

Another underlying, phenomenon is known as avalanche facilitation. This mechanism describes that when an atom is excited to the Rydberg state and undergoes a blackbody transition, it sets off a chain reaction, triggering a series of subsequent excitations. This cascade effect has been identified in prior experiments and is recognized as a significant limitation, especially when operating within atom ensembles or large arrays of single atoms with high atom density [56, 57, 199].

In our experiment, a challenge we consistently face is the statistical loading of our tweezer array. This results in an average loading probability of approximately 50%. However, the filling rate is crucial for observing the avalanche effect due to its close association with the dipolar interaction range.

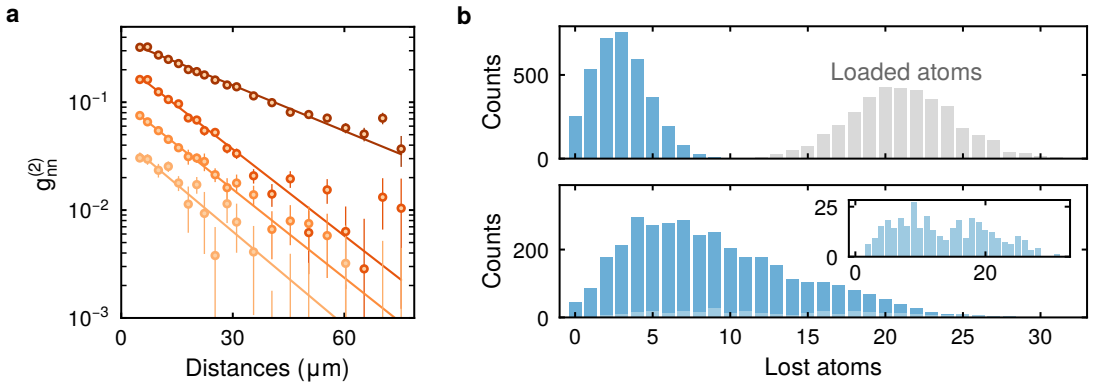

Figure 4.22 Avalanche facilitation processes. Figures are adapted from [78]. **a.** The graph displays two-body correlations at varying distances within the 3×16 atom array, with different Rabi couplings. These couplings range from dark to light orange and are represented as $\Omega/2\pi = (410, 205, 103, 51)\,\mathrm{kHz}$. For each measurement, the dressing duration was adjusted such that 60% of the atoms were recaptured. Solid lines denote exponential fits, with extracted decay lengths as follows (ordered from dark to light orange): $30.8 \pm 1.1\,\mu\mathrm{m}$, $16.2 \pm 0.7\,\mu\mathrm{m}$, $15.9 \pm 1.3\,\mu\mathrm{m}$, and $15 \pm 1.9\,\mu\mathrm{m}$. The grey bares present the loading distribution within the array **b.** This panel showcases the distribution of lost atoms (depicted in blue) for a specific Rabi coupling of $\Omega/2\pi = 424 \pm 8\,\mathrm{kHz}$ and a detuning of $\Delta/2\pi = -3\,\mathrm{MHz}$. The upper plot represents data collected without any UV exposure time, while the lower plot indicates results from a UV exposure time of $0.6\,\mathrm{ms}$. The inset in the lower plot captures data from the same experimental settings, but with postselection based on scenarios where 26 atoms were initially loaded into the array.

We evaluate atom losses across three distinct scenarios in one experiment. In the first scenario, we don't apply any Rydberg dressing pulse. This means any observed atom losses come from imaging losses or insufficient RSC, which leads to trap losses when the trap depth decreases. In the second scenario, we analyze the trap losses after a dressing duration of $0.6\,\mathrm{ms}$, which corresponds to a total loss of 40% of the atoms. In the third scenario, we apply the same dressing duration, but we limit our analysis to samples with an initial load of 26 atoms, equivalent to a filling fraction of 54%. When analyzing the third scenario, as shown in Fig. 4.22, there's a noticeable broadening in the distribution of lost atoms. This broadening can serve as an early sign of the bimodality observed in denser setups [57]. Enhancing the array filling, either through deterministic loading [79, 200] or filling via resorting [27], may allow us in the future to better contrast this bimodality.

Furthermore, we analyze the effects of varying Rabi coupling strengths on avalanche losses with the next set of measurements. For this, we systematically increase the Rabi coupling while maintaining the detuning unchanged. We set the dressing time such that we ensure a consistent loss of 60% of atoms across all observations. As shown in Fig. 4.22, the correlation amplitudes grow as the Rabi couplings increase. Interestingly, when applying an exponential decay fit to the measurements, we obtain comparable interaction ranges for the cases with

reduced Rabi couplings. Moreover, the correlation length gains a factor of two when increasing the Rabi coupling from $\Omega/2$ to $\Omega = 2\pi \times 410\,\mathrm{kHz}$.

Increased interaction strength might indicate the presence of avalanche processes. These processes become evident when studying higher-order correlations, where multiple facilitation events are expected in the event of avalanches. We explored this in our publication [78] using three- and four-point correlators. Our findings demonstrate that the amplitude of these higher-order correlators rises with an increase in Rabi coupling.

Our studies have clarified the challenges associated with black-body-induced losses and avalanche processes in Rydberg dressing. Understanding these limitations is essential, especially given their apparent limitations on coherence. We will now discuss several clever methods to overcome the issues posed by black-body contaminants:

- **Stroboscopic dressing:** The stroboscopic dressing technique, successfully implemented by various research groups, serves as an innovative approach to enhance the Rydberg lifetimes in atom ensembles or lattices with large filling densities [58, 107]. This method alternates between short dressing light pulses and dark periods T_D when no light is applied. These dark intervals are strategically timed to let impurity atoms decay and leave the trap. As discussed previously, the excited atoms, influenced by the ponderomotive potential of the trapping light and the recoil, leave the trap before decaying back to the ground state. To ensure the same effective interaction strength during this process, it's necessary to decrease the laser detuning. Moreover, instead of simply implementing these dark periods as waiting times, they can also be utilized for other operations. For example, during Floquet measurements [56], these intervals can be used to apply spin rotations.
- **Introduction of additional repulsive potential for Rydberg states:** A possible method to consider involves introducing an additional repulsive potential specific to Rydberg states, such as employing a light sheet focused on the atom array. While this light sheet acts as a trapping potential for atoms in the ground state, it effectively repels those in the Rydberg states. The key is to ensure a sufficiently strong shift, causing the contaminant atoms to move out of the array vertically, thus reducing motion within the array itself [75].
- **Depumping of black-body decayed atoms:** Another method to mitigate the effects of black-body decays in the system could be to rapidly depump these atoms to lower-lying states. These states neither induce notable dipolar shifts nor have a long lifetime, quickly transitioning further into the electronic ground states. It's essential that the depumping process is faster than any facilitation rate, which scales with the resonant Rabi couplings. A first experimental approach might focus on extracting contaminant states that exhibit the strongest coupling to the designated Rydberg state. In our configuration, this would involve targeting adjacent nS and nD states that are only tens of GHz away. One way to achieve this is by introducing another $973\,\mathrm{nm}$ light source to couple these contaminants to the $5P$ states. However, while this method

allows atoms to re-enter the system, it has a drawback: the reintroduced atoms may decay into random ground states, potentially leading to errors in spin detection.

All of the suggestions above are technically feasible. Notably, the stroboscopic approach stands out as it can be implemented in the experimental sequence without necessitating any changes to the current setup, providing a swift solution with minimal adjustments.

In this chapter, we have introduced different types of Rydberg interactions, explored the technique of Rydberg dressing, discussed potential applications in quantum technology, and highlighted the technical constraints inherent to our experiment. We investigated and analyzed the experimentally observed Rydberg dressed lifetime, identifying the excitation laser phase noise as a key contributor to the reduced lifetime. We also proposed several strategies to address these challenges, such as spectrally filtering the light using an optical cavity. Additionally, we investigated the dynamics of Ising-type interactions and discussed the sources of decoherence within the system. This led us to another significant source of decoherence, specifically, black-body-induced losses in the experiment, which we discussed within the context of Rydberg dressing. Addressing this effect necessitates the implementation of the strategies we discussed. Above all is the technique of stroboscopic dressing, which can be seamlessly integrated into the experimental sequence. Overall, there's optimism that these challenges will be improved in the near future.

Chapter 5

Tailoring spatially tunable spin interactions via two-color Rydberg dressing

Programmable quantum systems based on cold atoms provide a powerful tool for quantum simulators of many-body physics. While various realizations of cold atom-based spin-Hamiltonian have already been demonstrated, [66, 109, 170, 201–203], the most significant challenge remains to increase the system's flexibility via universally programmable analog qubit couplings.

In this chapter, we demonstrate the realization of freely tunable short-range XYZ-type spin interactions between atoms trapped in optical tweezer arrays and engineer spin-spin couplings by two-color Rydberg dressing, where the interaction strength and sign in each spin direction can be tuned with a corresponding choice of laser parameters. Our approach relies on the proposal of A. Glaetzle et al. [4]. Here, we encode the effective spin-1/2 system in two distinctive hyperfine manifolds within the electronic ground state and induce interactions depending on the spatially dependent van-der-Waals (vdW) interactions between different m_j hyperfine sublevels in the Rydberg part state manifold.

In Section 5.1, we provide the derivation of the interaction Hamiltonian. We then describe the experimental parameters required to engineer these interactions and discuss the necessary calibration measurements in Section 5.2. In Section 5.3, we present the experimental results for the interactions for two different sets of laser parameters, and we discuss the technical limitations of our implementation in Section 5.4.

This chapter is based on our publication [62]. Our results pave the way toward realizing universally programmable analog qubit couplings in programmable quantum systems based on cold atoms.

5.1 Derivation of the interaction Hamiltonian

The Heisenberg model is a quantum-mechanical approach to describe magnetism, which serves as an exemplary model for a host of emergent phenomena such as frustrated quantum magnetism, spin-class physics, and exotic states of matter like topologically, ordered quantum spin liquids [1, 204]. These examples aim to study the asymptotic properties of the model,

specifically the ground state or state with the lowest energy [2, 139]. The anisotropic Heisenberg Hamiltonian, also known as XYZ-Hamiltonian, can be written as

$$\hat{H}_{\mathrm{XYZ}} = \hbar \sum_{i,j} [J_{ij}^{x} \hat{\sigma}_i^{x} \hat{\sigma}_j^{x} + J_{ij}^{y} \hat{\sigma}_i^{y} \hat{\sigma}_j^{y} + J_{ij}^{z} \hat{\sigma}_i^{z} \hat{\sigma}_j^{z}] \,. \tag{5.1}$$

Here, $\hat{\sigma}^x$, $\hat{\sigma}^y$ and $\hat{\sigma}^z$ are the Pauli matrices describing the localized spin-1/2 particles at position j in a lattice, and $\{J_{ij}^x, J_{ij}^y, J_{ij}^z\}$ are the directional spin-exchange couplings. We can replace the Pauli matrices with the raising and lowering operators $\hat{\sigma}^+$, $\hat{\sigma}^-$ using

$$\begin{aligned} \hat{\sigma}_i^x &= \hat{\sigma}_i^+ + \hat{\sigma}_i^- \\ \hat{\sigma}_i^y &= \hat{\sigma}_i^+ - \hat{\sigma}_i^- . \end{aligned} \tag{5.2}$$

This allows us to write the Hamiltonian in Eq. (5.1) as

$$\hat{H} = \hbar \sum_{i,j} [J_{ij}^{+-} (\hat{\sigma}_i^+ \hat{\sigma}_j^- + \hat{\sigma}_i^- \hat{\sigma}_j^+) + J_{ij}^{++} (\hat{\sigma}_i^+ \hat{\sigma}_j^+ + \hat{\sigma}_i^- \hat{\sigma}_j^-) + J_{ij}^{z} \hat{\sigma}_i^{z} \hat{\sigma}_j^{z}] \tag{5.3}$$

where we used $J_{ij}^{+-} = J_{ij}^x + J_{ij}^y$ and $J_{ij}^{++} = J_{ij}^x - J_{ij}^y$. This formalism differentiates between three kinds of spin couplings J_{ij}^{γ}:

- The diagonal interaction between pairs of dressed ground states J_{ij}^z,
- The off-diagonal "flop-flop" interaction J_{ij}^{++} , which flips the sign of pairs of parallel spins, and
- The off-diagonal "flip-flop" interaction J_{ij}^{+-}, which acts between pairs of anti-parallel spins.

While dressing-induced Ising interactions J_{ij}^z have already been investigated in various experiments [56, 57, 99, 107, 130, 137, 205] and programmable long-range interactions have been shown in optical cavities [206], we focus on programmable J_{ij}^{++} and J_{ij}^{+-} interactions. Please note that in Section 4.6, we also studied the Ising-type interactions.

We now want to derive the spin-spin interactions in Eq. (5.3) and start by introducing a general model for two atoms with distinguishable positions within a tweezer array. We encode the spin-1/2 in two hyperfine ground states and assume that in a typical experiment, all atoms are initialized in one of them

$$\begin{aligned} |\uparrow\rangle &= |4S_{1/2}\rangle \, |F = 2,\, m_F = -2\rangle \\ &= |4S_{1/2}\rangle \, |m_j = -1/2\rangle \, |m_I = -3/2\rangle \\ |\downarrow\rangle &= |4S_{1/2}\rangle \, |F = 1,\, m_F = -1\rangle \\ &= |4S_{1/2}\rangle \left(|m_j = 1/2\rangle \, |m_I = -3/2\rangle - \sqrt{3} \, |m_j = -1/2\rangle \, |m_I = -1/2\rangle \right) /2. \end{aligned} \tag{5.4}$$

where m_I is the projection quantum number of the nuclear spin. The interactions between the ground states are introduced by two-color Rydberg dressing, where both states are individually coupled to neighboring Rydberg states

$$\begin{aligned} |r_\uparrow\rangle &= |62P_{3/2},\, m_j = -3/2\rangle \otimes |m_I = -3/2\rangle \\ |r_\downarrow\rangle &= |62P_{3/2},\, m_j = -1/2\rangle \otimes |m_I = -3/2\rangle \end{aligned} \tag{5.5}$$

Note that, in the case of $|\downarrow\rangle$, the coupling strength is reduced by the respective Clebsch-Gordon coefficient $1/2$ (see $m_I = -3/2$ contribution). To introduce interactions between the ground-state spins, we make use of a technique called Rydberg dressing, which was already presented in Section 4.2. In this technique, we use detuned couplings to the Rydberg states. The off-resonant coupling admixes the strong Rydberg-Rydberg van-der-Waals (vdW) interactions to the ground states and induces effective spin-spin interactions. The resulting Hamiltonian describing the interacting two-atom system can be written in the rotating-wave approximation [4, 46].

$$\hat{H}_{\text{two}} = \hat{H}_{\text{las}} + \hat{H}_{\text{int}} \tag{5.6}$$

consisting of the Rydberg pair interaction operator $\hat{H}_{\text{int}}$ and the Hamiltonian containing the laser coupling and energies of the unperturbed Rydberg states $\hat{H}_{\text{las}}$, which reads as

$$\begin{aligned} \hat{H}_{\text{las}}/\hbar = \sum_{i=1}^{2} \Big[&\Omega^{\uparrow}(|\uparrow\rangle\langle r^{\uparrow}|_i + |r^{\uparrow}\rangle\langle\uparrow|_i)/2 + \Omega^{\downarrow}(|\downarrow\rangle\langle r^{\downarrow}|_i + |r^{\downarrow}\rangle\langle\downarrow|_i)/2 \\ &- \Delta^{\uparrow}|r^{\uparrow}\rangle\langle r^{\uparrow}|_i - \Delta^{\downarrow}|r^{\downarrow}\rangle\langle r^{\downarrow}|_i \Big] . \end{aligned} \tag{5.7}$$

Here, the Rabi frequency Ω^{σ} determines the coupling strength between a ground state $|\sigma\rangle_i$ and a Rydberg state $|r^{\sigma}\rangle_i$ of one atom i, with $\sigma \in \{\uparrow, \downarrow\}$. The single atom detunings are described by Δ^{σ}. By choosing the appropriate laser polarizations and states, the dipole matrix elements between $|\uparrow\rangle_i$ and $|r^{\downarrow}\rangle_i$ and vice versa vanish, resulting in the absence of the single-atom Raman transitions.

The pair interaction Hamiltonian $\hat{H}_{\text{int}}$ describes the dipolar interactions between two Rydberg states. For the calculation, we use the PAIRINTERACTION software package [105], which numerically diagonalizes the interaction Hamiltonian to obtain the pair-separation d and -angle θ dependent eigenstates $|\Psi_{\alpha}^{(2)}\rangle$ with eigenenergies $E_{\alpha}(d, \theta)$. To make the diagonalization computationally practicable, the pair interaction software implemented restrictions reducing the basis of the matrix to states that particularly affect the interaction potentials. However, the constraints must be tested before each calculation as it depends on the selected quantum numbers, external fields, and many more. There are three possible constraints: Restricting the basis to states with similar energy (ΔE), limiting the size of momentum quantum numbers ($\Delta \ell$) and principal quantum numbers (Δn). For optimization, one usually starts with strong constraints and opens them up until the pair potentials

at the desired pair separation distance converge. In our case, we calculated the pair potentials at a pair distance of $4\,\mu\mathrm{m}$ and concluded to restrict the energy surroundings to $\Delta E_{\mathrm{atom}} = \pm 50\,\mathrm{GHz}$ around single atoms and $\Delta E_{\mathrm{pair}} = \pm 35\,\mathrm{GHz}$ for pairs of atoms and limited the involved momentum quantum number to $\Delta\ell = \pm 1$ and principal quantum number to $\Delta n = \pm 2$ (see alsoe Appendix B.1). After the diagonalization, the obtained eigenstates can be expressed in asymptotic pair states $|r^m r^n\rangle$ of m, n different Rydberg states as

$$|\Psi_\alpha^{(2)}\rangle = \sum_{m,n} c_\alpha^{mn}(d,\theta)|r^m r^n\rangle \tag{5.8}$$

with the distance- and angle-dependend admixture $c_\alpha^{mn}(d,\theta) = \langle\Psi_\alpha^{(2)}(d,\theta)|r^m r^n\rangle$. To improve the readability, we drop out the explicit d,θ-dependency in the followed derivation.

The dipolar interactions between any pair of Rydberg states $|r^m r^n\rangle$, where the pair of atoms is oriented perpendicular to the quantization axis, can be written in the pair basis $\{|r^m r^m\rangle, |r^m r^n\rangle, |r^n r^m\rangle, |r^n r^n\rangle\}$ in the form

$$\hat{H}_{\mathrm{int}} = \begin{array}{c} \\ |r^m r^m\rangle \\ |r^m r^n\rangle \\ |r^n r^m\rangle \\ |r^n r^n\rangle \end{array} \begin{array}{c} \begin{array}{cccc} \langle r^m r^m| & \langle r^m r^n| & \langle r^n r^m| & \langle r^n r^n| \end{array} \\ \begin{pmatrix} V^{mm,mm} & 0 & 0 & V^{mm,nn} \\ 0 & V^{mn,mn} & V^{mn,nm} & 0 \\ 0 & V^{nm,mn} & V^{nm,nm} & 0 \\ V^{nn,mm} & 0 & 0 & V^{nn,nn} \end{pmatrix} \end{array}. \tag{5.9}$$

In order to transfer the interactions to the dressed ground states, we adiabatically eliminate the Rydberg states, which is equivalent to the fourth-order perturbation theory as done in [4]. In the following sections, we will derive the concrete terms of the effective interactions, which add up in the effective Hamiltonian $\hat{H}_{\mathrm{eff}}$ in the $\{|\uparrow\uparrow\rangle, |\uparrow\downarrow\rangle, |\downarrow\uparrow\rangle, |\downarrow\downarrow\rangle\}$ basis:

$$\hat{H}_{\mathrm{eff}} = \begin{array}{c} \\ |\uparrow\uparrow\rangle \\ |\uparrow\downarrow\rangle \\ |\downarrow\uparrow\rangle \\ |\downarrow\downarrow\rangle \end{array} \begin{array}{c} \begin{array}{cccc} \langle\uparrow\uparrow| & \langle\uparrow\downarrow| & \langle\downarrow\uparrow| & \langle\downarrow\downarrow| \end{array} \\ \begin{pmatrix} W^{\uparrow\uparrow,\uparrow\uparrow} & 0 & 0 & W^{\uparrow\uparrow,\downarrow\downarrow} \\ 0 & W^{\uparrow\downarrow,\uparrow\downarrow} & W^{\uparrow\downarrow,\downarrow\uparrow} & 0 \\ 0 & W^{\downarrow\uparrow,\uparrow\downarrow} & W^{\downarrow\uparrow,\downarrow\uparrow} & 0 \\ W^{\downarrow\downarrow,\uparrow\uparrow} & 0 & 0 & W^{\downarrow\downarrow,\downarrow\downarrow} \end{pmatrix} \end{array}. \tag{5.10}$$

We can now compare the obtained effective Hamiltonian with Eq. (5.3) when expanding the latter on a ground state pair basis and identify the following interaction terms:

$$\begin{aligned} J_{ij}^{z} &= \frac{1}{4}\left(W^{\uparrow\uparrow,\uparrow\uparrow}(d_{ij},\theta_{ij}) + W^{\downarrow\downarrow,\downarrow\downarrow}(d_{ij},\theta_{ij}) - 2W^{\uparrow\downarrow,\uparrow\downarrow}(d_{ij},\theta_{ij})\right) \\ J_{ij}^{+-} &= \frac{1}{2}\left(W^{\uparrow\downarrow,\downarrow\uparrow}(d_{ij},\theta_{ij}) + W^{\downarrow\uparrow,\uparrow\downarrow}(d_{ij},\theta_{ij})\right) = W^{\uparrow\downarrow,\downarrow\uparrow}(d_{ij},\theta_{ij}) \\ J_{ij}^{++} &= \frac{1}{2}\left(W^{\uparrow\uparrow,\downarrow\downarrow}(d_{ij},\theta_{ij}) + W^{\downarrow\downarrow,\uparrow\uparrow}(d_{ij},\theta_{ij})\right) = W^{\uparrow\uparrow,\downarrow\downarrow}(d_{ij},\theta_{ij}) \end{aligned} \tag{5.11}$$

where we use $W^{\uparrow\downarrow,\uparrow\downarrow} = W^{\downarrow\uparrow,\downarrow\uparrow}$, $W^{\downarrow\uparrow,\uparrow\downarrow} = W^{\uparrow\downarrow,\downarrow\uparrow}$, and $W^{\uparrow\uparrow,\downarrow\downarrow} = W^{\downarrow\downarrow,\uparrow\uparrow}$ and restored the pair-separation and -angle dependence for clarity reasons. Finally, we obtained the spin-spin couplings depending on the dressing-induced effective couplings W from Eq. (5.10). In the following subsections, we will describe an intuitive picture for deriving those. As illustrated in Fig. 5.1, our derivation is based on a two-step adiabatic elimination of the Rydberg levels, starting with the singly-excited states. After this first step, we obtain an effective Λ system. In the second step, we eliminate the doubly-excited states and obtain the abovementioned spin couplings. This procedure is illustrated in Fig. 5.1, where we assume that there are only four relevant (i. e. near-resonantly) laser-coupled asymptotic pair states $\{|r^{\uparrow}r^{\uparrow}\rangle, |r^{\uparrow}r^{\downarrow}\rangle, |r^{\downarrow}r^{\uparrow}\rangle, |r^{\downarrow}r^{\downarrow}\rangle\}$.

5.1.1 The diagonal coupling terms for Ising-type interactions

In the following, we will present two approaches for deriving $W^{\sigma\sigma,\sigma\sigma}$, resulting in the same interaction potential. Both are based on the perturbative treatment of the Hamiltonian in Eq. (5.6), with the laser coupling part as a perturbation.

In the first approach, we perform a perturbative treatment up to the fourth order, as done in in references [104, 157, 158]. The system contains the ground state $|\sigma\sigma\rangle$, the intermediate state $|+^{\sigma}\rangle = (|\sigma r^{\sigma}\rangle + |r^{\sigma}\sigma\rangle)/\sqrt{2}$, and Rydberg manifold $|\Psi_{\alpha}^{(2)}\rangle(d,\theta)$. We assume that all atoms are initialized in $|\sigma\sigma\rangle$ at the beginning of the experiment. Note that the anti-symmetric dark state $|-^{\sigma}\rangle = (|\sigma r^{\sigma}\rangle - |r^{\sigma}\sigma\rangle)/\sqrt{2}$ is not coupled and is therefore ignored in the following approach. We again omit the distance and angle dependence of the Rydberg manifold for better readability. As described in Eq. (5.7), in the rotating frame, we couple the states via the dipole matrix elements

$$\begin{aligned} \langle\sigma\sigma|\hat{H}_{\text{las}}|+^{\sigma}\rangle &= \langle\sigma\sigma|\hat{H}_{\text{las}}(|\sigma r^{\sigma}\rangle + |r^{\sigma}\sigma\rangle)/\sqrt{2} = (2\hbar\Omega^{\sigma}/2/\sqrt{2}) = \hbar\Omega^{\sigma}/\sqrt{2} \\ \langle+^{\sigma}|\hat{H}_{\text{las}}|\Psi_{\alpha}^{(2)}\rangle &= 1/\sqrt{2}(\langle\sigma r^{\sigma}| + \langle r^{\sigma}\sigma|)\hat{H}_{\text{las}}|\Psi_{\alpha}^{(2)}\rangle = c_{\alpha}^{\sigma\sigma}\hbar\Omega^{\sigma}/\sqrt{2}, \end{aligned} \tag{5.12}$$

where the latter contains the state-dependent admixture $c_{\alpha}^{\sigma\sigma} = \langle\Psi_{\alpha}^{(2)}|r^{\sigma}r^{\sigma}\rangle$ of $|r^{\sigma}r^{\sigma}\rangle$ in close-by interacting pairstates $|\Psi_{\alpha}^{(2)}\rangle$, which reduces the Rabi coupling. In addition, we define the eigenenergies for the system as

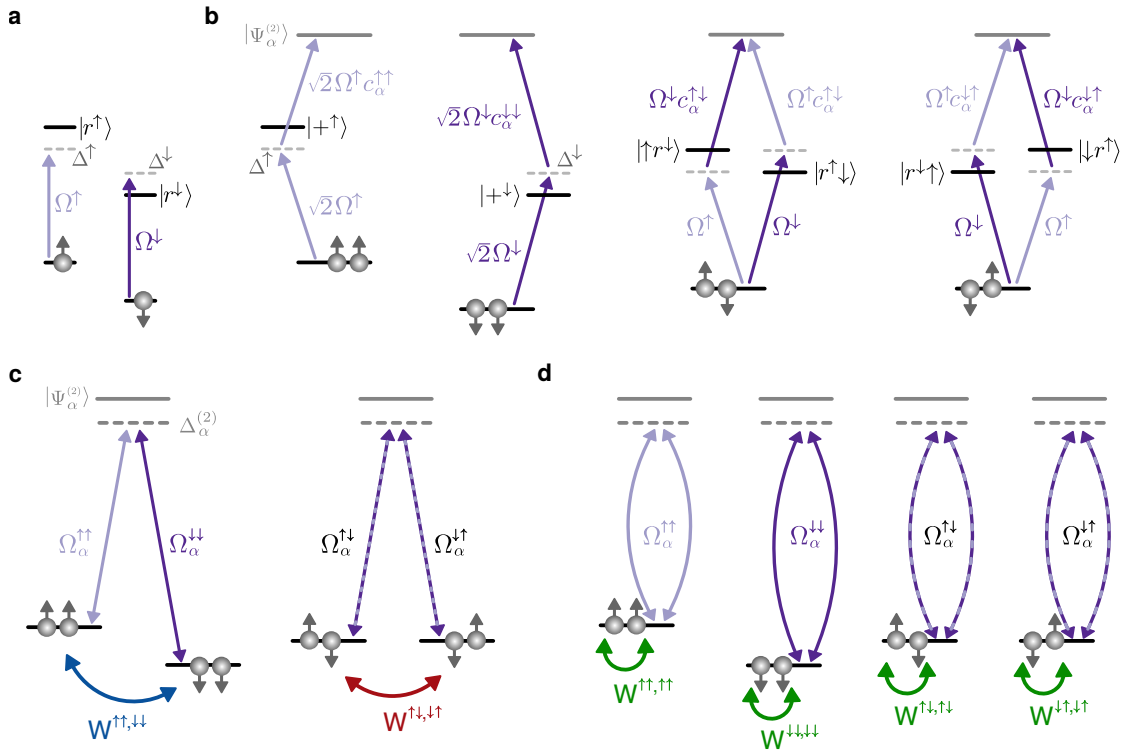

Figure 5.1 Step-by-step adiabatic elimination of excited states. a. Single atom excitation scheme. The spins $|\uparrow\rangle$, $|\downarrow\rangle$ are encoded in electronic ground states and coupled with Rabi frequencies ($\Omega^{\uparrow}$, $\Omega^{\downarrow}$) and detunings ($\Delta^{\uparrow}$, $\Delta^{\downarrow}$) to different Rydberg states $|r^{\uparrow}\rangle$, $|r^{\downarrow}\rangle$. **b.** Elimination of singly excited Rydberg states. Shown are the level schemes for different ground state spin-pair configurations ($|\uparrow\uparrow\rangle$, $|\downarrow\downarrow\rangle$, $|\uparrow\downarrow\rangle$, $|\downarrow\uparrow\rangle$), which are coupled to the Rydberg manifold. By adiabatic elimination of the singly excited states, we reduce the two photon excitation scheme to obtain effective pair state couplings $\Omega_\alpha^{\sigma\sigma'}$ to the eigenstates of the dipolar interaction Hamiltonian $|\Psi_\alpha^{(2)}\rangle$. **c, d.** Elimination of doubly excited states (Rydberg manifold). After the first adiabatic elimination of the singly excited states, we obtain an effective Λ-system. In a next step, we eliminate the doubly exited states $|\Psi_\alpha^{(2)}\rangle$ and end up with an effective ground state coupling for unequal initial and final states $W^{\uparrow\uparrow,\downarrow\downarrow}$, $W^{\downarrow\uparrow,\uparrow\downarrow}$ or an induced light shift for equal intial and final states $W^{\uparrow\uparrow,\uparrow\uparrow}$, $W^{\downarrow\downarrow,\downarrow\downarrow}$, $W^{\uparrow\downarrow,\uparrow\downarrow}$, and $W^{\downarrow\uparrow,\uparrow\downarrow}$. Figure adapted from [62].

$$\begin{aligned}\langle\sigma\sigma|\hat{H}_{\text{two}}|\sigma\sigma\rangle &= 0\\ \langle+^{\sigma}|\hat{H}_{\text{two}}|+^{\sigma}\rangle &= 1/2(\langle\sigma r^{\sigma}| + \langle r^{\sigma}\sigma|)\hat{H}_{\text{two}}(|\sigma r^{\sigma}\rangle + |r^{\sigma}\sigma\rangle) = \Delta^{\sigma}\\ \langle\Psi_\alpha^{(2)}|\hat{H}_{\text{two}}|\Psi_\alpha^{(2)}\rangle &= \Delta_\alpha^{(2)} = 2\Delta^{\sigma} + E_\alpha\end{aligned} \tag{5.13}$$

where E_α is the interaction-induced energy shift. With this equation, we can directly see that for an atom pair with large separation, the interaction vanishes, and the atoms can be treated as single atoms with an eigenenergy $2\Delta^{\sigma}$.

The different orders (k^{th}) of the perturbation series express the effect of exactly k virtual processes of the perturbation operator. As we have already discussed in Section 4.2, all odd orders cancel out, as one requires one relaxation process for every excitation step to end up in the ground state again [104].

The correction energy terms to the ground state up to the fourth order are

$$\begin{aligned} u_{(2)}^{\sigma\sigma} =& \frac{|\langle\sigma\sigma|\hat{H}_{\text{las}}|+^{\sigma}\rangle|^2}{\langle+^{\sigma}|\hat{H}_{\text{las}}|+^{\sigma}\rangle} = \frac{(\Omega^{\sigma})^2}{2\Delta^{\sigma}} \\ u_{(4)}^{\sigma\sigma} =& \sum_{\alpha}\left(\frac{|\langle\sigma\sigma|\hat{H}_{\text{las}}|+^{\sigma}\rangle\langle+^{\sigma}|\hat{H}_{\text{las}}|\Psi_{\alpha}^{(2)}\rangle|^2}{(\langle+^{\sigma}|\hat{H}_{\text{las}}|+^{\sigma}\rangle)^2\langle\Psi_{\alpha}^{(2)}|\hat{H}_{\text{las}}|\Psi_{\alpha}^{(2)}\rangle} - u_{(2)}^{\sigma\sigma}\frac{|\langle\sigma\sigma|\hat{H}_{\text{las}}|+^{\sigma}\rangle|^2}{(\langle+^{\sigma}|\hat{H}_{\text{las}}|+^{\sigma}\rangle)^2} - \mathcal{O}(u_{(1)}^{\sigma\sigma})\right) \\ =& \sum_{\alpha}\frac{(\Omega^{\sigma})^4\cdot(c_{\alpha}^{\sigma\sigma})^2}{4(\Delta^{\sigma})^2\cdot\Delta_{\alpha}^{(2)}} - \frac{(\Omega^{\sigma})^4}{4(\Delta^{\sigma})^3}\,. \end{aligned} \tag{5.14}$$

The second-order processes only account for a single excitation in the system and hence do not contain any interaction term. Instead, we obtain a constant offset term, also known as AC Stark shift, which distinguishes between a dressed and not dressed single atom. In contrast, in the fourth-order correction, we treat the excitation of two atoms and obtain pair-distance dependent terms besides the constant offsets. The corrections then sum up

$$\tilde{U}^{\sigma\sigma,\sigma\sigma} = u_{(2)}^{\sigma\sigma} + u_{(4)}^{\sigma\sigma} = \frac{(\Omega^{\sigma})^2}{2\Delta^{\sigma}} - \frac{(\Omega^{\sigma})^4}{4(\Delta^{\sigma})^3} + \sum_{\alpha}\left(\frac{(\Omega^{\sigma})^4 c_{\alpha}^{\sigma\sigma})^2}{4(\Delta^{\sigma})^2\Delta_{\alpha}^{(2)}}\right)\,. \tag{5.15}$$

Given that the interaction time scales are significantly shorter than the motion of the atoms within the tight tweezers, we assume that constant offset terms are irrelevant in our case. Thus, we subtract the asymptotic value, which is equivalent to the first and second order AC-Stark induced potentials [104, 107]

$$\tilde{U}^{\sigma\sigma,\sigma\sigma}(d_{mn}\to\infty) = \frac{(\Omega^{\sigma})^2}{2\Delta^{\sigma}} - \frac{(\Omega^{\sigma})^4}{4(\Delta^{\sigma})^3} + \frac{(\Omega^{\sigma})^4}{8(\Delta^{\sigma})^3}\,. \tag{5.16}$$

Note, that here we used the energy shift of the asymptotic Rydberg pair states $\Delta_{\alpha}^{(2)}(d_{mn}\to\infty) = 2\Delta^{\sigma}$. Subtracting Eq. (5.16) from Eq. (5.15) we end up with the interaction potential:

$$W^{\sigma\sigma,\sigma\sigma} = \frac{(\Omega^{\sigma})^4}{4(\Delta^{\sigma})^2}\sum_{\alpha}\left(\frac{(c_{\alpha}^{\sigma\sigma})^2}{\Delta_{\alpha}^{(2)}} - \frac{1}{2\Delta^{\sigma}}\right)\,. \tag{5.17}$$

The second option to derive the $W^{\sigma\sigma,\sigma\sigma}$ interaction potential consists of two consecutive steps of adiabatic elimination: We start with adiabatic elimination of the single excited state

$|+^\sigma\rangle$ to obtain an effective Λ-scheme consisting of the ground state $|\sigma\sigma\rangle$ and the Rydberg manifold as shown in Fig. 5.1 (the Λ-scheme will be more obvious when deriving the flop-flop and flip-flop terms in the next sections), coupled via the effective two-photon Rabi couplings, which now depend on the atom-pair distance $\Omega_\alpha^{\sigma\sigma}$: For large distances, we obtain the effective two-photon Rabi couplings $\Omega_{eff}^{\sigma\sigma}/2 = (\Omega^\sigma)^2/2\Delta^\sigma$. At short distances, the pair potentials in the m_j-subspace of the $62P_{3/2}$ manifold interact with each other via dipole-quadrupole interaction, which leads to avoided crossings and mixing of Rydberg states [207]. The corresponding admixture $c_\alpha^{\sigma\sigma} = \langle\Psi_\alpha^{(2)}|r^\sigma r^\sigma\rangle$ of $|r^\sigma r^\sigma\rangle$ in close-by interacting pairstates $|\Psi_\alpha^{(2)}\rangle$ reduces the effective Rabi frequencies to $\Omega_\alpha^{\sigma\sigma} = \Omega_{\text{eff}}^{\sigma\sigma} \cdot c_\alpha^{\sigma\sigma}$.

After this first step of adiabatic elimination of the singly excited states, we transform the light-atom Hamiltonian in Eq. (5.7) to a two-atom basis:

$$\begin{aligned}\hat{H}_{\text{las},2}/\hbar = \sum_\alpha \Big[&\Omega_\alpha^{\sigma\sigma}/2 \left(|\sigma\sigma\rangle\langle\Psi_\alpha^{(2)}| + |\Psi_\alpha^{(2)}\rangle\langle\sigma\sigma|\right) \\ &+ \Omega_\alpha^{\sigma\bar{\sigma}}/2 \left(|\sigma\bar{\sigma}\rangle\langle\Psi_\alpha^{(2)}| + |\Psi_\alpha^{(2)}\rangle\langle\sigma\bar{\sigma}|\right) + \Delta_\alpha^{(2)}|\Psi_\alpha^{(2)}\rangle\langle\Psi_\alpha^{(2)}|\Big] \,.\end{aligned} \tag{5.18}$$

In a second step, we then adiabatically eliminate the Rydberg states up to the second order (similar as done in Eq. (5.14)) and obtain

$$U^{\sigma\sigma,\sigma\sigma} = \sum_\alpha \frac{|\langle\sigma\sigma|\hat{H}_{\text{las},2}|\Psi_\alpha^{(2)}\rangle|^2}{\langle\Psi_\alpha^{(2)}|\hat{H}_{\text{las},2}|\Psi_\alpha^{(2)}\rangle} = \sum_\alpha \frac{(\Omega_\alpha^{\sigma\sigma})^2}{4\Delta_\alpha^{(2)}} = \sum_\alpha \frac{(\Omega^\sigma)^4 (c_\alpha^{\sigma\sigma})^2}{4(\Delta^\sigma)^2\Delta_\alpha^{(2)}} \tag{5.19}$$

with the two-photon detuning from the corresponding Rydberg pairstate $\Delta_\alpha^{(2)}$ is as shown in Fig. 5.1. Similar to the first derivation, we evaluate the asymptotic value, which is in this case

$$U^{\sigma\sigma,\sigma\sigma}(d_{mn} \to \infty) = \frac{(\Omega^\sigma)^4}{8(\Delta^\sigma)^3} \tag{5.20}$$

and substract this term to obtain the interaction potential identical to Eq. (5.17).

The derivation of the diagonal interactions of an anti-symmetric pair $W^{\sigma\bar{\sigma},\sigma\bar{\sigma}}$ (with $\sigma \neq \bar{\sigma}$) is similar: As shown in Fig. 5.1 there are two excitation paths from $|\sigma\bar{\sigma}\rangle$ to $|\Psi_\alpha^{(2)}\rangle$, via the intermediate states $|\sigma r^{\bar{\sigma}}\rangle$ and $|\bar{\sigma} r^\sigma\rangle$. Eliminating all singly excited states, we obtain the effective two-photon coupling $\Omega_\alpha^{\sigma\bar{\sigma}}/2 = \Omega^\sigma\Omega^{\bar{\sigma}} c_\alpha^{\sigma\bar{\sigma}} \cdot (1/4\Delta^\sigma + 1/4\Delta^{\bar{\sigma}})$. Same as before, we then in a second step adiabatically eliminate $|\Psi_\alpha^{(2)}\rangle$ and obtain

$$U^{\sigma\bar{\sigma},\sigma\bar{\sigma}} = \sum_\alpha \frac{(\Omega^\sigma)^2(\Omega^{\bar{\sigma}})^2(c_\alpha^{\sigma\bar{\sigma}})^2}{16\Delta_\alpha^{(2)}} \left(\frac{1}{(\Delta^\sigma)^2} + \frac{1}{(\Delta^{\bar{\sigma}})^2} + \frac{1}{\Delta^\sigma\Delta^{\bar{\sigma}}}\right) \tag{5.21}$$

and remove a constant offset by subtracting the $d \to \infty$ asymptotic value to obtain the last term in the Ising interaction in Eq. (5.11)

$$W^{\sigma\bar{\sigma},\sigma\bar{\sigma}} = \left(\frac{1}{(\Delta^{\sigma})^2} + \frac{1}{(\Delta^{\bar{\sigma}})^2} + \frac{1}{\Delta^{\sigma}\Delta^{\bar{\sigma}}}\right) \frac{(\Omega^{\sigma})^2(\Omega^{\bar{\sigma}})^2}{16} \times \sum_{\alpha} \left(\frac{(c_{\alpha}^{\sigma\bar{\sigma}})^2}{\Delta_{\alpha}^{(2)}} - \frac{1}{2\Delta^{\sigma}} - \frac{1}{2\Delta^{\bar{\sigma}}}\right) . \tag{5.22}$$

Finally, we obtain terms for the Ising interaction via step-by-step adiabatic elimination of the excited states. Note that the asymptotic value of this derivation corresponds solely to the second-order light shift for two atoms. In contrast, the light shift of single atoms is bypassed in this approach.

5.1.2 The off-diagonal terms for flop-flop interactions

The flop-flop coupling terms $W^{\sigma\sigma,\bar{\sigma}\bar{\sigma}}$ between the two ground states $|\uparrow\uparrow\rangle$ and $|\downarrow\downarrow\rangle$ are derived analogously. The energy required to bridge the ground state splitting between $|\uparrow\rangle$ and $|\downarrow\rangle$ is provided by the two-color excitation photons. In the rotating wave approximation, we obtain two intermediate states for each excitation leg $|+^{\sigma}\rangle$, as shown in Fig. 5.1. As before, the derivation is split into two parts: After the adiabatic elimination of these singly excited states, we obtain the effective two-photon Rabi couplings $\Omega_{\alpha}^{\sigma\sigma} = \Omega_{\text{eff}}^{\sigma\sigma} \cdot c_{\alpha}^{\sigma\sigma}$ with the couplings $\Omega_{\text{eff}}^{\sigma\sigma}$ as described in Section 5.1.1. An example of the distance and angular dependent Rydberg manifold is shown in Fig. 5.2, where we used the PAIR INTERACTION software [105] to calculate the Rydberg pair potentials fixing one degree of freedom (pair distance or angle). The calculations are done for a magnetic offset field of 1 G defining the quantization axis.

In a second step, we adiabatically eliminate the Rydberg pair states and obtain the flop-flop coupling term:

$$\begin{aligned} W^{\sigma\sigma,\bar{\sigma}\bar{\sigma}} &= \sum_{\alpha} \frac{\langle\sigma\sigma|\hat{H}_{\text{las}}|\Psi_{\alpha}^{(2)}\rangle\langle\Psi_{\alpha}^{(2)}|\hat{H}_{\text{las}}|\bar{\sigma}\bar{\sigma}\rangle}{\langle\Psi_{\alpha}^{(2)}|\hat{H}_{\text{las}}|\Psi_{\alpha}^{(2)}\rangle} \\ &= \sum_{\alpha} \frac{\Omega_{\alpha}^{\sigma\sigma}\Omega_{\alpha}^{\bar{\sigma}\bar{\sigma}}}{\Delta_{\alpha}^{(2)}} \\ &= \sum_{\alpha} \frac{(\Omega^{\sigma}\Omega^{\bar{\sigma}})^2}{4\Delta^{\sigma}\Delta^{\bar{\sigma}}} \cdot \frac{c_{\alpha}^{\sigma\sigma}c_{\alpha}^{\bar{\sigma}\bar{\sigma}}}{\Delta_{\alpha}^{(2)}} \end{aligned} \tag{5.23}$$

The absence of offsets at large distances for off-diagonal terms arises from the fact that two different asymptotic pair state overlaps are involved, and one of them must vanish asymptotically. Specifically, the two-color excitation laser beams need to be detuned from each other by a frequency that matches the energy difference between the initial and

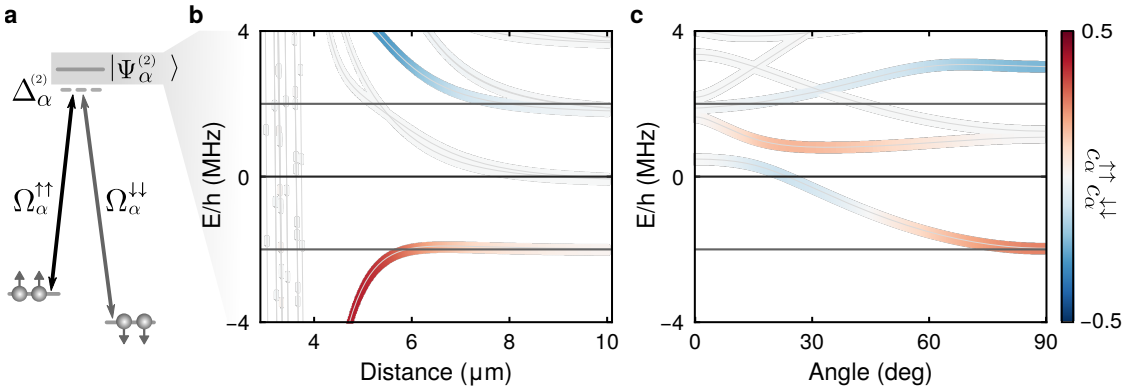

Figure 5.2 Rydberg manifold for different pair distances and angles. a. Schematic for the flop-flop interaction J_{ij}^{++} between two atoms i and j. Via adiabatic elimination of the singly excited pair states, we reduce the four-photon process to an effective Λ-scheme. The pairs of ground state atoms are coupled with the effective Rabi couplings ($\Omega_\alpha^{\uparrow\uparrow}$, $\Omega_\alpha^{\downarrow\downarrow}$) to Rydberg pair states $|\Psi_\alpha^{(2)}\rangle$. $\Delta_\alpha^{(2)}$ is the two-photon detuning to each $|\Psi_\alpha^{(2)}\rangle$, which includes interaction induced shifts. **b, c.** Calculated eigenenergies of $\hat{H}_{\text{Ryd}}$ depending on the atom pair distance d at an angle of $\theta = 90\,^\circ$ (b.) and atom pair angle θ at a distance $d = 6\,\mu\text{m}$ (c.). The color scale corresponds to the overlap $c_\alpha^{\uparrow\uparrow} c_\alpha^{\downarrow\downarrow}$. The solid lines at $\pm 2\,\text{MHz}$ mark the energy of the asymptotic Rydberg pair state ($|r_\downarrow r_\downarrow\rangle$, $|r_\uparrow r_\uparrow\rangle$). The theoretical results are obtained by exact diagonalization of H_{Ryd} using the PAIRINTERACTION software package [105]. Figures taken from [62].

final states such that energy conservation is fulfilled. The laser detunings must be set to $\Delta^\uparrow - \Delta^\downarrow = E_z$, where E_z is the Zeeman splitting between $|r^\uparrow\rangle$ and $|r^\downarrow\rangle$. This condition ensures the maximal transfer of population between the two ground states.

5.1.3 The off-diagonal terms for flip-flop interactions

We use the same procedure as before to derivate the flip-flop interaction term $W^{\sigma\bar{\sigma},\bar{\sigma}\sigma}$. The virtual four-photon process is split into two parts: Once again, we adiabatically eliminate the single excited states $|r^\sigma \bar{\sigma}\rangle$ and obtain the reduced two-photon Rabi couplings $\Omega_\alpha^{\sigma\bar{\sigma}} = (\Omega^\sigma \Omega^{\bar{\sigma}}/4\Delta^\sigma + \Omega^\sigma \Omega^{\bar{\sigma}}/4\Delta^{\bar{\sigma}}) \cdot c_\alpha^{\sigma\bar{\sigma}}$. Here, we recognize that the effective two-photon coupling vanishes when the detunings are set to equal magnitude but opposite sign. This can be understood as destructive interference of the two excitation paths. In the experimental realization, later, we can cancel the flip-flop interaction by a corresponding set of laser detunings (see Section 5.3.1).

Via adiabatic elimination of the Rydberg manifold, we obtain the flip-flop coupling term:

$$\begin{aligned} W^{\sigma\bar{\sigma},\bar{\sigma}\sigma} &= \sum_{\alpha} \frac{\langle \sigma\bar{\sigma}|\hat{H}_{\text{las}}|\Psi_{\alpha}^{(2)}\rangle\langle\Psi_{\alpha}^{(2)}|\hat{H}_{\text{las}}|\bar{\sigma}\sigma\rangle}{\langle\Psi_{\alpha}^{(2)}|\hat{H}_{\text{las}}|\Psi_{\alpha}^{(2)}\rangle} \\ &= \sum_{\alpha} \frac{\Omega_{\alpha}^{\sigma\bar{\sigma}}\Omega_{\alpha}^{\bar{\sigma}\sigma}}{\Delta_{\alpha}^{(2)}} \\ &= \sum_{\alpha} \left(\frac{\Omega^{\sigma}\Omega^{\bar{\sigma}}}{4\Delta^{\sigma}} + \frac{\Omega^{\bar{\sigma}}\Omega^{\sigma}}{4\Delta^{\bar{\sigma}}}\right)^{2} \frac{c_{\alpha}^{\sigma\bar{\sigma}}c_{\alpha}^{\bar{\sigma}\sigma}}{\Delta_{\alpha}^{(2)}} \end{aligned} \tag{5.24}$$

We have derived the interaction terms for the Ising-type, flop-flop, and flip-flop interaction as defined in Eq. (5.11). Additionally, we have obtained the detuning dependence of the flip-flop interaction, which can be activated or deactivated simply by choosing the appropriate laser detuning. The flop-flop interaction requires the two excitation paths at the Raman condition.

5.2 Experimental setup and procedure

We will now describe the procedure of a typical interaction measurement. We focus on the J^{++} and J^{+-} interactions as Ising interactions have already been studied in various publications [56, 57, 99, 107, 130, 137, 205]. See also Section 4.6 for our results on Ising interaction measurements.

To experimentally study the dependence of the interaction strengths on the geometric arrangement, we load single atoms in optical tweezer arrays with freely adjustable geometries. We select the simplest possible setting of three in-line traps with various nearest-neighbor distances d and angles θ, as shown in Fig. 5.3. Here, θ is the angle between the interatomic separation vector $\mathbf{d}$ and the magnetic field $\mathbf{B}$ defining the quantization axis. We use 14 replications of these triplets to increase statistics and space the groups by more than $20\,\mu\text{m}$ to ensure that interactions only appear within one group but not between different neighboring groups. After the loading procedure described in Section 3.1, we take a first fluorescence image to check for the presence of an atom in the trap. Due to the statistical loading, we obtain an average loading probability of $50\,\%$. Fig. 5.3 shows a typical first fluorescence picture [75, 80]. Afterward, we optically pump and prepare the atoms in the $|\uparrow\rangle$ state with σ^{-}-polarized pumping and repumping light on the D1-line as described in Section 3.4.1. We then apply Raman sideband cooling [80] as described in Section 3.4.2 to lower the trap depth to a minimum of $h \cdot 80\,\text{kHz}$ before gravity opens the trap. We must lower the overall trap depth during the dressing measurements due to the trap-depth inhomogeneities, which would otherwise break the Raman condition described in Section 5.1.2. The influence of the trap inhomogeneities will be discussed in Section 5.4.2. In addition, we apply a magnetic

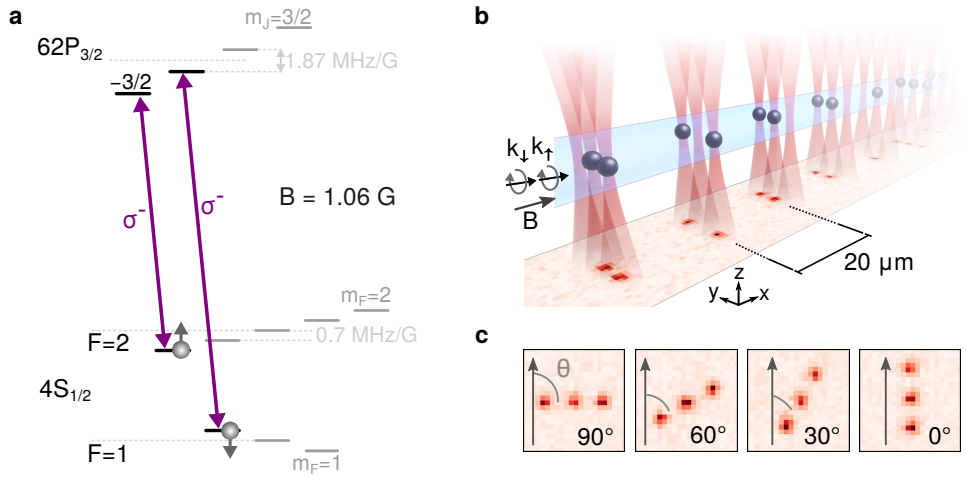

Figure 5.3 Experimental two-color Rydberg dressing settings. a. Level scheme for the two-color Rydberg excitation consisting of two beams, driving each σ^- transitions at a magnetic field of $1.06\,\mathrm{G}$. This will result in a Rydberg Zeeman splitting of $E_z/h = 1.98\,\mathrm{MHz}$. **b.** Sketch of the experimental setting. The Rydberg excitation beams ($\mathbf{k}_\uparrow$, $\mathbf{k}_\downarrow$, light blue) are aligned along the magnetic field **B**. They illuminate all tweezer groups, each with three linearly arranged tweezers (red). The tweezers are statistically loaded with atoms (black spheres). At the bottom of the illustration, a single-shot fluorescence image shows the statistical single-atom filling. **c.** Exemplary images for various angles θ at a distance of $5.2\,\mu\mathrm{m}$. Figures taken from reference [62].

field aligned parallel with our Rydberg excitation beams, with an amplitude of $B = 1.06\,\mathrm{G}$, which leads to the Zeeman splitting of the Rydberg states $E_z/h = 1.98\,\mathrm{MHz}$.

We use the laser setup for the Rydberg dressing pulse as described in Section 4.3.1. For the two-color excitation, we split the UV beam into two paths, each with an acousto-optical modulator (AOM)[1] with frequencies of $\pm 230.275\,\mathrm{MHz}$ [2], which we use for intensity stabilization and bridging the hyperfine ground state splitting. Both beams require the same polarization, so we overlap them using a non-polarizing beam splitter[3]. After passing the polarization cleaning optics, consisting of a set of waveplates[4] and a thin film polarizer[5], the beams are focused onto the atoms with a horizontal (in-plane) waist of $40\,\mu\mathrm{m}$ and a vertical (out-of-plane) waist of $10\,\mu\mathrm{m}$. The Rydberg excitation beams propagate parallel to the magnetic field and drive σ^- transitions. Single-atom Raman couplings are thus suppressed by choice of beam polarization and polarization extinction of the used optics.

[1] AOMs are from *G&H I-M200-3C10BB-3-GH27*, and we use high-power RF amplifiers *RFbay MPA-40-40* to provide the required $4\,\mathrm{W}$ of RF power.
[2] We use the signal generator *Rigol DSG815*, referenced to the 10MHz rubidium clock *SI FS725*.
[3] UV plate beamsplitter *Newport UVBS14-1*
[4] Zero-order crystalline quartz waveplates from *Altechna* have been proven to sustain high UV intensities.
[5] *Brewster type thin film polarizer* from *Altechna*.

To ensure proper alignment of the excitation beams onto the atoms, we follow a two-step procedure. First, we roughly align both beams onto the same spot on a spatial detector[6] placed after the science vacuum chamber. Then, in the second step, we fine-tune the alignment by optimizing the Rabi couplings of both beams in a large-spaced tweezer array. This alignment procedure is similar to the one described in Section 4.3.1 with the addition of a piezo-controlled mirror mount for individual control of the second excitation beam. Since the full Rydberg excitation path is free space, the system is sensitive to thermalization-induced changes in the beam pointing. However, we found that our system remained stable without requiring resetting of the UV beam position when thermalized. For the measurements described in the following sections, we typically apply a Rydberg dressing pulse of $50\,\mu\mathrm{s}$ of both beams.

As state-selective imaging is not possible at present, we remove one spin state from the system to investigate interaction-induced spin-flips. Therefore, after the Rydberg excitation pulse, we adjust the overall trap depth to $20\,\%$ of the initial loading power and apply a pulse to heat the $|\uparrow\rangle$ atoms with resonant D2-light on the $|4P_{3/2}\,F' = 3,\, m_{F'} = -3\rangle$ cycling transition. This leaves only the atoms in the $|\downarrow\rangle$ state trapped, which we capture with a second fluorescence image. By comparing both fluorescence images, we can deduce the spin interactions based on spin flips and their correlations.

Alternatively, we could also prepare the atoms in the $|\downarrow\rangle$ state by applying a π-pulse between both ground states (see Section 3.4.1) and detect spin changes via trap losses. Unfortunately, in this case, we would not be able to differentiate interaction-induced losses from other loss mechanisms, such as off-resonant single-atom Rydberg excitations (dressed Rydberg lifetime). However, if we prepare the atoms in the $|\uparrow\rangle$ state, we are blind to such losses, which requires us to check for them separately, as it will be discussed in the next Section 5.2.1 and in Section 5.4.1 and Appendix B.3.

5.2.1 Calibration measurements

Prior to each measurement, we independently check the Rabi coupling and spectroscopy signal for both excitation beams. We scan the Rabi frequencies in a free-space configuration without trapping light. The typical uncertainty of the oscillation fits of the observed Rabi frequencies is $0.01\,\mathrm{MHz}$, consistent for all listed couplings for the measurements presented in the next sections. As discussed in Section 4.3.1 we observe a degradation of the UV power to $50\,\%$ of the original output power within one week of usage. We implemented intensity stabilization of the UV pulses to maintain the excitation power constant until completing one measurement set. In addition, we observe a long thermalization duration of the UV laser setup of approximately $12\,\mathrm{h}$, during which the UV beam alignment drifts.

Due to our spin-insensitive imaging method and the required heat-out pulse, we have to check for residual atom losses separately. Our in-trap lifetime exceeds several tens of

[6] We use a 2D beam position measurement and alignment system from *TEM*: *μAligna 140* for this purpose.

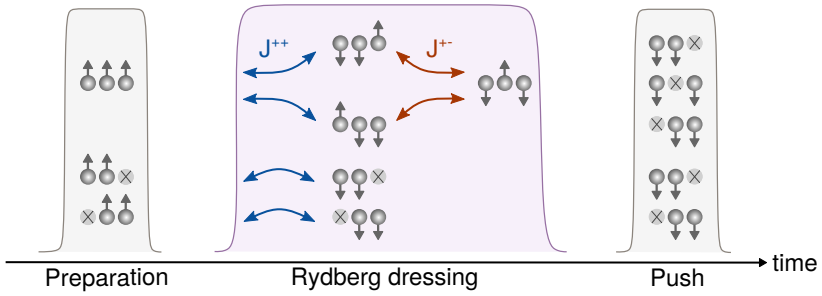

Figure 5.4 Experimental sequence for spin flip detection. We initiate all atoms in the $|\uparrow\rangle$ state using an optical pumping pulse. Then, we continue with a Rydberg dressing of $50\,\mu$s and push-out pulse period, where the latter only leaves us with atoms in the $|\downarrow\rangle$ state. Finally, to evaluate for flop-flop and flip-flop interaction, we post-select two initial configurations: The atom in the center plus one extra atom or all three atoms. This initial configuration enables flop-flop (blue arrow) and flip-flop processes (red arrow). Figure adapted from reference [62].

seconds, which is much longer than one experimental run of approximately $1\,$s. Hence, the majority of the atom loss is due to off-resonant single-atom Rydberg excitation, quantified by the dressed Rydberg lifetime, as defined in Section 4.2.2. The ideal lifetime of the dressed ground state atoms scales quadratically with the Rydberg admixture $\beta = 2\Omega/\Delta$. Assuming a phase-noise-free laser, we expect a black-body radiation-limited lifetime of $\tau_\mathrm{r} = 1.7\,\mathrm{ms}$ for $\Delta_\downarrow = -2\pi \times 0.6\,\mathrm{MHz}$ and $\Omega_\downarrow = 2\pi \times 0.4\,\mathrm{MHz}$. However, the experimentally observed lifetime is reduced to $70 \pm 7\mu s$ due to laser noise [75]. The influence of the laser phase noise will be discussed in Section 5.4.1.

Moreover, we have to quantify the number of false positives, which are detected atoms in the second fluorescence picture that did not undergo any Rydberg interaction. They can be caused by two main reasons: Inefficient state preparation and insufficient push-out pulse, leading to a constant offset. In each measurement evaluation, we check for single-loaded tweezer groups.

Comparing the two fluorescence images taken before and after the Rydberg dressing pulse, we reconstruct the occurred spin interactions. For the analysis, we focused on the original loading configurations where nearest-neighbor tweezer pairs are occupied, corresponding to either a fully loaded group ($|\uparrow\uparrow\uparrow\rangle$) or two out of three at the nearest neighbor distance pairs ($|\circ\uparrow\uparrow\rangle$, $|\uparrow\uparrow\circ\rangle$). The presence of flop-flop interactions would lead to pairwise spin-flips and recapture of $|\circ\downarrow\downarrow\rangle$ or $|\downarrow\downarrow\circ\rangle$ in the second image.

In the first calibration measurement, we scanned flop-flop processes while tuning the two-atom Raman condition, as shown in Figure 5.5. A fulfilled Raman condition $\Delta E = E_z - \Delta^\uparrow + \Delta^\downarrow$ is necessary for observing flop-flop processes. We fitted a characteristic $\mathrm{sinc}(f)$ envelope, which we expect for a Fourier limited rectangular pulse of $50\,\mu$s duration.

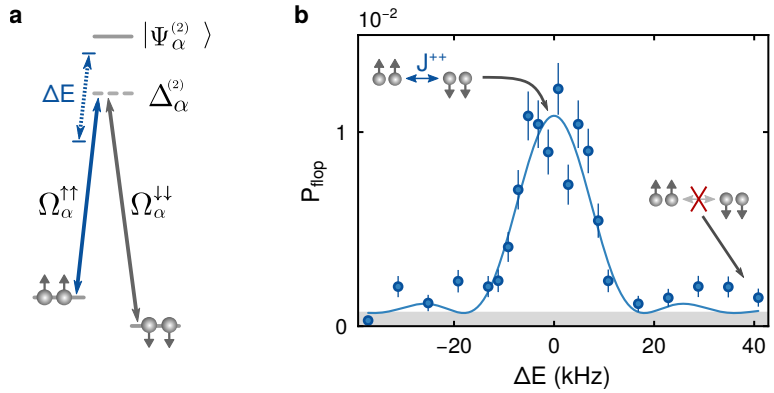

Figure 5.5 Raman condition for flop-flop interactions. a. Schematic for the flop-flop interaction between two atoms. Shown is the effective Λ-scheme with effective two-photon Rabi couplings $\Omega_\alpha^{\sigma\sigma}$ between the pairs of ground state atoms and Rydberg pair states $\Psi_\alpha^{(2)}$. $\Delta_\alpha^{(2)}$ is to the two-photon detuning to the corresponding $\Psi_\alpha^{(2)}$. For the Raman condition scan in b, we scan the detuning of one excitation arm (blue). **b.** Flop-flop processes versus two-atom Raman detuning $\Delta E = E_z - \Delta^\uparrow + \Delta^\downarrow$. The fit shows the characteristic sinc^2 envelope of a Fourier limited rectangular pulse with a full width half maximum FWHM $= (18.2 \pm 0.2)\,\mathrm{kHz}$. The grey-shaded area represents the detection limit, accounting for a false positive probability due to single spin flips and inefficient state preparation and push out. Figure adapted from reference [62].

Now that we introduced the typical measurement procedure, we want to observe the spin interactions in the following sections.

5.3 Spin coupling measurements

The desired interactions' strength can be fully controlled by experimental parameters, such as laser coupling, detuning, and the geometric arrangement of the atom pairs to the quantization axis, as derived before. In the following, we scan for interaction processes for different conditions. For the first set of measurements in Section 5.3.1, we tune the laser detunings of the two excitation paths to have the same amplitude but with opposite signs, such that flip-flop interactions vanish, and we only observe flop-flop interactions. In a second set in Section 5.3.2, we use an asymmetric set of detunings, which enables flip-flop interactions in addition to flop-flop interactions. In Section 5.4, we will discuss the experimental restraints limiting coherent dynamics.

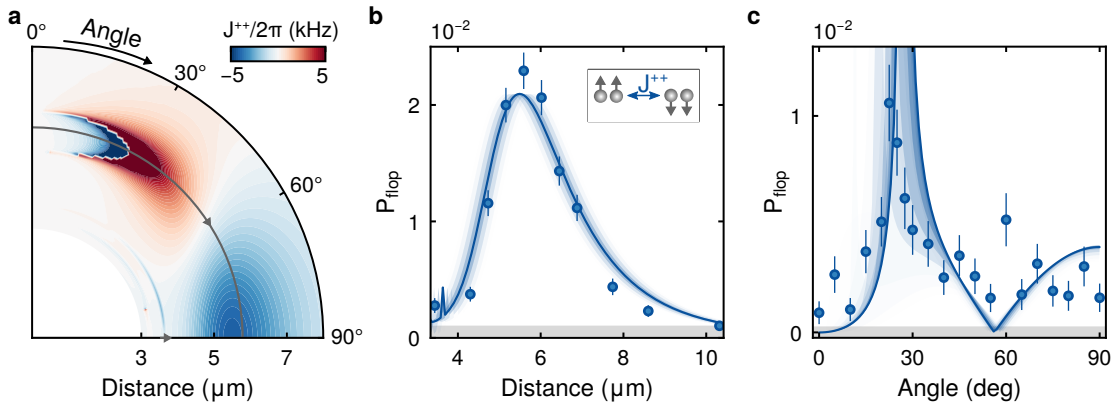

Figure 5.6 Flop-flop interactions. a. Calculation of J^{++} as a function of θ and d for $\Delta_\uparrow = -\Delta_\downarrow = 2\pi \times 1\,\mathrm{MHz}$. We identify a resonance in the spin-spin couplings. Calculation of J^{++} as a function of θ and d for $\Delta_\uparrow = -\Delta_\downarrow = 2\pi \times 1\,\mathrm{MHz}$. We identify a resonance in the spin-spin couplings appearing as a singularity around $\theta = 30\,^\circ$ at a distance of $5 - 6\,\mu\mathrm{m}$. **b.** Observed flop-flop probability P_{flop} for different atom pair distances at $\theta = 90\,^\circ$. A small false positive probability sets the detection limit (grey area) taking into account single spin flips and inefficient state preparation and push out. Error bars indicate 1 s.e.m. The solid line is the scaled theoretical prediction, where the amplitude has been scaled to match the experimental values due to broadening effects. The blue shading indicates the effect of the finite radial size of the atomic wavepacket σ_{rad} in $\sigma_{\mathrm{rad}}/2$-steps up to $\pm 3\sigma_{\mathrm{rad}}$. **c.** Angular dependence of the flop-flop interaction at a distance of $5.6\,\mu\mathrm{m}$. Figures taken from reference [62].

5.3.1 Flop-flop interactions

First, we experimentally investigate the flop-flop interactions obtained for the most straightforward parameter set. We choose the laser detuning to be symmetric $\Delta^\uparrow = -\Delta^\downarrow$, which cancels flip-flop terms by destructive interference of the excitation paths (see Section 5.1.3).

We simulate the expected interactions for distances for a 2D plane ranging from $3 - 8\,\mu\mathrm{m}$ and an angle of $0 - 90\,^\circ$, as shown in Fig. 5.6. Here, we observe a vanishing interaction strength at approximately $60\,^\circ$, resulting from the destructive interference of all interaction contributors. Additionally, we note a diverging interaction behavior around $25\,^\circ$, where a Rydberg pair state is shifted on resonance with the lasers detunings. The advantage of working close to Rydberg pair resonances while keeping a large single atom detuning will be discussed in Section 5.4.4 and has been previously proposed in reference [139].

To characterize the interactions, we scan the pair distance behavior, preparing the atoms aligned perpendicular to the quantization axis and thus avoiding any crossing of Rydberg pair state resonance. The experimental sequence is the same as described in Section 5.2. Before the measurement, we prepare a set of SLM phase patterns for each specific atom distance. Then, at the beginning of each iteration step, we update the SLM with a new pattern, giving enough buffer time for the SLM to react during the MOT loading time of $250\,\mathrm{ms}$.

The distance dependence of the interaction is shown in Fig. 5.6 for Rabi couplings of $\Omega^{\uparrow} = 2\pi \times 0.52\,\mathrm{MHz}$, $\Omega^{\downarrow} = 2\pi \times 0.36\,\mathrm{MHz}$. Overall, the experimental data and the amplitude-scaled theoretical expectation are in good qualitative agreement. We checked that we did not measure significant single-atom recapture or increased single spin flips in every interaction measurement, proving the suppression of single-atom Raman processes. The small spin-flip probability of a few percent is due to several reasons, which are described in more detail in Section 5.4.

One of the major reasons for the small interaction probability is the laser phase noise, limiting the dressing time due to an approximately 20-fold increased scattering rate appearing as atom loss. In addition, there are several broadening effects that contribute to the experimental uncertainties. For instance, the finite size of the atoms' thermal wavepacket in the radial and axial direction in the traps, leading to an averaging effect over a range of atom pair separations and angles within the radial ground state wavepacket size of $\sigma^0_{\mathrm{rad}} = 0.15\,\mu\mathrm{m}$ and the axial thermal wavepacket size $\sqrt{2}\sigma^0_{\mathrm{ax}}\sqrt{k_B T/\hbar\omega_{\mathrm{ax}}} \approx 0.86\,\mu\mathrm{m}$ for the axial trapping frequency $\omega_{\mathrm{ax}} = 2\pi \times 1.7\,\mathrm{kHz}$, where k_B is the Boltzmann constant and T is the temperature. Another prominent broadening effect is the line shifts due to tweezer-to-tweezer inhomogeneities. For the used arrays, the average trap depth difference is $\overline{|\Delta U|} = h \cdot (10.6 \pm 1.6)\,\mathrm{kHz}$.

These broadening effects are also present for the second set of measurements, where we map out the angular dependence of the flop-flop interaction for a fixed distance of $5.6\,\mu\mathrm{m}$ and Rabi couplings $(\Omega^{\uparrow}, \Omega^{\downarrow}) = 2\pi \times (0.55, 0.30)\,\mathrm{MHz}$ for the same laser detunings as before. For these parameters, we observe a singularity in the spin-spin interaction at $\theta \approx 30\,^{\circ}$ due to the Rydberg pair state resonance mentioned earlier. As a result, the measurement shows a peaked interaction around this resonance, as shown in Fig. 5.6. The broadening effect is responsible for the weak atom loss caused by direct Rydberg pair excitation on resonance (see Appendix B.3).

5.3.2 Combination of flop-flop and flip-flop interactions

In the following set of measurements, we activate both flop-flop and flip-flop interactions. We set the detunings to $\Delta^{\uparrow} = 2\pi \times 1.4\,\mathrm{MHz}$ and $\Delta^{\downarrow} = -2\pi \times 0.6\,\mathrm{MHz}$ and Rabi couplings to $\Omega^{\uparrow} = 2\pi \times 0.5\,\mathrm{MHz}$ and $\Omega^{\downarrow} = 2\pi \times 0.36\,\mathrm{MHz}$. To observe flip-flop interactions, we post-select fully loaded tweezer groups and require the specific chronology of spin couplings depicted in Fig. 5.4. In an initial $|\uparrow\uparrow\uparrow\rangle$ occupation, flop-flop processes introduce the ($|\downarrow\downarrow\uparrow\rangle$, $|\uparrow\downarrow\downarrow\rangle$) spin state, and in combination with flip-flop interactions, this leads to the detection of $|\downarrow \circ \downarrow\rangle$. Thus, this procedure requires flop-flop interactions to initiate the flip-flop dynamics from the fully polarized initial state. To detect flop-flop interactions, we will post-select tweezer groups where two out of three traps at the nearest neighbor distance are occupied.

First, we simulate the interaction geometry for J^{++} and J^{+-} with the abovementioned detuning and Rabi couplings. We expect different spatial dependencies as shown in Fig. 5.7. Note that the plots shown are radial interpolations for discrete simulation steps of $70\,\mathrm{nm}$

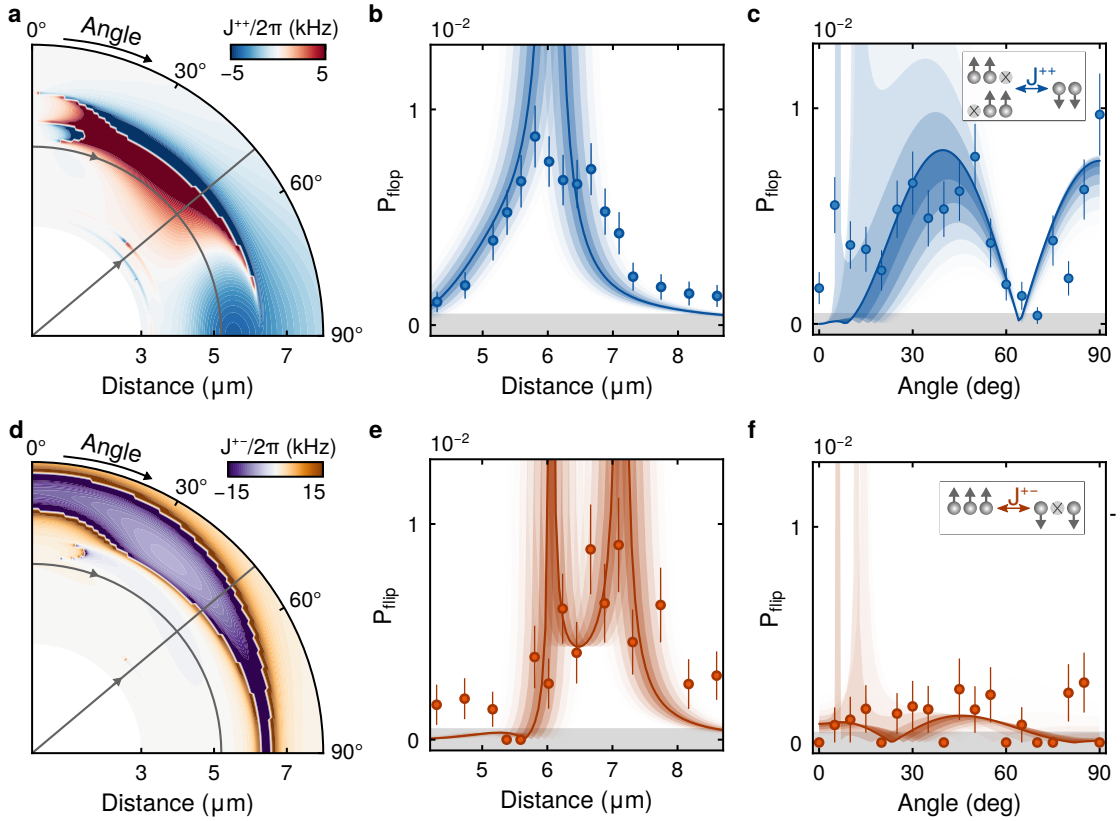

Figure 5.7 Flop-flop and flip-flop interactions. a, d. Calculation of the distance- and angular-dependent flop-flop and flip-flop interaction for an asymmetric detuning $\Delta^{\uparrow} = 2\pi \times 1.4\,\mathrm{MHz}$ and $\Delta^{\downarrow} = -2\pi \times 0.6\,\mathrm{MHz}$ and Rabi couplings $\Omega^{\uparrow} = 2\pi \times 0.5\,\mathrm{MHz}$ and $\Omega^{\downarrow} = 2\pi \times 0.36\,\mathrm{MHz}$. Grey lines indicate the trace for the measurements in this figure. **b, e.** Preparing the atoms at a fixed angle of $\theta = 50\,^{\circ}$ and scan the distance-dependence of the J^{++} and J^{+-} interactions. **c, f.** Preparing the atoms at a fixed distance of $5.3\,\mu\mathrm{m}$ and scan the angular-dependence of the J^{++} and J^{+-} interactions. Shadings reveal the effect of the spatial elongation of the atomic wavepacket in the radial direction, thus indicating the detection limit. Error bars represent 1 s.e.m. Figures taken from reference [62].

for distances between $3 - 8\,\mu\mathrm{m}$ and $0.5\,^{\circ}$ angular steps between $0 - 90\,^{\circ}$. For the flip-flop interaction, we obtain two singularities for the chosen detuning set. Additionally, we note that J^{+-} exhibits stronger interaction compared to J^{++}. This is due to the interplay of the small detuning to the Rydberg pair states with large a large product overlap $c_{mn}^{\uparrow\downarrow} \cdot c_{mn}^{\downarrow\uparrow}$. This spatial dependence of the interaction is consistent with the theoretical prediction in reference [4].

In the first measurement, we prepare the atoms at a fixed angle of $50\,^{\circ}$ and scan the spatial dependence of both interactions. For the flop-flop interaction, we surpass a Rydberg pair state resonance at $\approx 6\,\mu\mathrm{m}$. While this singularity enhances the interaction strength, it can also cause resonant excitation to pair states and lead to losses (Appendix B.3). Our data in

Fig. 5.7 reveals the amplitude-scaled interaction shape. Slight discrepancies between theory and measurement may be due to systematic errors in the calibration of the imaging system, which we estimate to be less than 5%. In addition, the occurrence of the $|\downarrow \circ \downarrow\rangle$ state is now non-zero, indicating the presence of flip-flop interactions. In this case, we predict two singularities in qualitative agreement with our data. The theory fit of the flip-flop interactions in Fig. 5.7 also considers the prerequired flop-flop interactions.

In the previous section, we demonstrated that we could vanish flip-flop interactions by choosing a set of symmetric detunings. In this section, however, we show that the interactions can also be suppressed by the choice of the geometrical arrangement of the atoms. For the second set of measurements, we prepare the atoms at a fixed distance of $5.3\,\mu\mathrm{m}$ and scan the angular dependence of the interactions in steps of five degrees. To evaluate the flop-flop interaction, we post-select on initial $|\circ \uparrow\uparrow\rangle$ and $|\uparrow\uparrow \circ\rangle$ states, as shown in Fig. 5.7. The minimum at $65\,^\circ$ arises from the destructive interference of the different interaction contributions on the two-atom level. The contributors are different Rydberg pair states $|\Psi_\alpha^{(2)}\rangle$ with product overlap $c_\alpha^{\uparrow\uparrow} c_\alpha^{\downarrow\downarrow}$ of opposite sign. The sum over all contributors results in a vanishing J^{++} interaction. We do not measure any $|\downarrow \circ \downarrow\rangle$ state occurrence, which agrees with our prediction.

In summary, we have demonstrated two-color Rydberg-dressing as a new technique for achieving tunable, XYZ-type short-range spin interactions. We used the flexible arrangement of optical tweezers to investigate the spatial shape of the desired interactions and employed the laser detunings to tune flip-flop interactions. Nevertheless, the measured spin-spin interaction probability is only a few percent, and the interactions are in the incoherent regime. We, therefore, require a detailed discussion of the limitations and possible improvements in the next section.

5.4 Discussion of technical limitations

Currently, technical limitations hinder us from accessing the coherent regime. This section aims to explore these limitations in detail and propose possible solutions to overcome them, paving the way towards achieving coherence. The two primary limitations arise from laser phase noise and tweezer-to-tweezer inhomogeneity, as detailed in sections Section 5.4.1 and Section 5.4.2. Laser phase noise limits the duration of our dressing pulses and determines the lower threshold of the interaction coupling strength. Meanwhile, trap depth inhomogeneities require us to work at the lowest possible trap depth. This has an impact on the atoms' positional uncertainty coming from the in-trap wavepacket size, as described in Section 5.4.3. There are even more possibilities to improve the performance of the experiment, which are listed in Section 5.4.4. We will discuss the realistically reachable figure of merit according to the experimental improvements in Section 6.2.

5.4.1 Decoherence due to excitation laser phase noise

The phase noise of our Rydberg excitation laser leads to an incoherently enhanced population of the Rydberg states. As we will see in the following, this results in a dephasing of the interaction dynamics and defines an upper limit for the duration of the Rydberg dressing pulses. For more details about the noise of the excitation laser and possible solutions, please refer to Section 4.4.

To estimate the impact of the phase noise, we first want to calculate the parameters for an "ideal" laser with negligible noise: Here, the Rydberg population is defined by $\beta^2 = \Omega^2/4\Delta^2$. The Rydberg excitation rate then scales as $\beta^2\gamma_r$, where γ_r^{-1} is the Rydberg-state lifetime. Our measurement for the Rydberg dressed lifetime is based on observing trap losses after a certain period of the excitation pulse, as described in Section 4.2.2. These trap losses occur because excited atoms, influenced by both the ponderomotive potential of the trapping light and the excitation's recoil, exit the trap before decaying back to the ground state with a probability of one. We expect a black-body limited dressed Rydberg lifetime of $2.2\,\mathrm{ms}$, assuming a phase-noise-free laser for the laser for a symmetric detuning as in Section 5.3.1 and Rabi couplings of $\Omega^{\uparrow} = 2\pi \times 0.537\,\mathrm{kHz}$. However, we measure a $1/e$-decay of the trap occupation of $101 \pm 5\,\mu\mathrm{s}$, corresponding to a 22-fold increased scattering rate. We obtain a similar ratio for the laser parameters in Section 5.3.2, where we chose an asymmetric detuning set ($2\pi \times 0.6\,\mathrm{MHz}$, $2\pi \times 1.4\,\mathrm{MHz}$). In this case, we calculate an "ideal" dressed lifetime of $1.7\,\mathrm{ms}$ and measure a reduced lifetime of $70 \pm 7\,\mu\mathrm{s}$.

The phase noise of the Rydberg excitation laser can be reduced by implementing optical filter cavities or employing feed-forward techniques, as already successfully implemented by different groups [169, 192, 208]. These and other techniques are discussed in detail in Section 4.4.1.

In summary, reducing the phase noise of the excitation laser is essential for future dressing experiments working close to resonance [57, 139]. Moreover, it boosts the interaction coherence due to less high-frequency noise [208].

5.4.2 Effect of trap depth inhomogeneities

The flop-flop interactions require energy conservation to be fulfilled at any time and, therefore, both excitation paths in Raman configuration. Hence, as the trap remains on during the excitation pulse, differences in trap depth between tweezer-to-tweezer present a severe problem as they might break the Raman condition.

To resolve these trap depth differences, we measure the AC Stark shift on the D1-line spectroscopically to determine the trap depth of the individual tweezers in the array. Here, the light shift of the ground state is equal to the trap depth, and by knowing the ratio between the anti-trapped, excited, and trapped ground states, we can calculate the exact trap depth [60].

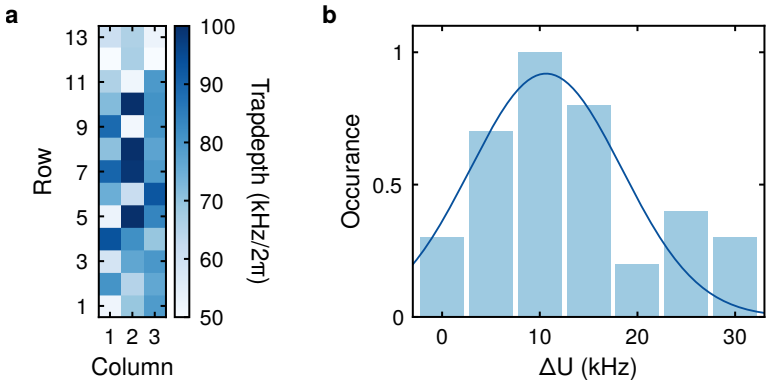

Figure 5.8 Trap depth inhomogeneities. a. Exemplary 3×13 tweezer array consisting of groups of three horizontally spaced tweezers at a distance of $\approx 30\,\mu\mathrm{m}$(columns). The columns are spaced by $5.6\,\mu\mathrm{m}$. **b.** Distribution of the trap depth difference $|\Delta U|$ for two tweezers at the nearest neighbor distance and for the minimum trap depth as shown in a. The Gaussian fit (solid line) reveals an average trap depth difference of $\overline{|\Delta U|} = h \cdot (10.6 \pm 1.6)\,\mathrm{kHz}$. For our tweezers generated with $1064\,\mathrm{nm}$ light, the magnitude of the ponderomotive potential for the Rydberg states approximately equals the trap depth for the ground states but is of the opposite sign. Hence, the difference in the line shifts of the ground states-Rydberg transition for neurest-neighbor pairs is about $2\,|\Delta U|$. Figure adapted from reference [62].

We start by optically pumping the atoms into the $|F = 2, m_F = -2\rangle$ state. Afterward, we set the magnetic field perpendicular to the optical pumping beam, allowing different polarizations. When the excitation beam is on resonance with the transition of $|4S_{1/2}, F = 2\rangle$ to $|4P_{1/2}, F' = 2\rangle$, the atoms are statistically transferred to the ground state hyperfine manifold. We apply a pulse duration of $20\,\mu\mathrm{s}$, three orders of magnitude larger than the lifetime of the excited states of $26\,\mathrm{ns}$ [59] to ensure multiple scattering processes. Afterward, we rotate the magnetic field parallel to the direction of the laser beam and remove all atoms in the $F = 2$ manifold with light resonant to the $|F = 2, m_F = 2\rangle$ to $|F' = 3, m_{F'} = 3\rangle$ cycling transition of the D2-line. For a linear polarisation and the trapping wavelength of $1064\,\mathrm{nm}$, we calculate the excited state lightshift to be -5.66 times larger compared to the ground state [60], where the sign indicates the anti-trapping potential. Note that we use the D1-line for the spectroscopy measurements, as the individual F and m_F states do not have differential shifts for linearly polarized traps. As we perform the spectroscopy measurement at 20% of the tweezer power (average trap depth of $200\,\mu\mathrm{K}$), we need to scale the results to the minimal trap depth (0.5% tweezer power) used for the experiments described before.

In Fig. 5.8, we show the trap depth difference $|\Delta U|$ of nearest-neighbor tweezer pairs in a 3×13 tweezer array. Applying a Gaussian fit, we estimate an average trap depth difference of $\overline{|\Delta U|} = h \cdot (10.6 \pm 1.6)\,\mathrm{kHz}$. As the ponderomotive potential for the Rydberg states is anti-trapped with roughly the same amplitude as the trap depth of the ground states, the effect on the probed interactions is even more severe, with the difference of the Rydberg line shifts being approximately $2\,|\Delta U|$.

To address this issue, it is necessary to improve the array uniformity. Other groups have already demonstrated arrays with less than $1.1\,\%$ inhomogeneity [209], which represents a tenfold improvement compared to our arrays. The central refinement lies in employing a feedback algorithm, which levels the trap depths of the array after creating a new phase pattern. Moreover, working at the same trap depth would result in a $2\,|\Delta U|$ shift smaller than the current interaction amplitude between $2\pi \times (5 - 15)$ kHz. Assuming this level of trap depth difference, and a spin-spin interaction coupling of $2\pi \times 5\,\mathrm{kHz}$, we could prepare the atoms at an average trap depth of $h \cdot 0.5\,\mathrm{MHz}$. This will increase the radial and axial trapping frequencies by a factor of $\sqrt{0.5/0.08} \approx 2.5$, resulting in a decreased axial and radial wavepacket size by a factor of $1/\sqrt{2.5} \approx 0.5$.

In addition to optimizing the array homogeneity, implementing a light sheet perpendicular to the direction of the tweezers, as presented in Section 3.4.2, could allow us to lower the trap depth further and, therefore, decrease the absolute difference within the array.

On the other hand, improving the array homogeneity would also enable working at larger trap depths, which would decrease the in-trap wavepacket size of the atoms, as discussed in the next section.

5.4.3 Impact of the ground state wavepacket size

The Rydberg dressing measurements presented in this chapter are limited by the trap depth inhomogeneities within the tweezer arrays, which forces us to perform the measurements at a minimal trap depth of $h \cdot 80\,\mathrm{kHz}$. This corresponds to radial and axial trapping frequencies of $\omega_{\mathrm{rad}} = 2\pi \times 11\,\mathrm{kHz}$ and $\omega_{\mathrm{ax}} = 2\pi \times 1.7\,\mathrm{kHz}$. After Raman sideband cooling, the atoms' temperature are on average $k_B T = h \cdot 4.2\,\mathrm{kHz}$ as measured in [60]. With these parameters, we calculate the ground state wavepacket size in the radial and axial direction, which are $\sigma^0_{\mathrm{rad}} = \sqrt{\hbar/(m\omega_{\mathrm{rad}})} = 0.15\,\mu\mathrm{m}$ and $\sigma_{\mathrm{ax}} = \sqrt{\hbar/(m\omega_{\mathrm{ax}})} = 0.39\,\mu\mathrm{m}$, respectively.

Since the temperature is below the radial trapping frequency, we evaluate the ground state wavepacket size to consider the fluctuations of the radial pair-distances with $\sigma_{\mathrm{rad}} \approx \sqrt{2}\sigma^0_{\mathrm{rad}}$. Here, the factor $\sqrt{2}$ describes the movement of two individual atoms. The influence of the radial motion on the interaction measures is indicated by the shading in the measurements in Fig. 5.6 and Fig. 5.7.

In the axial direction, on the other hand, we estimate the out-of-plane fluctuations for two atoms with the thermal wavepacket size in a harmonic potential of the trap to have an root mean square (RMS) width for two atoms moving w.r.t. each other $\sqrt{2k_B T/m\omega^2_{\mathrm{ax}}} \approx 0.86\,\mu\mathrm{m}$. Here, the large temperature limit is used to assess the position fluctuations, as $k_B T > \hbar\omega_{\mathrm{ax}}$. The impact of this motion depends on the angle between the atom pair and the quantization axis. For a $90\,^\circ$ pair orientation, an out-of-plane movement will solely lead to washed-out atom distances towards larger separations. Contrary, the contribution for small angles is more severe, as it removes the zero of the interactions at a mean angle of $\theta = 0°$. This

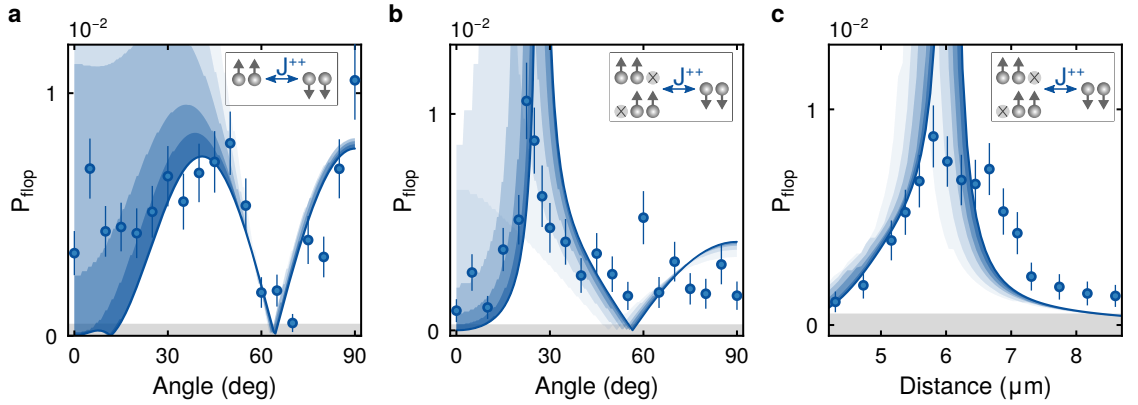

Figure 5.9 Influence of the out-of-plane position fluctuations. Data points are the same as in Fig. 5.6 and Fig. 5.7 with corresponding selection on the initial tweezer group configuration as shown by the inset. The shading represents the effect of the axial motion of the atoms in the traps, where the motion along this axis is converted to new pair angles and larger pair distances. The shadings depict the difference between the initial flop-flop potential and the potential seen by the atoms due to a position shift in the axial axis. The shadings are plotten in $\sigma_{ax}/2$-steps up to $\pm 3\sigma_{ax}$. Figures adapted from reference [62].

explains the comparably strong flop-flop interactions for small angles in the measurements shown in Fig. 5.9.

Hence, the motion of the atoms in the radial and axial axis leads to blurred interaction detection. The origin of this severe limitation are the tweezer depth inhomogeneities, which result in a less efficient (over the array averaged) Raman sideband cooling. Furthermore, these constraints are the reason why the experiment has to be performed at the lowest possible trap depth.

Improving the homogeneity of the array mentioned earlier will facilitate more efficient Raman sideband cooling, subsequently reducing line broadening attributed to the Doppler shift. Such broadening could otherwise restrict the coherence of spin interactions. As detailed in Section 3.4.2, the average ground state probability of the entire array after the cooling process is on average $37\% \pm 18\%$. This cooling efficiency is primarily restricted by trap inhomogeneities and low axial trapping frequencies. Nonetheless, the best-cooled single tweezer within the array achieves a ground state probability of 69%, suggesting that an improvement is both feasible and necessary. It is worth noting that this measured ground state fraction for a single tweezer was obtained with cooling parameters optimized for the entire array. To compensate for the small axial trapping frequency, one can introduce an additional confinement perpendicular to the tweezer plane [95], such as the light sheet discussed in Section 3.4.2. This additional light sheet also offers the opportunity for adiabatic cooling of the atoms by further lowering the tweezer trap depth. Clearly, there exists significant potential for enhancement, which is realistically achievable.

In summary, implementing these measures allows us to perform the measurements at more confined traps, lower atoms' temperature, and decrease dephasing effects due to the motion of the atoms.

5.4.4 Further experimental improvements

As discussed, the main technical limitations affecting the performance of our experiment are the excitation laser phase noise, the trap inhomogeneities, and the large ground state (thermal) wavepacket size. Nevertheless, we can improve the experimental performance by implementing the following measures:

- **Increase Rabi coupling**: We currently overlap both Rydberg excitation beams using a non-polarizing beam splitter, as both beams require the same polarization at the atoms. Unfortunately, this setup leads to a loss of half of the optical power. Using a polarized beam splitter for overlapping both beams instead, we could increase the Rabi couplings of each path by a factor of $\sqrt{2}$. The spin interactions, scaling with Ω^4, will then directly increase by a factor of four. However, this requires a different choice of Rydberg states, where the two excitation paths possess opposite polarizations.
- **Vanish influence of magnetic field fluctuations**: Instead of employing the stretched states $|F = 2, m_F = -2\rangle$ and $|F = 1, m_F = -1\rangle$, we could encode the spins in the $m_F = 0$ hyperfine substates. As these states are insensitive to magnetic fields [38], we reduce the effect of decoherence and dephasing caused by magnetic field noise. However, these states do not have a good projection of the angular quantum number, reducing the coupling to Rydberg states.
- **Increase statistics**: Until now, we load the tweezer array statistically with a probability of $\approx 50\%$. The probability of obtaining only a nearest neighbor tweezer pair loaded within a group of three tweezers is 25%. The chance to initialize a fully loaded tweezer group is 12.5%. For one set of measurements, we take, on average, $15,000$ shots and increase the statistics above by preparing arrays of several tweezer groups spaced far enough not to interfere with each other. By implementing resorting and preparing fully-loaded tweezer groups, we could tremendously increase the statistics [26, 27].
- **Increase interaction coupling**: It has been shown that the observed Rydberg pair state resonances can be utilized to enhance the coherence of Rydberg dressing [139]. Furthermore, we can use C3-couplings to increase the interaction strength further [210].

Overall, implementing these modifications could significantly improve the experimental performance by increasing the coherence time, statistics, and interaction strength. Nevertheless, we must carefully consider the trade-offs associated with these modifications.

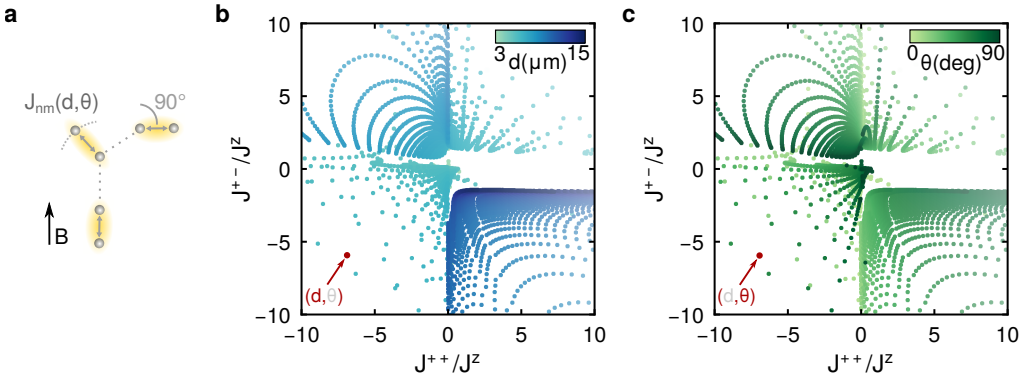

Figure 5.10 Tunable XYZ interaction ratios in 1D atom chains. (**a.**) Exemplary sketch for freely adjustable atom pair geometries **b, c.** Both figures are taken from reference [62] and show the same calculation, demonstrating the distance (**b.**) and angle (**c.**) dependence of the ratios J_{ij}^{++}/J_{ij}^{z} and J_{ij}^{+-}/J_{ij}^{z}. The interactions are calculated for the detunings $\Delta^{\uparrow} = 2\pi \times 1.4\,\mathrm{MHz}$, $\Delta^{\downarrow} = -2\pi \times 0.6\,\mathrm{MHz}$ and in steps of $100\,\mathrm{nm}$ and $1\,^{\circ}$. Quadrants II and IV illustrate a smooth tunability, while the ratios in quadrants I and III seem to be more spackled caused by close-by Rydberg pair-state resonances. In the latter case, the system shows a higher sensitivity of the control parameters and, therefore, requires higher stability..

5.5 Pioneering interaction programmability

By implementing the measures discussed in the previous section, we can expect a significant improvement in the maximum figure of merit (FOM), which is described by the product of the peak interaction strength and the coherence time. Based on the current laser technology, we estimate that the maximum realistically achievable FOM is in the order of one hundred.

In our experiment, the ratio of the spin interactions in the different channels can be easily controlled with the laser parameters and the freely adjustable geometries of nearest and next-nearest-neighbor atom pairs. The tunable interactions are rooted in the non-monotonic spatial dependence of the interaction amplitude. We can engineer the relative coupling strength of the spin-spin interactions J^{+-}/J^{z} and J^{++}/J^{z} as visualized exemplarily in Fig. 5.10. Here, we chose an asymmetric set of laser detunings and couplings corresponding to the measurements in Section 5.3.2. On top of that, we can switch off specific couplings globally by choice of laser detuning, as discussed in Section 5.1.3. Further investigation can exploit the tunable interactions to design couplings in two dimensions. Nevertheless, in a 2D configuration, the situation and the path toward an optimal set of experimental parameters are even more complex. In any case, the angular dependence of the interaction provides a unique opportunity to engineer nearest-neighbor or even longer-ranged interactions. Imagine scenarios where every second atom is placed at the interference minimum shown in Fig. 5.7, and thus interactions only occur between next-nearest neighbor pairs, but not between nearest neighbors. Alternatively, consider a design merging flip-flop with flop-flop interactions by forming triangular tweezer groups at a 90-degree angle. In this design, one

group aligns with the quantization axis, permitting only flip-flop interactions, while the perpendicular group, for example, exclusively experiences flop-flop interactions. The range of possibilities is extensive. Yet, the experimental ralization will open new pathways to realizing a versatile and programmable analog quantum simulation platform for many-body quantum spin problems. Controlling these interactions is of great interest, particularly in the field of condensed matter physics.

In this chapter, we delved into two-color Rydberg-dressing as a pioneering technique to engineer tunable, XYZ-type short-range spin interactions in optical tweezer arrays. Despite certain technical limitations hindering the probing of coherent interactions, we explained possible improvements that promise to boost the performance of the experiment. We demonstrated the distance and angular adjustability of the interactions, spanning distances as concise as $3.5\,\mu\mathrm{m}$ to approximately $10\,\mu\mathrm{m}$ and angles of one full quadrant from $0 - 90\,^{\circ}$. Our measurements affirm that this methodology paves the way for the establishment of a versatile, programmable analog quantum simulation platform tailored for many-body quantum spin problems. The uniqueness lies not just in controlling the ratio of spin interactions across different channels but also in adjusting the ratio between nearest and next-nearest neighbor interactions. This versatility stems from the non-monotonic spatial behavior of the interactions, an attribute that can be used to design interactions in two dimensions. Such a framework offers potential for the realization of various frustrated geometries [4], and static [138] or dynamic gauge fields [211]. Another advantage of our approach could be the practical relevance of the interference of Hamiltonians underlying spectra obtained in nuclear magnetic resonance experiments in chemistry and biology, as discussed in reference [8].

Chapter 6

Summary and outlook

6.1 Summary

In this thesis, we present an optical tweezer platform employing potassium atoms for quantum simulation. We explain and contrast the lengthscales of Rydberg properties and interactions with those of optical tweezer arrays. Additionally, we introduce Rydberg dressing as a technique to simulate spin models. By exciting two distinct ground states to respective different Rydberg states, we can design a complex spin interaction Hamiltonian, paving the way for exploring, for instance, frustrated spin models and systems.

After introducing the concept of Rydberg atoms, we detail the properties of these atoms and outline our experimental procedure to load, cool, and prepare single atoms in a defined quantum state. The preparation fidelity of the $|F = 2, m_F \pm 2\rangle$ states exceeds $99\,\%$. Subsequently, we employ Raman sideband cooling (RSC) to bring the atoms close to their motional ground state, achieving an average ground state occupation of $37 \pm 18\,\%$. This approach offers multiple benefits: Firstly, it decreases the Doppler broadening of the atoms from $\Delta_D/2\pi = 160\,\mathrm{kHz}$ to $\Delta_D/2\pi = 50\,\mathrm{kHz}$. This reduction proves essential during resonant Rydberg excitations when the trapping potentials are briefly switched off. After RSC and additional adiabatic cooling due to gradual reduction of the trap potential, we manage to switch off the trap for $20\,\mu\mathrm{s}$ without any loss. In comparison, a non-cooled system exhibits losses after just $2\,\mu\mathrm{s}$. Secondly, RSC allows for a reduction of the overall trapping power, which in turn allows us to minimize the absolute value differences between the traps to a few kHz. This becomes crucial during Rydberg dressing pulses when atoms remain trapped, and varying trapping potentials could lead to trap-dependent detunings. However, there is certainly potential to enhance the cooling efficiency of our RSC implementation. Our cooling approach is initially optimized for larger tweezer arrays with more than 25 tweezers, and we report a trap depth inhomogeneity of about $10\,\%$. By improving the array homogeneity, we expect to achieve more effective cooling and also a reduction in cooling time since we currently need time-intensive frequency sweeps to accommodate tweezers of varying depths.

In our experiment, we employ a single-photon Rydberg excitation operating at $286\,\mathrm{nm}$ to excite atoms to Rydberg P-states. We describe our home-built laser setup, which generates an output power of $1\,\mathrm{W}$, and discuss the challenges posed by the UV wavelength on the

optical parts. Upon conducting the first Rydberg dressing measurements, we observe a detuning-dependent reduction in the Rydberg dressed lifetime. This decrease is primarily due to the seed laser's phase noise. We not only provide a comprehensive characterization of this issue but also suggest potential solutions that can be adopted in the future to mitigate the phase noise.

Subsequently, we discuss atom losses in tweezer arrays, caused by black-body-radiation-induced excitation of Rydberg atoms. In this scenario, black-body radiation induced decays to adjacent Rydberg states introduce dipolar C3-type interaction potentials. This can render a previously detuned laser resonant with the pair potential, facilitating pair excitations within the array. By measuring the correlation length at various detunings, we obtain a microscopic mapping of the cumulative spread of all C3 pair potentials. Additionally, we explore how the recoil stemming from Rydberg excitations can trigger atom movement, further enhancing this process as the atoms in motion surpass various distances within the array. Building upon this, we find that amplifying the coupling strength provides evidence of avalanche losses, an phenomenon similarly documented in bulk systems [57].

We further explore various spin interactions within the tweezer array. Through Ramsey interferometry, our focus is on Ising-type spin interactions in a Rydberg-dressed atom array consisting of atom pairs. This method incorporates an additional ground state that does not couple with the Rydberg state. For the interferometric measurement, we induce spin rotations via Raman transitions between the two ground states (one Rydberg-coupled and the other uncoupled). The interactions, which can be optically controlled and switched, are induced sequentially within this measurement. We demonstrate a dynamic measurement of the dressed interaction strength at $U/2\pi \approx 5\,\mathrm{kHz}$, with atoms approximately spaced at $3.4\,\mu\mathrm{m}$. A notable limitation in our approach is the increased Rydberg contamination. This arises primarily from laser phase noise and aligns with the dressed lifetime measurements discussed previously. It is worth noting that this limitation has also been identified in other Rydberg dressing experiments [56, 57]. Building on these insights, we introduce simultaneous dressing of both ground states to examine the more complex XYZ-type spin interactions. Our approach uses the spatially-dependent van der Waals interactions between the distinct m_j-sublevels within the Rydberg pair state manifold. This strategy facilitates the design of distance and angular-dependent couplings, specifically the flop-flop J^{++}, flip-flop J^{+}, and Ising type interaction J^{z}. The capability to merge angular and distance-dependent ratios among these interactions opens up possibilities for realizing models with various magnetic phenomena, including frustration and topology.

6.2 Outlook

The field of optical tweezers and Rydberg atoms in quantum simulation has experienced significant growth in recent years, overcoming many technical challenges and achieving noteworthy results. Despite these accomplishments, as emphasized throughout this thesis,

several limitations persist. We aim to summarize the upcoming improvements and modifications that are either already in progress or soon to be implemented in our experiment:

Technical upgrades

Homogeneous trap depths: The essential initial step is the enhancement of trap depth homogeneity within the tweezer array. Until now, we have been working with inhomogeneities on the order of $10\,\%$. A tenfold improvement would substantially elevate the experiment's efficiency. Importantly, this level of improvement is within reach, given that other research groups have already showcased array inhomogeneities on the order of $1\,\%$. This refinement will improve the experiment in several aspects:

- *Fluorescence imaging*: As discussed in Section 3.2, our pulsed imaging method, which alternates between trapping and resonant light, effectively circumvents the pronounced light shift (anti-trapping) of the D2-line. Nevertheless, this method shortens the lifetime of atoms using the chopped red molasses to $332\,\mathrm{ms}$ for a $1\,\mathrm{mK}$ trap [78], leading to an atom loss rate of $2.7\,\%$ after each imaging sequence. Hence, transitioning to an in-trap imaging technique, as done in Section 3.3 and illustrated in reference [79], emerges as a feasible solution. While we have endeavored to integrate this approach, persisting array inhomogeneity of $4.5\,\%$ has prevented us from concurrently imaging all tweezers effectively. However, once this inhomogeneity is reduced, as suggested by reference [61], the imaging technique exhibits an impressive detection efficiency (exceeding $99\,\%$) across a span of over 100 images.
- *Raman sideband cooling efficiency*: Thus far, after RSC, our average vibrational numbers are $\langle \bar{n}_{rad} \rangle = 0.225 \pm 0.217$ for the radial axis and $\langle \bar{n}_{ax} \rangle = 1.04 \pm 1.05$ for the axial axis. For an individual tweezer optimized to its best performance, we have recorded values of $\bar{n}_{rad} = 0.13$ radially and $\bar{n}_{ax} = 0.23$ axially. Therefore, refining the array trap depth inhomogeneity would align the overall ground state fraction closer to that of the optimized single tweezer.
- *Enhancement in dressing measurements*: As described in Section 5.4.2, optimizing the homogeneity of the array will significantly benefit dressing measurements and mitigate the detunings between tweezers, which arise from varying trap depths. Even when operating at the minimal trap depth, the current inhomogeneities are larger than the anticipated spin-spin couplings. A significant reduction in the array's inhomogeneity (of one order of magnitude) would ensure its absolute variation remains smaller than the predicted interaction strength.

Light sheet for tweezer loading: The next major advancement for the experiment involves introducing a light sheet that aligns with the plane of the tweezer array. This additional dipole trap will play a crucial role in loading the tweezers more effectively, thereby reducing unwanted loading into Talbot planes. The Talbot effect, determined by the trapping wavelength λ and grating period a, is roughly $z_T \approx 2a^2/\lambda$. It is important to note that this

effect behaves differently when using holographic techniques, leading to slightly distorted planes [75]. With tweezer spacings around $2.5\,\mu\mathrm{m}$, we expect Talbot planes to appear at approximately $11\,\mu\mathrm{m}$. This is significantly farther than the waist of the light sheet described in Section 3.4.2, which has a width of $3.4\,\mu\mathrm{m}$. This difference highlights the advantage of employing a light sheet to prevent loading into various tweezer planes. Furthermore, the light sheet could increase the axial trapping frequency during Raman sideband cooling, thereby enhancing cooling performance along this axis.

Increase statistics: Another technical improvement aims to increase the experimental statistics by utilizing fully filled arrays, in contrast to the statistically filled arrays discussed in this thesis. The current approach to statistical filling relies on a pair-repulsion sequence: a red-detuned beam is employed to remove all paired atoms, leaving only traps with an odd number of atoms occupied by a single atom [76]. To improve this filling method, we can adopt techniques like deterministic loading, which uses blue-detuned light to facilitate collisions after the initial loading process [79, 212]. This approach ensures that only individual atoms remain in the trap. Looking ahead, we also plan to rearrange atoms within the array by shifting them from a reservoir array to the primary 'science' array, using acousto-optic deflectors [26, 27]. This method is becoming increasingly standard and has been successfully implemented in numerous experiments.

Reducing phase noise in the Rydberg excitation laser: The next critical step involves enhancing the phase noise performance of our Rydberg excitation laser setup, as elaborated in Section 4.4.1. In this section, we have introduced various techniques and have shown some improvement in phase noise, particularly when using an optical cavity for the spectral filtering of the infrared seed light. Looking ahead, we plan to integrate this cavity filtering approach with our home-built UV seed laser at $1143\,\mathrm{nm}$, featuring a longer external cavity and thus offers improved phase noise performance. Despite these advances, it was evident that the phase noise suppression was insufficient, particularly in the strong-dressing regime with detunings within just a few MHz. Translated into infrared photon terms, this corresponds to a detuning of less than $1\,\mathrm{MHz}$. To address this issue, a more narrowly focused optical cavity could provide a solution. Therefore, our next step will be to employ an active feed-forward mechanism to further mitigate phase noise near the carrier frequency [213].

Route towards improved interaction coherence

The discussed technical limitations, currently prevent us from probing coherent spin dynamics for the implementation of th XYZ-type spin interactions as shown in Chapter 5. These challenges are well-understood, and various research groups have already demonstrated innovative solutions for individual tasks [169, 208, 209, 214–216]. Up to this point, their simultaneous implementation has been technically challenging due to the requirements of the respective experimental setup. Nevertheless, considering the rapid progress in technical

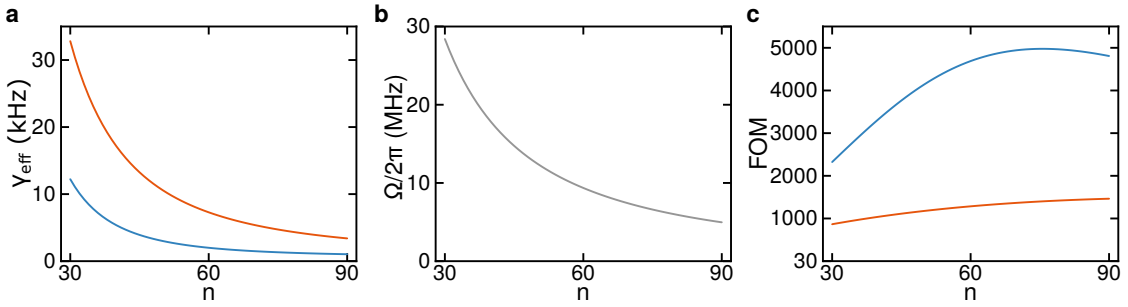

Figure 6.1 Figure of merit for Rydberg dressing. Figures are taken from [62]. **a.** Calculation of the effective decoherence for different principal quantum numbers $nP_{3/2}$ Rydberg states for two different environmental temperatures $300\,\mathrm{K}$ (orange) and $4\,\mathrm{K}$ (blue). **b.** Calculated Rabi couplings to the $nP_{3/2}$ Rydberg states for a single photon excitation laser with a beam waist of $10\,\mu\mathrm{m}$ and power of $250\,\mathrm{mW}$. **c.** The figure of merit is defined as the ratio of Rabi coupling and effective decoherence $\Omega/2\pi\gamma_{\mathrm{eff}}$ for the same temperatures as in a. The flattened blue curve can be explained by the increased influence of γ_{Las} compared to γ_r.

improvements, it is probable that Rydberg dressing achieved near-optimal performance in terms of the figure of merit (FOM) in the future. To elaborate further, assuming a negligible array inhomogeneity and Doppler effect, we define the FOM as the ratio of coherent interaction U to effective decoherence $\gamma_{\mathrm{eff}} = \gamma_r + \gamma_{\mathrm{Las}}$. Here, the lifetime of the Rydberg states γ_r defines a fundamental upper limit. The phase noise of the excitation laser, characterized as γ_{Las}, is the technical parameter with room for improvement (see Section 5.4.1).

In the simplified case of a single photon "standard" Rydberg dressing, the FOM can be described by $U/\gamma_{\mathrm{eff}} = \beta \cdot \Omega/\gamma_{\mathrm{eff}}$, where $\beta = \Omega/(2\Delta)$ is the Rydberg admixture (see Section 4.2). The admixture reduces the FOM of resonant Rydberg physics, which is defined as $\Omega/\gamma_{\mathrm{eff}}$. Fig. 6.1 illustrates the experimentally attainable Rabi couplings to $\ell = 1$ Rydberg states for different principal quantum numbers. Here, we consider an excitation beam with a $10\,\mu\mathrm{m}$ beam waist and a power of $250\,\mathrm{mW}$, which are reasonable values compared to the laser output power of $1W$. Our calculations show that Rabi frequencies of $2\pi \times 5\,\mathrm{MHz}$ are realistically reachable in a 1D geometry for states with a lifetime of $200\,\mu\mathrm{s}$. This results in a ratio $\Omega/\gamma_{\mathrm{eff}} \gtrsim 1000$ for a realistic $\gamma_{\mathrm{Las}} = 2\pi \times 100\,\mathrm{Hz}$, which is comparable to those obtained for other atomic species [54, 57, 137, 217]. Generally, Rydberg dressing experiments select a Rydberg admixture $\beta \ll 1$, altered to the particular experimental conditions [57, 137, 140]. Note that here we talk about the theoretically Rydberg probability, not taking into account additional excitations due to laser noise. For instance, when the probability of a single atom being in the Rydberg state is 1% (i.e., $\beta = 0.1$), the obtained FOM for "standard" Rydberg dressing is on the order of 100.

Furthermore, reference [139] suggests that Rydberg dressing can increase the FOM $U/\gamma_{\mathrm{eff}} \gtrsim 1000$ when the detunings are set far from the single atom asymptote but near a pair state. This method also applies to the two-color dressing scheme, where the reduction factors due to the different pair state admixtures $c_\alpha^{\sigma\sigma'}$ differ from unity. Therefore, a FOM of 100

appears to be reasonable for two-color Rydberg dressing. It would be interesting to further investigate whether this approach can exceed the performance of single-color Rydberg dressing in specific settings [139, 142].

Moreover, working in a cryogenic environment will further suppress decoherence introduced by black-body radiation, as shown in Fig. 6.1. This can lead to an improved FOM of Rydberg dressing to $U/\gamma_{\text{eff}} \gtrsim 4000$ (400) for both "standard" and two-color Rydberg-dressing.

Overcoming these technical limitations is essential for effectively controlling the XYZ-type spin-1/2 Hamiltonian. This thesis represents a significant stride in that direction, outlining the challenges and proposing strategies for their mitigation. Tuning the interaction strengths will enable new prospects for studying quantum many-body physics, including phenomena as frustrated quantum systems [4] or variational quantum optimization [47, 48, 50]. We emphasize the potential of Rydberg dressing in shaping analog quantum simulators, which facilitates handling intricate many-body challenges presented in nature.

Appendix A

D1 and D2 laser lock configurations

In the updated laser setup, as detailed in Section 3.3, we employ four lasers with respective locking methods at the potassium-39 D1 transition at $770.108\,\mathrm{nm}$ and the D2 transition at $776.701\,\mathrm{nm}$ [59]. The locking configurations are illustrated in Fig. A.1 and correspond to the laser setup in Fig. 3.5.

The magneto-optical trap (MOT) laser is stabilized using a potassium vapor cell. To lock the laser, we employ modulation transfer spectroscopy (MTS) [218], targeting the transition from $4S_{1/2}\,F = 1$ to $4P_{3/2}$ (indicated as red 1 in the diagram). The fundamental principle of MTS involves using two counter-propagating beams. One of these beams is modulated with a radio frequency ω, thereby creating sidebands around the laser frequency. When these two beams are overlapped again, the modulation of the probe beam is detected as a beat signal on a photodiode. More details on the specific implementation of the locking method in our setup can be found in the thesis of Nikolaus Lorenz [60]. Due to the unresolved hyperfine structure in the excited state, we cannot assign a specific F quantum number to the $4P_{3/2}$ state. Next, we insert an acousto-optic modulator[1] (AOM) in a double-pass arrangement, shifting the laser frequency by $2 \times 106.5\,\mathrm{MHz}$. This shifts the laser onto the crossover between the $4S_{1/2}\,F = 1,\ F = 2$ to $4P_{3/2}$ transitions (marked as red 2).

From this point, the laser beam is divided into three pathways: the cooler, repumper, and Zeeman slower. Each of the cooler and repumper paths includes another AOM[2] in double-pass configuration, allowing us to precisely detune the light for the respective transitions by δ_{MOTC} and δ_{MOTR} (red 3 and 4). For the Zeeman slower path, we use an AOM[3] in double-pass configuration to shift the beam frequency $-2 \times 95.75\,\mathrm{MHz}$ and an electro-optic modulator (EOM) to introduce sidebands matching the ground state splitting at $461.7\,\mathrm{MHz}$.

Next, the imaging laser (IMG) is offset-locked to the MOT laser at a beat frequency denoted by $\delta_{\mathrm{beat}} = -765\,\mathrm{MHz}$ (yellow 1). This beam is then shifted using another AOM[4] in a double-pass setup by $2 \times 194\,\mathrm{MHz}$, shifting it onto the $4S_{1/2}\,F = 2$ to $4P_{3/2}\,F' = 3$ transition (yellow 2), which is necessary for absorption imaging. When capturing fluorescence images of trapped atoms, we adjust the beat frequency accordingly.

[1] Gooch & Housego AOM 3100-125.
[2] Gooch & Housego AOM 3100-125.
[3] Gooch & Housego AOM 3110-125.
[4] Gooch & Housego AOM 3200-125.

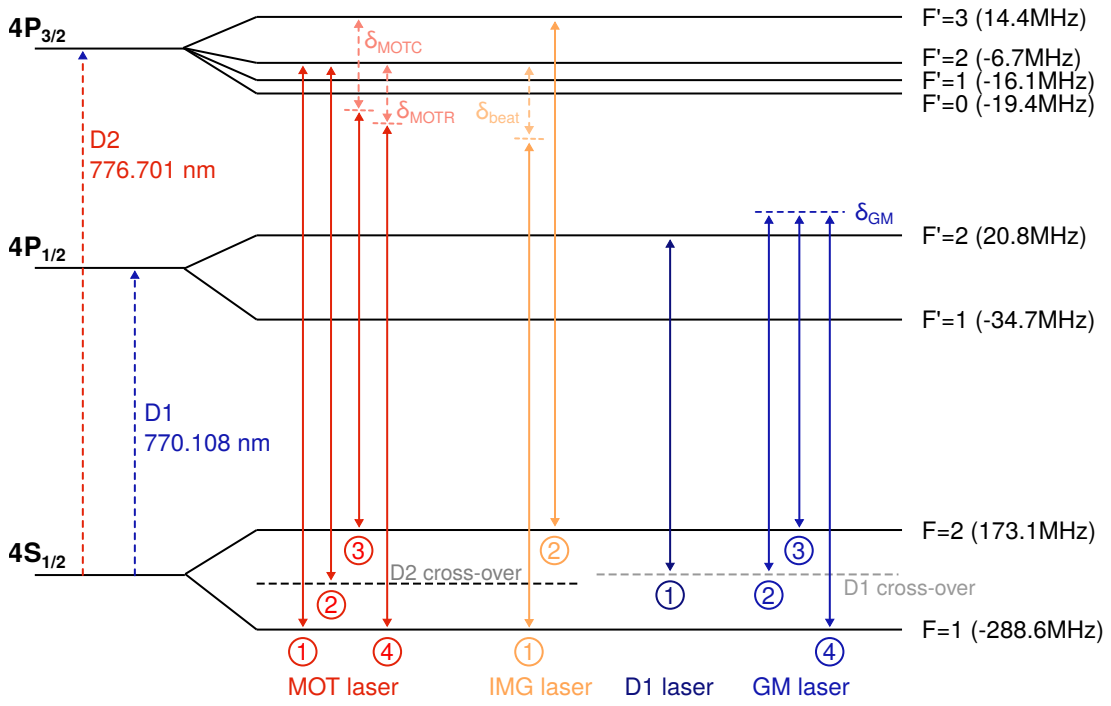

Figure A.1 ^{39}K D1 and D2 transitions and laser locking schemes for the MOT, IMG, D1 Master and GM laser.

We adopt a similar locking strategy for the ^{39}K D1 line at $770.108\,\mathrm{nm}$. A D1 laser is stabilized using a potassium vapor cell, locking on the crossover from $4S_{1/2}\,F = 1,\ F = 2$ to the $4P_{1/2}\,F' = 2$ (represented as blue 1). The grey molasses (GM) laser is then beat-locked to this reference laser, and an AOM[5] shifts its frequency in double-pass configuration by $2 \times (180 - 240)\,\mathrm{MHz}$ (beat and AOM shift result in blue 2).

In this setup, we use a broadband AOM, allowing for frequency ramps without relying on external locking mechanisms. The beat lock also enables dynamic tuning between free-space GM cooling and the cooling of atoms trapped in optical tweezers, as described in Section 3.3. Finally, we split the beam into two paths for the Cooler and Repumper transitions (blue 3 and 4), analog to the AOM setup used for the MOT laser. To successfully apply GM cooling, both lasers must meet the lambda condition and be blue-detuned at approximately $\approx 40\,\mathrm{MHz}$ [77].

[5] Gooch & Housego AOM 3200-124.

Appendix B

Details on analysis of the interaction detection

Additional information on the spin interaction measurements of Chapter 5.

B.1 Pair interaction parameter space

For the calculation of the Rydberg pair potentials, we use the PairInteraction software package [105]. This software numerically diagonalizes the interaction Hamiltonian, yielding the interaction energy as a function of atom pair distance and relative orientation w.r.t. the quantization axis. Additionally, it facilitates the computation of pair potentials for Rydberg atoms influenced by external electric and magnetic fields. To ensure computational feasibility during diagonalization, the PairInteraction software constrains the size of the basis set. Consequently, calculations include a finite number of states instead of considering all possible Rydberg atom states. The chosen basis set size influences the accuracy of the results. Thus, a balance between computational efficiency and desired accuracy is essential and must be evaluated for each state separately. We imposed three constraints:

- Energy surroundings for both individual atoms ΔE_{atom} and atom pairs ΔE_{pair} to restrict the basis to states with similar energy.
- The momentum quantum number $\Delta\ell$ and
- the principal quantum number Δn.

Typically, to find the optimal parameter space, one initiates with strong constraints and gradually opens them until the pair potentials at the final pair distance converge.

The evaluation is depicted in Fig. B.1. As a reference, we determined the flop-flop interaction strength J_0^{++} within an expanded parameter space: $\Delta E_{\text{single}} = \pm 100\,\text{GHz}$ for single atoms, $\Delta E_{\text{pair}} = \pm 40\,\text{GHz}$ for atom pairs, $\Delta\ell = \pm 2$ for the momentum quantum number and $\Delta n = 3$ for the principal quantum number. Under these conditions, we calculated the flop-flop interaction strength at a distance of $d = 5.5\,\mu\text{m}$ and a pair angle of $50\,^\circ$ to be $J_0^{++} = 2\pi \cdot 4.36\,\text{kHz}$. These settings near a Rydberg pair resonance, as shown in Fig. 5.7, render the system highly sensitive to even minor variations in pair interaction energies. Calculating this interaction strength required a total computation time of $\approx 70\,\text{min}$. For

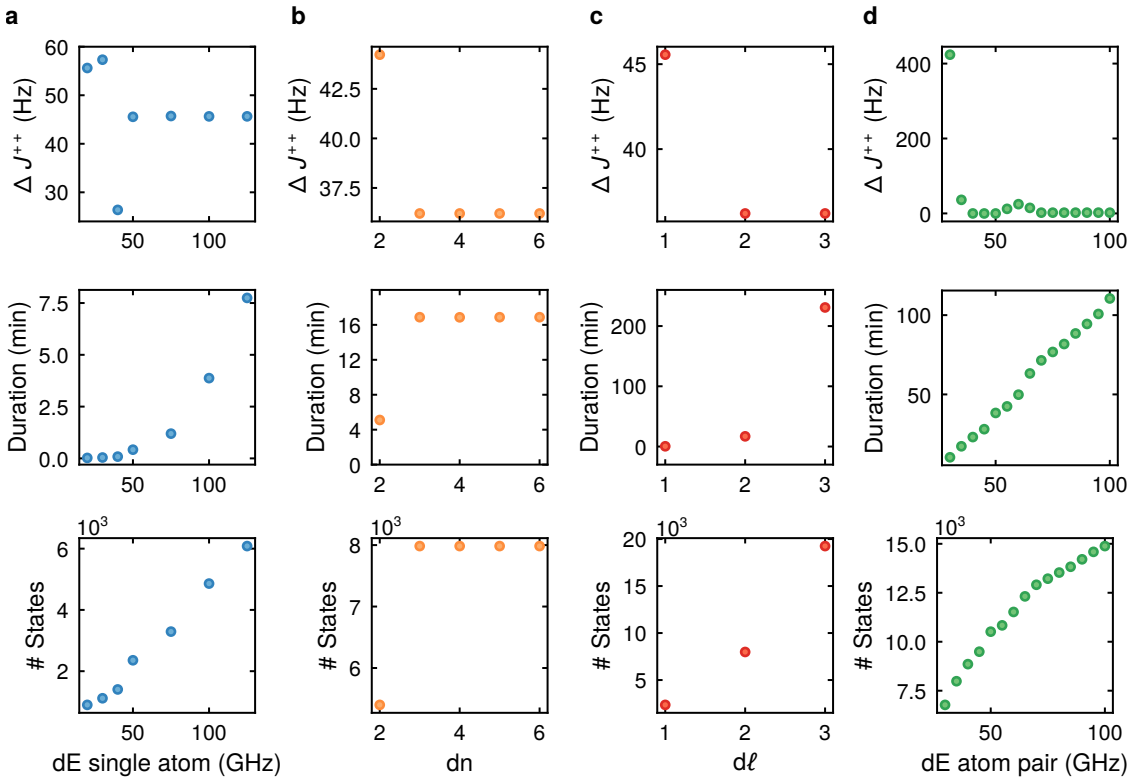

Figure B.1 Pairinteraction parameter space characterization for interaction simulation. Shown are the difference in flop-flop interaction strength of J_0^{++} of a large parameter space ($\Delta E_{\text{single}} = \pm 100\,\text{GHz}$, $\Delta n = \pm 3$, $\Delta \ell = \pm 2$, $\Delta E_{\text{pair}} = \pm 40\,\text{GHz}$) with the interaction obtained with the varied basis set. For each paramter, we also plot the required computation time and the number of states involved for this calculation.
a. Varying ΔE_{single} with the parameters, $\Delta n = \pm 8$, $\Delta \ell = \pm 1$, $\Delta E_{\text{pair}} = \pm 35\,\text{GHz}$.
b. Varying Δn with the parameters, $\Delta E_{\text{single}} = \pm 50\,\text{GHz}$, $\Delta \ell = \pm 2$, $\Delta E_{\text{pair}} = \pm 35\,\text{GHz}$.
c. Varying $\Delta \ell$ with the parameters, $\Delta E_{\text{single}} = \pm 50\,\text{GHz}$, $\Delta n = \pm 3$, $\Delta E_{\text{pair}} = \pm 35\,\text{GHz}$.
d. Varying ΔE_{pair} with the parameters, $\Delta E_{\text{single}} = \pm 50\,\text{GHz}$, $\Delta n = \pm 3$, $\Delta \ell = \pm 2$.

the calculations shown in Fig. B.1, we calculated the deviation between this J_0^{++} and the flop-flop interaction strength of the changed basis.

Having a closer look at the interaction deviation for the varied basis set in Fig. B.1, we observe that the single atom energy space converges at $50\,\text{GHz}$. Regarding the principal quantum number, the deviation achieves convergence after $\Delta n = \pm 3$. In the main text simulations, we chose $\Delta n = \pm 2$. This decision was influenced by the minor difference of approximately $10\,\text{Hz}$, which is over two orders of magnitude smaller than the interaction itself while having a four-fold reduction in computation time. A similar trend is noticeable with the momentum quantum number, where convergence is evident after $\Delta \ell = \pm 2$. The shift from $\Delta \ell = \pm 1$ to $\Delta \ell = \pm 2$ introduces a variation of less than $10\,\text{Hz}$, but elongates the

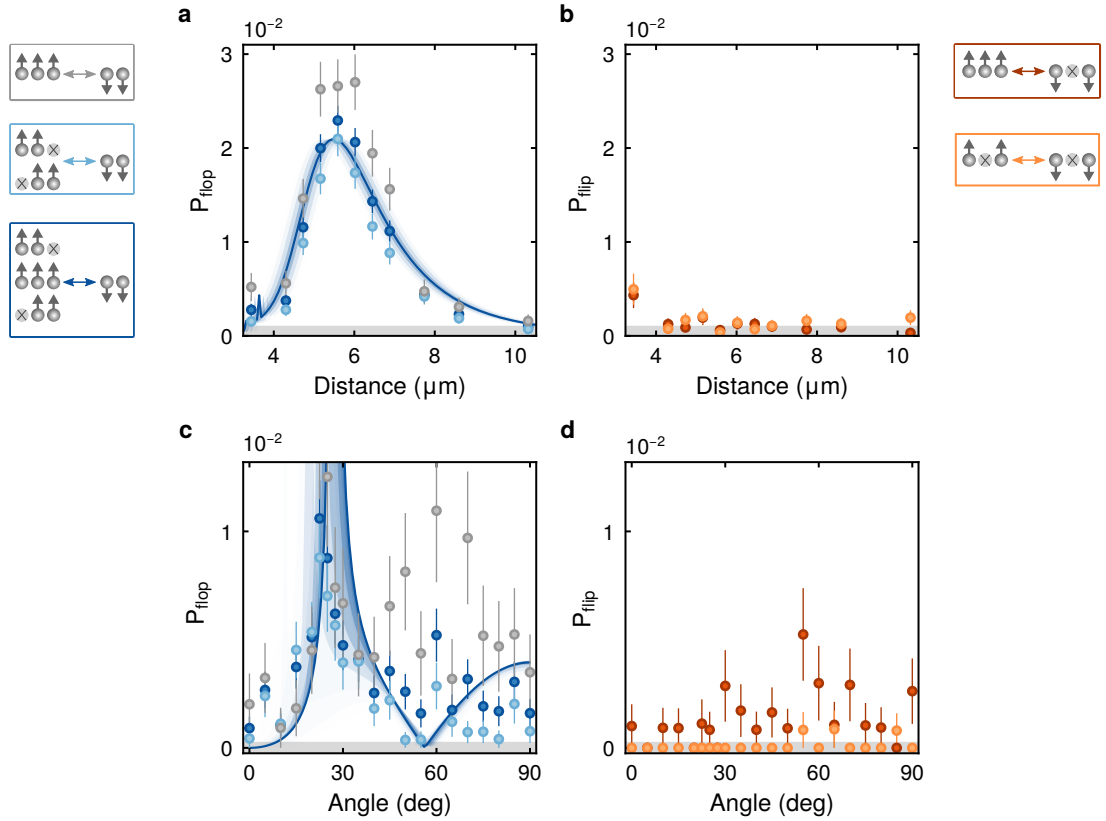

Figure B.2 Possible spin detection settings for symmetric laser detuning set. The measurements presented here are identical to those in Fig. 5.6. This visualization showcases the different post-selection options on both the flop-flop and flip-flop interactions.

computation time from $0.4\,\mathrm{min}$ to $17\,\mathrm{min}$. Consequently, we chose $\Delta\ell = \pm 1$ to be more time-efficient. When analyzing the atom pair energy space, convergence appears to occur around $40\,\mathrm{GHz}$. Nevertheless, for the main text simulations, we selected $\Delta E_{\mathrm{pair}} = 35\,\mathrm{GHz}$, tolerating a slight interaction deviation below 50Hz to enhance computational efficiency. This difference is roughly two orders of magnitude smaller than the interaction itself.

B.2 Different spin recapture options

To investigate both flop-flop and flip-flop interactions under symmetric and asymmetric detuning conditions in Section 5.3.1 and Section 5.3.2, we employ post-selection techniques based on different initial loading configurations within the tweezer groups. In the case of the symmetric detuning measurements, as shown in Fig. 5.6, we specifically post-select tweezer groups in which at least two out of the three nearest-neighbor tweezers are occupied. To validate this post-selection approach, we outline the different scenarios of the identical

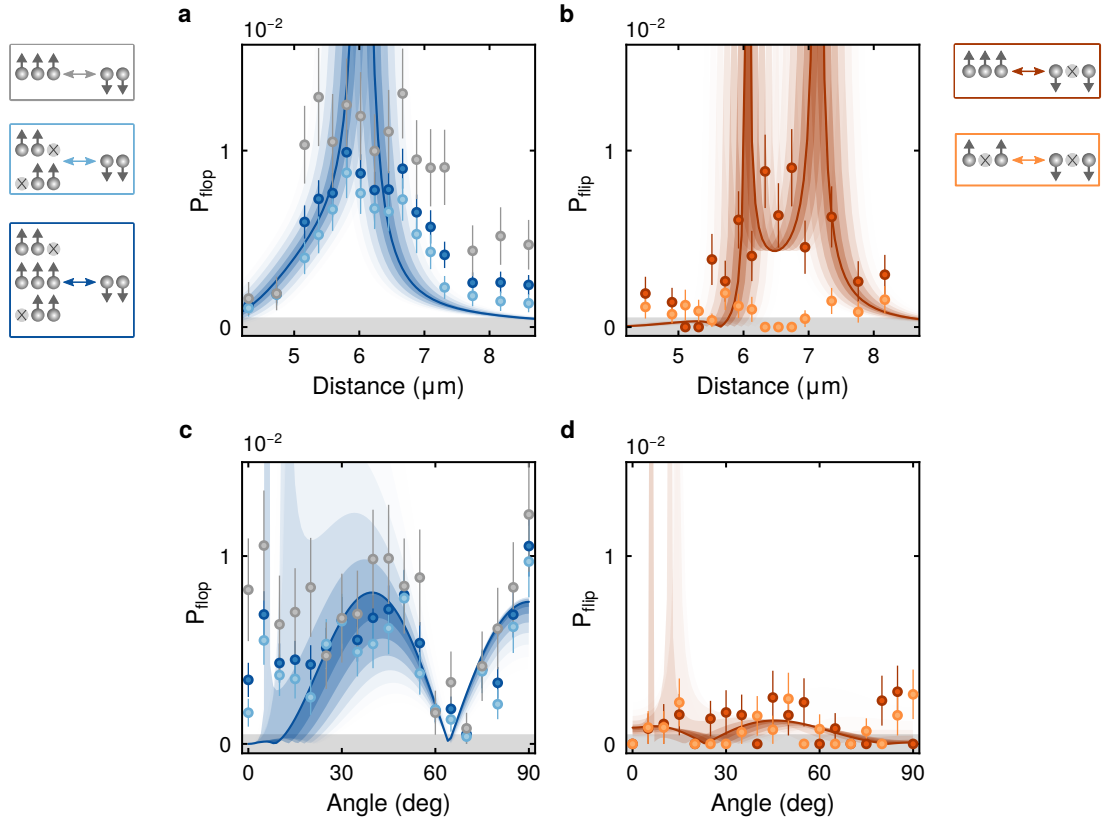

Figure B.3 Possible spin detection settings for antisymmetric laser detuning set. The measurements presented here are identical to those in Fig. 5.7. However, this visualization showcases the different post-selection options on both the flop-flop and flip-flop interactions.

measurement dataset in Fig. B.2, including fully loaded groups (grey), tweezer groups with two out of three nearest-neighbor traps occupied (light blue), and combinations of both (dark blue).

When tuning the flop-flop interaction by adjusting the atom pair distance, we observe good agreement across these three post-selection options. In contrast, changing the angle of the atoms w.r.t. the magnetic field results in an increased signal spike at the interference point around $60\,^{\circ}$, but only for tweezer groups that are initially fully loaded. This spike occurs despite our initial prediction that flip-flop occurrences would be negligible (dark orange). As this increase is absent in partially loaded tweezer groups, this occurrence might indicate the possibility of underlying multi-body interactions.

In the case of asymmetric detuning, where we also allow for flip-flop interactions to occur, we differentiate between different post-selection settings as illustrated in Fig. B.3. Interestingly, when we adjust the interactions by varying the distances between atom pairs, we observe a broadening effect in flop-flop interactions in fully loaded tweezer groups. Conversely, when

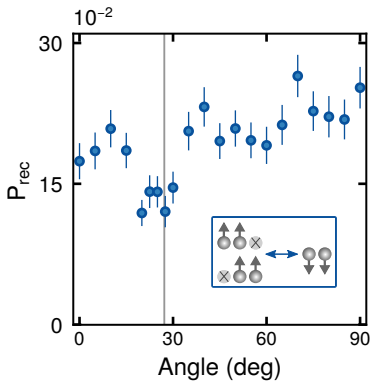

Figure B.4 Losses due to resonant Rydberg pair state excitations. The measurement settings are identical to those in Fig. 5.6. The gray vertical line indicates the pair state resonance's expected distance. No push-out pulse was applied after the Rydberg dressing pulse. Notably, while atom loss on resonance is evident, it remains small given our chosen parameters. Figure taken from [62].

we post-select based on the presence of two nearest-neighbor atoms, the resulting interaction signatures are considerably narrower and more aligned with theoretical predictions than those observed in fully loaded traps. We attribute this observed broadening to the influence of strong flip-flop interactions. This picture is further supported when we compare different post-selection settings while adjusting the strength of the interactions at various angles. In this particular case, we do not find any broadening that can be attributed to flip-flop interactions. The results from various post-selections remain closely aligned within their respective error bars.

B.3 Losses for Rydberg pair states

The lifetime of the dressed ground states scales with the Rydberg state probability $1/\beta^2$. With our specified parameters $\Delta^{\downarrow} = -2\pi \cdot 0.6\,\mathrm{MHz}$ and $\Omega^{\downarrow} = 2\pi \cdot 0.4\,\mathrm{MHz}$, and when considering a laser without phase noise, we expect a dressed lifetime constrained by black-body radiation to be approximately $\tau_{dr} = 1.7\,\mathrm{ms}$. Yet, experimental observations show the lifetime to be reduced to $70\,\mu\mathrm{s}$, a consequence of laser phase noise [78]. Meanwhile, another loss mechanism we must consider is the resonant excitation to Rydberg pair potentials, illustrated in Fig. B.4. For the measurement shown in this figure, we apply the same experimental procedure as done for the measurement in Fig. 5.7. However, we did not apply any end-sequence push-out pulses to ensure spin-insensitive imaging, and we post-selected on nearest neighbor tweezer pairs initially loaded. The results show that excitations to Rydberg pair resonances induce only a small atom loss.

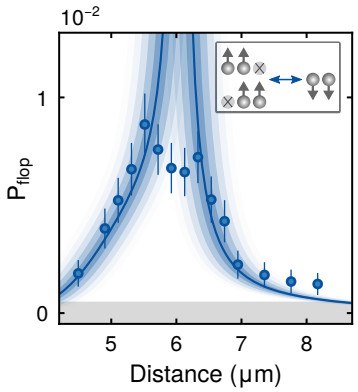

Figure B.5 Influence of imaging calibration on spatial interaction analysis. Impact of imaging calibration on spatial interaction analysis. Displayed are the identical simulations and data points from Fig. 5.7. Yet, the measurement's pair distance has been recalibrated to account for a 5% error in imaging magnification.

B.4 Imaging calibration errors

Upon closely reviewing the simulations and measurements of the interactions presented in Fig. 5.7, we notice a slight discrepancy between our experimental results and the theoretical predictions. One possible reason for this difference might be a calibration error associated with the imaging magnification, as pointed out in Fig. B.5. Within that figure, a potential 5% misalignment in the pair distances across the array due to imaging calibration is considered. Nevertheless, verifying this hypothesis would necessitate a rigorous recalibration. Specifically, to ensure accuracy, we would need to fine-tune both the tweezer spacing and the imaging system. This could be accomplished by overlaying an interference pattern atop the tweezer array, serving as a reference for calibration.

Danksagung

Diese Arbeit wäre ohne die Unterstützung vieler weiter Menschen nicht so zustande gekommen. Ihnen allen gilt mein tief empfundener Dank für die gemeinsam verbrachte Zeit, in der sie mich als Doktorandin begleitet und unterstützt haben.

Allen voran mein besonderer Dank an Christian Groß: Danke Christian, dass ich meine Doktorandenzeit am Kalium-Experiment verbringen durfte. Es ist dir immer gelungen, im Labor eine Atmosphäre der Inspiration und Motivation zu schaffen. Danke, dass deine Tür stets für mich offen stand. Es hat mich immer wieder erstaunt, wie du, wenn es auch mal nicht nach Plan lief, immer eine Lösung auf Lager hattest. Deine Begeisterung und dein Enthusiasmus für Physik haben mich stets fasziniert und geprägt.

Mein weiterer Dank gilt dem Kalium-Team insbesondere der „ersten Generation", Nikolaus Lorenz und Lorenzo Festa. Ihr habt mich ans Experiment herangeführt und allen in der AG Bloch vorgestellt. Von euch konnte ich unglaublich viel lernen, von den kleinen „Lifehacks" im Labor bis hin zu, wie man das Experiment „am Laufen" hält. Ebenso danke ich Arno Trautmann, für die vielen guten Diskussionen und die wertvolle Zeit im Labor, geprägt von intensiven und herausfordernden Momenten ebenso wie von Erfolgserlebnissen. Ich wünsche dem Kalium-Experiment viel Erfolg und eine immer „laufende Maschine".

Ein spezieller Dank geht auch an unsere engagierten ehemaligen Masterstudenten Ludwig Müller und Roxana Wedowski. Danke Ludwig, für deine Unterstützung am UV-Setup und die tolle Teamarbeit beim Tausch des CLBO. Roxana, ich hätte mir keinen besseren Reisepartner für den Austausch mit Japan vorstellen können. Vielen Dank für die gemeinsamen Frühstücke, Abendessen und die vielen Gespräche – sowohl über unsere Projekte als auch über Themen jenseits der Physik. Euch beiden wünsche ich alles Gute für eure Zukunft.

Bedanken möchte ich mich auch bei Anton Mayer und Karsten Förster am MPQ und Norbert Stockmaier an der Uni Tübingen. Mein aufrichtiger Dank geht auch an das Team der MPQ-Werkstatt und der Werkstatt in Tübingen. Ohne eure wertvolle Unterstützung wären wir oft ratlos gewesen. Danke für jeden technischen Rat und für die Sonderanfertigungen, die uns im Labor so oft gerettet haben.

Mein herzlicher Dank auch an das ErLi- und Cryo-Sr-Team in Tübingen, sowie an die Teams des Rubidium-, Moleküle-, Lithium-, und Strontium-Labors am MPQ. Danke, für die wertvollen Diskussionen, gemeinsamen Mittagessen und alle Dinge, die ihr uns ausgeliehen habt und die, wie es der Zufall so wollte, dauerhaft in unserem Experiment verbaut wurden.

Ein Danke auch an alle, die sich die Zeit genommen haben und diese Arbeit Korrektur gelesen haben: Arno Trautmann, Jan Trautmann, Pascal Weckesser, Ludwig Müller, Raphael Nold, Roxana Wedowski, Lisa Schwarz und Philipp Nellißen.

Ein ganz liebes Dankeschön geht an die Physiker-Skifoan-Gruppe: Jens, Raphi, Malte und Manuel. Ich danke euch für den wertvollen Ausgleich und die unverzichtbare Verdauungshilfe nach den extrem fettigen Essen auf den Skihütten.

Ein ganz besonderer Dank gebührt meinen Eltern, Monika und Bernhard. Ihr habt mich stets bestärkt, und eure unerschütterliche Unterstützung war mein Anker. Worte können nicht ausdrücken, wie unendlich dankbar ich euch bin.

Und Philipp, danke für deine stetige Unterstützung, deinen Rat, meine Kräfte richtig einzuteilen und deine unendliche Geduld, besonders wenn ich gedanklich wieder im Labor war.

Bibliography

[1] Moessner, R. and A. P. Ramirez. *Geometrical frustration*, Physics Today **59.**, 24–29 (Feb. 2006). DOI: 10.1063/1.2186278 (cit. on pp. 1, 82).

[2] Balents, L. *Spin liquids in frustrated magnets*, Nature **464.**, 199–208 (Mar. 2010). DOI: 10.1038/nature08917 (cit. on pp. 1, 83).

[3] Islam, R., C. Senko, W. C. Campbell, S. Korenblit, J. Smith, A. Lee, E. E. Edwards, C. C. Wang, J. K. Freericks, and C. Monroe. *Emergence and frustration of magnetism with variable-range interactions in a quantum simulator*, Science **340.**, 583–587 (May 2013). DOI: 10.1126/science.1232296 (cit. on p. 1).

[4] Glaetzle, A. W., M. Dalmonte, R. Nath, C. Gross, I. Bloch, and P. Zoller. *Designing Frustrated Quantum Magnets with Laser-Dressed Rydberg Atoms*, Physical Review Letters **114.**, 173002 (Apr. 2015). DOI: 10.1103/PhysRevLett.114.173002 (cit. on pp. 1, 2, 41, 46, 82, 84, 85, 99, 107, 113).

[5] Bednorz, J. G. and K. Müller. *Possible High Tc Superconductivity in the Ba - La- Cu- 0 System*, Zeitschrift für Physik B **64.**, 189–193 (Apr. 1986). DOI: 10.1007/BF01303701 (cit. on p. 1).

[6] Hofstetter, W., J. I. Cirac, P. Zoller, E. Demler, and M. D. Lukin. *High-Temperature Superfluidity of Fermionic Atoms in Optical Lattices*, Physical Review Letters **89.**, 220407 (Nov. 2002). DOI: 10.1103/PhysRevLett.89.220407 (cit. on p. 1).

[7] Lee, P. A., N. Nagaosa, and X.-G. Wen. *Doping a Mott insulator: Physics of high-temperature superconductivity*, Reviews of Modern Physics **78.**, 17–85 (Jan. 2006). DOI: 10.1103/RevModPhys.78.17 (cit. on p. 1).

[8] Sels, D. and E. Demler. *Quantum generative model for sampling many-body spectral functions*, Physical Review B **103.**, 014301 (Jan. 2021). DOI: 10.1103/PhysRevB.103.014301 (cit. on pp. 1, 107).

[9] Lobanov, M. Y. and O. V. Galzitskaya. *The Ising model for prediction of disordered residues from protein sequence alone*, Physical Biology **8.**, 035004 (June 2011). DOI: 10.1088/1478-3975/8/3/035004 (cit. on p. 1).

[10] Li, R. Y., S. Gujja, S. R. Bajaj, O. E. Gamel, N. Cilfone, J. R. Gulcher, D. A. Lidar, and T. W. Chittenden. *Quantum processor-inspired machine learning in the biomedical sciences*, Patterns **2.**, 100246 (June 2021). DOI: 10.1016/j.patter.2021.100246 (cit. on p. 1).

[11] Cirac, J. I. and P. Zoller. *Goals and opportunities in quantum simulation*, Nature Physics **8.**, 264–266 (Apr. 2012). DOI: 10.1038/nphys2275 (cit. on p. 1).

[12] Georgescu, I. M., S. Ashhab, and F. Nori. *Quantum simulation*, Reviews of Modern Physics **86**. (2014). DOI: 10.1103/RevModPhys.86.153 (cit. on p. 1).

[13] Feynman, R. P. *Simulating Physics with Computers*, International Journal of Theoretical Physics **21.**, 467–488 (1982). DOI: 10.1007/BF02650179 (cit. on p. 1).

[14] Saffman, M. *Quantum computing with atomic qubits and Rydberg interactions: Progress and challenges*, Journal of Physics B: Atomic, Molecular and Optical Physics **49.**, 202001 (Oct. 2016). DOI: 10.1088/0953-4075/49/20/202001 (cit. on p. 1).

[15] De Leon, N. P., K. M. Itoh, D. Kim, K. K. Mehta, T. E. Northup, H. Paik, B. S. Palmer, N. Samarth, S. Sangtawesin, and D. W. Steuerman. *Materials challenges and opportunities for quantum computing hardware*, Science **372**. (Apr. 2021). DOI: 10.1126/science.abb2823 (cit. on p. 1).

[16] Bloch, I. *Quantum coherence and entanglement with ultracold atoms in optical lattices*, Nature **453.**, 1016–1022 (June 2008). DOI: 10.1038/nature07126 (cit. on p. 1).

[17] Gross, C. and I. Bloch. *Quantum simulations with ultracold atoms in optical lattices*, Science **357.**, 995–1001 (Sept. 2017). DOI: 10.1126/science.aal3837 (cit. on p. 1).

[18] Morgado, M. and S. Whitlock. *Quantum simulation and computing with Rydberg-interacting qubits*, AVS Quantum Science **3.**, 023501 (June 2021). DOI: 10.1116/5.0036562 (cit. on pp. 1, 2).

[19] Anderson, S. E., K. C. Younge, and G. Raithel. *Trapping Rydberg Atoms in an Optical Lattice*, Physical Review Letters **107.**, 263001 (Dec. 2011). DOI: 10.1103/PhysRevLett.107.263001 (cit. on p. 1).

[20] Nogrette, F., H. Labuhn, S. Ravets, D. Barredo, L. Béguin, A. Vernier, T. Lahaye, and A. Browaeys. *Single-Atom Trapping in Holographic 2D Arrays of Microtraps with Arbitrary Geometries*, Physical Review X **4.**, 21034 (May 2014). DOI: 10.1103/PhysRevX.4.021034 (cit. on p. 1).

[21] Labuhn, H., D. Barredo, S. Ravets, S. De Léséleuc, T. Macrì, T. Lahaye, and A. Browaeys. *Tunable two-dimensional arrays of single Rydberg atoms for realizing quantum Ising models*, Nature **534.** (June 2016). DOI: 10.1038/nature18274 (cit. on pp. 1, 40).

[22] Kim, H., W. Lee, H.-G. Lee, H. Jo, Y. Song, and J. Ahn. *In situ single-atom array synthesis using dynamic holographic optical tweezers*, Nature Communications **7.** (Oct. 2016). DOI: 10.1038/ncomms13317 (cit. on p. 1).

[23] Barredo, D., V. Lienhard, S. De Léséleuc, T. Lahaye, and A. Browaeys. *Synthetic three-dimensional atomic structures assembled atom by atom*, Nature **561.**, 79–82 (Sept. 2018). DOI: 10.1038/s41586-018-0450-2 (cit. on pp. 1, 46).

[24] Cooper, A., J. P. Covey, I. S. Madjarov, S. G. Porsev, M. S. Safronova, and M. Endres. *Alkaline-Earth Atoms in Optical Tweezers*, Physical Review X **8.**, 41055 (Dec. 2018). DOI: 10.1103/PhysRevX.8.041055 (cit. on p. 1).

[25] Kaufman, A. M. and K.-K. Ni. *Quantum science with optical tweezer arrays of ultracold atoms and molecules*, Nature Physics, 1–10 (Nov. 2021). DOI: 10.1038/s41567-021-01357-2 (cit. on pp. 1, 2, 8).

[26] Barredo, D., S. de Léséleuc, V. Lienhard, T. Lahaye, and A. Browaeys. *An atom-by-atom assembler of defect-free arbitrary two-dimensional atomic arrays*, Science **354**., 1021–1023 (Nov. 2016). DOI: 10.1126/science.aah3778 (cit. on pp. 1, 105, 111).

[27] Endres, M., H. Bernien, A. Keesling, H. Levine, E. R. Anschuetz, A. Krajenbrink, C. Senko, V. Vuletic, M. Greiner, and M. D. Lukin. *Atom-by-atom assembly of defect-free one-dimensional cold atom arrays*, Science **354**., 1024–1027 (Nov. 2016). DOI: 10.1126/science.aah3752 (cit. on pp. 1, 34, 79, 105, 111).

[28] Ohl de Mello, D., D. Schäffner, J. Werkmann, T. Preuschoff, L. Kohfahl, M. Schlosser, and G. Birkl. *Defect-Free Assembly of 2D Clusters of More Than 100 Single-Atom Quantum Systems*, Physical Review Letters **122**., 203601 (May 2019). DOI: 10.1103/PhysRevLett.122.203601 (cit. on p. 1).

[29] Schäffner, D., T. Preuschoff, S. Ristok, L. Brozio, M. Schlosser, H. Giessen, and G. Birkl. *Arrays of optical tweezers based on 3D-printed microlens arrays*, Optics Express **28.**, 8640–8645 (Mar. 2020). DOI: 10.1364/OE.386243 (cit. on p. 1).

[30] Grimm, R., M. Weidemüller, and Y. B. Ovchinnikov. *Optical dipole traps for neutral atoms*, Advances In Atomic, Molecular, and Optical Physics, Academic Press, **42.**, 95–170 (2000). DOI: 10.1016/S1049-250X(08)60186-X (cit. on pp. 1, 42).

[31] Adams, C. S., J. D. Pritchard, and J. P. Shaffer. *Rydberg atom quantum technologies*, Journal of Physics B: Atomic, Molecular and Optical Physics **53**., 012002 (Jan. 2020). DOI: 10.1088/1361-6455/ab52ef (cit. on pp. 2, 8, 40).

[32] Lukin, M. D., M. Fleischhauer, R. Cote, L. M. Duan, D. Jaksch, J. I. Cirac, and P. Zoller. *Dipole Blockade and Quantum Information Processing in Mesoscopic Atomic Ensembles*, Physical Review Letters **87**. (July 2001). DOI: 10.1103/PhysRevLett.87.037901 (cit. on pp. 2, 4, 8, 33, 34, 38–40).

[33] De Léséleuc, S., V. Lienhard, P. Scholl, D. Barredo, S. Weber, N. Lang, H. P. Büchler, T. Lahaye, and A. Browaeys. *Observation of a symmetry-protected topological phase of interacting bosons with Rydberg atoms*, Science **365**., 775–780 (Aug. 2019). DOI: 10.1126/science.aav9105 (cit. on pp. 2, 38).

[34] Madjarov, I. S., A. Cooper, A. L. Shaw, J. P. Covey, V. Schkolnik, T. H. Yoon, J. R. Williams, and M. Endres. *An Atomic-Array Optical Clock with Single-Atom Readout*, Physical Review X **91**. Publisher: American Physical Society, 41052 (Dec. 2019). DOI: 10.1103/PhysRevX.9.041052 (cit. on p. 2).

[35] Norcia, M. A., A. W. Young, W. J. Eckner, E. Oelker, J. Ye, and A. M. Kaufman. *Seconds-scale coherence on an optical clock transition in a tweezer array*, Science **366**., 93–97 (Oct. 2019). DOI: 10.1126/science.aay0644 (cit. on p. 2).

[36] Saskin, S., J. T. Wilson, B. Grinkemeyer, and J. D. Thompson. *Narrow-Line Cooling and Imaging of Ytterbium Atoms in an Optical Tweezer Array*, Physical Review Letters **122.**, 143002 (Apr. 2019). DOI: 10.1103/PhysRevLett.122.143002 (cit. on pp. 2, 41).

[37] Graham, T. M., M. Kwon, B. Grinkemeyer, Z. Marra, X. Jiang, M. T. Lichtman, Y. Sun, M. Ebert, and M. Saffman. *Rydberg-Mediated Entanglement in a Two-Dimensional Neutral Atom Qubit Array*, Physical Review Letters **123.**, 230501 (Dec. 2019). DOI: 10.1103/PhysRevLett.123.230501 (cit. on pp. 2, 32, 33, 39, 40).

[38] Levine, H. *et al. Parallel Implementation of High-Fidelity Multiqubit Gates with Neutral Atoms*, Physical Review Letters **123.**, 170503 (Oct. 2019). DOI: 10.1103/PhysRevLett.123.170503 (cit. on pp. 2, 21, 32, 33, 39, 40, 105).

[39] Madjarov, I. S., J. P. Covey, A. L. Shaw, J. Choi, A. Kale, A. Cooper, H. Pichler, V. Schkolnik, J. R. Williams, and M. Endres. *High-fidelity entanglement and detection of alkaline-earth Rydberg atoms*, Nature Physics **16.**, 857–861 (Aug. 2020). DOI: 10.1038/s41567-020-0903-z (cit. on pp. 2, 54).

[40] Semeghini, G. *et al. Probing topological spin liquids on a programmable quantum simulator*, Science **374.**, 1242–1247 (Dec. 2021). DOI: 10.1126/science.abi8794 (cit. on p. 2).

[41] Byun, A., M. Kim, and J. Ahn. *Finding the Maximum Independent Sets of Platonic Graphs Using Rydberg Atoms*, PRX Quantum **3.**, 030305 (July 2022). DOI: 10.1103/PRXQuantum.3.030305 (cit. on p. 2).

[42] Bluvstein, D. *et al. A quantum processor based on coherent transport of entangled atom arrays*, Nature **604.**, 451–456 (Apr. 2022). DOI: 10.1038/s41586-022-04592-6 (cit. on p. 2).

[43] Urban, E., T. A. Johnson, T. Henage, L. Isenhower, D. D. Yavuz, T. G. Walker, and M. Saffman. *Observation of Rydberg blockade between two atoms*, Nature Physics **5.**, 110–114 (Feb. 2009). DOI: 10.1038/nphys1178 (cit. on pp. 2, 33, 39, 40).

[44] Gaëtan, A., Y. Miroshnychenko, T. Wilk, A. Chotia, M. Viteau, D. Comparat, P. Pillet, A. Browaeys, and P. Grangier. *Observation of collective excitation of two individual atoms in the Rydberg blockade regime*, Nature Physics **5.**, 115–118 (Feb. 2009). DOI: 10.1038/nphys1183 (cit. on p. 2).

[45] Wilk, T., A. Gaëtan, C. Evellin, J. Wolters, Y. Miroshnychenko, P. Grangier, and A. Browaeys. *Entanglement of Two Individual Neutral Atoms Using Rydberg Blockade*, Physical Review Letters **104.** (Jan. 2010). DOI: 10.1103/PhysRevLett.104.010502 (cit. on pp. 2, 33, 39, 40).

[46] Saffman, M., T. G. Walker, and K. Mølmer. *Quantum Information with Rydberg Atoms*, Reviews of Modern Physics **82.**, 2313–2363 (2010). DOI: 10.1103/RevModPhys.82.2313 (cit. on pp. 2, 4, 8, 33–36, 38–40, 84).

[47] Lechner, W., P. Hauke, and P. Zoller. *A quantum annealing architecture with all-to-all connectivity from local interactions*, Science Advances **1**., e1500838 (Oct. 2015). DOI: 10.1126/sciadv.1500838 (cit. on pp. 2, 113).

[48] Glaetzle, A. W., R. M. W. van Bijnen, P. Zoller, and W. Lechner. *A Coherent Quantum Annealer with Rydberg Atoms*, Nature Communications **8**. (June 2017). DOI: 10.1038/ncomms15813 (cit. on pp. 2, 33, 39, 40, 113).

[49] Bernien, H. *et al. Probing many-body dynamics on a 51-atom quantum simulator*, Nature **551**., 579–584 (Nov. 2017). DOI: 10.1038/nature24622 (cit. on pp. 2, 40).

[50] Ebadi, S. *et al. Quantum optimization of maximum independent set using Rydberg atom arrays*, Science **376**, 1209–1215 (June 2022). DOI: 10.1126/science.abo6587 (cit. on pp. 2, 113).

[51] Ebadi, S. *et al. Quantum phases of matter on a 256-atom programmable quantum simulator*, Nature **595.**, 227–232 (July 2021). DOI: 10.1038/s41586-021-03582-4 (cit. on p. 2).

[52] Scholl, P. *et al. Microwave-engineering of programmable XXZ Hamiltonians in arrays of Rydberg atoms*, PRX Quantum **3**. (Apr. 2022). DOI: 10.1103/PRXQuantum.3.020303 (cit. on pp. 2, 38, 40).

[53] Bluvstein, D. *et al. Controlling quantum many-body dynamics in driven Rydberg atom arrays*, Science **371**., 1355–1359 (Mar. 2021). DOI: 10.1126/science.abg2530 (cit. on p. 2).

[54] Jau, Y.-Y., A. M. Hankin, T. Keating, I. H. Deutsch, and G. W. Biedermann. *Entangling atomic spins with a Rydberg-dressed spin-flip blockade*, Nature Physics **12.**, 71–74 (Jan. 2016). DOI: 10.1038/nphys3487 (cit. on pp. 2, 32, 41, 46, 47, 112).

[55] Zeiher, J., J.-y. Choi, A. Rubio-Abadal, T. Pohl, R. van Bijnen, I. Bloch, and C. Gross. *Coherent Many-Body Spin Dynamics in a Long-Range Interacting Ising Chain*, Physical Review X **7.**, 041063 (Dec. 2017). DOI: 10.1103/PhysRevX.7.041063 (cit. on pp. 2, 47).

[56] Borish, V., O. Marković, J. A. Hines, S. V. Rajagopal, and M. Schleier-Smith. *Transverse-Field Ising Dynamics in a Rydberg-Dressed Atomic Gas*, Physical Review Letters **124.**, 63601 (Feb. 2020). DOI: 10.1103/PhysRevLett.124.063601 (cit. on pp. 2, 41, 46, 47, 73, 75, 78, 80, 83, 92, 109).

[57] Zeiher, J., R. Van Bijnen, P. Schauss, S. Hild, J.-Y. Choi, T. Pohl, I. Bloch, and C. Gross. *Many-body interferometry of a Rydberg-dressed spin lattice*, Nature Physics **12**, 1095–1099 (Aug. 2016). DOI: 10.1038/nphys3835 (cit. on pp. 2, 41, 46, 47, 67–69, 72, 75, 78, 79, 83, 92, 101, 109, 112).

[58] Hines, J. A., S. V. Rajagopal, G. L. Moreau, M. D. Wahrman, N. A. Lewis, O. Marković, and M. Schleier-Smith. *Spin Squeezing by Rydberg Dressing in an Array of Atomic Ensembles*, Physical Review Letters **131.**, 063401 (Aug. 2023). DOI: 10.1103/PhysRevLett.131.063401 (cit. on pp. 2, 40, 41, 80).

[59] Tiecke, T. “Feshbach resonances in ultracold mixtures of the fermionic quantum gases 6Li and 40K.” OCLC: 701095491. PhD thesis. Amsterdam: Universiteit van Amsterdam, Dec. 15, 2009 (cit. on pp. 2, 102, 114).

[60] Lorenz, N. “A Rydberg Tweezer Platform with Potassium Atoms.” PhD thesis. München: Ludwig-Maximilians-Universität München, Feb. 1, 2021 (cit. on pp. 2, 11, 13, 18, 21, 23–26, 46, 48, 101–103, 114).

[61] Ang’Ong’A, J. “Towards Synthetic Rydberg Lattices with Optical Tweezer Arrays.” PhD thesis. Urbana, Illinois: University of Illinois Urbana-Champaign, 2021 (cit. on pp. 2, 110).

[62] Steinert, L.-M., P. Osterholz, R. Eberhard, L. Festa, N. Lorenz, Z. Chen, A. Trautmann, and C. Gross. *Spatially Tunable Spin Interactions in Neutral Atom Arrays*, Physical Review Letters **130**., 243001 (June 2023). DOI: 10.1103/PhysRevLett.130.243001 (cit. on pp. 2, 47, 59, 82, 87, 91, 93, 95–97, 99, 102, 104, 106, 112, 120).

[63] De Léséleuc, S., D. Barredo, V. Lienhard, A. Browaeys, and T. Lahaye. *Analysis of imperfections in the coherent optical excitation of single atoms to Rydberg states*, Physical Review A **97**., 53803 (May 2018). DOI: 10.1103/PhysRevA.97.053803 (cit. on pp. 2, 27, 53, 54, 59).

[64] Rydberg, J. *XXXIV. On the structure of the line-spectra of the chemical elements*, Philosophical Magazine and Journal of Science **29**., 331–337 (1890). DOI: 10.1080/14786449008619945 (cit. on p. 4).

[65] Gallagher, T. F. *Rydberg Atoms*, Rep. Prog. Phys. **51**, 143 (1988). DOI: 10.1088/0034-4885/51/2/001 (cit. on pp. 4, 8, 9, 34, 36, 40).

[66] Browaeys, A. and T. Lahaye. *Many-body physics with individually controlled Rydberg atoms*, Nature Physics **16**., 132–142 (Feb. 2020). DOI: 10.1038/s41567-019-0733-z (cit. on pp. 4, 40, 82).

[67] Martinson, I. and L. Curtis. *Janne Rydberg – his life and work*, Nuclear Instruments and Methods in Physics Research Section B: Beam Interactions with Materials and Atoms **235**., 17–22 (July 2005). DOI: 10.1016/j.nimb.2005.03.137 (cit. on p. 4).

[68] Sibalic, N., J. Pritchard, C. Adams, and K. Weatherill. *ARC: An open-source library for calculating properties of alkali Rydberg atoms*, Computer Physics Communications **220.**, 319–331 (Nov. 2017). DOI: 10.1016/j.cpc.2017.06.015 (cit. on pp. 4–7, 9, 39, 40, 75).

[69] Corsey, J., D. Schwab, J. Tsai, and R. Dragoset. *Atomic Weights and Isotopic Compositions (version 4.1)*. Version Online Available: http://physics.nist.gov/Comp (2017, March, 14). Gaithersburg, MD, 2015 (cit. on p. 5).

[70] Lorenzen, C.-J. and K. Niemax. *Quantum Defects of the $n\,^2P_{1/2,3/2}$ Levels in ^{39}K I and ^{85}Rb I*, Physica Scripta **27**., 300–305 (Apr. 1983). DOI: 10.1088/0031-8949/27/4/012 (cit. on p. 5).

[71] Pritchard, J. D. *A spotlight on circular states*, Nature Physics **18.**, 480–481 (May 2022). DOI: 10.1038/s41567-022-01572-5 (cit. on pp. 5, 41).

[72] King, B. E. *Angular Momentum Coupling and Rabi Frequencies for Simple Atomic Transitions*. Apr. 29, 2008. DOI: 10.48550/arXiv.0804.4528 (cit. on p. 7).

[73] Le Kien, F., P. Schneeweiss, and A. Rauschenbeutel. *Dynamical polarizability of atoms in arbitrary light fields: general theory and application to cesium*, The European Physical Journal D **67.**, 92 (May 2013). DOI: 10.1140/epjd/e2013-30729-x (cit. on p. 7).

[74] Löw, R., H. Weimer, J. Nipper, J. B. Balewski, B. Butscher, H. P. Büchler, and T. Pfau. *An experimental and theoretical guide to strongly interacting Rydberg gases*, J. Phys. B: At. Mol. Phys. **45.**, 113001 (Dec. 2012). DOI: 10.1088/0953-4075/45/11/113001 (cit. on pp. 7, 8).

[75] Festa, L., N. Lorenz, L.-M. Steinert, Z. Chen, P. Osterholz, R. Eberhard, and C. Gross. *Blackbody-radiation-induced facilitated excitation of Rydberg atoms in optical tweezers*, Physical Review A **105**. (Jan. 2022). DOI: 10.1103/PhysRevA.105.013109 (cit. on pp. 11, 13, 15, 16, 47, 74, 80, 92, 95, 111).

[76] Hutzler, N. R., L. R. Liu, Y. Yu, and K.-K. Ni. *Eliminating light shifts for single atom trapping Related content Extending a release-and-recapture scheme to single atom optical tweezer for effective temperature evaluation*, New Journal of Physics **19**. (Feb. 2017). DOI: 10.1088/1367-2630/aa5a3b (cit. on pp. 12, 14, 22, 111).

[77] Salomon, G., L. Fouché, P. Wang, A. Aspect, P. Bouyer, and T. Bourdel. *Gray-molasses cooling of 39K to a high phase-space density*, Europhysics Letters **104**. (Dec. 2013). DOI: 10.1209/0295-5075/104/63002 (cit. on pp. 12, 115).

[78] Festa, L. "Black-body radiation induced correlated excitation of Potassium Rydberg atoms in tweezer arrays." PhD thesis. München: Ludwig Maximilians Universität München, Nov. 8, 2021 (cit. on pp. 13, 46, 59, 77–80, 110, 120).

[79] Ang'ong'a, J., C. Huang, J. P. Covey, and B. Gadway. *Gray molasses cooling of K 39 atoms in optical tweezers*, Physical Review Research **4.**, 013240 (Mar. 2022). DOI: 10.1103/PhysRevResearch.4.013240 (cit. on pp. 13, 15, 18, 79, 110, 111).

[80] Lorenz, N., L. Festa, L.-M. Steinert, and C. Gross. *Raman sideband cooling in optical tweezer arrays for Rydberg dressing*, SciPost Phys **10.**, 52 (Mar. 2021). DOI: 10.21468/SciPostPhys.10.3.052 (cit. on pp. 15, 21, 23–27, 92).

[81] Kerman, A., V. Vuletić, C. Chin, and S. Chu. *Beyond Optical Molasses: 3D Raman Sideband Cooling of Atomic Cesium to High Phase-Space Density*, Physical Review Letters **84.**, 439–442 (Jan. 2000). DOI: 10.1103/PhysRevLett.84.439 (cit. on pp. 21, 23).

[82] Jones, M. P. A., J. Beugnon, A. Gaëtan, J. Zhang, G. Messin, A. Browaeys, and P. Grangier. *Fast quantum state control of a single trapped neutral atom*, Physical Review A **75.**, 040301 (Apr. 2007). DOI: 10.1103/PhysRevA.75.040301 (cit. on p. 21).

[83] Monroe, C., D. M. Meekhof, B. E. King, S. R. Jefferts, W. M. Itano, D. J. Wineland, and P. Gould. *Resolved-Sideband Raman Cooling of a Bound Atom to the 3D Zero-Point Energy*, Physical Review Letters **75**., 4011–4014 (Nov. 1995). DOI: 10.1103/PhysRevLett.75.4011 (cit. on pp. 21, 23).

[84] Hamann, S. E., D. L. Haycock, G. Klose, P. H. Pax, I. H. Deutsch, and P. S. Jessen. *Resolved-Sideband Raman Cooling to the Ground State of an Optical Lattice*, Physical Review Letters **80.**, 4149 (May 1998). DOI: 10.1103/PhysRevLett.80.4149 (cit. on pp. 21, 23).

[85] Kaufman, A. M., B. J. Lester, and C. A. Regal. *Cooling a Single Atom in an Optical Tweezer to Its Quantum Ground State*, Physical Review X **2**., 41014 (Nov. 2012). DOI: 10.1103/PhysRevX.2.041014 (cit. on pp. 21–23).

[86] Thompson, J. D., T. G. Tiecke, A. S. Zibrov, V. Vuletić, and M. D. Lukin. *Coherence and Raman Sideband Cooling of a Single Atom in an Optical Tweezer*, Physical Review Letters **110**., 133001 (Mar. 2013). DOI: 10.1103/PhysRevLett.110.133001 (cit. on pp. 21, 23, 25).

[87] Kaufman, A. M. "Laser-cooling atoms to indistinguishability : Atomic Hong-Ou-Mandel interference and entanglement through spin exchange." PhD thesis. University of Colorado, 2015 (cit. on p. 21).

[88] Lester, B. J., A. M. Kaufman, and C. A. Regal. *Raman cooling imaging: Detecting single atoms near their ground state of motion*, Physical Review A **90**. (July 2014). DOI: 10.1103/PhysRevA.90.011804 (cit. on p. 23).

[89] Norcia, M. A., A. W. Young, and A. M. Kaufman. *Microscopic Control and Detection of Ultracold Strontium in Optical-Tweezer Arrays*, Physical Review X **8**., 41054 (Dec. 2018). DOI: 10.1103/PhysRevX.8.041054 (cit. on pp. 23, 41).

[90] Yu, Y., N. R. Hutzler, J. T. Zhang, L. R. Liu, J. D. Hood, T. Rosenband, and K.-K. Ni. *Motional-ground-state cooling outside the Lamb-Dicke regime*, Physical Review A **97.**, 063423 (June 2018). DOI: 10.1103/PhysRevA.97.063423 (cit. on pp. 23, 25).

[91] Cheuk, L. W., M. A. Nichols, M. Okan, T. Gersdorf, V. V. Ramasesh, W. S. Bakr, T. Lompe, and M. W. Zwierlein. *Quantum-Gas Microscope for Fermionic Atoms*, Physical Review Letters **114**. (May 2015). DOI: 10.1103/PhysRevLett.114.193001 (cit. on pp. 25, 29).

[92] Tuchendler, C., A. M. Lance, A. Browaeys, Y. R. P. Sortais, and P. Grangier. *Energy distribution and cooling of a single atom in an optical tweezer*, Physical Review A **78.**, 33425 (Sept. 2008). DOI: 10.1103/PhysRevA.78.033425 (cit. on p. 27).

[93] De Léséleuc, S. "Quantum simulation of spin models with assembled arrays of Rydberg atoms." PhD thesis. Paris: Université Paris-Saclay, 2018 (cit. on p. 27).

[94] Ryabtsev, I. I., I. I. Beterov, D. B. Tretyakov, V. M. Entin, and E. A. Yakshina. *Doppler- and recoil-free laser excitation of Rydberg states via three-photon transitions*, Physical Review A **84.**, 053409 (Nov. 2011). DOI: 10.1103/PhysRevA.84.053409 (cit. on p. 27).

[95] Young, A. W., W. J. Eckner, W. R. Milner, D. Kedar, M. A. Norcia, E. Oelker, N. Schine, J. Ye, and A. M. Kaufman. *Half-minute-scale atomic coherence and high relative stability in a tweezer clock*, Nature **588.**, 408–413 (Dec. 2020). DOI: 10.1038/s41586-020-3009-y (cit. on pp. 27, 104).

[96] Omran, A. *et al. Generation and manipulation of Schrödinger cat states in Rydberg atom arrays*, Science **365**., 570–574 (Aug. 2019). DOI: 10.1126/science.aax9743 (cit. on pp. 33, 39, 40).

[97] Ma, S., A. P. Burgers, G. Liu, J. Wilson, B. Zhang, and J. D. Thompson. *Universal Gate Operations on Nuclear Spin Qubits in an Optical Tweezer Array of Yb 171 Atoms*, Physical Review X **12**., 021028 (May 2022). DOI: 10.1103/PhysRevX.12.021028 (cit. on pp. 33, 39, 40).

[98] Schauss, P., M. Cheneau, M. Endres, T. Fukuhara, S. Hild, A. Omran, T. Pohl, C. Gross, S. Kuhr, and I. Bloch. *Observation of spatially ordered structures in a two-dimensional Rydberg gas*, Nature **490.** (Nov. 2012). DOI: 10.1038/nature11596 (cit. on pp. 33, 39, 40).

[99] Schauss, P., J. Zeiher, T. Fukuhara, S. Hild, M. Cheneau, T. Macrì, T. Pohl, I. Bloch, and C. Gross. *Crystallization in Ising quantum magnets*, Science **347**., 1455–1458 (Mar. 2015). DOI: 10.1126/science.1258351 (cit. on pp. 33, 34, 39, 40, 83, 92).

[100] Müller, L. "A Low Phase Noise Laser System for Rydberg Dressing." Master Thesis. Tübingen: Eberhard Karls Universität Tübingen, 2023 (cit. on pp. 33, 57, 60, 61).

[101] Bloch, I., J. Dalibard, and W. Zwerger. *Many-body physics with ultracold gases*, Reviews of Modern Physics **80.**, 885–964 (2008). DOI: 10.1103/RevModPhys.80.885 (cit. on p. 34).

[102] Löw, R., H. Weimer, U. Krohn, R. Heidemann, V. Bendkowsky, B. Butscher, H. P. Büchler, and T. Pfau. *Universal scaling in a strongly interacting Rydberg gas*, Physical Review A **80**., 1–5 (Sept. 2009). DOI: 10.1103/PhysRevA.80.033422 (cit. on p. 34).

[103] Browaeys, A., D. Barredo, and T. Lahaye. *Experimental investigations of the dipolar interactions between a few individual Rydberg atoms*, Journal of Physics B: Atomic, Molecular and Optical Physics **49**. (2016). DOI: 10.1088/0953-4075/49/15/152001 (cit. on p. 34).

[104] Henkel, N. "Rydberg-dressed Bose-Einstein condensates." PhD thesis. Dresdem: Technischen Universität Dresden, 2013 (cit. on pp. 34, 35, 86, 88).

[105] Weber, S., C. Tresp, H. Menke, A. Urvoy, O. Firstenberg, H. P. Büchler, and S. Hofferberth. *Calculation of Rydberg interaction potentials*, Journal of Physics B: Atomic, Molecular and Optical Physics **50.**, 133001 (June 2017). DOI: 10.1088/1361-6455/aa743a (cit. on pp. 34, 37, 39, 70, 71, 73, 77, 84, 90, 91, 116).

[106] Glaetzle, A. W., M. Dalmonte, R. Nath, I. Rousochatzakis, R. Moessner, and P. Zoller. *Quantum Spin-Ice and Dimer Models with Rydberg Atoms*, Physical Review X **4**., 41037 (Nov. 2014). DOI: 10/f3s3b5 (cit. on pp. 35, 36).

[107] Zeiher, J. "Realization of Rydberg-dressed quantum magnets." PhD thesis. München: Ludwig-Maximilians-Universität München, 2017 (cit. on pp. 36, 80, 83, 88, 92).

[108] Hollerith, S. "A microscopically and vibrationally resolved study of Rydberg macrodimers." PhD thesis. München: Ludwig-Maximilians-Universität München, Mar. 18, 2022 (cit. on p. 36).

[109] Barredo, D., H. Labuhn, S. Ravets, T. Lahaye, A. Browaeys, and C. S. Adams. *Coherent Excitation Transfer in a Spin Chain of Three Rydberg Atoms*, Physical Review Letters **114**. (Mar. 2015). DOI: 10.1103/PhysRevLett.114.113002 (cit. on pp. 38, 40, 82).

[110] De Léséleuc, S., D. Barredo, V. Lienhard, A. Browaeys, and T. Lahaye. *Local optical control of the resonant dipole-dipole interaction between Rydberg atoms*, Physical Review Letters **119**. (Aug. 2017). DOI: 10.1103/PhysRevLett.119.053202 (cit. on p. 38).

[111] Lienhard, V. *et al. Realization of a Density-Dependent Peierls Phase in a Synthetic, Spin-Orbit Coupled Rydberg System*, Physical Review X **10**., 021031 (May 8, 2020). DOI: 10.1103/PhysRevX.10.021031 (cit. on p. 38).

[112] Reinhard, A., T. C. Liebisch, B. Knuffman, and G. Raithel. *Level shifts of rubidium Rydberg states due to binary interactions*, Physical Review A **75**., 032712 (Mar. 2007). DOI: 10.1103/PhysRevA.75.032712 (cit. on p. 38).

[113] Heidemann, R., U. Raitzsch, V. Bendkowsky, B. Butscher, R. Löw, L. Santos, and T. Pfau. *Evidence for coherent collective rydberg excitation in the strong blockade regime*, Physical Review Letters **99**., 1–4 (Oct. 2007). DOI: 10.1103/PhysRevLett.99.163601 (cit. on p. 38).

[114] Walker, T. G. and M. Saffman. *Consequences of Zeeman degeneracy for the van der Waals blockade between Rydberg atoms*, Physical Review A **77**., 032723 (Mar. 2008). DOI: 10.1103/PhysRevA.77.032723 (cit. on p. 38).

[115] Béguin, L., A. Vernier, R. Chicireanu, T. Lahaye, and A. Browaeys. *Direct Measurement of the van der Waals Interaction between Two Rydberg Atoms*, Physical Review Letters **110**., 263201 (June 2013). DOI: 10.1103/PhysRevLett.110.263201 (cit. on p. 38).

[116] Ravets, S., H. Labuhn, D. Barredo, L. Béguin, T. Lahaye, and A. Browaeys. *Coherent dipole–dipole coupling between two single Rydberg atoms at an electrically-tuned Förster resonance*, Nature Physics **10**., 914–917 (Dec. 2014). DOI: 10.1038/nphys3119 (cit. on p. 38).

[117] Samboy, N. *Long-range interactions between rubidium and potassium Rydberg atoms*, Physical Review A **95**., 032702 (Mar. 2017). DOI: 10.1103/PhysRevA.95.032702 (cit. on p. 38).

[118] Kamenski, A. A., N. L. Manakov, S. N. Mokhnenko, and V. D. Ovsiannikov. *Energy of van der Waals and dipole-dipole interactions between atoms in Rydberg states*, Physical Review A **96**., 032716 (Sept. 2017). DOI: 10.1103/PhysRevA.96.032716 (cit. on p. 38).

[119] Paris-Mandoki, A., C. Braun, and S. Hofferberth. "Correlations between interacting Rydberg atoms," Proceedings of the 2nd International Conference on Advances in Materials, Machinery, Electronics. Xi'an City, China, 2018, p. 020001. DOI: 10.1063/1.5031690 (cit. on p. 38).

[120] Stecker, M., R. Nold, L.-M. Steinert, J. Grimmel, D. Petrosyan, J. Fortágh, and A. Günther. *Controlling the dipole blockade and ionization rate of Rydberg atoms in strong electric fields*, Physical Review Letters **125**. (Aug. 2020). DOI: 10.1103/PhysRevLett.125.103602 (cit. on p. 39).

[121] Stecker, M. "Spatial and temporal correlations in cold Rydberg gases." PhD thesis. Tübingen: Eberhard Karls Universität Tübingen, 2018 (cit. on p. 39).

[122] Firstenberg, O., C. S. Adams, and S. Hofferberth. *Nonlinear quantum optics mediated by Rydberg interactions*, Journal of Physics B: Atomic, Molecular and Optical Physics **49**., 152003 (Aug. 2016). DOI: 10.1088/0953-4075/49/15/152003 (cit. on pp. 40, 41).

[123] Cong, I., H. Levine, A. Keesling, D. Bluvstein, S.-T. Wang, and M. D. Lukin. *Hardware-Efficient, Fault-Tolerant Quantum Computation with Rydberg Atoms*, Physical Review X **12**., 021049 (June 2022). DOI: 10.1103/PhysRevX.12.021049 (cit. on p. 40).

[124] Wu, Y., S. Kolkowitz, S. Puri, and J. D. Thompson. *Erasure conversion for fault-tolerant quantum computing in alkaline earth Rydberg atom arrays*, Nature Communications **13**., 4657 (Aug. 2022). DOI: 10.1038/s41467-022-32094-6 (cit. on p. 40).

[125] Evered, S. J. *et al. High-fidelity parallel entangling gates on a neutral atom quantum computer*. Apr. 2023. DOI: 10.48550/arXiv.2304.05420 (cit. on p. 40).

[126] Brion, E., L. H. Pedersen, M. Saffman, and K. Mølmer. *Error Correction in Ensemble Registers for Quantum Repeaters and Quantum Computers*, Physical Review Letters **100**., 110506 (Mar. 2008). DOI: 10.1103/PhysRevLett.100.110506 (cit. on p. 40).

[127] Han, Y., B. He, K. Heshami, C.-Z. Li, and C. Simon. *Quantum repeaters based on Rydberg-blockade-coupled atomic ensembles*, Physical Review A **81**., 052311 (May 2010). DOI: 10.1103/PhysRevA.81.052311 (cit. on p. 40).

[128] Wu, Y., J. Liu, and C. Simon. *Near-term performance of quantum repeaters with imperfect ensemble-based quantum memories*, Physical Review A **101**., 042301 (Apr. 2020). DOI: 10.1103/PhysRevA.101.042301 (cit. on p. 40).

[129] Günter, G., H. Schempp, M. Robert-de-Saint-Vincent, V. Gavryusev, S. Helmrich, C. S. Hofmann, S. Whitlock, and M. Weidemüller. *Observing the Dynamics of Dipole-Mediated Energy Transport by Interaction-Enhanced Imaging*, Science **342.**, 954–956 (Nov. 2013). DOI: 10.1126/science.1244843 (cit. on p. 40).

[130] Lienhard, V., S. De Léséleuc, D. Barredo, T. Lahaye, A. Browaeys, M. Schuler, L. P. Henry, and A. M. Läuchli. *Observing the Space- and Time-Dependent Growth of Correlations in Dynamically Tuned Synthetic Ising Models with Antiferromagnetic Interactions*, Physical Review X **8.**, 1–17 (June 2018). DOI: 10.1103/PhysRevX.8.021070 (cit. on pp. 40, 83, 92).

[131] Kaubruegger, R., P. Silvi, C. Kokail, R. van Bijnen, A. M. Rey, J. Ye, A. M. Kaufman, and P. Zoller. *Variational Spin-Squeezing Algorithms on Programmable Quantum Sensors*, Physical Review Letters **123**. (Dec. 2019). DOI: 10.1103/PhysRevLett.123.260505 (cit. on p. 40).

[132] Eckner, W. J., N. D. Oppong, A. Cao, A. W. Young, W. R. Milner, J. M. Robinson, J. Ye, and A. M. Kaufman. *Realizing spin squeezing with Rydberg interactions in a programmable optical clock*. July 2023 (cit. on p. 40).

[133] Ramos, A., K. Moore, and G. Raithel. *Measuring the Rydberg constant using circular Rydberg atoms in an intensity-modulated optical lattice*, Physical Review A **96.**, 032513 (Sept. 2017). DOI: 10.1103/PhysRevA.96.032513 (cit. on p. 41).

[134] Chang, D. E., V. Vuletić, and M. D. Lukin. *Quantum nonlinear optics — photon by photon*, Nature Photonics **8.**, 685–694 (Sept. 2014). DOI: 10.1038/nphoton.2014.192 (cit. on p. 41).

[135] Gorniaczyk, H., C. Tresp, J. Schmidt, H. Fedder, and S. Hofferberth. *Single-Photon Transistor Mediated by Interstate Rydberg Interactions*, Physical Review Letters **113.**, 053601 (July 2014). DOI: 10.1103/PhysRevLett.113.053601 (cit. on p. 41).

[136] Balewski, J. B., A. T. Krupp, A. Gaj, S. Hofferberth, R. Löw, and T. Pfau. *Rydberg dressing: Understanding of collective many-body effects and implications for experiments*, New Journal of Physics **16.** (June 2014). DOI: 10.1088/1367-2630/16/6/063012 (cit. on pp. 41, 45, 46).

[137] Hollerith, S. *et al. Realizing Distance - Selective Interactions in a Rydberg-Dressed Atom Array*, Physical Review Letters **128.**, 113602 (Mar. 2022). DOI: 10.1103/PhysRevLett.128.113602 (cit. on pp. 41, 46, 47, 83, 92, 112).

[138] Wu, X., F. Yang, S. Yang, K. Mølmer, T. Pohl, M. K. Tey, and L. You. *Manipulating synthetic gauge fluxes via multicolor dressing of Rydberg-atom arrays*, Physical Review Research **4.**, L032046 (Sept. 2022). DOI: 10.1103/PhysRevResearch.4.L032046 (cit. on pp. 41, 46, 107).

[139] Bijnen, R. M. W. van and T. Pohl. *Quantum Magnetism and Topological Ordering via Rydberg Dressing near Förster Resonances*, Physical Review Letters **114.**, 243002 (June 2015). DOI: 10.1103/PhysRevLett.114.243002 (cit. on pp. 41, 46, 47, 74, 83, 97, 101, 105, 112, 113).

[140] Arias, A., G. Lochead, T. M. Wintermantel, S. Helmrich, and S. Whitlock. *Realization of a Rydberg-Dressed Ramsey Interferometer and Electrometer*, Physical Review Letters **122.** (Feb. 2019). DOI: 10.1103/PhysRevLett.122.053601 (cit. on pp. 41, 46, 112).

[141] Mitra, A., M. J. Martin, G. W. Biedermann, A. M. Marino, P. M. Poggi, and I. H. Deutsch. *Robust Mølmer-Sørensen gate for neutral atoms using rapid adiabatic Rydberg dressing*, Physical Review A **101**., 030301 (Mar. 2020). DOI: 10.1103/PhysRevA.101.030301 (cit. on pp. 41, 46, 47).

[142] Wang, J. and R. Côté. *Ultralong-range molecule engineering via Rydberg dressing*, Physical Review Research **2**., 023019 (Apr. 2020). DOI: 10.1103/PhysRevResearch.2.023019 (cit. on pp. 41, 46, 113).

[143] Eiles, M. T. *Formation of long-range Rydberg molecules in two-component ultracold gases*, Physical Review A **98**., 042706 (Oct. 2018). DOI: 10.1103/PhysRevA.98.042706 (cit. on p. 41).

[144] Shaffer, J. P., S. T. Rittenhouse, and H. R. Sadeghpour. *Ultracold Rydberg molecules*, Nature Communications **9**., 1965 (May 2018). DOI: 10.1038/s41467-018-04135-6 (cit. on p. 41).

[145] Engel, F., T. Dieterle, F. Hummel, C. Fey, P. Schmelcher, R. Löw, T. Pfau, and F. Meinert. *Precision Spectroscopy of Negative-Ion Resonances in Ultralong-Range Rydberg Molecules*, Physical Review Letters **123**., 073003 (Aug. 2019). DOI: 10.1103/PhysRevLett.123.073003 (cit. on p. 41).

[146] Hummel, F., P. Schmelcher, and M. T. Eiles. *Vibronic interactions in trilobite and butterfly Rydberg molecules*, Physical Review Research **5**., 013114 (Feb. 2023). DOI: 10.1103/PhysRevResearch.5.013114 (cit. on p. 41).

[147] Lis, J. W., A. Senoo, W. F. McGrew, F. Rönchen, A. Jenkins, and A. M. Kaufman. *Mid-circuit operations using the omg-architecture in neutral atom arrays*. June 2023. DOI: 10.48550/arXiv.2305.19266 (cit. on p. 41).

[148] Ma, S., G. Liu, P. Peng, B. Zhang, S. Jandura, J. Claes, A. P. Burgers, G. Pupillo, S. Puri, and J. D. Thompson. *High-fidelity gates with mid-circuit erasure conversion in a metastable neutral atom qubit*, (May 2023). DOI: 10.48550/arXiv.2305.05493 (cit. on p. 41).

[149] Cantat-Moltrecht, T., R. Cortiñas, B. Ravon, P. Méhaignerie, S. Haroche, J. M. Raimond, M. Favier, M. Brune, and C. Sayrin. *Long-lived circular Rydberg states of laser-cooled rubidium atoms in a cryostat*, Physical Review Research **2**., 022032 (May 2020). DOI: 10.1103/PhysRevResearch.2.022032 (cit. on p. 41).

[150] Muni, A., L. Lachaud, A. Couto, M. Poirier, R. C. Teixeira, J.-M. Raimond, M. Brune, and S. Gleyzes. *Optical coherent manipulation of alkaline-earth circular Rydberg states*, Nature Physics **18**., 502–505 (May 2022). DOI: 10.1038/s41567-022-01519-w (cit. on p. 41).

[151] Chew, Y., T. Tomita, T. P. Mahesh, S. Sugawa, S. De Léséleuc, and K. Ohmori. *Ultrafast energy exchange between two single Rydberg atoms on a nanosecond timescale*, Nature Photonics **16**., 724–729 (Oct. 2022). DOI: 10.1038/s41566-022-01047-2 (cit. on p. 41).

[152] Heckötter, J., M. Freitag, D. Fröhlich, M. Aßmann, M. Bayer, M. A. Semina, and M. M. Glazov. *Scaling laws of Rydberg excitons*, Physical Review B **96**., 125142 (Sept. 2017). DOI: 10.1103/PhysRevB.96.125142 (cit. on p. 41).

[153] Hattermann, H., D. Bothner, L. Y. Ley, B. Ferdinand, D. Wiedmaier, L. Sárkány, R. Kleiner, D. Koelle, and J. Fortágh. *Coupling ultracold atoms to a superconducting coplanar waveguide resonator*, Nature Communications **8**., 2254 (Dec. 21, 2017). DOI: 10.1038/s41467-017-02439-7 (cit. on p. 41).

[154] Kaiser, M. *et al. Cavity-driven Rabi oscillations between Rydberg states of atoms trapped on a superconducting atom chip*, Physical Review Research **4**., 013207 (Mar. 2022). DOI: 10.1103/PhysRevResearch.4.013207 (cit. on p. 41).

[155] Niederländer, M., J. Vogel, A. Schulze-Makuch, B. Gély, A. Mokhberi, and F. Schmidt-Kaler. *Rydberg ions in coherent motional states: a new method for determining the polarizability of Rydberg ions*, New Journal of Physics **25**., 033020 (Mar. 2023). DOI: 10.1088/1367-2630/acbf06 (cit. on p. 41).

[156] Johnson, J. E. and S. L. Rolston. *Interactions between Rydberg-Dressed Atoms*, Physical Review A **82.**, 033412 (Sept. 2010). DOI: 10.1103/PhysRevA.82.033412 (cit. on pp. 42, 46).

[157] Henkel, N., R. Nath, and T. Pohl. *Three-Dimensional Roton Excitations and Supersolid Formation in Rydberg-Excited Bose-Einstein Condensates*, Physical Review Letters **104**. (May 2010). DOI: 10.1103/PhysRevLett.104.195302 (cit. on pp. 43, 86).

[158] Shavitt, I. and R. J. Bartlett. *Many-body methods in chemistry and physics : MBPT and coupled-cluster theory*. Cambridge ; New York: Cambridge University Press, 2009 (cit. on pp. 43, 86).

[159] Baillard, X., A. Gauguet, S. Bize, P. Lemonde, P. Laurent, A. Clairon, and P. Rosenbusch. *Interference-filter-stabilized external-cavity diode lasers*, Optics Communications **266**., 609–613 (Oct. 2006). DOI: 10.1016/j.optcom.2006.05.011 (cit. on pp. 46, 58).

[160] Di Domenico, G., S. Schilt, and P. Thomann. *Simple approach to the relation between laser frequency noise and laser line shape*, Applied Optics **49**., 4801 (Sept. 2010). DOI: 10.1364/AO.49.004801 (cit. on pp. 46, 58).

[161] Schmid, F., J. Weitenberg, T. W. Hänsch, T. Udem, and A. Ozawa. *Simple phase noise measurement scheme for cavity-stabilized laser systems*, Optics Letters **44**., 2709 (June 2019). DOI: 10.1364/OL.44.002709 (cit. on pp. 46, 58).

[162] Honer, J., H. Weimer, T. Pfau, and H. P. Büchler. *Collective Many-Body Interaction in Rydberg Dressed Atoms*, Physical Review Letters **105**., 160404 (Oct. 2010). DOI: 10.1103/PhysRevLett.105.160404 (cit. on p. 46).

[163] Petrosyan, D. and K. Mølmer. *Binding Potentials and Interaction Gates between Microwave-Dressed Rydberg Atoms*, Physical Review Letters **113**., 123003 (Sept. 2014). DOI: 10.1103/PhysRevLett.113.123003 (cit. on p. 46).

[164] Keating, T., R. L. Cook, A. M. Hankin, Y.-Y. Jau, G. W. Biedermann, and I. H. Deutsch. *Robust quantum logic in neutral atoms via adiabatic Rydberg dressing*, Physical Review A **91**. (Jan. 2015). DOI: 10.1103/PhysRevA.91.012337 (cit. on pp. 46, 47).

[165] Gaul, C., B. J. Desalvo, J. A. Aman, F. B. Dunning, T. C. Killian, and T. Pohl. *Resonant Rydberg Dressing of Alkaline-Earth Atoms via Electromagnetically Induced Transparency*, Physical Review Letters **116**. (July 2016). DOI: 10.1103/PhysRevLett.116.243001 (cit. on p. 46).

[166] Hollerith, S., J. Zeiher, J. Rui, A. Rubio-Abadal, V. Walther, T. Pohl, D. M. Stamper-Kurn, I. Bloch, and C. Gross. *Quantum gas microscopy of Rydberg macrodimers*, Science **364**., 664–667 (May 2019). DOI: 10.1126/science.aaw4150 (cit. on p. 47).

[167] Drever, R. W. P., J. L. Hall, F. V. Kowalski, J. Hough, G. M. Ford, A. J. Munley, and H. Ward. *Laser phase and frequency stabilization using an optical resonator*, Applied Physics B Photophysics and Laser Chemistry **31**., 97–105 (June 1983). DOI: 10.1007/BF00702605 (cit. on p. 48).

[168] Hansch, T. and B. Couillaud. *Laser frequency stabilization by polarization spectroscopy of a reflecting reference cavity*, Optics Communications **35**., 441–444 (Dec. 1980). DOI: 10.1016/0030-4018(80)90069-3 (cit. on p. 49).

[169] Levine, H., A. Keesling, A. Omran, H. Bernien, S. Schwartz, A. S. Zibrov, M. Endres, M. Greiner, V. Vuletić, and M. D. Lukin. *High-Fidelity Control and Entanglement of Rydberg-Atom Qubits*, Physical Review Letters **121**., 123603 (Sept. 2018). DOI: 10.1103/PhysRevLett.121.123603 (cit. on pp. 54, 59, 60, 101, 111).

[170] Scholl, P. *et al. Quantum simulation of 2D antiferromagnets with hundreds of Rydberg atoms*, Nature **595**., 233–238 (July 2021). DOI: 10.1038/s41586-021-03585-1 (cit. on pp. 54, 59, 82).

[171] Frink, M. E., M. A. Folkman, and L. A. Darnton. "Evaluation of the ultraviolet/ozone technique for on-orbit removal of photolyzed molecular contamination from optical surfaces," ed. by Glassford, A. P. M. San Diego, CA, Dec. 18, 1992, pp. 286–294. DOI: 10.1117/12.140739 (cit. on p. 55).

[172] Canham, J. S. "Investigation of Contamination Effects on Laser Induced Optical Damage in Space Flight Lasers," Earth science technology conference proceedings. Palo Alto, CA, 2004 (cit. on p. 55).

[173] Kokkinos, D., H. Schroeder, K. Fleury-Frenette, M. P. Georges, W. Riede, G. Tzeremes, and P. Rochus. *Laser optics in space failure risk due to laser induced contamination*, CEAS Space Journal **9**., 153–162 (June 2017). DOI: 10.1007/s12567-016-0137-1 (cit. on p. 55).

[174] Schröder, H., W. Riede, H. Kheyrandish, D. Wernham, and Y. Lien. "Investigation of UV laser induced depositions on optics under space conditions in presence of outgassing materials," *International Conference on Space Optics — ICSO 2006*. International Conference on Space Optics 2006. Ed. by Armandillo, E., J. Costeraste, and N. Karafolas. Noordwijk, Netherlands: SPIE, Nov. 21, 2017, p. 32. DOI: 10.1117/12.2308066 (cit. on p. 55).

[175] Qiu, J.-w., W. Dai, and Z.-c. Shen. *Modeling and experimental results of UV enhancement effect on spacecraft molecular contamination*, Journal of Space Safety Engineering **8**., 297–303 (Dec. 2021). DOI: 10.1016/j.jsse.2021.07.004 (cit. on p. 55).

[176] Gangloff, D. *et al. Preventing and reversing vacuum-induced optical losses in high-finesse tantalum (V) oxide mirror coatings*, Optics Express **23**., 18014 (July 2015). DOI: 10.1364/OE.23.018014 (cit. on p. 56).

[177] Guo, C., M. Kong, D. Lin, and B. Li. *Fluoride coatings for vacuum ultraviolet reflection filters*, Applied Optics **54**., 10498 (Dec. 2015). DOI: 10.1364/AO.54.010498 (cit. on p. 56).

[178] Hobbs, D. S., B. D. MacLeod, A. Manni, E. Sabatino, D. M. Bernot, S. DeFrances, J. A. Randi, and J. G. Thomas. "CW laser damage testing of RAR nano-textured fused silica and YAG," *Laser-Induced Damage in Optical Materials 2017*. Laser-Induced Damage in Optical Materials 2017. Ed. by Exarhos, G. J., D. Ristau, V. E. Gruzdev, J. A. Menapace, and M. Soileau. Boulder, United States: SPIE, Nov. 23, 2017, p. 4. DOI: 10.1117/12.2280498 (cit. on p. 56).

[179] Wei, Y., F. Pan, Q. Zhang, and P. Ma. *Atomic layer deposition for fabrication of HfO2/Al2O3 thin films with high laser-induced damage thresholds*, Nanoscale Research Letters **10**., 44 (Dec. 2015). DOI: 10.1186/s11671-015-0731-8 (cit. on p. 56).

[180] Burkley, Z., L. De Sousa Borges, B. Ohayon, A. Golovizin, J. Zhang, and P. Crivelli. *Stable high power deep-uv enhancement cavity in ultra-high vacuum with fluoride coatings*, Optics Express **29**., 27450 (Aug. 2021). DOI: 10.1364/OE.432552 (cit. on p. 57).

[181] Schawlow, A. L. and C. H. Townes. *Infrared and Optical Masers*, Physical Review **112**., 1940–1949 (Dec. 1958). DOI: 10.1103/PhysRev.112.1940 (cit. on pp. 58, 59).

[182] Henry, C. *Theory of the linewidth of semiconductor lasers*, IEEE Journal of Quantum Electronics **18**., 259–264 (Feb. 1982). DOI: 10.1109/JQE.1982.1071522 (cit. on pp. 58, 59).

[183] Rincon Celis, R. L. and M. Martinelli. *Reducing the phase noise in diode lasers*, Optics Letters **44**., 3394 (July 2019). DOI: 10.1364/OL.44.003394 (cit. on p. 59).

[184] Matveev, A. N., N. N. Kolachevsky, J. Alnis, and T. W. Hänsch. *Spectral parameters of reference-cavity-stabilised lasers*, Quantum Electronics **38**., 391–400 (Apr. 2008). DOI: 10.1070/QE2008v038n04ABEH013680 (cit. on p. 59).

[185] Kolachevsky, N., J. Alnis, C. G. Parthey, A. Matveev, R. Landig, and T. W. Haensch. *Low phase noise diode laser oscillator for 1S-2S spectroscopy in atomic hydrogen*, Optics Letters **36**., 4299 (Nov. 2011). DOI: 10.1364/OL.36.004299 (cit. on p. 59).

[186] Cheng, X., S. Cui, X. Zeng, J. Zhou, and Y. Feng. *Spectral and RIN properties of a single-frequency Raman fiber amplifier co-pumped by ASE source*, Optics Express **29**., 15764 (May 2021). DOI: 10.1364/OE.424063 (cit. on pp. 59, 66).

[187] Moriya, P. H., Y. Singh, K. Bongs, and J. E. Hastie. *Sub-kHz-linewidth VECSELs for cold atom experiments*, Optics Express **28**., 15943 (May 2020). DOI: 10.1364/OE.390982 (cit. on p. 60).

[188] Moriya, P. H., R. Casula, G. A. Chappell, D. C. Parrotta, S. Ranta, H. Kahle, M. Guina, and J. E. Hastie. *InGaN-diode-pumped AlGaInP VECSEL with sub-kHz linewidth at 689 nm*, Optics Express **29**., 3258 (Feb. 2021). DOI: 10.1364/OE.416210 (cit. on p. 60).

[189] Nazarova, T. "Towards the Quantum Noise Limit in Ramsey-Borde Atom Interferometry." PhD thesis. Hannover: Gottfried Wilhelm Leibniz Universität Hannover, 2007 (cit. on p. 60).

[190] Hald, J. and V. Ruseva. *Efficient suppression of diode-laser phase noise by optical filtering*, Journal of the Optical Society of America B **22**., 2338 (Nov. 2005). DOI: 10.1364/JOSAB.22.002338 (cit. on p. 60).

[191] Zhang, Y., K. Hayasaka, and K. Kasai. *Efficient noise suppression of an amplified diode-laser by optical filtering and resonant optical feedback*, Applied Physics B **86**., 643–646 (Feb. 2007). DOI: 10.1007/s00340-006-2436-2 (cit. on p. 60).

[192] Li, L., W. Huie, N. Chen, B. DeMarco, and J. P. Covey. *Active Cancellation of Servo-Induced Noise on Stabilized Lasers via Feedforward*, Physical Review Applied **18**., 064005 (Dec. 2022). DOI: 10.1103/PhysRevApplied.18.064005 (cit. on pp. 60, 101).

[193] Bagheri, M., F. Aflatouni, A. Imani, A. Goel, and H. Hashemi. *Semiconductor laser phase-noise cancellation using an electrical feed-forward scheme*, Optics Letters **34**., 2979 (Oct. 2009). DOI: 10.1364/OL.34.002979 (cit. on p. 60).

[194] Parniak, M., I. Galinskiy, T. Zwettler, and E. S. Polzik. *High-frequency broadband laser phase noise cancellation using a delay line*, Optics Express **29**., 6935 (Mar. 2021). DOI: 10.1364/OE.415942 (cit. on p. 60).

[195] Okoshi, T., K. Kikuchi, and A. Nakayama. *Novel method for high resolution measurement of laser output spectrum*, Electronics Letters **16**., 630 (July 1980). DOI: 10.1049/el:19800437 (cit. on p. 63).

[196] Karpov, V. I. and W. R. L. Clements. “Amplification Properties of Raman Fiber Amplifiers for Narrowband Single Frequency Sources,” *2020 International Conference Laser Optics (ICLO)*. IEEE, Nov. 2, 2020. DOI: 10.1109/ICLO48556.2020.9285636 (cit. on p. 66).

[197] Ivanov, E. N. and L. Hollberg. “Wide-Band Suppression of Laser Intensity Noise,” *2007 IEEE International Frequency Control Symposium Joint with the 21st European Frequency and Time Forum*. 2007 IEEE International Frequency Control Symposium Joint with the 21st European Frequency and Time Forum. ISSN: 1075-6787. Geneva, Switzerland: IEEE, May 2007, pp. 1082–1087. DOI: 10.1109/FREQ.2007.4319246 (cit. on p. 67).

[198] Richerme, P., Z.-X. Gong, A. Lee, C. Senko, J. Smith, M. Foss-Feig, S. Michalakis, A. V. Gorshkov, and C. Monroe. *Non-local propagation of correlations in quantum systems with long-range interactions*, Nature **511**., 198–201 (July 2014). DOI: 10.1038/nature13450 (cit. on p. 72).

[199] Thaicharoen, N., S. A. Miller, and G. Raithel. *Expansion behavior and pair correlations in continuously excited Rydberg systems*, Physical Review A **98**., 023402 (Aug. 2018). DOI: 10.1103/PhysRevA.98.023402 (cit. on pp. 75, 78).

[200] Grünzweig, T., A. Hilliard, M. Mcgovern, and M. F. Andersen. *Near-deterministic preparation of a single atom in an optical microtrap*, Nature Physics **6.**, 951–954 (Dec. 2010). DOI: 10.1038/nphys1778 (cit. on p. 79).

[201] Weimer, H. “Quantum many-body physics with strongly interacting Rydberg atoms.” PhD thesis. Stuttgart: Universit¨at Stuttgart, 2010 (cit. on p. 82).

[202] Zeiher, J., P. Schauss, S. Hild, T. Macrì, I. Bloch, and C. Gross. *Microscopic Characterization of Scalable Coherent Rydberg Superatoms*, Physical Review X **5**. (Aug. 2015). DOI: 10.1103/PhysRevX.5.031015 (cit. on p. 82).

[203] Signoles, A., T. Franz, R. Ferracini Alves, M. Gärttner, S. Whitlock, G. Zürn, and M. Weidemüller. *Glassy Dynamics in a Disordered Heisenberg Quantum Spin System*, Physical Review X **11**., 011011 (Jan. 2021). DOI: 10.1103/PhysRevX.11.011011 (cit. on p. 82).

[204] Sachdev, S. *Quantum Phase Transitions*. 2nd edition. Harvard University, Massachusetts: Cambridge University Press, May 2011 (cit. on p. 82).

[205] Kim, K., M. S. Chang, S. Korenblit, R. Islam, E. E. Edwards, J. K. Freericks, G. D. Lin, L. M. Duan, and C. Monroe. *Quantum simulation of frustrated Ising spins with trapped ions*, Nature **465.**, 590–593 (June 2010). DOI: 10.1038/nature09071 (cit. on pp. 83, 92).

[206] Periwal, A., E. S. Cooper, P. Kunkel, J. F. Wienand, E. J. Davis, and M. Schleier-Smith. *Programmable interactions and emergent geometry in an array of atom clouds*, Nature **600.**, 630–635 (Dec. 2021). DOI: 10.1038/s41586-021-04156-0 (cit. on p. 83).

[207] Urvoy, A., Z. Vendeiro, J. Ramette, A. Adiyatullin, and V. Vuletić. *Direct Laser Cooling to Bose-Einstein Condensation in a Dipole Trap*, Physical Review Letters **122.**, 203202 (May 2019). DOI: 10.1103/PhysRevLett.122.203202 (cit. on p. 89).

[208] Li, M.-D., W. Lin, A. Luo, W.-Y. Zhang, H. Sun, B. Xiao, Y.-G. Zheng, Z.-S. Yuan, and J.-W. Pan. *High-powered optical superlattice with robust phase stability for quantum gas microscopy*, Optics Express **29.**, 13876 (Apr. 2021). DOI: 10.1364/OE.423776 (cit. on pp. 101, 111).

[209] Kim, D., A. Keesling, A. Omran, H. Levine, H. Bernien, M. Greiner, M. D. Lukin, and D. R. Englund. *Large-scale uniform optical focus array generation with a phase spatial light modulator*, Optics Letters **44.**, 3178 (June 2019). DOI: 10.1364/OL.44.003178 (cit. on pp. 103, 111).

[210] Guardado-Sanchez, E., B. M. Spar, P. Schauss, R. Belyansky, J. T. Young, P. Bienias, A. V. Gorshkov, T. Iadecola, and W. S. Bakr. *Quench Dynamics of a Fermi Gas with Strong Nonlocal Interactions*, Physical Review X **11.**, 21036 (May 2021). DOI: 10.1103/PhysRevX.11.021036 (cit. on p. 105).

[211] Tarabunga, P. S., F. M. Surace, R. Andreoni, A. Angelone, and M. Dalmonte. *Gauge-Theoretic Origin of Rydberg Quantum Spin Liquids*, Physical Review Letters **129.**, 195301 (Nov. 2022). DOI: 10.1103/PhysRevLett.129.195301 (cit. on p. 107).

[212] Lester, B. J., N. Luick, A. M. Kaufman, C. M. Reynolds, and C. A. Regal. *Rapid Production of Uniformly Filled Arrays of Neutral Atoms*, Physical Review Letters **115.**, 073003 (Aug. 2015). DOI: 10.1103/PhysRevLett.115.073003 (cit. on p. 111).

[213] Covey, J. P., I. S. Madjarov, A. Cooper, and M. Endres. *2000-Times Repeated Imaging of Strontium Atoms in Clock-Magic Tweezer Arrays*, Physical Review Letters **122.**, 173201 (May 2019). DOI: 10.1103/PhysRevLett.122.173201 (cit. on p. 111).

[214] Zhao, Y. *et al. High-finesse cavity external optical feedback DFB laser with hertz relative linewidth*, Optics Letters **37.**, 4729 (Nov. 2012). DOI: 10.1364/OL.37.004729 (cit. on p. 111).

[215] Samutpraphoot, P., S. Weber, Q. Lin, D. Gangloff, A. Bylinskii, B. Braverman, A. Kawasaki, C. Raab, W. Kaenders, and V. Vuletić. *Passive intrinsic-linewidth narrowing of ultraviolet extended-cavity diode laser by weak optical feedback*, Optics Express **22.**, 11592 (May 2014). DOI: 10.1364/OE.22.011592 (cit. on p. 111).

[216] Schymik, K.-N., B. Ximenez, E. Bloch, D. Dreon, A. Signoles, F. Nogrette, D. Barredo, A. Browaeys, and T. Lahaye. *In situ equalization of single-atom loading in large-scale optical tweezer arrays*, Physical Review A **106.**, 022611 (Aug. 2022). DOI: 10.1103/PhysRevA.106.022611 (cit. on p. 111).

[217] Aman, J. A., B. J. Desalvo, F. B. Dunning, T. C. Killian, S. Yoshida, and J. Burgdörfer. *Trap losses induced by near-resonant Rydberg dressing of cold atomic gases*, Physical Review A **93.**, 43425 (Apr. 2016). DOI: 10.1103/PhysRevA.93.043425 (cit. on p. 112).

[218] Camy, G., C. Bordé, and M. Ducloy. *Heterodyne saturation spectroscopy through frequency modulation of the saturating beam*, Optics Communications **41**., 325–330 (May 1982). DOI: 10.1016/0030-4018(82)90406-0 (cit. on p. 114).